UNIVERSITY OF SOUTHAMPTON

FACULTY OF ENGINEERING AND THE ENVIRONMENT

Astronautics Research Group

Asteroid Impact Risk

by

Clemens M. Rumpf

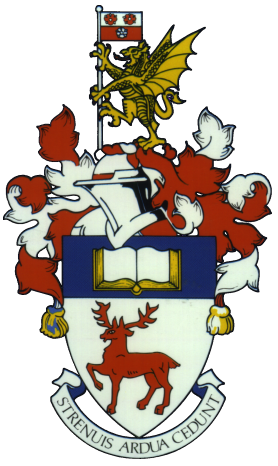

Supervisors:
Doctor Hugh G. Lewis
Professor Peter M. Atkinson

December 20th, 2016

UNIVERSITY OF SOUTHAMPTON

ABSTRACT

FACULTY OF ENGINEERING AND THE ENVIRONMENT
Astronautics Research Group

ASTEROID IMPACT RISK

by Clemens M. Rumpf

Asteroid impacts are a hazard to human populations. A method to assess the impact risk of hazardous asteroids was developed in this work, making use of the universal concept of risk culminating in the Asteroid Risk Mitigation Optimization and Research (ARMOR) tool. Using this tool, the global spatial risk distribution of a threatening asteroid can be calculated and expressed in the units of expected casualties (= fatalities). Risk distribution knowledge enables disaster managers to plan for a potential asteroid impact through identification of high risk regions and estimation of total risk as a scalar value. Expressing the risk in terms of expected casualties would allow the placement of the asteroid threat on the same scale as other human hazards. Thus, this unit provides an accessible way of defining thresholds for asteroid threat response protocols, of communicating the threat utilizing a new hazard scale, and of allocating adequate resources to address the hazard by comparison with other natural disasters. To accomplish risk estimation, vulnerability models were needed that relate the severity of impact effects (wind blast, overpressure shock, thermal radiation, cratering, seismic shaking, ejecta outthrow, and tsunami) on the human population and a novel comprehensive suite of such models were derived and presented. The need for high fidelity impact effect and vulnerability modelling, as opposed to a simplified, impact location based approach, for risk estimation of a specific asteroid threat was analysed and confirmed. Subsequently, the method of ARMOR was applied to asteroid 2015 RN35 to produce an example risk distribution output. Additional analysis shows that the general impact location distribution of asteroids is approximately uniform, confirming, for the first time, a common assumption made in planetary defense. Extensive global simulations were performed utilizing an artificial sample of 50,000 impactors with sizes up to 400 m to identify which impact effects are most hazardous to the human population. Aerothermal effects are most hazardous while tsunamis only contribute moderately to the overall hazard. The average land impactor is an order of magnitude more dangerous than a similar water impactor and asteroids smaller than 50-60 m (density $\approx 3100\,^{\mathrm{kg}}/_{\mathrm{m}^3}$) are expected to airburst rather than reach the surface. Furthermore, the average loss estimate for asteroid impactors enables fast threat analysis of newly discovered asteroids and helps determine the asteroid size that contributes most to the residual asteroid impact risk. These results provide new insights to inform efficient preparation for a future asteroid threat. In the future, ARMOR can be used to perform on-ground risk driven asteroid deflection mission design which would reduce risk of an incoming asteroid progressively and this is not accomplished with current methods.

Declaration of Authorship

I, Clemens M. Rumpf, declare that this thesis, titled *Asteroid Impact Risk*, and the work presented in it are my own and has been generated by me as the result of my own original research.

I confirm that:

1. This work was done wholly or mainly while in candidature for a research degree at this University;
2. Where any part of this thesis has previously been submitted for a degree or any other qualification at this University or any other institution, this has been clearly stated;
3. Where I have consulted the published work of others, this is always clearly attributed;
4. Where I have quoted from the work of others, the source is always given. With the exception of such quotations, this thesis is entirely my own work;
5. I have acknowledged all main sources of help;
6. Where the thesis is based on work done by myself jointly with others, I have made clear exactly what was done by others and what I have contributed myself;
7. Either none of this work has been published before submission, or parts of this work have been published as: Rumpf et al. (2016b,a, 2017b,a):

Signed: .....

Date: June 13, 2017

Contents

List of Figures

List of Tables

Nomenclature

AIDA	Asteroid Impact and Deflection Assessment
AIM	Asteroid Impact Monitoring
ARM	Asteroid Redirect Mission
ARMOR	Asteroid Risk Mitigation Optimization and Research (tool)
AU	Astronomical Unit ($= 1.4960 \times 10^8$ km)
BIC	Barycentric Inertial Coordinate system
DART	Double Asteroid Redirection Test
DCM	Direction Cosine Matrix
ECE	Earth Centred Ecliptic coordinate system
ECQ	Earth Centred Equatorial coordinate system
ESA	European Space Agency
IEO	Inner Earth Object
JAXA	Japanese Aerospace Exploration Agency
LIENAR	Lincoln Near-Earth Asteroid Research
LOV	Line of Variation
MOID	Minimum Orbit Intersection Distance
NASA	National Aeronautics and Space Administration
NEO	Near-Earth object
NEOWISE	NEO Wide-field Infrared Survey Explorer
PHO	Potentially Hazardous Object
SMPAG	Space Mission Planning Advisory Group
TAI	International Atomic Time
TBSA	Total Body Surface Area (applies to thermal radiation inury)
TNT	Trinitrotoluene
UT	Universal Time
UTC	Universal Time Coordinated
WISE	Wide-field Infrared Survey Explorer

A	Tsunami wave amplitude
A_{fr}	Final crater area
a	Semi major axis
C_D	Drag coefficient
c_0	Speed of sound

D	Distance
D_{tc}	Transient crater diameter
D_1	Yield energy scaled distance for blast wave
D_x	Blast wave scale distance
E	Energy
e	Epoch
f_p	Pancake factor
G	Universal Gravitational constant ($6.67428 \times 10^{-11}\,\mathrm{m^3/kg\,s^2}$)
GM	Gravitational Constant of a body with mass M
g_0	Standard gravitational acceleration of the Earth ($9.80665\,\mathrm{m/s^2}$)
H	Absolute Magnitude (Brightness)
h_{sea}	Sea depth at impact site
i_{seis}	Seismic Intensity (Modified Mercalli Intensity)
L_0	Asteroid Diameter at top of atmosphere
$L(z)$	Altitude dependent asteroid diameter
L_{disp}	Dispersion length scale
M	Seismic Richter scale magnitude
M_{eff}	Effective seismic Richter scale magnitude
m	Mass
P	Polynomial or Probability
$\boldsymbol{p}$	Asteroid Position Vector
p	Asteroid Trajectory
p_0	Airburst overpressure parameter
p_a	Ambient air pressure
p_e	Ejecta blanket load (pressure)
p_D	Peak overpressure at distance D
p_x	Scale pressure
q_h	Thermal energy flux density from airburst at a given altitude h
q_E	Thermal energy flux density from airburst at at the target
R	Risk or Radius
R_f	Fireball radius
$\boldsymbol{r}$	Position Vector
r	Earth Trajectory
S	Severity (Risk)
s	Beach slope
T	Orbital period
t	Time
U	Tsunami wave run-up
u	Wind speed
V	Vulnerability
$\boldsymbol{v}$	Velocity Vector

v	Speed (scalar velocity)
w	Tsunami wave length
Y_i	Impactor yield strength
z	altitude
z_*	Break up altitude
z_b	Airburst altitude
α	Asteroid albedo (reflectance) value
β	Airburst overpressure parameter
γ	Impact Angle
η_{lum}	Luminous efficiency
Θ	Sidereal Time Angle
λ	Longitude
ρ_0	Atmospheric ground density
ρ_e	Ejecta material density
ρ_i	Impactor density
ρ_t	Target density
$\rho(z)$	Atmospheric density at altitude z
τ	Normalized Time
Φ	Latitude
ϕ	Thermal radiative energy
Ψ	Exposure (Risk)
ξ	Irribaren number

Acknowledgements

I want to sincerely thank my two supervisors Dr Hugh G. Lewis and Prof Peter M. Atkinson for their unparalleled guidance, discussions and support. Hugh always provided new perspectives on problems leading to solutions which made this research possible. His calm reasoning and multi directional interest never failed to open a new window of opportunity when I sensed all close to failing. Equally, Pete was persistently available with his enthusiasm and feedback which was essential in producing the results and papers during this research period. His expertise in geography and risk analysis were crucial components in this multi-disciplinary project. Many of the exceptional side opportunities of this PhD such as winning a conference competition, writing for the guardian, participating in their podcast, presenting at the United Nations and representing the UK Space Agency twice during SMPAG meetings would not have materialized without the support and push from Hugh and Pete who complement each other amazingly as a supervisor team.

Thank you Hugh and Pete!

I would like to extend my sincere thanks to Giovanni B. Valsecchi for the productive discussions and assistance in the use of OrbFit.

Steven Chesley has dedicated his time to a number of paper reviews and provided us with a sample population of near-Earth objects.

Finally, I would like to thank my family who provided my with the liberty to follow my passion.

The authors acknowledge the use of the IRIDIS High Performance Computing Facility, and associated support services at the University of Southampton, in the completion of this work.

The work was supported by the Marie Curie Initial Training Network Stardust, FP7-PEOPLE-2012-ITN, Grant Agreement 317185.

I was sitting in the porch of the house at the trading station of Vanovara at breakfast time ... when suddenly in the north ... the sky was split in two and high above the forest the whole northern part of the sky appeared to be covered with fire. At that moment I felt great heat as if my shirt had caught fire; this heat came from the north side. I wanted to pull off my shirt and throw it away, but at that moment there was a bang in the sky, and a mighty crash was heard. I was thrown to the ground about three sajenes [about 7 meters] away from the porch and for a moment I lost consciousness... The crash was followed by noise like stones falling from the sky, or guns firing. The earth trembled, and when I lay on the ground I covered my head because I was afraid that stones might hit it.

- S.B. Semenov, eyewitness of 1908 Tunguska impact, 60 km south of impact

Chapter 1

Introduction

Asteroid impacts have been responsible for at least two major disruptions in the evolution of life (Alvarez et al., 1980; Plane, 2012) and today, they remain a potential hazard for the human population (Chyba et al., 1993; Popova et al., 2013).

During the formation of the Solar System, primordial gas and dust accreted to form the planets along with a myriad of smaller objects that are known as asteroids. Today, Earth collides with about 100 t of these objects on a daily basis (Plane, 2012) demonstrating that asteroid collisions with the Earth are more common than intuitively expected. Most of these objects - less than a meter across - are on the small end of the size spectrum, and produce nothing more than a captivating meteor during their passage through the atmosphere. On the other end of the spectrum, asteroids can reach sizes of many kilometres in diameter and a collision with such an object would have truly disastrous consequences for the planet. While it is practically certain that a kilometre sized impact event will not take place in the next 100 years (Boslough, 2013a), Earth frequently collides with asteroids of a few meters in diameter (NASA, 2014b). Such smaller impacts occur about once or twice per year (Brown et al., 2002). Objects measuring tens of meters can cause destruction on a local level if they hit a populated area. The events over Tunguska (Boslough, 2013a) in 1908 and Chelyabinsk (Brown et al., 2013) in 2013 are palpable examples for this category of impacts. Asteroids can impact any region on Earth (Rumpf et al., 2016b) and, thus, the asteroid hazard concerns the entire world population. Asteroid impacts fall into the category of natural disasters but unlike other natural disasters, the occurrence of an asteroid impact can be accurately predicted and turned into a non-event by deflecting the asteroid.

Asteroid deflection technology only became feasible recently, during the space age. In fact, the feasibility of one deflection method has already been demonstrated by the Deep Impact mission (A'Hearn et al., 2005) that deliberately collided with a comet in 2005. With the realization that asteroid deflection is possible, self preservation provides a strong motivation for our civilization to actually develop technologies and implement

procedures that will enable us to deflect an asteroid. This is recognized at the international level where, in 2013, the United Nations formally endorsed the recommendation to establish the Space Mission Planning Advisory Group (SMPAG) and the International Asteroid Warning Network (IAWN) to lead the international effort to produce coherent threat response procedures and capabilities, and to warn about threatening asteroids (UNCOPOUS and ESA, 2014).

While asteroid deflection is possible in principle, it can only be accomplished when an incoming asteroid has been discovered before impact. Currently, sky surveys such as Pan-STARRS and Catalina Sky Survey increase our knowledge about the asteroid environment in the Solar System. More capable systems are planned to extend this knowledge base and to focus on smaller asteroids (tens of meters diameter) of which less than 1% have been discovered (Shapiro et al., 2010).

Today, about 15,000 near Earth-objects (NEO) have been discovered, and with continuously improving observational capabilities, this number is poised to increase to over 500,000 (larger than 30 m) in the next 10 years (Shapiro et al., 2010). With the growing NEO catalogue there is a better chance that an incoming asteroid will be discovered before impact and this allows humankind to react to the threat. In the event of such a discovery, a response procedure needs to be in place that triggers actions based on the asteroid characteristics (size, composition, trajectory), reaction time and the risk that the asteroid poses to the population and associated structures (Schweickart, 2009). For small asteroids (maximum diameter of a few tens of meters) and/or short reaction times (<3 years), evacuation of the threatened region might be the appropriate response (Norlund, 2013). For larger asteroids, and given enough reaction time, a deflection mission can be conceived (NASA, 2006) (Appendix D introduces possible deflection technologies). In either case, the risk for the population on the ground will play a vital role in determining the appropriate response to the threat.

Risk is a key element in formulating an adequate response to the asteroid hazard and this work's primary motivation was to develop a framework that estimates risk in an improved way compared to what is available today. Specifically, the risk needs to be quantifiable in such a way as to facilitate determination of an adequate threat response to the background hazard as well as to a current threat. Ultimately, the work should enable deflection mission design that reduces risk and protects the population while the impact point is moved across the Earth by means of a deflection mission. Today's deflection techniques do not consider on-ground risk and this setup allows for the possibility that the deflection mission moves the impact point by accident to a position where the population is more vulnerable, exacerbating the threat. These goals require a tool that can resolve impact risk spatially on the global map and that can determine impact outcomes at any given impact point.

Beyond the satisfaction of this work's goals, such a tool would also be able to help increase understanding of the asteroid impact hazard. A non-exhaustive list of relevant questions is:

- Are some regions more at risk than others?
- How detailed need simulation efforts be to produce sufficiently accurate risk estimates?
- What is the expected outcome of a given impact in terms of damage/casualties?
- What is the impact experience and which impact effects dominate the scenario?
- Is there a significant difference in outcomes between water and land impactors?

In this research, the Asteroid Risk Mitigation and Optimization Research (ARMOR) tool was developed and applied to the goals and questions raised above. A general introduction to the nature of asteroids, what is known about them and how this is relevant to planetary defense is given in chapter 2. To accomplish asteroid risk assessment, the ARMOR tool has been developed and its methodology is presented in chapter 3. Results concerning the distribution of asteroid impact location, impact speed, impact angle, as well as risk analysis and investigation of impact effect dominance are provided in chapter 4. An overall discussion of the work performed during the course of this research and how it ties into the field of planetary defense is presented in chapter 5. Finally, chapter 6 and chapter 7 draw conclusions and recommend future work that builds on the results presented here.

In this work, the term casualties has been used synonymously with the term fatalities.

Chapter 2

Asteroids and Planetary Defense

Asteroids are remnants of the solar system formation process and are thus part of the natural environment in space. All asteroids were originally formed by the accretion of primordial dust into planetesimals that underwent processes such as internal and external heating, internal differentiation, collisions and breakups (Gradie and Tedesco, 1982; Chapman et al., 1978).

Asteroids are concentrated mainly in a region between Mars and Jupiter called the Asteroid Belt and it is visualized in Figure 2.1. For the sake of completeness two other asteroid rich regions shall be mentioned. The Kuiper belt is located beyond Pluto's orbit and the Oort Cloud extends one quarter the distance to our closest star, Proxima Centauri. All of these regions can be the source of asteroids travelling through the inner solar system when gravitational perturbations place them on such orbits. Specifically, the asteroids of the Asteroid Belt are perturbed chiefly by Jupiter's gravitational attraction and these perturbations can cause asteroids to move onto eccentric orbits, crossing the orbit of the Earth such that they are on a potential collision course with the Earth. Planetary Defense is the scientific field that deals with the potential threat of asteroids colliding with the Earth. In fact, the Earth shows many signs of its collisional history and section 2.1 reports on this historical record.

2.1 Historical Collision Record

The Earth has a rich collisional record but many impact features are hard to detect because processes such as erosion, plate tectonics and the influence of weather and vegetation rejuvenate the Earth's surface continuously. Nonetheless, a significant record of past collisions exist and are introduced in this section.

Currently, asteroids collide with the Earth frequently on a daily basis and these collisions amount to about 100 t of asteroid material being delivered to the Earth daily (Plane,

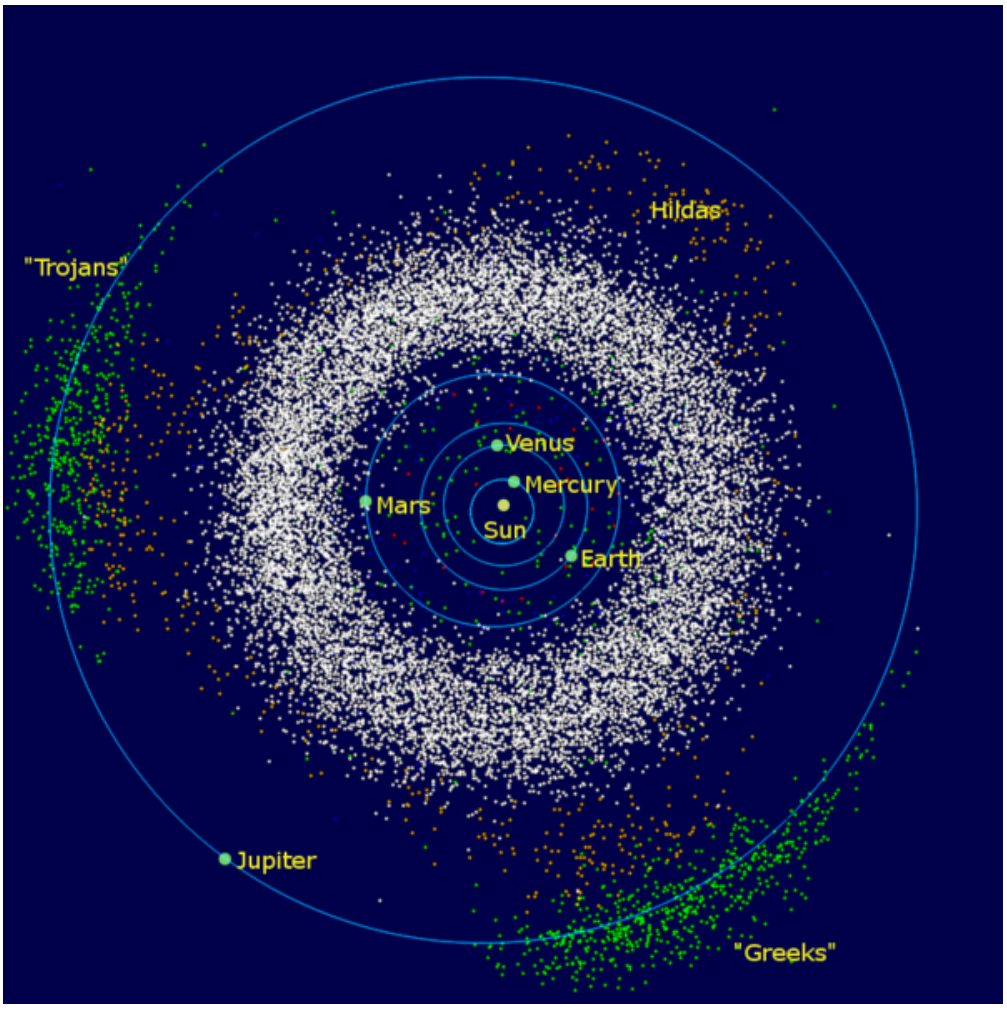

Figure 2.1: Map of the inner solar system with the asteroid belt (white dots) and asteroid concentrations in Jupiter orbit (green and red dots). (Commons, 2014)

2012) or up to 500 t when averaged over longer periods of time (10 years) (Ceplecha, 1992). Of course, the majority of these collisions are with the much more numerous small particles (see section 2.2.3) and these only produce a small meteor, also known as a shooting star. However, larger asteroid sizes release more energy and in the metre size regime, asteroids explode in mid air in an event called an airburst.

2.1.1 Airbursts

Airbursts occur multiple times per year and their explosion signature is recorded by a global network of infrasound microphones originally installed to enforce the nuclear test ban treaty (Silber et al., 2009). Figure 2.2 shows the locations of these high energy asteroid explosions in the period between 2000 and 2013. The data show that twice a year asteroids explode in the Earth's atmosphere with an energy equivalent of the Hiroshima bomb (B612 Foundation et al., 2014). Notable instances of historic airburst

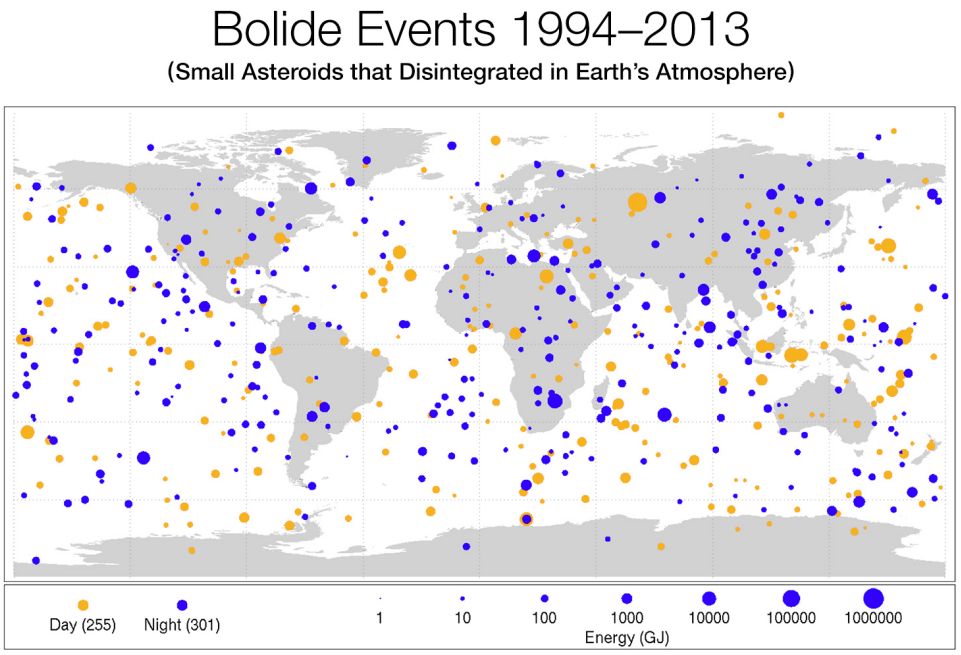

Figure 2.2: Recorded atmospheric asteroid explosions between 1994 and 2013. Their estimated kinetic energy is specified in Giga Joule. For comparison: The nuclear bomb detonated over Hiroshima corresponded to about 54000 GJ or 13 kt_{TNT}. The Chelyabinsk event is the large, orange marker in northern Russia. (NASA, 2014b)

events are the Tunguska event in 1908, the Chelyabinsk event in 2013 and the Lybian desert glass event.

Tunguska, 1908 On June 30th, 1908, an asteroid with a diameter of about 50 m entered the atmosphere over Siberia in Russia (Brown et al., 2002; Chyba et al., 1993; Boslough and Crawford, 2008). It disintegrated before impacting the ground creating a hot blast wave that reached the surface. The blast carried enough energy to burn and flatten 2000 km^2 of forest (Boslough and Crawford, 2008)[1]. This region of Earth is scarcely populated and, thus, no casualties were reported but an eyewitness account of this dramatic event is given in the opening of this work.

Chelyabinsk, 2013 At 09:20 local time on February 15th, 2013, an asteroid exploded at an altitude of about 30 km and about 50 km away from the city of Chelyabinsk in Russia (Popova et al., 2013). The blast had an estimated equivalent energy yield of 470 kt_{TNT}. It was strong enough to shatter the windows in Chelyabinsk injuring about 1500 people. Fragments from the 20 m asteroid fell to the ground of which many were later recovered. The incident was well documented because it is common for cars in that area to operate dashboard cameras that recorded the event.

[1]The area is comparable to today's Greater London area.

Glass in the Libyan Desert An area of 6500 km^2 in the Libyan desert was melted into glass about 29 million years ago and the likely cause for this phenomenon is a high energy airburst. The airburst created a plasma with a temperature of roughly 5000 K (Boslough and Crawford, 2008) that descended to the ground and melted the sand near the surface to glass. A similar but larger event (690,000 km^2) is suspected to have occurred over the Muong-Nong area in South-East Asia.

2.1.2 Surface Impact

Surface impacts occur when the incoming asteroid is of sufficiently large size - larger than $\approx$ 50 m. Notable examples are the Barringer Crater in the USA or Manicouagan in Canada (Figure 2.3). In fact, these large structures are visible from space testifying to the enormous energies that can be released during an asteroid impact.

Figure 2.3: Manicouagan impact crater in Canada is visible in the centre of the image. The impact structure forms a circular lake and is seen from the International Space Station (ISS) with Aurora Borealis above the horizon. (Pettit, 2012)

While most impact features fade away on the Earth's surface due to erosive processes, the common occurrence of asteroid collisions is visible on the Moon where the surface is covered with craters because no protective atmosphere shields from smaller asteroids and the lack of erosive processes preserves the crater record. Still, hundreds of impact features have been discovered on the Earth and they are mapped in Figure 2.4. The realization that asteroid collisions are, in fact, a common natural occurrence provides additional motivation to study them and their potential consequences for humankind.

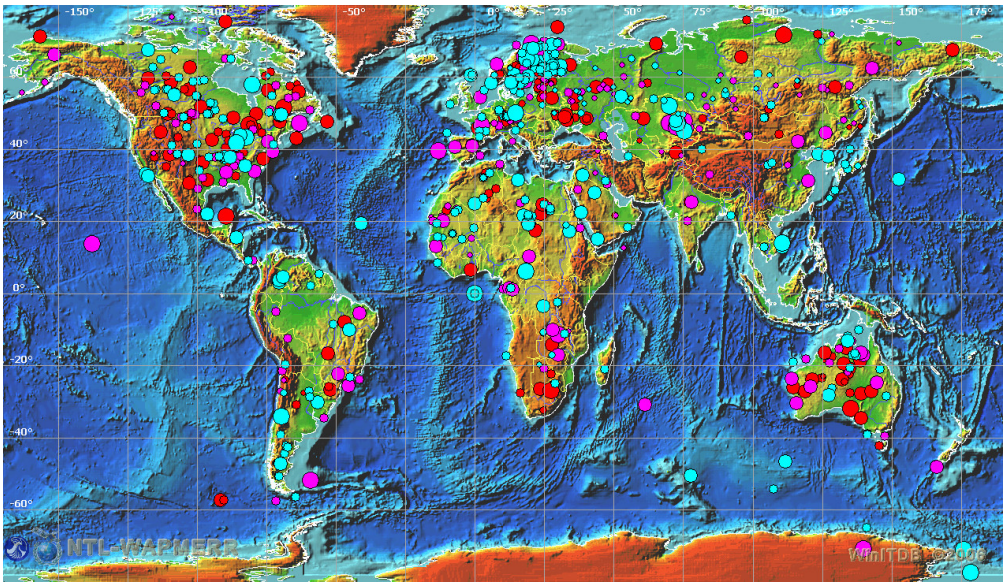

Figure 2.4: Map of confirmed (red), prospective for verification (magenta) and proposed for further study (blue) impact structures on the Earth. Size of circles is proportional to the crater diameter. Altogether almost 800 structures are shown. (EDEIS et al., 2006)

Section 2.2 presents some of the past and current efforts in characterizing and increasing understanding of the asteroid population.

2.2 Observation and Exploration

Asteroids have been observed with ground based telescopes, in principle, similar to the one utilized by Guiseppe Piazi to discover the first asteroid (now dwarf planet) Ceres in 1801. Ground based observations remain an important contributor to the discovery of new objects and their characterization. Complementing ground based observations are deep space exploration missions that visit asteroids to explore them in situ and space based telescopes that aid discovery and characterization.

2.2.1 Ground Based Projects

Until about 1990, asteroids were predominantly discovered by human observers equipped with telescopes. Since then, automatic surveys have become the norm and some of them are listed below.

SpaceWatch Project This observation programme is operated by the Lunar and Planetary Laboratory at the University of Arizona. In 1990 the SpaceWatch project was the first survey to use automatic detection of asteroids. Its observational facilities

are two telescopes with mirror diameters of 0.9 m and 1.8 m. The telescopes are located on the summit of Kitt Peak in Arizona.

Lincoln Near-Earth Asteroid Research (LINEAR) The project is a joint-venture between the US Air Force, NASA and Massachusetts Institute of Technology. It had the highest discovery rate of all surveys between 1998 and 2005 (NASA, 2014a) when Catalina Sky Survey became more successful. LINEAR is comprised of two 1 m and one 0.5 m telescopes that are located at the White Sands Missile Range in New Mexico, USA.

Catalina Sky Survey The Catalina Sky Survey is operated by the University of Arizona. The survey utilizes two 1.5 m telescopes on the summit of Mt. Lemmon and one 0.68 m telescope near Mt. Bigelow in Arizona, USA. Until 2014, Catalina was responsible for most NEO discoveries each year having surpassed LINEAR in 2005.

PanSTARRS The acronym PanSTARRS is short for Panoramic Survey Telescope and Rapid Response System. The survey is operated by a collaboration of scientific institutions including the University of Hawaii. Two 1.8 m telescopes located at Haleakala in Hawaii are the instruments used by PanSTARRS. As of 2014, PanSTARRS discovers most asteroids compared to other surveys.

Large Synoptic Survey Telescope The LSST is under construction in Chile at the time of writing and it is planned to be operational in 2022. Using a 8 m mirror, its purpose also includes the discovery of asteroids and it is expected to observe over five million main belt asteroids (as opposed to the currently known 500,000) (Ivezic et al., 2014). Due to its large field of view of 3.5 °, the LSST is capable of covering wide areas of the sky which makes it especially useful for asteroid surveys.

2.2.2 Space Based Projects

In addition to observational campaigns, space missions visit asteroids and comets to explore their nature and aid discovery. Comets are very similar to asteroids but distinguish themselves through a much lower density (typically around $1\,{}^{\mathrm{kg}}/_{\mathrm{m}^3}$) and through the presence of volatiles such as water in their physical composition. These volatiles are prone to evaporate due to solar radiation, especially near their perihelion, causing the development of a cometary atmosphere called coma around the comet nucleus and the formation of a tail. Comets are chiefly found in the asteroid regions beyond Jupiter and can come close to the Earth when they are on highly eccentric orbits but are much rarer

than asteroids in Earth's vicinity. This section lists the space missions in chronological order with respect to their launch date[2] that visited asteroids and comets.

Giotto The European Space Agency (ESA) launched Giotto on July 2nd 1985. Giotto flew by Halley's comet at a distance of 596 km on March 14th, 1986 and successfully took pictures of the comet (Keller et al., 1986). The spacecraft was hit by debris multiple times during the flyby which caused mission interruptions but no critical failure.

Stardust Stardust was launched by NASA on February 7th, 1999. Its objective was to collect coma[3] particles from comet Wild 2 and return these to the Earth (Tsou, 2003). On its way to Wild 2, the spacecraft made a flyby of the asteroid Annefrank. Samples of Wild 2 were successfully collected on January 2nd, 2004 and returned to Earth on January 16th, 2006. After the Earth flyby to return the sample, Stardust's mission was extended to image the asteroid Tempel 1 and successfully flew by that comet on February 15th, 2011 at a distance of 181 km (Veverka et al., 2012) and retrieved imagery. Tempel 1 is the same asteroid that was previously visited by Deep Impact and the encounter thus enabled an analysis of the topography's temporal change.

Hayabusa The Japanese Aerospace Exploration Agency (JAXA) conducted the first successful asteroid sample return mission with Hayabusa. Hayabusa launched on May 9th, 2003 from Japan on a trajectory to rendezvous with the asteroid Itokawa. Despite some technical problems, the spacecraft landed on Itokawa on November 19th, 2005 for the first time. A second landing was performed on November 25th. The collected samples were returned to the Earth on June 13th, 2010. Even though the sampling mechanism did not work as intended, the sample capsule did contain asteroid traces that could be analysed.

Rosetta Rosetta is an ESA mission that was launched on March 2nd, 2004 and arrived at its target comet 67P/Churymov-Gerasimenko on August 6th, 2014. The mission consisted of two vehicles, the orbiter Rosetta and the lander Philae. While Rosetta studied the comet remotely, Philae touched down on November 12th, 2014 and probed the comet's surface for 64 hours. The mission came to an end on September 30th, 2016.

Deep Impact NASA launched the Deep Impact mission on January 12th, 2005 to fly by and explore the comet Tempel 1 (A'Hearn et al., 2005). Part of the mission was an impactor spacecraft that collided with the comet the same year on July 4th. Prior to impact, the impactor separated from the main spacecraft and modified its trajectory

[2] Some of the missions are not launched yet. In these cases, the planned launch date is used.
[3] A coma is the dust cloud around a comet.

slightly to place itself on a collision course with Tempel 1. The near parallel trajectories allowed the main spacecraft to observe the impact and to obtain visual spectra of the ejecta. After the successful encounter with Tempel 1, the mission was extended and it subsequently visited comet Hartley in 2010. It is currently en route to visit asteroid 2002 GT in 2020.

NEO Wide-field Infrared Survey Explorer (NEOWISE) The space based telescope Wide-field Infrared Survey Explorer (WISE) was launched in 2009 and its main instrument is an actively cooled infrared 0.4 m telescope. The mission's original objective was the observation of the entire sky in the infrared wavelength. After its hydrogen coolant (needed to operate the main instrument) was depleted, the telescope was recommissioned to focus on the detection of NEOs with its secondary instruments (Mainzer et al., 2014). The new mission was called NEOWISE and ran in 2010 for 4 months. In 2013, NASA announced that NEOWISE will be restarted to aid in the discovery of Potentially Hazardous Objects (PHOs).

Hayabusa 2 JAXA currently operates the successor mission to Hayabusa and Hayabusa 2 launched on December 3rd, 2014 with an arrival date at the asteroid 1999JU3 in July 2018. Once there, it will release the mobile lander MASCOT (Mobile Asteroid Surface Scout), a project by the German Aerospace Center (DLR) and the French space agency (CNES), and two MINERVA-II surface robots by JAXA. MASCOT and MINERVA-II will be able to relocate themselves on the surface of the asteroid to take measurements. Hayabusa 2 also carries an explosive impactor that will generate a crater on the asteroid surface to reveal deeper surface layers for study. The explosion will eject surface particles into space of which some are to be collected by Hayabusa 2. The collected particles will be delivered to the surface of the Earth at the end of 2020 when the mission returns.

OSIRIS-REx This is an asteroid sample return mission conceived by NASA and it is planned to launch in late 2016 to visit asteroid Bennu in 2023 (Dworkin, 2014). Upon sample extraction, the mission will return the sample to the Earth in 2023.

AIDA: Asteroid Impact and Deflection Assessment AIDA is a planned, joint mission between ESA and NASA in which ESA builds the observing spacecraft AIM (Asteroid Impact Monitoring) and NASA contributes the impactor DART (Double Asteroid Redirection Test). AIM's launch date is October 2020 to arrive at the binary asteroid system Didymos in May 2022 for remote science operations (Cheng et al., 2013). Meanwhile, DART's launch is foreseen in July 2021 and would impact the smaller companion of the Didymos system in October 2022. For the first time, this mission would measure the momentum transfer between an impactor vehicle and an asteroid with implications for potential asteroid deflection mission design.

Asteroid Redirect Mission NASA has currently allocated a significant share of its resources to the planning and development of the Asteroid Redirect Mission (ARM). The mission is designed to capture a small asteroid (10 m size regime) and place it in lunar orbit. A manned mission to visit the asteroid in lunar orbit could happen no earlier than 2021. This mission would provide a great opportunity to have relatively easy access to an asteroid to study it.

2.2.3 Current Asteroid Knowledge

This section provides information about the asteroid population and the concept of absolute magnitude is important in this context.

Absolute Magnitude Absolute magnitude H is a measure of brightness for an asteroid and is used as indication of its size. The value describes the brightness of an object that is 1 AU away from the observer and illuminated by the Sun at 1 AU distance. The object is also assumed to be in opposition from the Sun relative to the observer. This geometry is physically impossible because it would require an observer to be placed within the Sun. However, the definition is useful as it provides an absolute brightness measure to compare objects that were observed in varying conditions. Brightness H is commonly assumed to be an indicator for asteroid diameter L_0 in metres based on the following empirical relationship[4]:

$$L_0 \approx \frac{1329}{\sqrt{\alpha}} 10^{-0.2H} \tag{2.1}$$

where α is the albedo value for the asteroid. Albedo is the fraction of the incident light that is reflected and this value has implications for the asteroid's size estimation. The European Space Agency uses an average value of 0.1 for asteroid size estimation according to Equation 2.1 (Universita Di Pisa and ESA, 2014) while NASA uses 0.14 (NASA, 2014a; Harris and D'Abramo, 2015).

2.2.3.1 Asteroid Population

Thanks to the missions and projects mentioned in section 2.2, the catalogue of known asteroids is growing (584,826 asteroids are known as of December 19th, 2016) and the understanding of their nature and physical properties is increasing. Figure 2.5 visualizes the distribution of the asteroid population over their absolute magnitude H (which is used for size estimation; see section 2.2.3) and it is clear that many more small asteroids (corresponding to large H) exist than larger ones (small H). Furthermore, the figure shows the current state of the catalogue of known asteroids. The catalogue is nearly

[4] According to ESA at: http://neo.ssa.esa.int/web/guest/risk-page

complete for very large asteroids sized > 1 km, which approximately corresponds to magnitude 18 (see next paragraph), because larger asteroids are easier to discover as they reflect more light. Most of the smaller asteroids remain undiscovered with only about 1% of asteroids larger than 140 m (≈ magnitude 22) observed today. An even lower proportion of smaller asteroids is known and this is why modern survey efforts need to target this size regime (<140 m) because asteroids larger than 15 m are a concern in terms of planetary defense.

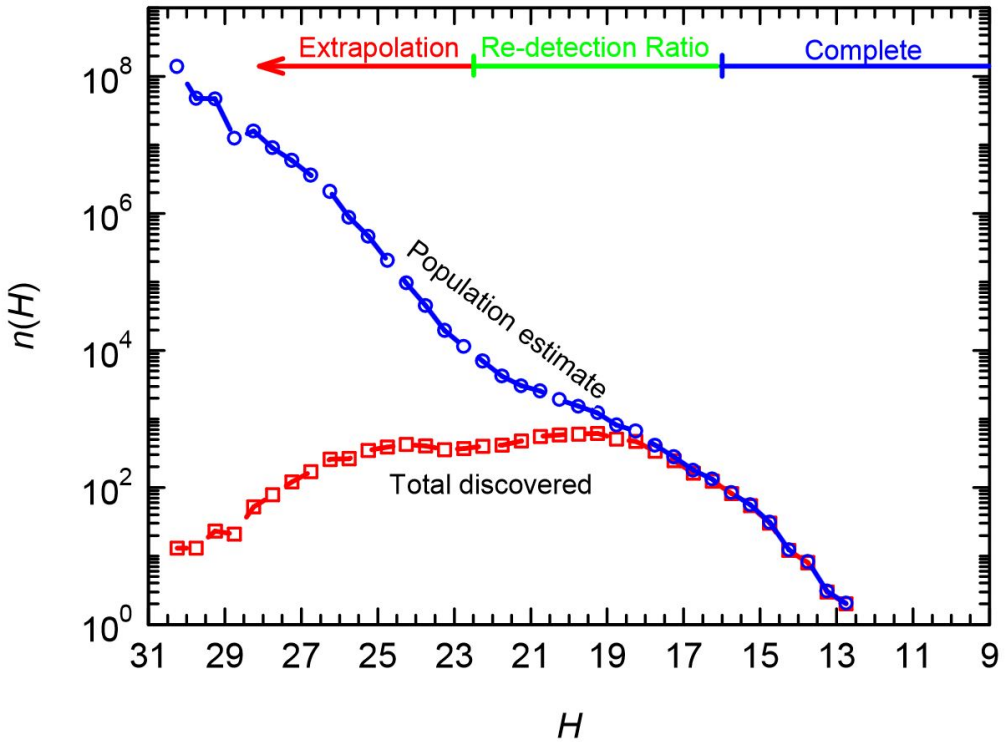

Figure 2.5: Known asteroid population in comparison with the estimated total asteroid population categorized by their absolute magnitude H (indicates approximately size) (Harris, 2014).

.

2.2.3.2 Physical Properties

The physical properties of asteroids are driven by their formation process and most asteroids were part of larger bodies, called planetessimals, that subsequently broke apart. While being in the planetesimal stage, the chemical components separated in the differentiation process driven by self induced gravity that acted on the components according to their densities. Subsequent breakups then produced objects that are highly concentrated in certain chemical components and this process explains the occurrence of objects such as metallic M-class asteroids (Bell et al., 1989) that can collide with the Earth. The chemical component distribution within the asteroid belt is not random but

shows distinct distributions with increasing semi major axis (Gradie and Tedesco, 1982). In general, it is assumed that most asteroids are loose "rubble piles" in which denser blocks are embedded in a loose conglomeration of particles. Missions such as Rosetta and AIDA are crucial to learn more about the internal composition of asteroids. The physical properties of asteroids are important for planetary defense because parameters such as density, structure, material, and albedo (to name a few) affect the estimated energy that is released during a collision and will also influence deflection mission design.

For the present work, asteroid densities were of special importance as this value allows to derive the asteroid mass following a size estimate and mass is important to calculate impact energy. The asteroid population density distribution is still connected with large uncertainties primarily due to the challenges of measuring physical characteristics of asteroids in general (Carry, 2012). One way of deducing asteroid densities is investigating data from meteorites which are asteroids that have fallen to the surface of the Earth.

Meteorite fall statistics indicate that the majority, or about 75%, of all meteorites are ordinary chondrites (average density: 3100 $^{kg}/_{m^3}$, albedo: 0.03 - 0.10) while roughly 15% are other chondrites (average density: 3100 $^{kg}/_{m^3}$, albedo: 0.10 to 0.22), and about 5-10% are metallic (average density: 7000 $^{kg}/_{m^3}$, albedo: 0.1–0.2) (Britt, 2014; Zellner, 1979). These statistics are reflected in table 2.1. Ordinary chondrites are linked to S-complex

Meteorite Type	**Density** $[^{kg}/_{m^3}]$	**Meteorite Occurrence Rate**
Ordinary Chondrites	≈ 3100	75 %
Other Chondrites	≈ 3100	15 %
Metallic	≈ 7000	5-10 %

Table 2.1: Meteorite types with their densities and occurrence rates (Britt, 2014).

asteroids (DeMeo et al., 2015) and a sample of 50 S-complex asteroids shows that these asteroids exhibit densities of around $2000 - 4000\,^{kg}/_{m^3}$ as shown in Figure 2.6 (Carry, 2012). Based on these findings, a bulk density value of 3100 $^{kg}/_{m^3}$ has been selected for this work.

It should be noted that statistical density distributions have been published which indicate a lower average density value of roughly 2200 $^{kg}/_{m^3}$ than used in this thesis (Mathias et al., 2017). While Mathias et al. (2017) acknowledge that density estimates remain a subject of great uncertainty, their work represents a good methodological approach to the problem of density estimation and should be considered in the future.

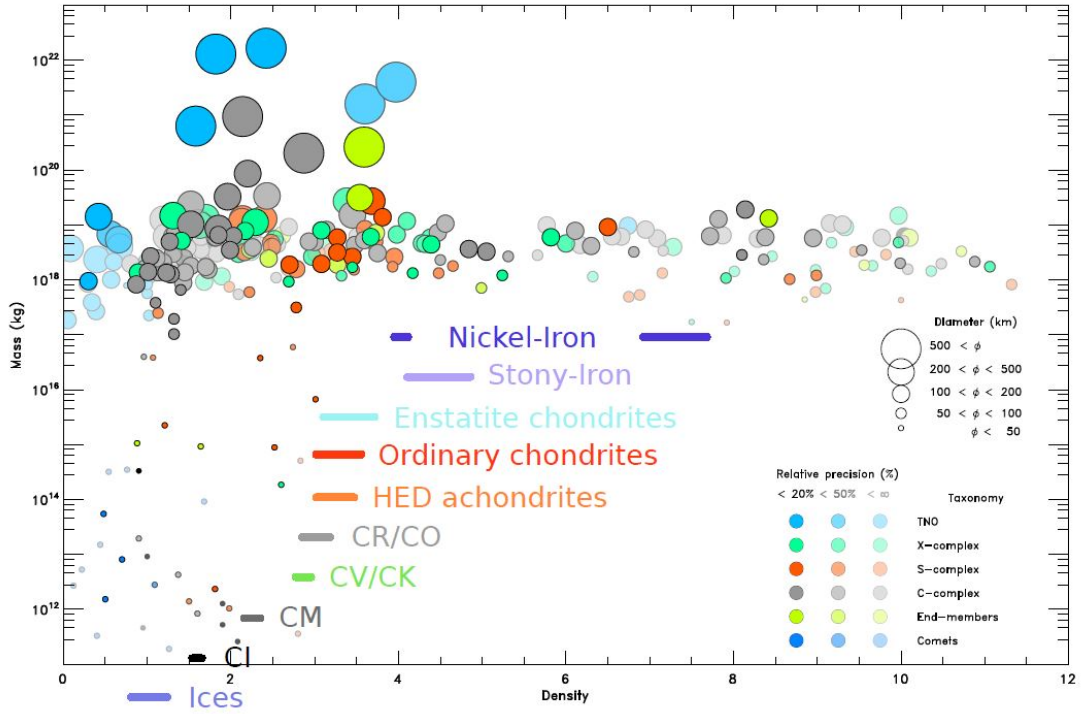

Figure 2.6: Density vs mass statistics for a sample of 6 taxonomical asteroid classes. In addition, meteorite densities are indicated as thick coloured lines. Figure published in (Carry, 2012).

2.3 Asteroid Impact Hazard

Classifications such as near-Earth objects or potentially hazardous asteroids have been divised to facilitate research on the topic of the hazard of Earth colliding asteroids. Quantification of the threat is another important subject that addresses the asteroid impact hazard and these concepts are introduced here.

2.3.1 Near-Earth Objects

Near-Earth objects (NEOs) are asteroids that can potentially impact the Earth due to their orbital geometry which brings them close to Earth's orbit. The discovered number of NEOs is visualized in Figure 2.7. Again, it becomes clear that most asteroids larger than 1 km have been discovered because after a notable increase in new discoveries around 2000, the number plateaus after 2010. The rate of discovery continues to increase for smaller asteroids as more observatories become operational.

Four NEO Groups Finer classification of the orbital geometry of NEOs allows them to be subdivided into the four groups of Apollos, Atens, Armors and inner Earth objects (IEOs) as shown in Figure 2.8. Apollos are the most numerous group because these NEOs

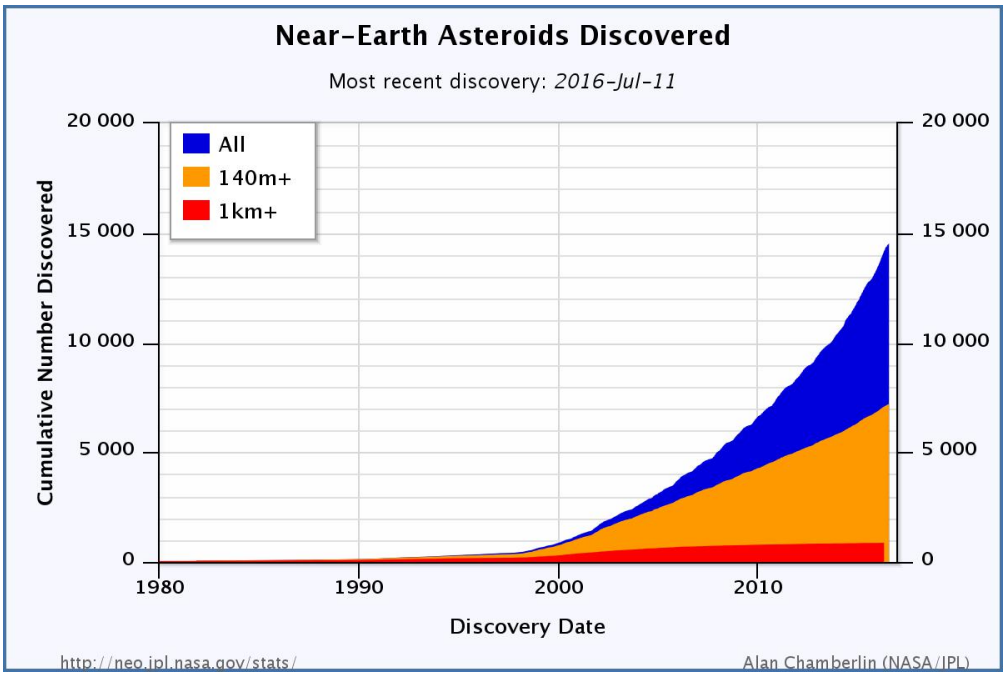

Figure 2.7: Historical NEO discovery statistics (NASA, 2014a)

can have an eccentric orbit that puts their aphelion into the asteroid belt from where most NEOs originate. Atens are less known because their orbit is mainly inside Earth's orbit and a smaller number of them exist. However, Apollos and Atens are the two NEO groups that have orbits which cross the one of Earth. Amors are completely outside the orbit of Earth but stay within roughly 0.3 AU of Earth's orbit which facilitates discovery because they can be fully illuminated while close to Earth. In contrast to Amors, IEOs are located inside Earth's orbit and observers on Earth may, thus, only see the dark side of these objects when they are close to the Earth. This geometry hampers discovery and this is the reason why only few IEOs have been discovered to date.

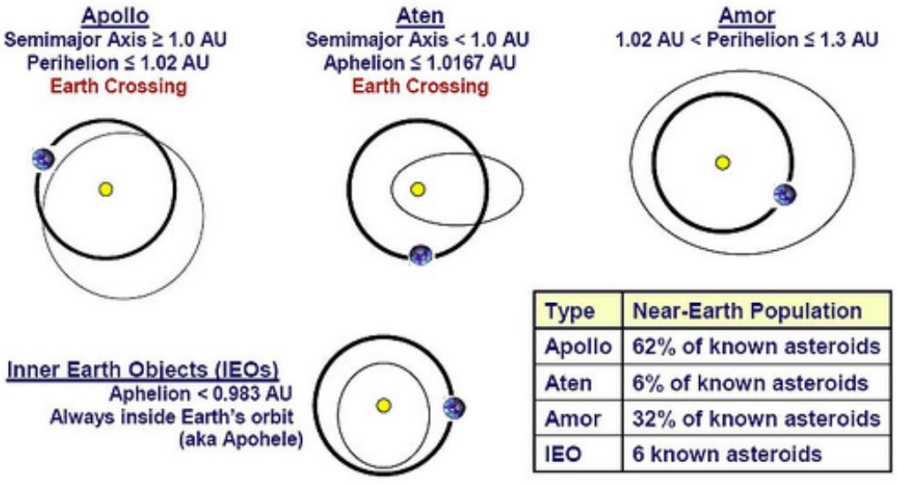

Figure 2.8: Categorization of NEO asteroids. Even though the table is not current, it reflects the rough distribution of discovered NEOs. (NASA, 2014a)

Potentially Hazardous Asteroids NEOs are classified as potentially hazardous asteroids when they meet the criteria in Table 2.2 which mandates that Potentially Hazardous Asteroids (PHAs) need to be very close to Earth's orbit and of a minimum absolute magnitude. The minimum orbit intersection distance (MOID) has to be smaller than 0.05 AU which corresponds to roughly 20 times the distance from the Earth to the Moon and this is a necessary condition for a possible future collision with the Earth. Furthermore, the maximum absolute magnitude of 22 relates to the minimum size of the object and translates to about 140 m. The size threshold of 140 m originates from a 1992

PHA criterion	Value
MOID	≤ 0.05 AU
H	≤ 22

Table 2.2: List of PHA criteria. Note that smaller absolute magnitude (H) corresponds to larger asteroid diameter.

US Congress mandate in response to the Spaceguard Survey Report which instructed NASA to discover 90% of these objects by 2012 (Morrison, 1992). This goal was not reached on time because of insufficient funding. In any case, new research (Boslough and Crawford, 2008) and the events in Chelyabinsk demonstrate that it could be sensible to redefine the target asteroid discovery size to a lower threshold because of the significant risk that these smaller objects still pose for the human population (as seen by Tunguska, Chelyabinsk and shown in current research (Boslough, 2013a)).

2.3.2 Asteroid Hazard Scales

To quantify the hazard level of discovered objects with a non-zero collision chance with the Earth in the future, two hazard scales are in use today. The Torino scale aims to communicate hazard levels to the general public while the Palermo scale is focused at the expert audience. Both scales rely on kinetic energy of the collision as a proxy for impact consequences as well as impact probability to emphasize more likely events. The scores of the scales are abstract numbers that allow for qualitative threat statements relative to other impact events but have only limited value in absolute terms as they do not describe actual impact consequences. In the following sections, both scales are introduced in detail and, later in this thesis, a new risk scale is proposed that allows quantitative statements about the hazard level in terms of the risk of expected casualties.

2.3.2.1 Torino Scale

The Torino scale was introduced by Binzel (2000) and aims to communicate threat levels through a simple eleven point scale with the general public. Impact probability and kinetic energy determine the Torino threat level of a given asteroid according to the

map shown in Figure 2.9. A low probability object with low kinetic energy receives a rating of zero while a high probability object with high kinetic energy is rated at up to ten.

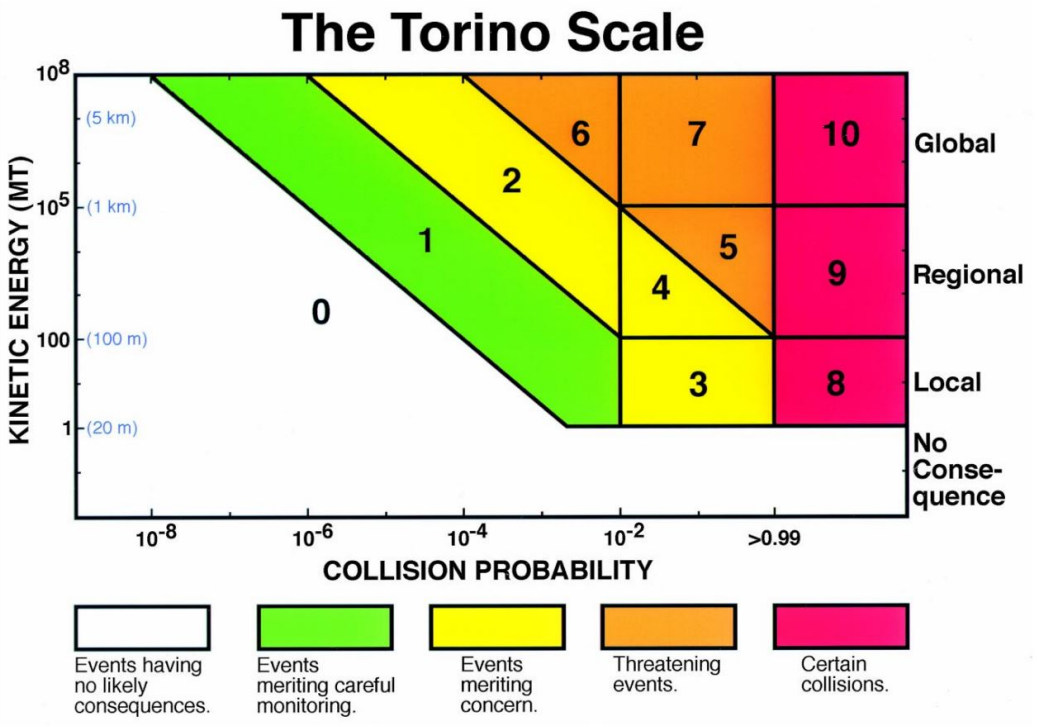

Figure 2.9: Torino scale impact probability - energy space and its categories. (Binzel, 2000)

.

Asteroid Apophis holds the record for highest Torino scale rating of 4 in the year 2004 but was subsequently revised to 0 when new observations became available.

The Torino scale is insensitive to asteroid properties such as material and density, the impact angle, impact location, and the population that might be at risk. As such, the Torino scale represents a quick method for a rough understanding of the hazard level of a given object.

2.3.2.2 Palermo Scale

The Palermo scale was introduced in Chesley et al. (2002) and provides a continuous hazard rating as opposed to the 11 distinct levels used by the Torino scale. In addition to impact probability and impact energy, the Palermo scale also takes into account lead time until the possible collision and the statistical threat of being hit by a similarly sized (or larger) object in the same timeframe. In other words, the Palermo scale indicates how significant the threat of the observed object is compared to the statistical background

threat. This comparison factor is expressed as the base ten logarithm and may thus take negative or positive values. The mathematical expression of the Palermo scale is:

$$S_P = \log_{10} \frac{P}{f_b \Delta t} \tag{2.2}$$

where S_P is the Palermo rating, P is the impact probability, Δt is the lead time in years, and f_b is the impact frequency of the background population of similar impact energy or larger. The background impact frequency f_b per year was approximated as:

$$f_b = \frac{3}{100} E^{-4/5} \tag{2.3}$$

In this equation, E is kinetic energy in megatons of TNT equivalent ($1\,\mathrm{Mt\ TNT} = 4.2 \times 10^{15}\,\mathrm{J}$) .

Typical Palermo scale values are in the interval $[-2, 2]$ and a value of -2 means that the concerned asteroid poses a 100 times smaller hazard than an arbitrary impact from the background population while a rating of $+2$ signifies a 100 times larger hazard. To date, asteroid Apophis received the highest Palermo rating since the inception of the scale with a value of 1.10 that represents a hazard that is 12.6 times higher than the background hazard. Subsequent measurements decreased the impact probability and Apophis received an unremarkable, lower rating.

2.4 Asteroid Impact Risk

To address the motivation and aims identified in section 1, the asteroid hazard needed to be expressed in a new way that allows to resolve the hazard level spatially and is more attuned to the specific impact situation. Both, the Torino and Palermo scales, rely on kinetic energy of the collision and collision probability as major parameters to determine the hazard level. However, this formalism does not make use of all information that is available immediately after the discovery of a new object such as possible impact locations and impact conditions (angle, speed). In the work presented in this thesis, the concept of risk is applied to the asteroid hazard and in its implementation it utilizes more of the early information to estimate the true risk of an asteroid and expresses that risk in terms of expected casualties.

The concept of risk is applicable to a wide variety of subjects (e.g. finance, insurance, politics and decision making). Risk for a given hazard, defined as the expected loss, is the product of three factors:

- **probability** - the likelihood that an event occurs
- **exposure** - the value that is at stake (or exposed)

- **vulnerability** - the portion of the exposed value that is affected if the event occurs

Here, the asteroid impact hazard is amenable to the risk formulation and can be stated in mathematical terms as:

$$R = P \times \Psi \times V(S) \tag{2.4}$$

where the terms are probability of the hazard (P), exposure to the hazard (Ψ) and the vulnerability to the hazard (V) as a function of hazard severity (S).

Probability The probability term in the risk equation represents the impact probability of an asteroid and this value can be determined using orbit determination under consideration of observational uncertainties. What is more, in this work, the spatial impact distribution on the surface of the Earth is calculated to obtain local impact probabilities as described in section 3.1.

Exposure To estimate the exposure term, the global human population distribution is used. The global population map can be combined with the spatial impact probability map to identify areas of high impact risk. A world population database is available online at CIESIN et al. (2005) and a map showing the world population as estimated for the year 2015 is shown in Figure 2.10 with a resolution of about $4.6 \times 4.6\,\mathrm{km}^2$.

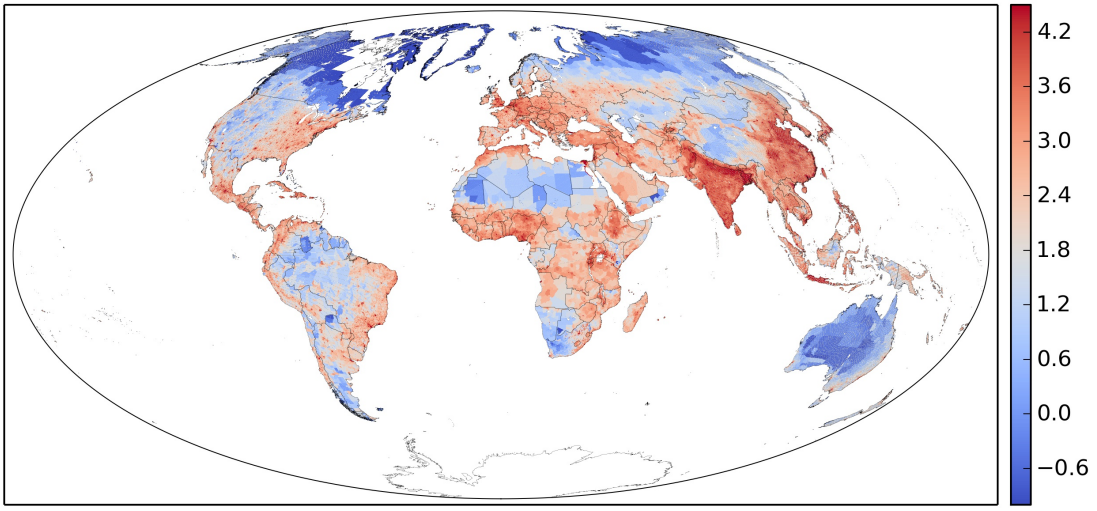

Figure 2.10: Estimate of world population for the year 2015. The data CIESIN et al. (2005) has a resolution of 2.5'x2.5' and represented population count per map cell on a logarithmic scale.

Vulnerability Finally, the vulnerability term describes the population vulnerability to the impact effects that are generated by an asteroid impact. To this end, an asteroid

impact is simulated in each possible impact location, determined by the impact probability distribution, and the impact effects are propagated over the population within the reach of that impact zone. The severity of the impact effects attenuates with distance and the vulnerable population that counts towards risk can be identified through propagation of these effects. In section 3.2 the impact effect models that estimate severity are described and in section 3.3 the vulnerability models are derived and presented.

The concept of risk is well suited to communicating asteroid threat levels because, through the unit of expected casualties, it makes the threat comparable to other natural disasters, and, thus, facilitates alignment of disaster response protocols with those for other natural disasters. The international community, represented by the Space Mission Planning Advisory Group (Drolshagen, 2014), is currently establishing response protocols to answer an asteroid threat on the international level. To establish this protocol, hazard thresholds need to be defined that trigger response actions such as focusing observational capabilities on the incoming object, sending a characterisation mission, evacuating the affected area, or launching a deflection mission. The method can be used to establish hazard threshold values in comparison to other natural disasters and can, thus, provide a means of quantifying appropriate resources to be allocated in response to the asteroid hazard. Utilizing risk as a threat measure also makes the subject of the asteroid threat more accessible to the general public by providing an intuitive threat level unit (expected casualties) and by consolidating a counter intuitive threat situation that features very low impact probability but very high consequences into one number. Finally, adopting the concept of risk to describe the asteroid hazard, the tool that needed to be developed would also enable research into the nature of impacts as it needs to model impact events on a detailed level in terms of their effect on the population.

In section 3, the method that is outlined here, is explained in detail and, subsequently, applied.

Chapter 3

Asteroid Risk Mitigation Optimization and Research Tool

To enable asteroid risk estimation, a software tool has been developed during the course of this research, that projects the impact probability of potentially impacting asteroids as a spatial distribution onto the Earth and simulates the asteroid's passage through the atmosphere with the associated impact effects. Impact effects interact with the human population and this process allows risk estimation in terms of expected casualties. The system, written in Python, was named Asteroid Risk Mitigation Optimization and Research (ARMOR) tool, and its entire method is described in this chapter.

3.1 Impact Location Calculation

Asteroid risk estimation as introduced in section 2.4 requires establishment of possible impact locations for a given asteroid on the Earth. ARMOR works in conjunction with OrbFit, an open source software that is used to find initial conditions for possible impact instances inside the uncertainty region of impacting asteroids which are known as virtual impactors (VI) (Milani et al., 2000). By sampling the ephemeris region around each VI, the potential impact corridor can be established on the surface of the Earth.

In section 3.1.1, the uncertainty region of asteroid ephemeris is introduced and it is explained how the open source software OrbFit utilizes this region to find virtual impactors. The solar system propagator of ARMOR calculates the final approach of impactors and the propagator is presented in section 3.1.2 along with propagation accuracy validation. Using the propagated trajectory, the collision location, and time are calculated analytically with a polynomial formalism described in section 3.1.3. The sampling of the ephemeris region around the virtual impactor is described in section 3.1.4 and this is used to establish the impact corridor on the surface of the Earth along with the spatial

impact probability projection. Impact angle and speed can be deduced from trajectory geometries as described in sections 3.1.4.2 and 3.1.4.3. Finally, the entire collision algorithm is validated against external simulation results and actually observed asteroid collisions of the two smaller NEOs 2008 TC3 and 2014 AA in section 3.1.5.

3.1.1 Initial Conditions of Virtual Impactors

Asteroids that can experience an Earth impact are listed on the two NEO risk lists by ESA (Universita Di Pisa and ESA, 2014) and by NASA's Jet Propulsion Laboratory (JPL) (NASA, 2014a). Upon discovery of an asteroid, the systems behind the NEO risk lists compute the nominal orbit solution for this asteroid. The nominal orbit solution is a set of ephemeris that best fits the available measurements. However, because all measurements have inherent uncertainty, the ephemeris are associated with an uncertainty region. The asteroid is most likely located at the nominal orbit solution but may be located anywhere within the uncertainty region. In fact, it is generally unlikely that an asteroid is discovered whose nominal orbit solution yields a future collision with the Earth. Instead, some locations within the orbit solution's uncertainty region will correspond to future Earth collisions. Finding these locations within the uncertainty region is accomplished with the open source software tool OrbFit (Milani et al., 1997). OrbFit samples the uncertainty region and identifies those samples that result in a future Earth impact. Each sample is called a virtual impactor (VI).

A telescopic observation of an asteroid provides high certainty in the angular position of that asteroid but little information about radial distance. The radial distance is important to determine the semi major axis of the asteroid's orbit and has do be deduced from a series of observations. Orbital speed of an object is closely related to its semi major axis and this link is demonstrated in Equation 3.1 where T is the orbital period and a is the semi major axis. The universal gravitational constant is G =6.67428 $\times$ 10^{-11} $\mathrm{m^3/kg\,s^2}$ and M is the mass of the central body.

$$T = 2\pi\sqrt{\frac{a^3}{GM}} \tag{3.1}$$

variations in semi major axis result in differences in orbital period and, thus, position variations along the orbit of the object over time. A smaller semi major axis corresponds to higher speed causing the object to move ahead on the orbit relative to the nominal orbit solution while a larger semi major axis corresponds to slower speed which would cause the object to fall behind. That is why the uncertainty region stretches along the orbit of the asteroid and envelops a relatively thin region around the orbit. The weak direction of the uncertainty region is called the Line of Variation (LOV) and it coincides with the orbit direction of the asteroid in the "vast majority of cases" (Milani et al., 2005). Figure 3.1 is a depiction of this concept. Another way to view this concept is

that the geometry of the orbit is generally well known but the actual position of the asteroid on that orbit is less certain (Milani et al., 2002).

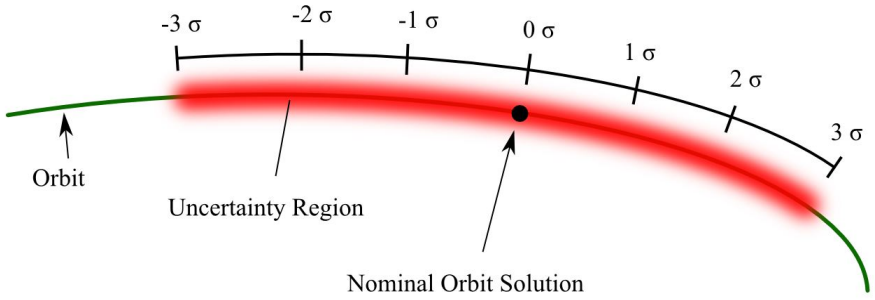

Figure 3.1: Principal shape of the uncertainty region associated with an asteroid orbit.

Instead of trying to find out precisely where the asteroid might be located, OrbFit identifies the locations inside the uncertainty region that would yield an Earth impact if the asteroid is located there. The authors of OrbFit describe the method to find VIs in greater detail in their publication (Milani et al., 2005). Subsequently, the initial conditions of the VIs are used as input to ARMOR's solar system propagator to determine the precise impact location and time.

3.1.2 Solar System Propagator

OrbFit delivers the VI's initial conditions for an epoch of about 10 days prior to the collision with the Earth and the final trajectory propagation until collision is performed by ARMOR's solar system propagator. The propagator utilizes a solar system model that considers gravitational forces from the Sun, the barycenters of the planetary systems and Pluto as well as point sources for the Earth and the Moon. The positions of the attracting bodies are retrieved from a lookup table that is based on the JPL DE430 planetary ephemerides (Folkner et al., 2014) and the interpolation scheme between the table points achieves millimeter level accuracy. The resulting gravitational acceleration $\ddot{r}$ for the VI, calculated in an inertial frame with origin in the solar system barycentre, is given by:

$$\ddot{\boldsymbol{r}}_j = \sum_{i=1}^{11} -\frac{GM_i}{|\boldsymbol{r}_{ij}|^3}\boldsymbol{r}_{ij} \tag{3.2}$$

where subscript j denotes the VI, subscript i denotes the attracting body, $\boldsymbol{r}_{ij}$ is the position vector connecting the attracting body to the VI and GM_i is the gravitational constant of the attracting body. The gravitational differential equation is numerically solved using the variable time step, predictor-corrector ADAMS method of the Livermore Solver for Ordinary Differential Equations (LSODE) (Radhakrishnan and Hindmarsh, 1993) package that is used in the Python scipy.integrate.odeint function.

3.1.2.1 Propagator Validation

Since the solar system propagator's performance is critical to the quality of all results obtained with ARMOR, the propagation accuracy was validated against ephemeris generated by HORIZONS (Giorgini and Yeomans, 2013). Three test cases have been selected at random from NASA's NEO risk list and the NEOs are: 1950 DA, 2010 NH and 2011 EB.

The NEOs were propagated over a period of 15 years and the positional discrepancy between HORIZONS provided data and propagated data is calculated after each year. Positional discrepancy is the norm of the vector connecting the two asteroid positions as given by HORIZONS and the propagator. A NEO can generally be considered to represent a challenging case for the propagator because of its proximity to major attracting bodies such as the Earth. Figure 3.2 showcases the position discrepancy evolution. The error tends to increase with longer simulation times and this behaviour can be expected for a propagator as the integration error accumulates over time.

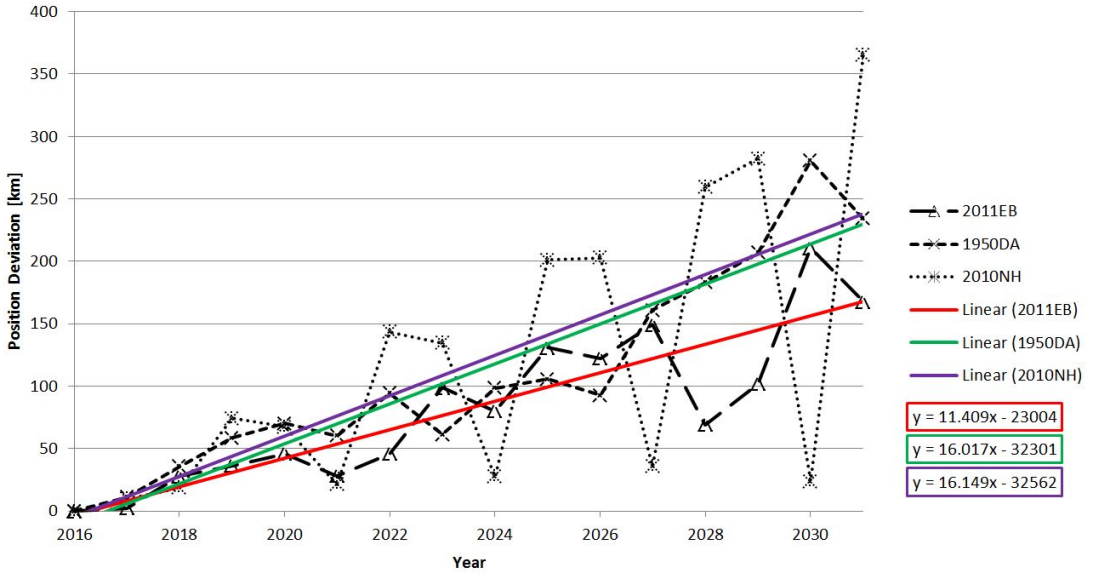

Figure 3.2: Position discrepancy between the propagator and HORIZONS for three NEOs over a 15 years simulation starting in 2016.

To characterize the increase in position discrepancy over time, a linear fit has been calculated for each test case and the corresponding equations are given in Figure 3.2. The slope of the linear equation shows the increase of positional discrepancy per year. For the three cases, the slopes are: 16.0 $^{\mathrm{km}}/_{\mathrm{year}}$; 11.4 $^{\mathrm{km}}/_{\mathrm{year}}$ and 16.1 $^{\mathrm{km}}/_{\mathrm{year}}$. It should be noted that typical propagation times in this work spanned 10 days and thus are much shorter than analysed in these validation cases. Therefore, the position error is expected to be on the order of $\frac{10\,\mathrm{days}}{365\,^{\mathrm{days}}/_{\mathrm{year}}} \times 16\,^{\mathrm{km}}/_{\mathrm{year}} \approx 0.44\,\mathrm{km}$ over a 10-day propagation time.

The validation cases show, first, that the propagation works correctly and that it achieves good accuracy considering that the scale of solar system distances (semi-major axis of the Earth is 1.496×10^8 km). Secondly, the validation outcomes are sufficiently accurate to have confidence in future results that are based on the propagator's performance.

3.1.3 Collision Detection

An important component of ARMOR is collision detection to, subsequently, identify impact locations and this section describes the corresponding method.

The algorithm determines numerically the closest approach between the centre of the Earth and the asteroid. This is accomplished by calculating the distance between the Earth and asteroid trajectories at coarse time sample points along the trajectories to identify the closest approach region. Subsequently, the vicinity of this closest approach is scrutinized with a finer resolution to determine a more precise close approach time and position. This step is repeated iteratively, until the propagation resolution of 100 s is reached. Finally, an analytical method is applied to determine the precise time and distance of close approach. To this end, the trajectories of the Earth and the asteroid are approximated as polynomials or, if this fails, as lines in the vicinity of the closest approach. The analytical method of finding the time and distance of closest approach is derived here.

3.1.3.1 Polynomial Approximation

The trajectory of the Earth and the asteroid are known as a distinct series of x, y and z coordinates in the vicinity of the time of closest approach. In order to find an analytical expression for the time and point of closest approach, the trajectories are approximated as polynomials. Polynomials are power series with degree d and are of the form:

$$P(t) = c_0 + c_1 t + c_2 t^2 + ... + c_d t^d \tag{3.3}$$

In this work, the default polynomial degree is three but the algorithm that accomplishes the approximation can select a lower degree or switch to linear approximation presented in section 3.1.3.2 if the default approximation failed.

Table 3.1 lists the symbols used to annotate bodies in the solar system.

The polynomial expression for Earth's x component is:

$$P_{♁,x}(t) = c_{0,♁,x} + c_{1,♁,x} t + c_{2,♁,x} t^2 + ... + c_{d,♁,x} t^d \tag{3.4}$$

Symbol	Body
♁	Earth
✠	Asteroid
⌀	Solar System Barycentre

Table 3.1: Astronomical symbols for solar system bodies.

and for the asteroid's x component it is:

$$P_{✠,x}(t) = c_{0,✠,x} + c_{1,✠,x}t + c_{2,✠,x}t^2 + ... + c_{d,✠,x}t^d \tag{3.5}$$

The polynomials for the other cartesian coordinates, $P_{♁,y}, P_{♁,z}, P_{✠,y}$ and $P_{✠,z}$ are determined similarly. The next step is to subtract the Earth and asteroid polynomials corresponding to each Cartesian component. This is demonstrated here for the x component:

$$\begin{aligned} P_{♁✠,x}(t) &= P_{♁,x}(t) - P_{✠,x}(t) & (3.6)\\ &= (c_{0,♁,x} - c_{0,✠,x}) + (c_{1,♁,x} - c_{1,✠,x})t + ... + (c_{d,♁,x} - c_{d,✠,x})t^d & (3.7) \end{aligned}$$

In accordance with Pythagoras, the difference polynomials for each component are squared and summed in order to reproduce the square of the distance between the Earth and the asteroid:

$$D^2_{♁✠}(t) = P^2_{♁✠,x}(t) + P^2_{♁✠,y}(t) + P^2_{♁✠,z}(t) \tag{3.8}$$

The result of this computation is $D^2_{♁✠}$ and is a polynomial in itself. Differentiating 3.8 with respect to time yields the rate of approach of the asteroid and Earth $\dot{D}^2_{♁✠}$. The rate of approach is once again a polynomial. At the time of closest approach, the rate of approach will be zero $\dot{D}^2_{♁✠} = 0$. The roots of the expression $\dot{D}^2_{♁✠} = 0$ can be complex but the one real root is the time of closest approach between the two bodies[1]. The time of closest approach serves as free parameter for Equation 3.8 and yields the closest approach distance. An impact occurs if the closest approach distance is smaller than the radius of the Earth.

Impact Determination When it is known that the closest approach between two trajectories yields an impact, Equation 3.8 is also used to find the point and time of impact. To find impact coordinates, the distance D is set equal to Earth's radius.

$$R^2_{♁}(t) = P^2_{♁✠,x}(t) + P^2_{♁✠,y}(t) + P^2_{♁✠,z}(t) \tag{3.9}$$

[1] Due to numerical inaccuracies, more than one real root may be found. In this case intelligent tests (such as knowledge about the general closest approach period) was sufficient to determine the correct value.

There are two real roots associated with this expression. The first is the time of impact and the second is the theoretical time of when the asteroid leaves the sphere of Earth. Thus, the time of impact is the smaller real root of Equation 3.9. Time of impact is used with the three polynomials that express the Cartesian components of the asteroid's trajectory (compare Equation 3.5 for the x component) to obtain the coordinates of the impact.

Time Normalization In the previous sections, it was required to determine the roots of polynomials. Generally, built-in functions find roots in a normalized expression. In other words, the roots are output between the interval 0 and 1. This makes sense because polynomial approximations of functions are most accurate in the vicinity of the argument being 0. Thus, the time component associated with the polynomials needed to be normalized and de-normalized in the process of finding closest approach and impact points. The solar system propagator's time unit is seconds. This means that the argument for the polynomials would quickly get very large and the polynomial would not be fitted properly to the data. To work around this problem, the time span over which the trajectories are approximated is normalized. This means that the time span t is transformed into the interval $\tau \in [0...1]$. The following equation provides the corresponding transformation:

$$\tau = \frac{t - t_{min}}{t_{max} - t_{min}} \tag{3.10}$$

The normalized time is transformed back to seconds after the calculations in the polynomial space are completed. The return transformation can easily be derived from Equation 3.10:

$$t = \tau \left(t_{max} - t_{min}\right) + t_{min} \tag{3.11}$$

3.1.3.2 Line Approximation

Trajectory portions in the vicinity of closest approach can be approximated as lines. The following sections will provide more information about how a close approach and impact can be determined analytically using the line approximation.

Closest Approach The trajectories (approximated as lines) of Earth $\boldsymbol{r}$ and of the asteroid $\boldsymbol{p}$ are given by:

$$\boldsymbol{r} = \boldsymbol{r}_0 + \dot{\boldsymbol{r}}t \tag{3.12}$$

$$\boldsymbol{p} = \boldsymbol{p}_0 + \dot{\boldsymbol{p}}t \tag{3.13}$$

where t is the time and $\boldsymbol{r}_0$ and $\boldsymbol{p}_0$ are the initial cartesian position vectors. The relative position vector between the two objects is obtained through subtraction of 3.12 and

3.13.

$$\boldsymbol{r} - \boldsymbol{p} = \boldsymbol{r}_0 - \boldsymbol{p}_0 + (\dot{\boldsymbol{r}} - \dot{\boldsymbol{p}})\, t \tag{3.14}$$

And the distance D of the objects is the Euclidean norm of Equation 3.14.

$$D = \|\boldsymbol{r} - \boldsymbol{p}\| = \|\boldsymbol{r}_0 - \boldsymbol{p}_0 + (\dot{\boldsymbol{r}} - \dot{\boldsymbol{p}})\, t\| \tag{3.15}$$

Writing out Equation 3.15 yields:

$$D = \sqrt{(r_{0x} - p_{0x} + (\dot{r}_x - \dot{p}_x)\, t)^2 + (r_{0y} - p_{0y} + (\dot{r}_y - \dot{p}_y)\, t)^2 + (r_{0z} - p_{0z} + (\dot{r}_z - \dot{p}_z)\, t)^2}$$

Squaring this equation, multiplying out the square parenthesis and collecting terms produces:

$$\begin{aligned} D^2 \;=\; & (\dot{r}_x - \dot{p}_x)^2\, t^2 + 2\,(r_{0x} - p_{0x})\,(\dot{r}_x - \dot{p}_x)\, t + r_{0x}^2 + p_{0x}^2 + 2 r_{0x} p_{0x} + \\ & (\dot{r}_y - \dot{p}_y)^2\, t^2 + 2\,(r_{0y} - p_{0y})\,(\dot{r}_y - \dot{p}_y)\, t + r_{0y}^2 + p_{0y}^2 + 2 r_{0y} p_{0y} + \\ & (\dot{r}_z - \dot{p}_z)^2\, t^2 + 2\,(r_{0z} - p_{0z})\,(\dot{r}_z - \dot{p}_z)\, t + r_{0z}^2 + p_{0z}^2 + 2 r_{0z} p_{0z} \end{aligned} \tag{3.16}$$

The time derivative of Equation 3.16 is the next step to calculate the minimum distance between the two objects.

$$\begin{aligned} \frac{dD^2}{dt} \;=\; & 2\,(\dot{r}_x - \dot{p}_x)^2\, t + 2\,(r_{0x} - p_{0x})\,(\dot{r}_x - \dot{p}_x) + \\ & 2\,(\dot{r}_y - \dot{p}_y)^2\, t + 2\,(r_{0y} - p_{0y})\,(\dot{r}_y - \dot{p}_y) + \\ & 2\,(\dot{r}_z - \dot{p}_z)^2\, t + 2\,(r_{0z} - p_{0z})\,(\dot{r}_z - \dot{p}_z) \end{aligned} \tag{3.17}$$

This equation evaluates to zero at local minima. Solving for t after setting $^{dD^2}/_{dt}$ equal to zero gives:

$$t = -\frac{(r_{0x} - p_{0x})\,(\dot{r}_x - \dot{p}_x) + (r_{0y} - p_{0y})\,(\dot{r}_y - \dot{p}_y) + (r_{0z} - p_{0z})\,(\dot{r}_z - \dot{p}_z)}{(\dot{r}_x - \dot{p}_x)^2 + (\dot{r}_y - \dot{p}_y)^2 + (\dot{r}_z - \dot{p}_z)^2} \tag{3.18}$$

Since this method is only applied in a restricted space and given the problem's nature, one can safely assume that Equation 3.18 represents the desired time of closest approach.

Impact Time Earth is a sphere with a mean radius of 6371 km. However, to account for the thickness of the atmosphere, the value used here is $R_{\oplus} = 6371\,\text{km} + 100\,\text{km}$ and this value corresponds to the Karman line, or where space begins by definition. An impact only occurred, when the asteroid's closest approach is smaller (or equal) than $R_{\oplus}$. If this is the case, the next step is calculation of the time of impact. Impact time is different from time of closest approach because of Earth's spherical shape. The asteroid impacts Earth when it first reaches a distance equal to the radius of Earth $D = R_{\oplus}$ to Earth's centre. An analytical expression can be found to calculate the precise time and

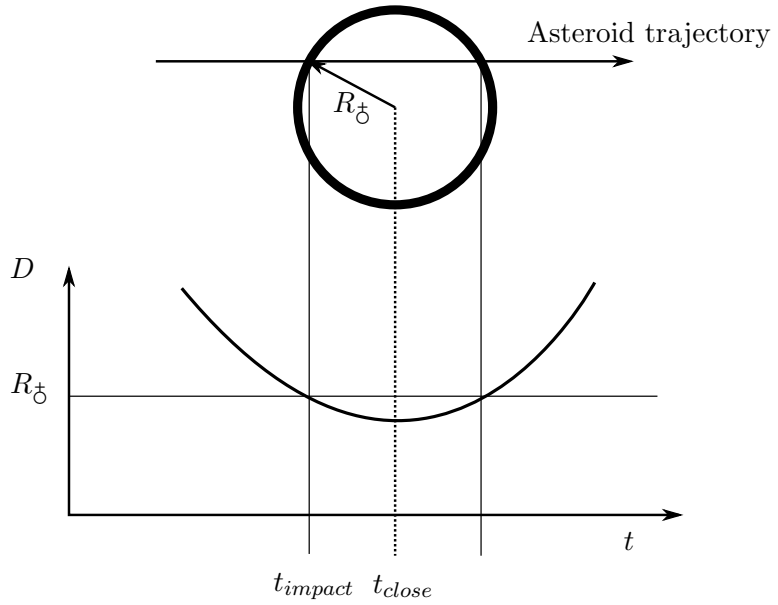

Figure 3.3: Plot of the approach distance over time as the asteroid enters the mathematical sphere of the Earth and exits it again. The times of impact and closest approach are marked on the time axis.

position of impact. Starting from Equation 3.16, the distance is set equal to Earth's radius $D = R_{\oplus}$ and the terms were collected according to the powers of their time factors.

$$\begin{aligned} 0 \;=\; & \left[(\dot{r}_x - \dot{p}_x)^2 + (\dot{r}_y - \dot{p}_y)^2 + (\dot{r}_z - \dot{p}_z)^2\right] t^2 + \\ & 2\left[(r_{0x} - p_{0x})(\dot{r}_x - \dot{p}_x) + (r_{0y} - p_{0y})(\dot{r}_y - \dot{p}_y) + (r_{0z} - p_{0z})(\dot{r}_z - \dot{p}_z)\right] t + \\ & r_{0x}^2 + p_{0x}^2 - 2r_{0x}p_{0x} + r_{0y}^2 + p_{0y}^2 - 2r_{0y}p_{0y} + r_{0z}^2 + p_{0z}^2 - 2r_{0z}p_{0z} - R_{\oplus}^2 \end{aligned} \tag{3.19}$$

This equation is now in a form paralleling the quadratic equation:

$$0 = at^2 + bt + c \tag{3.20}$$

Thus the terms a, b and c correspond to the following terms from Equation 3.19:

$$a = \left[(\dot{r}_x - \dot{p}_x)^2 + (\dot{r}_y - \dot{p}_y)^2 + (\dot{r}_z - \dot{p}_z)^2\right] \tag{3.21}$$

$$b = 2\left[(r_{0x} - p_{0x})(\dot{r}_x - \dot{p}_x) + (r_{0y} - p_{0y})(\dot{r}_y - \dot{p}_y) + (r_{0z} - p_{0z})(\dot{r}_z - \dot{p}_z)\right] \tag{3.22}$$

$$c = r_{0x}^2 + p_{0x}^2 - 2r_{0x}p_{0x} + r_{0y}^2 + p_{0y}^2 - 2r_{0y}p_{0y} + r_{0z}^2 + p_{0z}^2 - 2r_{0z}p_{0z} - R_{\oplus}^2 \tag{3.23}$$

Employing the solution to quadratic equations, the two possible times of collision may be obtained.

$$t_{1/2} = \frac{-b \pm \sqrt{b^2 - 4ac}}{2a} \tag{3.24}$$

A look at Figure 3.3 reveals how two collision times make sense. One solution is the time when the asteroid collides with Earth. The other solution is the time when the asteroid

exits Earth's sphere again if it could pass Earth without interacting with it. Thus, the time of impact is the one solution corresponding to the earlier time.

3.1.3.3 Trajectory Approximation Validation

In the previous sections (sections 3.1.3.1 and 3.1.3.2), the trajectories of the Earth and the asteroid were approximated as 3rd or 2nd order polynomials, or as lines if polynomial algebra failed. These approximations were applied to the trajectories in very close proximity to the encounter point corresponding to a roughly 10 min time period. In this section, the approximation accuracy is validated using a simple test case. Therefore, a asteroid-Earth encounter time of 10 min was selected and the cartesian y-coordinate of the Earth's orbit was calculated on a circular segment for this time period. The y-coordinate sequence was subsequently approximated using a 3rd and 2nd order polynomial as well as a line. Finally, the approximations were compared to the originally calculated y-coordinate sequence of the Earth's orbit. Figure 3.4 visualizes the approximation error for the three approximation methods.

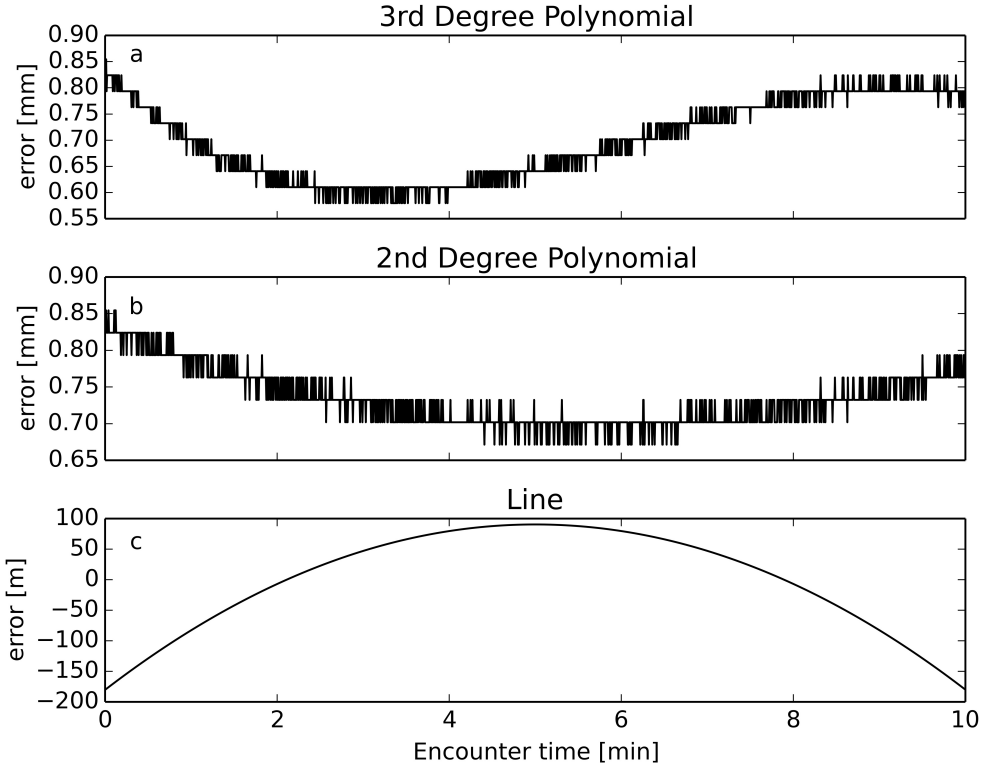

Figure 3.4: Approximation error of one cartesian component of the Earth's orbit using 3rd (plot a), 2nd (plot b) and line (plot c) approximation over a typical encounter time.

The 3rd and 2nd order polynomial approximations (plots 3.4 a&b) yield very good approximation accuracy with errors on the order of 1 mm. The line approximation

is utilized as a fall-back option in the code in case numerical instabilities render the polynomial approximation without results. For a line approximated trajectory (plot 3.4 c), the position error was less than 200 m which is an acceptable result considering that ARMOR produces results on an Earth surface grid with a grid cell size of $4.6 \times 4.6\,\mathrm{km}^2$. In summary, the trajectory approximation will typically produce accurate trajectory data (with mm-level error) while in the worst case, the line approximation could produce errors an order of magnitude smaller than the size of an Earth's surface grid cell and these results suggest that the present algorithm is suitable for its intended use.

3.1.4 Impact Corridor Calculation

The Impact Corridor Calculation module determines the possible impact points of an asteroid on the surface of the Earth. OrbFit produces an ephemeris that yields the first impact point after propagation. Starting at this ephemeris, the epoch is varied forwards and backwards in time effectively creating more virtual asteroids to conduct impact analysis with. If the new virtual asteroid is still on an impacting trajectory, the new impact location is recorded and the variation continues. A good step size for epoch variation was found to be 25 sec because this step size yields a typical number of 100 virtual impactors to construct the impact corridor with. After continuous epoch variation, a new virtual asteroid eventually misses the Earth. In this case, the epoch variation step size is gradually decreased to 0.01 sec while the search algorithm finds the last virtual asteroid that just barely impacts Earth. This case is called a grazing case because the virtual asteroid is on a near tangential trajectory with respect to the surface of the Earth. Two grazing cases exist: one where the virtual asteroid just barely hits the leading edge of the Earth and one where it barely hits the trailing edge of the Earth. The risk corridor spans between the leading and the trailing grazing cases and can be constructed along the intermediate impact points.

Sampling by varying the VI orbit solution epoch is equivalent to assuming that the LOV stretches in a similar direction as the VI's velocity vector. However, it is possible that the geometry of the LOV is distorted if an asteroid experienced significant close encounters before impact. In this case, the impact corridor would be centred on one correct impact point (that of the VI orbit solution) but would stretch along an incorrect direction. The misalignment depends on the degree to which the LOV direction varies from the VI velocity vector. However, this phenomenon is researched in (Milani et al., 2005) and it is stated there that in the "vast majority of cases" the uncertainty region will stretch along the orbit and the calculated impact corridor will match the real impact corridor.

3.1.4.1 Mapping of Spatial Impact Probability Distribution

The recorded intermediate impact points are used to construct a spline in-between the leading and trailing grazing impact cases. However, the asteroid's true collision point may not necessarily lie exactly on the connecting line but may instead lie to one side of it within a certain distance. This is because the orbit solution of a potentially impacting asteroid has an ellipsoidal uncertainty region associated with it that stretches along the line of variation and also extents, to a smaller degree, in cross LOV direction. Typically, a Gaussian distribution is assumed to model the uncertainty ellipsoid around the orbital solution of an asteroid (Milani, 2004). Therefore, the connecting spline between the impact points forms the centre line of the impact corridor and a Gaussian distribution centred on the connecting spline represents the projection of the orbit solution ellipsoid on the Earth. This representation assigns highest impact probability to the centre line (connecting spline) but allows for potential collisions points that lie to the side of it. NASA's Near Earth Object (NEO) risk list provides the 1-σ width of the orbit solution uncertainty region for each asteroid and this value is assigned to the impact corridor to scale its width.

At this time, the corridor reflects the geometry of the orbital uncertainty region of a potential impactor projected onto the surface of the Earth. In a next step, the integral of the distribution needs to reflect the impact probability of the potential impactor. To this end, the impact corridor is first normalized such that its integral is equal to one and, subsequently, it is multiplied by the impact probability of the potential impactor. After these steps, the integral of the impact probability distribution equals the global impact probability of the impactor. Furthermore, individual pixels of the corridor reflect the local chance of impact in that region.

Figure 3.5 shows an example of an impact corridor expressed as the spatial impact probability distribution formed by a Gaussian distribution centred on the impact location centre line.

3.1.4.2 Impact Angle

The impact angle is the angle of that trajectory relative to the local horizontal plane at the impact location[2]. In the case an asteroid impacts Earth on a trajectory parallel to the local horizontal, an impact angle of 0 ° is observed. Conversely, an asteroid that hits the surface perpendicularly is on a 90 ° collision course. To calculate the impact angle, the impact position vector from the centre of Earth to the impact location $\boldsymbol{r}^b_{♁}$ (further explanation of the notation form may be found in appendix B) and the relative impact velocity vector $\boldsymbol{v}^b_{♁}$ are calculated. The impact position vector $\boldsymbol{r}^b_{♁}$ is the normal of

[2]The simplifying assumption being that Earth is a sphere

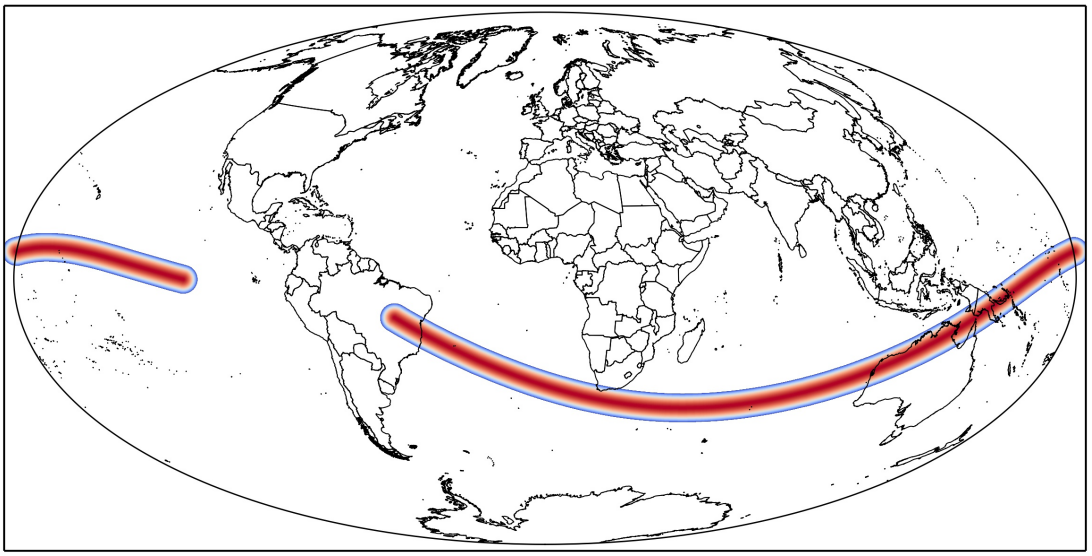

Figure 3.5: Illustration of the spatial impact probability of asteroid 2000 SG344 represented by a Gaussian distribution centred on the impact corridor centre line.

the local horizontal plane and it is calculated with Equation B.1. The normalized form of this vector is required and can be found with:

$$\hat{\boldsymbol{r}}^b_{♁✠} = \frac{\boldsymbol{r}^b_{♁✠}}{\left|\boldsymbol{r}^b_{♁✠}\right|} \tag{3.25}$$

The relative impact velocity $\boldsymbol{v}^b_{♁✠}$ is found by subtracting Earth velocity from the velocity of the asteroid at impact

$$\boldsymbol{v}^b_{♁✠} = \boldsymbol{v}^b_{⊙✠} - \boldsymbol{v}^b_{⊙♁} \tag{3.26}$$

Again, the normalized form of the relative velocity vector is required:

$$\hat{\boldsymbol{v}}^b_{♁✠} = \frac{\boldsymbol{v}^b_{♁✠}}{\left|\boldsymbol{v}^b_{♁✠}\right|} \tag{3.27}$$

The norm of the cross product of $\hat{\boldsymbol{r}}^b_{♁✠}$ and $\hat{\boldsymbol{v}}^b_{♁✠}$ is equal to the cosine of the impact angle. Hence, the impact angle is:

$$\gamma = \left|\cos^{-1}\left(\left|\hat{\boldsymbol{r}}^b_{♁✠} \times \hat{\boldsymbol{v}}^b_{♁✠}\right|\right)\right| \tag{3.28}$$

The geometry of this equation is visualized in Figure 3.6

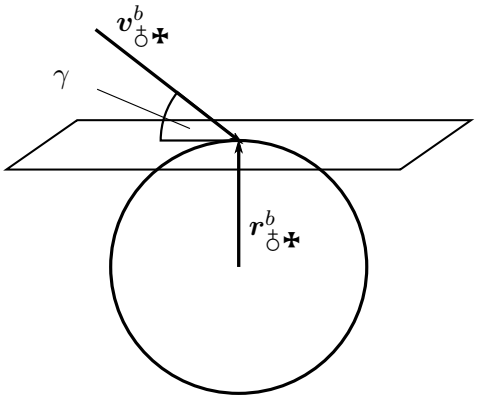

Figure 3.6: Impact angle geometry diagram.

3.1.4.3 Relative Impact Velocity

The relative impact velocity depends on the asteroid's velocity at impact, Earth velocity and the impact location. Impact location is important because the location's distance from Earth rotational axis $\left|\boldsymbol{r}^q_{\sharp\oplus,xy}\right|$ determines the ground speed due to the rotation of Earth. The angular speed of Earth's rotation is defined by one revolution in one sidereal day:

$$\dot{\psi}_\sharp = \frac{2\pi}{86164.09053\,\mathrm{s}} = 7.292115855377074 \times 10^{-5}\,{}^1\!/_\mathrm{s} \tag{3.29}$$

The ground velocity vector at the impact location due to the rotation of Earth is perpendicular to the plane spanned by the relative impact location vector $\hat{\boldsymbol{r}}^q_{\sharp\oplus}$ and by Earth rotation axis $= [0,0,1]^q$. It is defined as:

$$\hat{\boldsymbol{v}}^q_{\sharp,rot} = [0,0,1]^q \times \hat{\boldsymbol{r}}^q_{\sharp\oplus} \tag{3.30}$$

The ground velocity magnitude follows the relationship that the tangential velocity of a rotating body is equal to the radius projected in the body xy plane (which is normal to rotation axis) multiplied by the angular speed. The direction of the ground velocity is determined by $\hat{\boldsymbol{v}}^q_{\sharp,rot}$. Ground velocity at the point of impact is:

$$\boldsymbol{v}^q_{\sharp,rot} = \hat{\boldsymbol{v}}^q_{\sharp,rot}\left|\boldsymbol{r}^q_{\sharp\oplus,xy}\right|\dot{\psi}_\sharp \tag{3.31}$$

The combination of Earth's orbital velocity and ground velocity is subtracted from the asteroid's speed at time of impact to obtain the impact velocity. Impact speed is the magnitude of the impact velocity vector.

$$v_\oplus = \left|\boldsymbol{v}^q_{\oslash\oplus} - \left(\boldsymbol{v}^q_{\oslash\sharp} + \boldsymbol{v}^q_{\sharp,rot}\right)\right| \tag{3.32}$$

3.1.5 Impact Corridor Validation

Over the course of this project, three validation cases were undertaken with asteroids 2011 AG5, 2008 TC3 and 2014 AA. The purpose of the first case, asteroid 2011 AG5, was to validate impact angle and velocity calculations as this was a cross validation with an external calculation and did not rely on actual observations. In contrast, both of the other asteroids were special because they already collided with the Earth, yet, they were discovered before their collisions and their impacts were observed. The latter two asteroids served to validate predictive accuracy of ARMOR with respect to determining the impact location of asteroids and the shape of their impact corridors.

3.1.5.1 Case 2011 AG5

To validate the calculation of impact angle and velocity, impact points for asteroid 2011 AG5 with a possible impact[3] on February 5th 2040 were computed. The result is shown in Fig. 3.7 and can be compared to the result obtained by Adamo (2012) shown in Fig. 3.8.

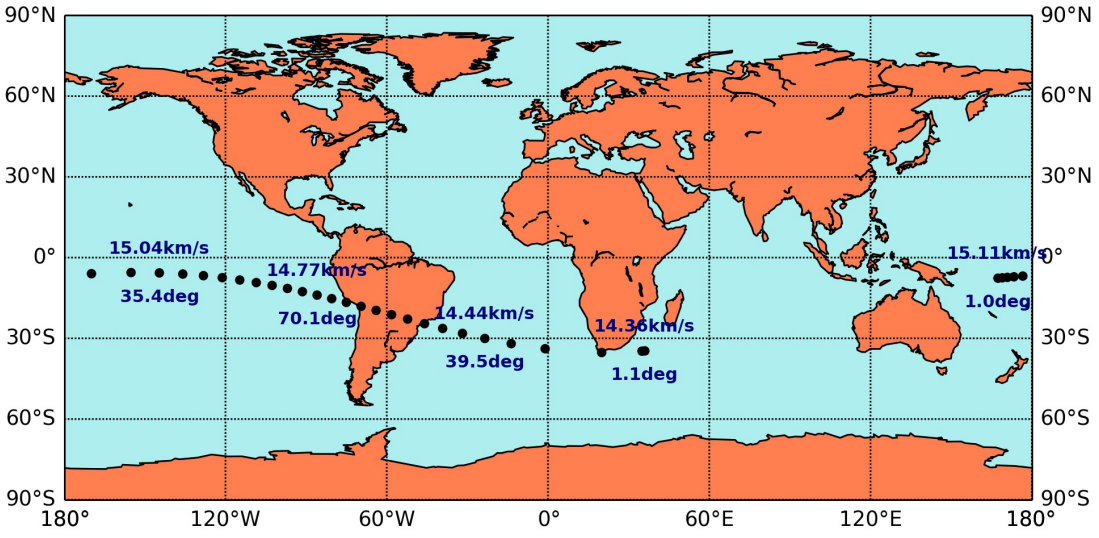

Figure 3.7: Recorded impact points for 2011 AG5. Impact speed and angle are noted above and below the impact point, respectively. A zero degree impact angle corresponds to a tangential impact and marks a grazing case.

The shape and locations of the impact points coincide well based on visual inspection. Impact velocities are similar and only differ by less than 0.1 km/s in the regions where the data are available in Fig. 3.8. It was expected that impact angles decrease to

[3]NASA's and ESA's Near Earth Object (NEO) risk lists are updated continuously. Thus, asteroids can always be removed or added to the list depending on newly made observations. This is why it is possible that some of the asteroids mentioned in this publication might be removed from the risk list after publishing. At the time of writing, 2011 AG5 was removed from NASA's and ESA's risk list because new observations ruled out the possibility of a future impact.

zero degrees at both ends of the impact location line corresponding to near tangential impacts. In fact, this behaviour can be observed in Fig. 3.7. One data point is labelled with the impact angle in Fig. 3.8 and the angle agrees by 1.5 ° with a similarly located point in Fig. 3.7. Impact angle and velocity are important to determine physical impact effects and, both, impact angle and velocity calculations, show good agreement with the results by Adamo (2012).

Figure 3.8: Impact line for 2011 AG5 as published by Adamo (2012). The flight path angle in the middle of the corridor is marked as -71.6 ° and its norm corresponds to the impact angle.

The slight variation of impact angle in the two results can be explained by recognizing that the impact angle is not calculated for exactly the same location. The two sample points are slightly offset along the impact corridor and that can account for a different impact angle realization. In general, impact effects show higher sensitivity to varying impact angles on the order of a few degrees than to impact velocity variations of a few 100 m/s (see section C). Based on the good agreement between the results, it can be expected that physical impact effect calculation is insensitive to the level of accuracy that is shown here. Overall, impact angles and velocities agree to a sufficient degree and suggested accurate performance of this part of ARMOR.

3.1.5.2 Case 2008 TC3

Asteroid 2008 TC3 was discovered shortly before entering the Earth's atmosphere. Its entry point was predicted and the resulting bolide was observed by eye witnesses, satellite and infra-sound sensors (Chesley et al., 2014). For validation, ARMOR used the nominal orbital solution for 2008 TC8 and predicted the atmospheric entry point as well as the ground track 3.9. The predicted nominal entry point agrees to within 0.39 ° longitude and 0.12 ° latitude at 65.4 km altitude. This difference corresponds to a surface distance of about 44.3 km. Furthermore, the shape of the ground track agrees well with the literature (Chesley et al., 2014). This validation result demonstrate sufficient accuracy of ARMOR for the problems addressed in this work.

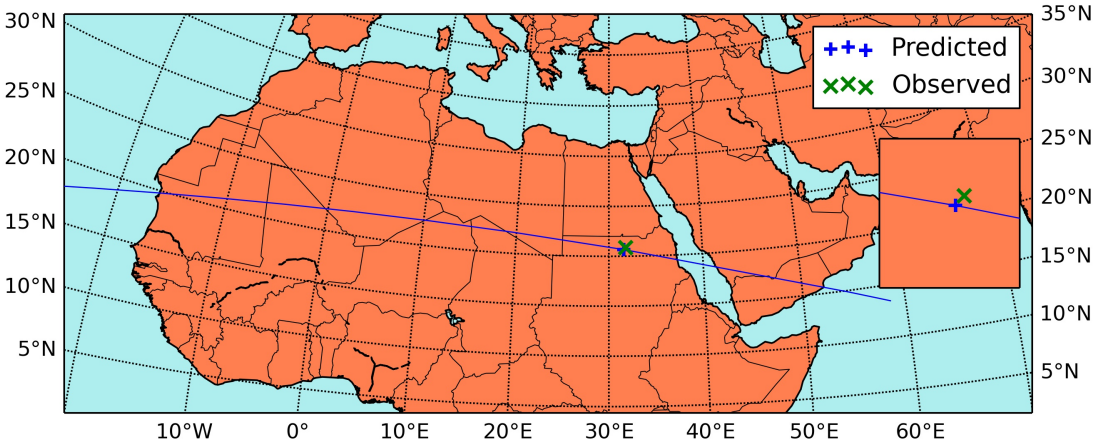

Figure 3.9: Observed and predicted entry point for asteroid 2008TC3. The blue plus sign marks the point of the nominal entry solution while the green cross gives the solution of the observed entry point at the same altitude of 65.4 km. The insert provides a 5 fold magnified view.

3.1.5.3 Case 2014 AA

Similarly to 2008 TC3, asteroid 2014 AA was discovered few hours before impact with the Earth. Based on the available observations, the entry point could be constrained to lie in the southern Atlantic ocean. A global network of infra-sound microphones recorded and triangulated the impact event at the coordinates 314.153 ° longitude and 13.048 ° latitude North. ARMOR predicted the nominal entry point at 313.58 ° longitude and 12.98 ° latitude North. Figure 3.10 shows the calculation results. This corresponds to a surface distance of about 65.5 km demonstrating sufficient accuracies for the intended purposes.

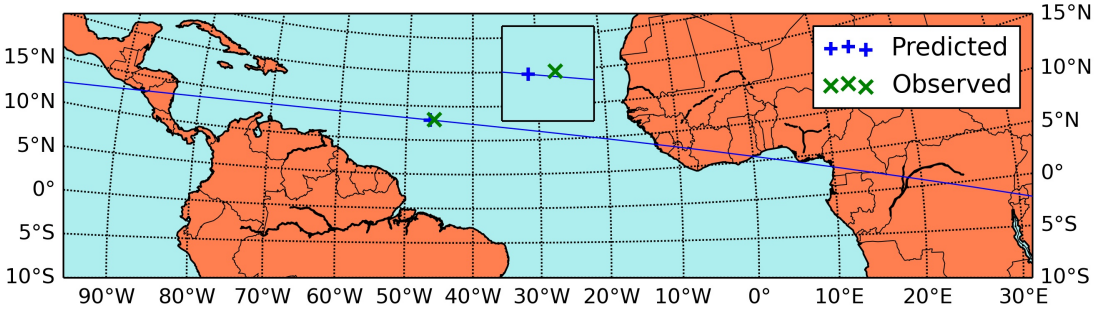

Figure 3.10: Observed and predicted entry point for asteroid 2014 AA. The blue plus sign marks the point of the nominal entry solution while the green cross gives the solution of the observed entry point. The insert provides a 7 fold magnified view.

3.1.5.4 Validation Conclusions

The positional discrepancy between observed and predicted impact point can be explained by several factors. The asteroid ephemeris is not known perfectly and the real and propagated trajectories differ through this error in the initial conditions. The propagator has an inherent propagation error that results in a deviation from the real trajectory. ARMOR uses a spherical Earth model (radius = 6371 km) and does not presently account for the oblateness of the Earth. This means that the impact location is effectively calculated at a different altitude than the observed one. Given a non-perpendicular impact trajectory with respect to the local horizon, the difference in altitude will produce a position error in the horizontal plane. Furthermore, the collision determination algorithm does not account for atmospheric interaction in the trajectory calculation while a real asteroid will experience drag and lift forces during atmospheric entry. The aerodynamic forces affect the flight path of the asteroid. It is also expected that thermo-chemical interactions such as ablation and the resulting mass loss affect the asteroid trajectory and these effects are not modelled in ARMOR. Given the modelling constraints of ARMOR, the predicted impact points are reasonably close to the observed ones and the validation results demonstrate that the impact point and corridor line calculations work robustly.

3.2 Impact Effect Modelling

The previous sections describe how to obtain the impact locations and spatial impact probability of an asteroid in the form of a Gaussian impact probability distribution. For risk calculation, impact effects need to be included into the analysis to estimate the region and population on the ground that is affected by the impact.

In this work, analytical models were utilized to simulate the effects of an impact because the impact corridor, which represents all possible impact locations on the five by five km world grid, consists of hundreds of thousands of possible impact locations in the form of grid cells. Analytical models are fast enough to allow for this quantity of calculations to be performed in a reasonable amount of time while producing good estimates of the outcome of an impact event. The alternative approach to analytical modelling is numerical modelling which allows for higher fidelity simulations and this is especially useful when the analysis focuses on understanding the process of asteroid entry, disruption and/or impact. Numerical modelling is more computationally demanding and is typically only performed to study a single impact scenario and its atmospheric passage (Boslough and Crawford, 2008; Artemieva and Shuvalov, 2001; Shuvalov et al., 2013; Gisler et al., 2011; Collins et al., 2012). In this work, the outcome of an asteroid impact was of more significance than the entry process itself and the quantity of impact simulations that need to be performed for each impact corridor prohibits use of numerical models. The main source for the analytical models that describe the atmospheric passage and impact effects of an incoming asteroid is (Collins et al., 2005), where such models are derived based on experiments, the results of numerical simulations and basic physics.

This chapter introduces the models that describe the atmospheric passage as well as impact effects and the section ordering is aligned with this physical process. Figure 3.11 shows the flow of events that leads to three atmospheric passage scenarios that a meteoroid can experience upon collision with the Earth. In the first scenario, the asteroid enters the atmosphere and starts to break up due to the aerodynamic pressure. The dispersing asteroid fragments increase the effective, aerodynamic surface area which further increases pressure leading to a runaway situation yielding a cascade of breakups. This self reinforced breakup process can lead to sudden energy release in mid air called airburst. In the second scenario, the asteroid starts to break up but the fragments impact the surface before an airburst occurs. Here, most of the asteroid's energy is delivered to the ground by the fragments and released during surface impact instead of the mid air explosion. In the third scenario, the asteroid passes the atmosphere intact and releases most of its energy during the surface impact. Large or metallic asteroids are likely to follow the third scenario while smaller, more porous asteroids tend to break up before reaching the surface.

The models describing the atmospheric passage of an asteroid until the possible, subsequent surface impact, are described in section 3.2.1. Sections 3.2.2 to 3.2.6.2 cover

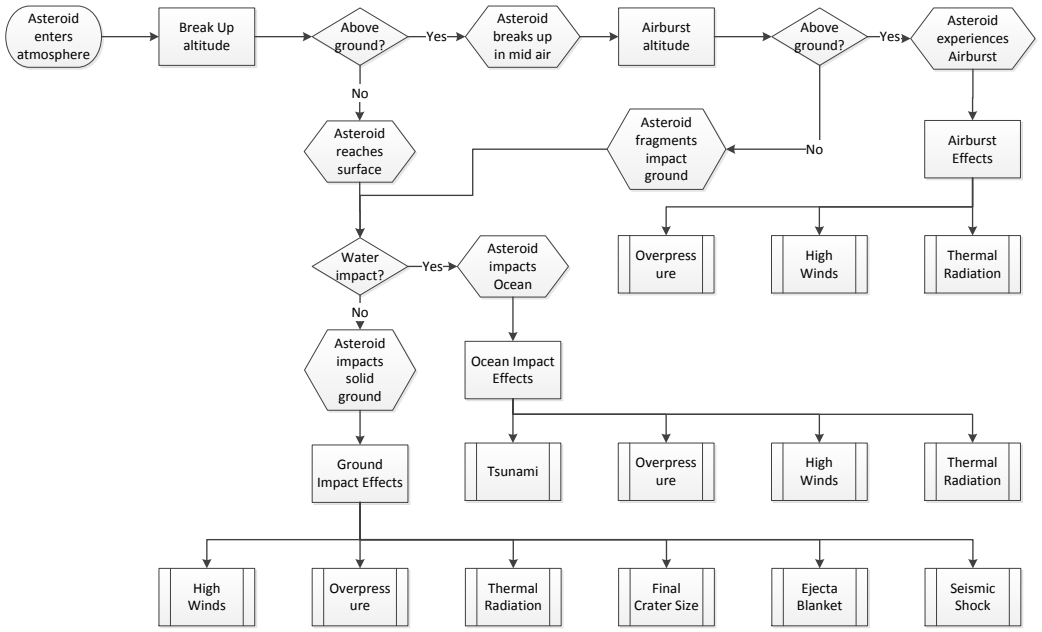

Figure 3.11: Impact effect modelling flow chart.

models for the generation and propagation of impact effects such as wind blast, overpressure shock, thermal radiation, crater formation, seismic shaking as well as ejecta deposition. Special attention is paid to the effect of a tsunami which can be triggered by an ocean impact and this effect is covered in section 3.2.7.

3.2.1 Atmospheric Passage

To enable impact effect calculation, the atmospheric passage needs to be modelled and this process starts by determining the break up altitude. The algorithm generally assumes a spherical shape of the asteroid.

3.2.1.1 Break Up Altitude

An asteroid breaks up due to the aerodynamic pressure difference between its leading and trailing edge. Aerodynamic pressure is high at the stagnation point while it is low in the wake of the asteroid. When the pressure difference exceeds the yield strength of the asteroid's material, the asteroid breaks up. (Collins et al., 2005) derive an analytical approximation for break up altitude in the form of:

$$z_* = -h_0 \left[\ln \frac{Y_i}{\rho_0 v_i^2} + 1.308 - 0.314 I_f - 1.303 \sqrt{1 - I_f} \right] \tag{3.33}$$

where $h_0 := 8\,\text{km}$ is the atmospheric scale height, Y_i is the yield strength of the asteroid, $\rho_0 := 1\,\text{kg/m}^3$ is the surface atmospheric density and I_f is given by:

$$I_f = 4.07\frac{C_D h_0 Y_i}{\rho_i L_0 v_i^2 \sin\gamma} \tag{3.34}$$

where $C_D := 2$ is the asteroid's drag coefficient, ρ_i is the asteroid's density, L_0 is the asteroid's diameter and v_i is the asteroid's speed. The yield strength of an asteroid in Pascal is estimated as a function of its density[4] with:

$$\log_{10} Y_i = 2.107 + 0.0624\sqrt{\rho_i} \tag{3.35}$$

Typical asteroid densities along with their natural meteorite occurrence rate are listed in table 2.1. In this work, a bulk density value of $3100\,\text{kg/m}^3$ was used.

3.2.1.2 Airburst Altitude

If the break up altitude is above the ground, the meteoroid may experience an airburst. During a break up, the meteoroid fragments into several pieces that increase the overall drag by expanding the effective area. Increased drag facilitates further break up. This process creates a self reinforcing feedback cycle that leads to explosive dissipation of the meteoroid's kinetic energy in the atmosphere. This event is called an airburst. Accurate modelling of the airburst mechanics requires complex hydrocodes that model the structure fluid interactions during atmospheric passage. A numerical approach is not practical in this thesis' application. (Chyba et al., 1993; Hills and Goda, 1993) proposed the 'Pancake' model where the asteroid is a strength-less liquid that flattens out in the presence of atmospheric drag - much like pancake dough poured into a pan. The airburst occurs when the asteroid covers seven times its original drag area[5]. This factor is the pancake factor $f_p := 7$. An analytical expression for the airburst altitude z_b is derived in (Collins et al., 2005).

$$z_b = z_* - 2h_0 \ln\left[1 + \frac{L_{disp}}{2h_0}\sqrt{f_p^2 - 1}\right] \tag{3.36}$$

where L_{disp} is the dispersion length scale which is given by:

$$L_{disp} = L_0 \sin\gamma \sqrt{\frac{\rho_i}{C_D \rho(z)}} \tag{3.37}$$

The atmospheric density $\rho(z)$ is calculated using an exponential atmospheric model.

$$\rho(z) = \rho_0 e^{-z/h_0} \tag{3.38}$$

[4]The relation is derived in the regime $1000 - 8000\,\text{kg/m}^3$ that covers most meteoroids (Britt, 2014)

[5]The model is intended for factors of magnitude two to four (Ivanov et al., 1997). However, (Chyba et al., 1993) found that seven aligns better with Tunguska-like events.

3.2.1.3 Airburst Speed

In an airburst, most of the asteroid's energy is dissipated in an explosion-like event. Kinetic energy of the meteoroid at the time of the airburst will allow the estimation of the damage potential. The meteoroid's speed at the time of airburst determines the kinetic energy. Until break up occurs, the speed can be estimated with (Collins et al., 2005):

$$v(z) = v_0 \exp -\frac{3\rho(z) C_D h_0}{4\rho_i L_0 \sin\gamma} \tag{3.39}$$

Equation 3.39 allows the calculation of the meteoroid's speed at break up $v(z_*)$. Subsequently, it is possible to calculate the meteoroid's speed at the airburst altitude with this relation from (Collins et al., 2005):

$$v(z_b) = v(z_*) \exp\left(-\frac{3C_D\rho(z_*)}{4\rho_i L_0^3 \sin\gamma}\frac{L_{disp}L_0^2}{24}\alpha\left[8\left(3+\alpha^2\right)+3\alpha\frac{L_{disp}}{h_0}\left(2+\alpha^2\right)\right]\right) \tag{3.40}$$

with $\alpha := \sqrt{f_p^2 - 1}$.

3.2.1.4 Post Break Up Impact Speed

In case a meteoroid breaks up but does not undergo airburst, the fragments impact the ground and can cause significant impact effects. The fragment impact speed can be calculated using the following relations from (Collins et al., 2005):

$$\begin{aligned} v(0) = v(z_*) \exp\{&-\frac{3C_D\rho(z_*)}{4\rho_i L_0^3 \sin\gamma}\frac{H^3 L_0^2}{3L_{disp}^2} \\ &\left(3\left[4+\left(\frac{L_{disp}}{h_0}\right)^2\right]e^{z_*/h_0} + 6e^{2z_*/h_0} - 16e^{3z_*/2h_0} - 3\left(\frac{L_{disp}}{h_0}\right)^2 - 2\right)\} \end{aligned} \tag{3.41}$$

3.2.2 Crater Formation

When an meteoroid impacts the ground, an impact crater forms. The cratering process is complex in itself and occurs in several steps. In a first step, a transient crater is formed which is the dynamical response to the impacting meteoroid. It is useful to calculate the transient crater because the final crater shape depends on the intermediate step of the transient crater. In fact, the energy delivered by the asteroid is so big and the speed of the mechanical interaction between asteroid and ground is so fast that the target material (water or ground) react like a fluid and thus can be described with the same formalism. A transient crater is generally an unstable structure and is similar to the crown-like shape that forms in a water surface immediately after a droplet falls into it. The "crown ring" surrounds the impact point that forms a bowl shaped depression and represents the crater bottom. A transient crater is not self-supporting and collapses under the

influence of gravity to form the final crater shape. The transient crater diameter D_{tc} is given in (Collins et al., 2005) with:

$$D_{tc} = 1.161 \left(\frac{\rho_i}{\rho_t}\right)^{1/3} L_0^{0.78} v_i^{0.44} g_0^{-0.22} \sin^{1/3}\gamma \tag{3.42}$$

where ρ_t is the target density. Typical target densities are given in table 3.2. Earth's standard gravitational acceleration is $g_0 = 9.80665\,\mathrm{m/s^2}$.

Target Type	**Density** $[\mathrm{kg/m^3}]$
Crystalline Rock	≈ 2750
Sedimentary Rock	≈ 2500
Water	1000

Table 3.2: Ground target types and their densities.

With the collapse of the transient crater, the final crater forms. In a sensitivity analysis as part of this work, it has been determined that the final crater diameter D_{fr} is typically 25 % bigger than the transient crater diameter. This estimate is found to be accurate to within 5 % for asteroids in the diameter regime of 0-500 m. The sensitivity analysis considered impact speed, impact angle, asteroid density and target density. This simple scaling law is a good compromise between final crater diameter estimation accuracy and computational efficiency. Figure 3.12 provides a diagram of the crater dimensions of a transient crater and the subsequent formation of a simple or complex crater.

3.2.3 Impact Crater Ejecta

In addition to plastically deforming and partially melting the impact site, the asteroid impact also ejects ground material outwards from its impact site and the removed material is called ejecta. It can cause immediate damage as bigger fragments cause destruction where they land as well as delayed damage due to a blanket of ashes that covers the surrounding region. (Collins et al., 2005) derive two analytical expressions for ejecta blanket thickness and mean ejecta fragment diameter.

Ejecta blanket thickness t_e is a function of transient crater size D_{tc} and distance from impact site D:

$$t_e = \frac{D_{tc}^4}{112 D^3} \tag{3.43}$$

Mean ejecta fragment diameter L_e is a function of final crater size D_{fr} and distance from the impact site:

$$L_e = 2400\,(0.0005 D_{fr})^{-1.62} \left(\frac{D_{fr}}{2D}\right)^{2.65} \tag{3.44}$$

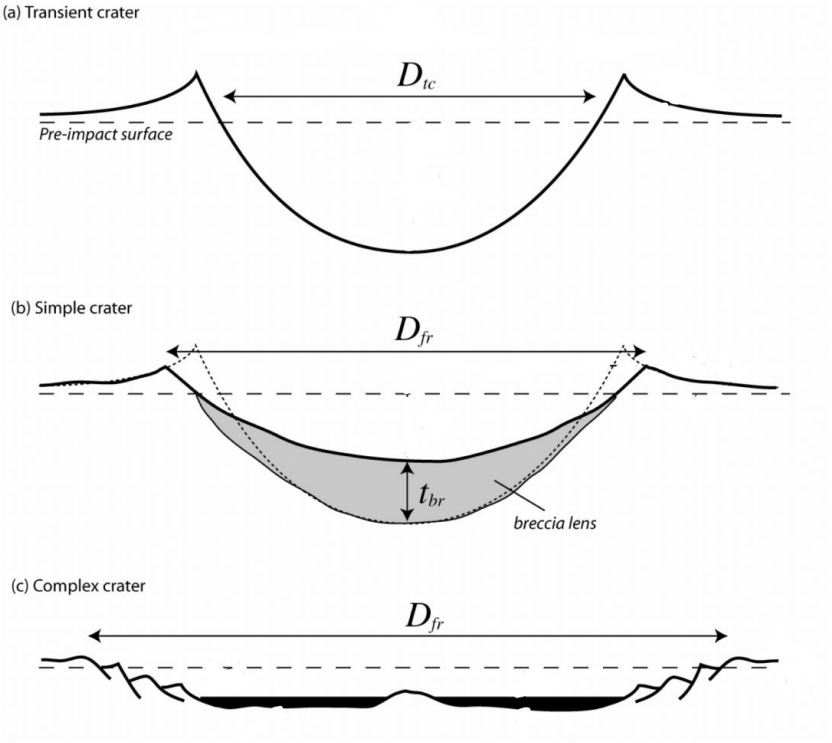

Figure 3.12: Crater dimensions for the (a) transient crater, (b) simple final crater or (c) complex final crater. (Modified from (Collins et al., 2005).)

3.2.4 Seismic Shock

The seismic shock is expressed in terms of the Gutenberg-Richter scale magnitude. It is assumed that a fraction of 10^{-4} of the impacting kinetic energy is transformed into seismic shaking (Schultz and Gault, 1975). The Gutenberg-Richter magnitude energy relation provided the magnitude of the expected shock as:

$$M = 0.67 \log_{10} E - 5.87 \tag{3.45}$$

where E is the impacting kinetic energy in Joules, and M is the magnitude on the Richter scale. With increasing distance from the impact site, the force of the shocks decreases and (Collins et al., 2005) present an empirical law that describes the effective magnitude M_{eff} at a distance D from the impact site:

$$M_{eff} = \begin{cases} M - 2.38 \times 10^{-5} D & | \quad D < 60 \times 10^3 \,\mathrm{m} \\ M - 4.8 \times 10^{-6} D - 1.1644 & | \quad 60 \times 10^3 \,\mathrm{m} \leq D < 700 \times 10^3 \,\mathrm{m} \\ M - 1.66 \log_{10} \Delta - 6.399 & | \quad 700 \times 10^3 \,\mathrm{m} \leq D \end{cases} \tag{3.46}$$

The angle Δ around the centre of the Earth connects the impact point with the observer point at distance D. It is calculated as:

$$\Delta = \frac{D}{R_{\oplus}} \tag{3.47}$$

The effective magnitude can be related to the expected destruction at the given distance from the impact point and determines vulnerability.

3.2.5 Air Blast

An asteroid impacts or airbursts in an explosion like process. The explosion generates a shock wave that raises the atmospheric pressure at the wave front and also causes strong winds. This phenomenon is called air blast. Experiments by the US Department of Defense were utilized to deduct analytical expressions for peak overpressure and wind speeds (Glasstone and Dolan, 1977). Because these experiments were conducted using 1 kt TNT explosions, the expressions needed to be scaled according to their explosive yield energy. Yield scaling is accomplished by scaling the distance at which the effect is observed and the corresponding expression is:

$$D_1 = \frac{D}{E_{kt}^{1/3}} \tag{3.48}$$

where D_1 is the yield scaled distance, D is the physical distance and E_{kt} is the equivalent yield energy in kilotons TNT.

Air blasts are caused by asteroid impacts in the ground but also by airburst events where the asteroid disintegrates rapidly in mid air. It should be noted that recent literature suggests that airburst effects may be underestimated using data from static detonations. The main difference between the US Department of Defense experiments and real asteroid explosions is that the asteroids are travelling at high speeds when they disintegrate. (Boslough and Crawford, 2008) found that the effect of momentum conservation during the detonation had significant implications for the pressure wave that reaches the ground. Air blast effects due to airbursts might be significantly more powerful than estimated here. However, the new findings lacked analytical descriptions and this situation rendered them impractical here. This work continued to use the older analytical expressions in (Collins et al., 2005) and derived from (Glasstone and Dolan, 1977) knowing that they might be out of date.

3.2.5.1 Air Blast from Ground Impact

The overpressure in an impact event at a distance D is calculated with (Collins et al., 2005):

$$p_D = \frac{p_x D_x}{4D_1}\left(1 + 3\left[\frac{D_x}{D_1}\right]^{1.3}\right) \tag{3.49}$$

In this equation, p_D is the pressure in Pa at distance D and the two definitions p_x and D_x are set to $p_x = 75000\,\text{Pa}$ and $D_x = 290\,\text{m}$.

3.2.5.2 Air Blast from Airburst

In the event of an airburst, the blast wave interacts with the ground in two distinct mechanisms. The cause for the different mechanisms is constructive interference between the direct blast wave and the one reflected from the ground. Far away from the explosion, both these waves approach a perpendicular orientation with respect to the ground. They are almost parallel which allows them to experience constructive interference. This region is called Mach zone. Expression 3.49 describes the behaviour in this distance regime provided that the scale distance D_x is modified as a function of burst altitude:

$$D_x = 289 + 0.65 z_{b1} \tag{3.50}$$

Close to the ground point directly below the explosion, the direct and the deflected blast wave do not interact. This region is called regular reflectance zone. No interference occurs and the pressure decays exponentially:

$$p_D = p_0 e^{-\beta D_1} \tag{3.51}$$

Parameters p_0 and β are functions of burst altitude (Collins et al., 2016, 2005):

$$p_0 = 3.14 \times 10^{11} z_{b1}^{-2.6} + 1.8 \times 10^{7} z_{b1}^{-1.13} \tag{3.52}$$

$$\beta = 34.87 z_{b1}^{-1.73} \tag{3.53}$$

The distance at which constructive interference occurs is a function of airburst altitude:

$$D_{m1} = \frac{550 z_{b1}}{1.2(550 - z_{b1})} \tag{3.54}$$

where D_{m1} and z_{b1} are subject to yield energy scaling according to relation 3.48. Note that at airburst altitudes higher than $z_{b1} > 550\,\text{m}$ it is assumed that no constructive interference occurs and overpressure behaved as described in equation 3.51.

3.2.5.3 Wind blast during Airburst

Besides the shock induced by overpressure, a wind blast is another hazardous part of an airburst. The wind speed is calculated in accordance with (Glasstone and Dolan, 1977) with:

$$u = \frac{5p_D}{7p_a} \frac{c_0}{(1 + {}^{6p_D}/_{7p_a})^{0.5}} \tag{3.55}$$

where p_a is the ambient air pressure and c_0 is the speed of sound.

3.2.6 Thermal Radiation

Similarly to the air blast effect, thermal radiation can be caused by a ground impact or by an airburst and the generation of thermal radiation is modelled differently in each case.

3.2.6.1 Thermal Radiation from Ground Impact

If the impacting meteoroid travels in excess of 15 $^{\text{km}}/_{\text{s}}$, enough energy is released to evaporate the asteroid and some of the ground material. This violent event generates a plume with very high pressure (>100 GPa) and temperature (≈10000 K) that rapidly expands. This is called the fireball. As a result of the high temperature, the plume is ionized and appears opaque to thermal radiation due to the plasma's radiation absorption characteristics. Consequently, the plume expands adiabatically and only starts to radiate outwards when the plasma cools to the transparency temperature T_* (Zel'dovich and Raizer, 1966). (Collins et al., 2005) find an empirical relationship for the fireball radius when it reaches transparency temperature as a function of impact energy E:

$$R_f = 0.002E^{1/3} \tag{3.56}$$

Assuming that the fireball expands with the impact speed of the meteoroid until it reaches the size R_f, the time of maximum thermal radiation is calculated:

$$t_{t_{max}} = \frac{R_f}{v_i} \tag{3.57}$$

Only a fraction of the kinetic energy released during impact is transformed into thermal radiation (Nemtchinov et al., 1998). This fraction is called the luminous efficiency η_{lum} and (Ortiz et al., 2000) determined that it is on the order of 10^{-4} - 10^{-2}. The received thermal energy per area unit (assuming a hemispheric dissipation of heat radiation) is given by (Collins et al., 2005):

$$\phi = f\frac{\eta_{lum}E}{2\pi D^2} \tag{3.58}$$

where f is the fraction of the fireball that is visible over the horizon at distance D and is calculated as:

$$f = \frac{2}{\pi}\left(\cos^{-1}\frac{(1-\cos\Delta)R_{\odot}^{\pm}}{R_f} - \frac{(1-\cos\Delta)R_{\odot}^{\pm}}{R_f}\sin\left[\cos^{-1}\frac{(1-\cos\Delta)R_{\odot}^{\pm}}{R_f}\right]\right) \tag{3.59}$$

Equation 3.47 provides the definition for the term Δ. The received thermal radiative energy can be related to thermal ignition energies of specific materials to enable damage estimates.

3.2.6.2 Thermal Radiation from Airburst

Besides the air blast, some of the kinetic energy carried by the meteoroid that is released during airburst dissipates as thermal radiation. (Nemtchinov et al., 1994) investigated the radiation emitted by meteors and the following airburst thermal radiation model derived here was based on this research. Equation (11) of the reference provides an expression for thermal energy flux density based on airburst intensity:

$$\phi = q_h\left[\frac{L_0}{2D_{\text{los}}}\right]^2 5 \tag{3.60}$$

where ϕ is the energy flux density in $[\mathrm{W/m^2}]$ at the target distance, $q_h(v)$ (the reference uses q_∞) is the energy flux density emitted by the meteoroid at a given altitude as a function of speed, L_0 is the meteoroid diameter and D_{los} is the line of sight distance from the airburst to the target. Table 1 of the reference provides values for $q_h(v)$ as a function of speed for the two altitudes of 25 km and 40 km. Here, an interpolation function was built that produces $q_h(v)$ values for any given speed, altitude pair based on table 1 in the reference. To this end, a six degree polynomial was least square fitted to the data describing $q_{h=25}$ at 25 km altitude as a function of speed v:

$$\begin{aligned} q_{h=25}(v) = (-4\times10^{-16}v^6) + (7\times10^{-11}v^5) - (5\times10^{-6}v^4) \\ + (0.176v^3) - (3160.6v^2) + (3\times10^{7}v) - 1\times10^{11} \end{aligned} \tag{3.61}$$

The polynomial has a correlation coefficient of 0.9868 with the data. Only three data points were available for the data for $q_{h=40}$. However, the data fits perfectly on a line described by:

$$q_{h=40}(v) = 700000v - 1\times10^{10} \tag{3.62}$$

Finally, a linear interpolation scheme estimates q_h for any given airburst altitude z_b based on the calculated values for $q_{h=25}$ and $q_{h=40}$.

$$q_{h=z_b} = \frac{q_{25}-q_{40}}{15000}(40000 - z_b) + q_{40} \tag{3.63}$$

The distance D_{los} was estimated using Pythagoras' relationship with airburst altitude z_b and ground distance D as parameters:

$$D_{\text{los}} = \sqrt{z_b^2 + D^2} \tag{3.64}$$

With these relations, Equation 3.60 can be solved and a thermal energy flux density may be obtained for any airburst event.

Note that the unit of Equation 3.60 is $[\text{W}/\text{m}^2]$ and that for subsequent analysis the thermal radiation energy density $[\text{J}/\text{m}^2]$ was needed. Based on visual observations of the Chelyabinsk (Popova et al., 2013) and other meteors (Borovička and Kalenda, 2003) it was determined that a break-up occurs within a time span on the order of one second. Therefore, one second was assumed as the default break-up duration for airbursts and the unit $[\text{W}/\text{m}^2]$ is equivalent to the energy density $[\text{J}/\text{m}^2]$ when integrated for this timespan because energy is the integral of energy flux [W]=[J/s] over time [s]. This relation is expressed by the following example equation assuming that energy flux is constant over time:

$$1\,\text{J} = 1\,\text{W} \times 1\,\text{s} = 1\,\text{J}/\text{s} \times 1\,\text{s} \tag{3.65}$$

3.2.7 Tsunami

For asteroids that reach the Earth's surface intact, a water impact is twice as likely as a ground impact because water covers about double the surface area compared to ground. When an asteroid impacts a water surface, a circular wave pattern is generated and these waves may reach tens of meters in amplitude. Such waves are referred to as tsunamis and, when large enough, they cause devastation at coastlines where they inundate inhabited zones.

Tsunami modelling due to asteroid impacts has received some attention in recent decades but high uncertainties with respect to the expected wave heights, not just in deep water but especially at the interface between sea and land, remain (Wünnemann et al., 2010; Korycansky and Lynett, 2007; Ward and Asphaug, 2000; Van Dorn et al., 1968; Gisler et al., 2011). However, a comparative analysis was conducted in Wünnemann et al. (2010) and a suitable, analytical description of wave amplitude $A(D)$ propagation in deep water as a function of transient water cavity diameter D_{tc} and distance D was given as:

$$A(D) = \min\left(0.14 D_{tc}, h_{\text{sea}}\right)\left(\frac{D_{tc}}{2D}\right) \tag{3.66}$$

where h_{sea} is the ocean depth at the impact site.

This equation adopts a $1/D$ wave distance attenuation relationship which seems to match observations made for the 2004 Sumatra tsunami (Weiss et al., 2006; Fritz et al., 2007) The transient cavity diameter D_{tc} may be calculated with Equation 3.42 using the

constant factor 1.365 instead of 1.161 (Collins et al., 2005).

$$D_{tc} = 1.365 \left(\frac{\rho_i}{\rho_t}\right)^{1/3} L_0^{0.78} v_i^{0.44} g_0^{-0.22} \sin^{1/3}\gamma \tag{3.67}$$

To determine the coastline that is affected by an impact generated tsunami, a fast ray tracing algorithm was employed. The algorithm has a priori knowledge of how far the closest coastline is away from the impact point and only starts the numerically intensive ray tracing from this distance outwards. Consequently, the algorithm is able to extract such coastlines that are directly "visible" from the impact site. Actual wave propagation across the ocean is more complex because refraction of waves around land features, and subsequent interference of the wave with itself may occur. However, in this research, the impact problem is treated in a statistical manner and the resulting need for multiple impact point wave propagation did not allow for computationally expensive numerical methods. Instead, the analytical approach chosen here compensates for some of the complex wave propagation aspects through its statistical nature while also offering a computationally efficient solution. The approach is statistical because it treats impact point distributions instead of a singular impact point and it is, thus, capable of exposing coastlines that might be hidden for a singular impact point calculation using a ray tracing algorithm.

The magnification of a tsunami wave as it approaches the shore is called run-up and this parameter ultimately determines how much of the coastal area is inundated and, thus, threatened. Run-up is treated in Korycansky and Lynett (2007) utilizing the concept of the "Irribaren number" ξ. The Irribaren number concept is promising because it showed good agreement with various modelling conditions, such as varying bathymetry profiles and wave heights. Much uncertainty in the field of tsunami modelling stems from the question if tsunami waves break at the continental shelf in what is coined the "Van Dorn" effect (Van Dorn et al., 1968). If the Van Dorn effect is real, much of the tsunami energy is dissipated at the continental shelf and the run-up of the wave would be greatly diminished (Melosh, 2003). The Van Dorn effect, introduces considerable uncertainty into direct run-up modelling efforts that take account of the local bathymetry. However, the Irribaren number concept seems to consolidate this discrepancy as demonstrated by comparison with numerical results and wave-tank experiments (Korycansky and Lynett, 2007). The Irribaren number is defined as (Hunt, 1959; Battjes, 1974):

$$\xi = s \left(\frac{2A_{800}}{w}\right)^{-\frac{1}{2}} \tag{3.68}$$

where A_{800} is the deep water wave amplitude when it reaches shallower waters (the threshold has been defined as 800 m in accordance with Korycansky and Lynett (2007)) s is the seabed slope from deep water (800 m) to the shore and w is wavelength. The Irribaren number approach suggests that run-up U scales as the product of deep wave

amplitude A_{800} and Irribaren number ξ:

$$U = 2A_{800}\xi \tag{3.69}$$

In the numerical asteroid ocean impact analysis of Gisler et al. (2011), the approximate, empirical relationship, that wavelength, w, is double the transient crater diameter, D_{tc}, can be found:

$$w = 2D_{tc} \tag{3.70}$$

Combining equations 3.68, 3.69, and 3.70 yields:

$$U = 2sA_{800}\left(\frac{A_{800}}{D_{tc}}\right)^{-\frac{1}{2}} \tag{3.71}$$

Run-up calculation requires determination of the slope of exposed shorelines and slope calculation is accomplished using bathymetry (or, more correctly, hypsography data when it also considers land topography) data which are available from Patterson and US National Park Service (2015). The dataset is visualized in Figure 3.13.

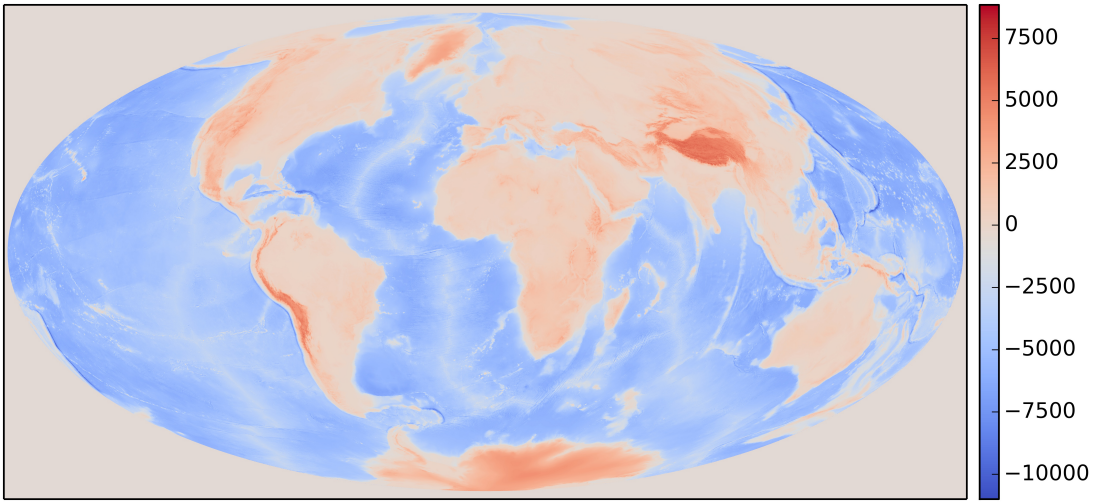

Figure 3.13: World hypsography data with elevation data in meters.

To calculate slope, the sea depth along the path of the tsunami is evaluated and the point where sea depth is less than 800 m is determined. If the impact point is in water that is shallower than 800 m, the depth of the impact point is considered instead. Slope is the ratio of height difference over distance to the shore. The height difference is, either 800 m, or the depth of the impact point (whichever is smaller). Similarly, distance is measured from the impact point or the point of 800 m sea depth in case of a shallow water impact.

3.2.8 Impact Effect Algorithm Implementation Validation

To ensure correct implementation of the effect models from Collins et al. (2005) in ARMOR, the results of two test impact scenarios were compared. The first scenario was an airburst by a 50 m object entering the atmosphere with 22 km/s at an angle of 55 ° and the observer is 2 km away. The second scenario simulated a ground impact by a 250 m object entering the atmosphere with 27 km/s at an angle of 35 ° and the observer is 10 km away. Furthermore, the object density in both scenarios was set to 3100 kg/m³ while the ground density in the second scenario was 2500 kg/m³. Table 3.3 presents the resulting impact effects as calculated by ARMOR and by Collins' "Earth Impact Effects Program" (EIEP). Errors between the two programs are small suggesting

Scenario 1, Airburst:

Aspect	ARMOR	EIEP	Error [%]
Kinetic Energy [J]	4.91×10^{16}	4.91×10^{16}	0.0
Breakup Altitude [m]	57128	57100	0.0
Airburst Altitude [m]	5115	5120	0.1
Post Airburst Speed [km/s]	6.527	6.53	0.0
Airburst Energy [J]	4.48×10^{16}	4.48×10^{16}	0.1
Overpressure [Pa]	171811	172000	0.1
Wind Speed [m/s]	266	258	3.1

Scenario 2, Ground Impact:

Aspect	ARMOR	EIEP	Error [%]
Kinetic Energy [J]	9.24×10^{18}	9.24×10^{18}	0.0
Breakup Altitude [m]	60406	60400	0.0
Impact Speed [km/s]	23.73	23.70	0.1
Impact Energy [J]	7.14×10^{18}	7.14×10^{18}	0.1
Transient Crater Diameter [km]	3.92	3.92	0.1
Final Crater Diameter [km]	4.90	4.71	3.9
Thermal Exposure [J/m²]	3.32×10^{7}	3.40×10^{7}	2.3
Seismic Shaking [Richter Mag]	6.76	6.80	0.6
Ejecta Thickness [m]	2.10	2.10	0.1
Overpressure [Pa]	1046182	1050000	0.4
Wind Speed [m/s]	807	781	3.4

Table 3.3: Result comparison between EIEP and ARMOR for airburst (1) and ground impact (2) scenarios.

correct implementation of the models and the errors can be attributed to the fact that EIEP values are only available in rounded format, to varying definitions of universal constants, and to incomplete descriptions about EIEP algorithm implementation.

3.3 Vulnerability Modelling

The third factor in risk calculation (see Equation 2.4) is vulnerability and it describes how much of the population would be lethally harmed by the effects of an impact. Vulnerability depends on the severity of the effects, and, in general, effects are most severe close to the impact site and attenuate with greater distance. This distance dependency was accounted for in the impact effect models presented in section 3.2. The way vulnerability changes with the severity of each impact effect is discussed in this section and the findings are published in the journal *Meteoritics and Planetary Science* (Rumpf et al., 2017b).

3.3.1 Impact Crater

Determining the vulnerability of the population due to crater formation was straight forward. People who were located within the final crater zone at the time of impact had no chance of survival and thus vulnerability was unity in this area. On the other hand, people outside the final crater zone were not affected by cratering.

The population map resolution of about $4.6 \times 4.6\,\mathrm{km}^2$ was coarse compared to expected crater diameters. To account for this fact, the final crater area was determined assuming a circular crater:

$$A_{fr} = \pi \left(\frac{D_{fr}}{2} \right)^2 \tag{3.72}$$

If the crater size is smaller than the area of one map cell, the vulnerability of this cell was equal to the ratio of crater area to map cell area. This corresponds to the percentage of the map cell area that is covered by the crater. For craters that extend beyond one map cell, the ratio of crater area in the partially covered map cells with respect to the total area of partially covered map cells was estimated. This ratio was assigned as the vulnerability to the partially covered map cells.

3.3.2 Seismic Shaking

The seismic intensity values that are calculated based on the model presented in section 3.2.4 are used to estimate human losses to seismic shaking. To this end, a literature review was conducted to find suitable data to support a seismic vulnerability model. Specifically, data was needed to relate seismic shaking intensity at a given location to the mortality rate at this location. However, typical earthquake records only report peak intensity and total losses and this data is too convoluted for usage here because it depends on population density and affected area in the location of the earthquake which are typically not reported (Norlund, 2013). The data reports fatalities that occur in an area that encompasses the entire earthquake region and relates this casualty figure to the

peak intensity shaking. However, not all fatalities occur at the location of peak shaking intensity (the epicentre) and some casualties are found at a distance to the epicentre. Thus, it would be wrong to use this data because it attributes the casualties of the entire earthquake region to the peak shaking intensity and would produce a overestimation for a given seismic intensity.

What was needed was a function that provided the mortality rate with respect to local shaking intensity because mortality varies with distance from the epicentre. In other words, the same earthquake produces a high mortality rate close to the epicentre where seismic shaking is severe and a lower mortality rate at a distance from the epicentre because seismic shaking attenuates with greater distance. (Wu et al., 2015) provide mortality rates as a logistic function of seismic intensity based on earthquake records in China and validate the derived models against four severe earthquake events. It should be noted that the reported mortality rates are equivalent to the vulnerability rates that are of interest here because the mortality rates describe the observed result of how many casualties occurred for a given seismic shaking intensity. The vulnerability logistic function that best fit the validation data (mean estimation error of 12 %) with seismic intensity (Modified Mercalli Intensity (US Geological Survey, 2015)) as free parameter is:

$$V_{i_{seis}} = \frac{1}{0.01 + 2.691 \times 10^6 \times 0.170^{i_{seis}}} \tag{3.73}$$

Collins et al. (2005) in Table 2 provide data that allow the translation of Modified Mercalli Intensity values into Richter magnitude values and this table is reproduced here in table 3.4.

Richter magnitude	**Modified Mercalli Intensity**
0-1	-
1-2	I
2-3	I-II
3-4	III-IV
4-5	IV-V
5-6	VI-VII
6-7	VII-VIII
7-8	IX-X
8-9	X-XI
9+	XII

Table 3.4: Translational data for Richter magnitude and Modified Mercalli Intensity (Collins et al., 2005)

Here, a linear function was least square fit to the data ($R^2 = 0.9887$) and it is:

$$i_{seis} = 1.4199 M_{eff} - 1.3787 \tag{3.74}$$

Equations 3.73 and 3.74 can be converted into a new logistic function that yields expected vulnerability with effective shaking expressed in Richter magnitude as free parameter:

$$V_{\text{seis}}^{\text{expected}} = \frac{1}{1 + e^{-2.51607678(M_{eff} - 8.68559246)}} \tag{3.75}$$

Furthermore, Figure 4 as well as Table 5 of (Wu et al., 2015) supplies data about the variability in vulnerability data and these two data sets are reproduced in Figure 3.14 and Figure 3.15, respectively.

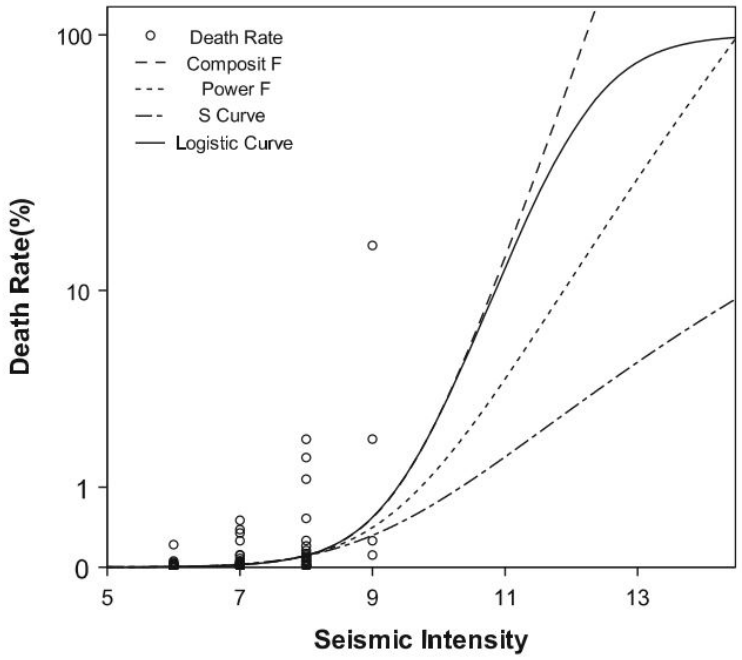

Figure 3.14: Figure 4 of Wu et al. (2015) showing variability in historical earthquake data and corresponding function fits.

	VI		VII		VIII		IX	
	Sample size	Standard deviation	Sample size	Standard deviation	Sample size	Standard deviation	Sample size	Standard deviation
Nationwide	23	0.044	27	0.130	21	0.551	4	7.277
Western region I	17	0.003	21	0.008	17	0.275	3	1.070

Figure 3.15: Table 5 of Wu et al. (2015) provides values and variability for historical earthquake data.

Based on this additional information the curves for best and worst case vulnerability to seismic shaking could be established. To determine the worst case vulnerability curve, the data that supports the expected case vulnerability curve was varied upwards

according to the standard deviation values provided in Table 5 in (Wu et al., 2015). The variability is smaller for the best case vulnerability and the S-curve fit from Figure 4 in (Wu et al., 2015) was used to represent the lower bound of the seismic vulnerability space. The equations describing the best and worst case vulnerability logistic functions are:

$$V_{\text{seis}}^{\text{best}} = \frac{1}{1 + e^{-2.50819825(M_{eff} - 9.58960178)}} \tag{3.76}$$

$$V_{\text{seis}}^{\text{worst}} = \frac{1}{1 + e^{-3.79723002(M_{eff} - 7.60044786)}} \tag{3.77}$$

All three seismic vulnerability curves are presented in Figure 3.16. Research conducted

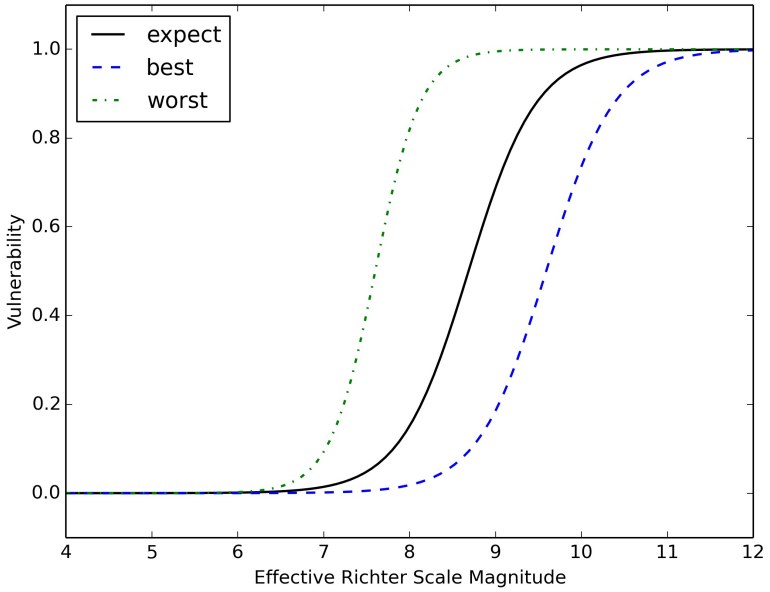

Figure 3.16: Best, expected and worst case seismic shaking vulnerability models.

by (Norlund, 2013) shows that earthquakes have a vulnerability of zero for seismic shaking magnitudes below 3.5 based on historic data and the present vulnerability models concur with this finding.

3.3.3 Overpressure

According to (Glasstone and Dolan, 1977), humans, like other mammals, are injured by the difference of body internal pressure to body external pressure. It is not the high pressure as such that is damaging but the pressure differential. The pressure differential exists because the external pressure increases rapidly due to an arriving overpressure shock wave without the necessary time for the internal pressure to equalize. The source provides overpressure estimates for vulnerability values of 0.0, 0.5 and 1.0.

Vulnerability	**Overpressure [Pa]**	**Overpressure [Bar]**
0.0	≤275790 (±68947)	≤2.8 (±0.69)
0.5	427474 (-82737 / +89631)	4.3 (-0.83 / +0.90)
1.0	≥634317 (-117210 / +158579)	≥6.3 (-1.17 / +1.59)

Table 3.5: Overpressure vulnerability data that was extrapolated from animal test to humans. Values in parenthesis provide bounding values. Modified from (Glasstone and Dolan, 1977)

Overpressure vulnerability V_p can be modelled as a function of pressure p in Pascal. To this end, three sigmoid functions were fitted to the experimental data in table 3.5 to approximate best, expected and worst case vulnerabilities according to the bounds provided:

$$V_p^{\text{best}} = \frac{1}{1 + e^{-0.0000189909087(p-542813.376)}} \tag{3.78}$$

$$V_p^{\text{expected}} = \frac{1}{1 + e^{-0.0000242498102(p-440430.986)}} \tag{3.79}$$

$$V_p^{\text{worst}} = \frac{1}{1 + e^{-0.0000284660390(p-352855.842)}} \tag{3.80}$$

Figure 3.17 provides a visual representation of the three models.

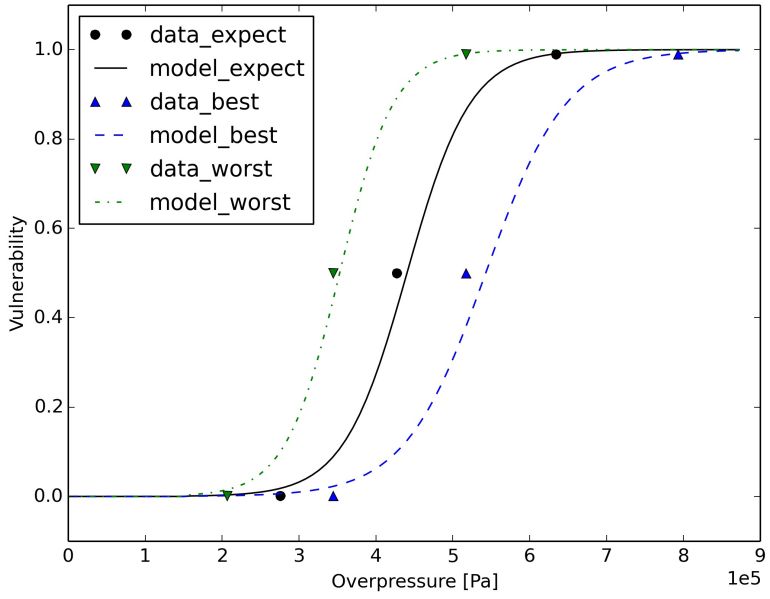

Figure 3.17: Best, expected and worst case overpressure vulnerability models.

3.3.4 Thermal Radiation

Thermal radiation is emitted from airbursts and ground impacts. Surfaces that are incident to the radiation heat up and can be burned or ignited. (Glasstone and Dolan, 1977) investigated the consequences of thermal radiation energy exposure on the human body as a consequence of nuclear detonations. The burn probability as a function of radiant exposure and explosion yield is given in Figure 12.65 of the reference and is reproduced in Figure 3.18.

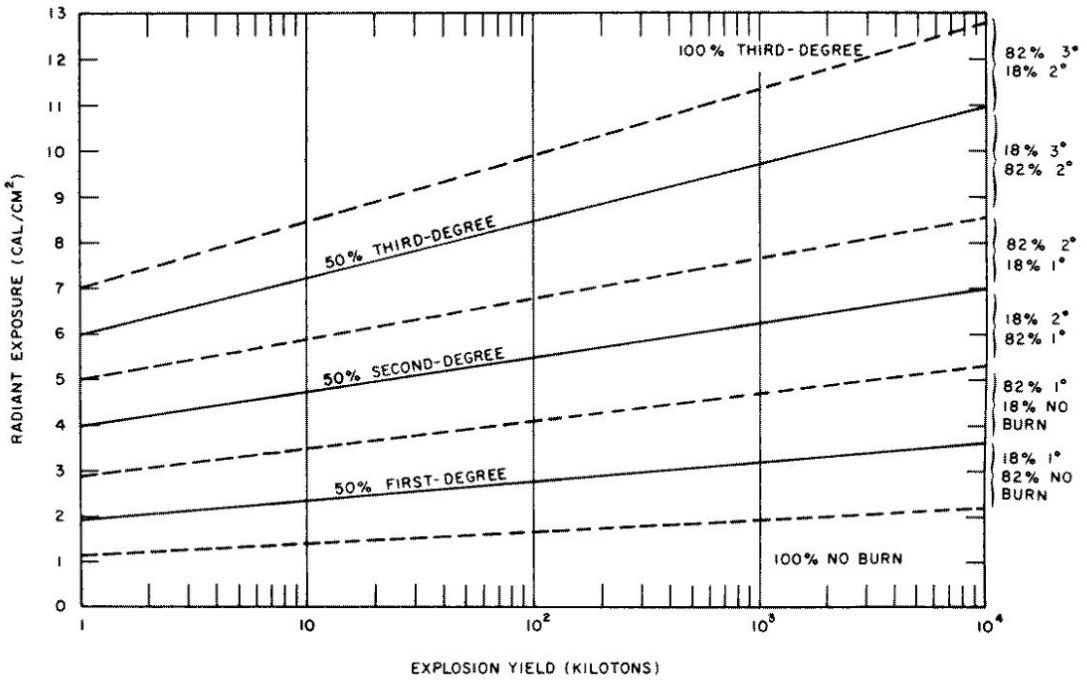

Figure 3.18: Figure 12.65 of Glasstone and Dolan (1977) yields data on skin burn probability as a function of radiant exposure.

While the dependency of burn probability to radiant exposure [J/m²] is obvious, its dependency on explosion yield should be explained.

The dependency on explosion yield is rooted in the observation that small yield explosions take less time than large yield explosions resulting in different energy flux rates. For smaller explosions, a given amount of radiant energy is delivered in a shorter time compared to a larger explosion and, thus, the radiation intensity differs with explosion yield. Higher radiation intensity causes injuries more readily than low intensity radiation even though the same cumulative energy might be delivered in both cases. The reason for this behaviour is that the heated surface has more time to dissipate the incident radiation energy in a low intensity radiation case. Unlike nuclear explosive devices, meteoroids are not optimized for explosion and it is thus assumed that their explosion signature is more comparable to that of a large nuclear device because the explosion

process takes relatively long. The data used to build the vulnerability model correspond to the results produced by a 1 Mton TNT equivalent yield nuclear device as shown in Figure 12.65 in reference (Glasstone and Dolan, 1977).

The burn severity distribution is a function of radiant exposure and the data in (Glasstone and Dolan, 1977) forms the basis for Figure 3.19 that shows which burn degree can be expected when exposed to a certain radiant energy.

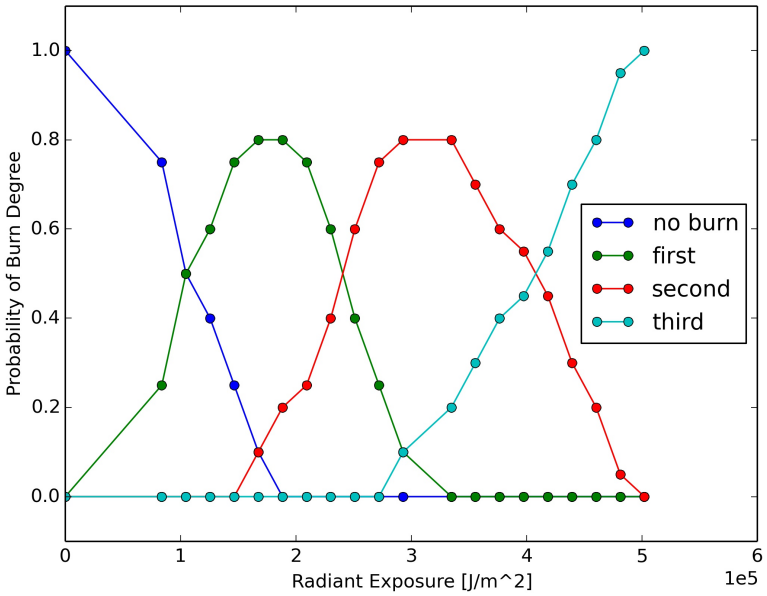

Figure 3.19: Burn degree distribution as a function of radiation intensity based on data in (Glasstone and Dolan, 1977) assuming the explosion signature of a 1 Mton TNT yield nuclear device.

Aside from burn degree, the total body surface area (TBSA) of a human that is burned determines the expected mortality. In (Phillips et al., 2012), statistical analysis of 143,199 burn victims in the United States were analysed for their mortality rate based on burned TBSA. The reported numbers apply to persons who have been treated in medical facilities after the burn injury. This means that the burn injury itself could be treated adequately but also that possible subsequent medical complications (pneumonia, infection) that are directly linked to the burn injury could be addressed. Here, it shall be assumed that mortality rates are twice as high because proper and timely treatment of burn injuries is unlikely in the event of an asteroid impact that will potentially affect a large region and its medical infrastructure. Figure 3.20 visualizes the data in Table 9 of (Phillips et al., 2012) and shows the mortality rate as a function of burnt TBSA for treated and untreated victims.

To relate radiant exposure to TBSA and, thus, to mortality rate, a scaling law is introduced that approximates TBSA based on the burn degree distribution as a function of radiant exposure. In general, every part of the body that is exposed to light from

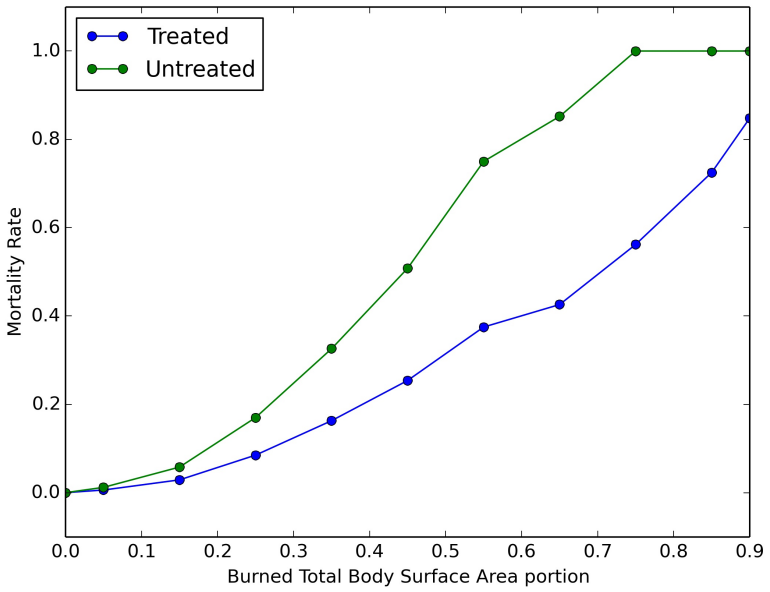

Figure 3.20: Mortality rate for treated and untreated burn victims as a function of burnt TBSA. Data from (Phillips et al., 2012).

the meteoroid explosion will be burned, but the severity of the burn differs. A superficial first degree burn, which is comparable to a bad sun burn, is less life threatening than a third degree burn that penetrates through all skin layers. To account for this distinction, a scaling law was introduced that yields TBSA as a function of burn degree distribution. The scaling law is the weighted sum (first degree has weight one, second degree has weight two and third degree has weight three) of the burn distribution as a function of radiant exposure.

$$\mathrm{TBSA}_{\mathrm{weighted}}(\phi) = \frac{1}{9}\left[1 \times \mathrm{burn}_{1^\circ}(\phi) + 2 \times \mathrm{burn}_{2^\circ}(\phi) + 3 \times \mathrm{burn}_{3^\circ}(\phi)\right] \tag{3.81}$$

Furthermore, the scaling law respects the observation that the thermal radiation from an asteroid impact arrives from only one direction. This situation permits only half of a human, or a maximum of 50 % TBSA, to be injured from thermal radiation. Moreover, clothing (as long as it does not burn itself) provides protection against a short lived energy burst of thermal radiation and it is therefore assumed that only one third of TBSA can be burned for people standing outside. Figure 3.21 visualizes the resulting TBSA curve as a function of radiant exposure.

Combining the data from (Glasstone and Dolan, 1977) about radiant exposure and the resulting burn severity with the scaling law to relate burn severity with TBSA and, finally, with the data from (Phillips et al., 2012) about mortality rate based on TBSA, mortality rate can be expressed as a function of radiant exposure. Figure 3.22 shows the relationship. This data is based recorded occurrences and the corresponding radiant exposure range is limited to these records. An asteroid impact can produce higher

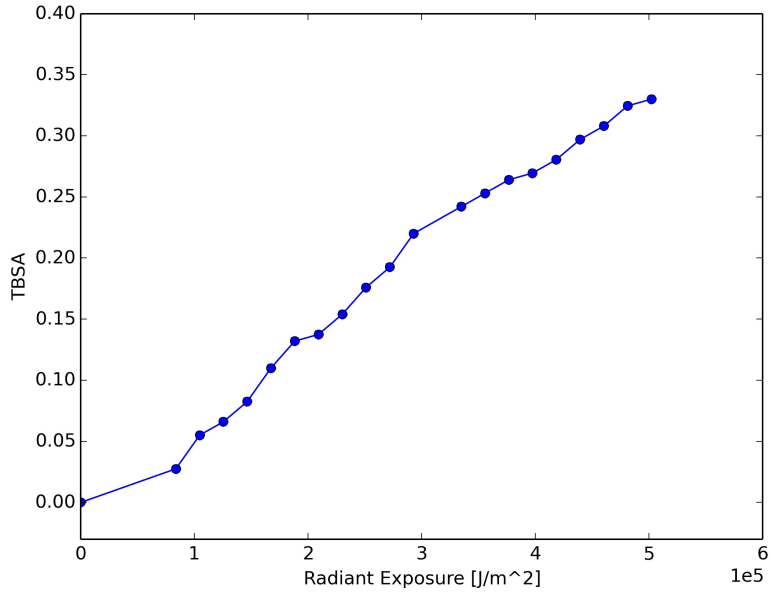

Figure 3.21: Visualization of TBSA-burn degree scaling law (Equation 3.81. The maximum TBSA is scaled to one third as clothing offers protection and radiation comes from one direction.

radiant energies and the mortality rate, thus, has to be expanded to higher values of radiant exposure.

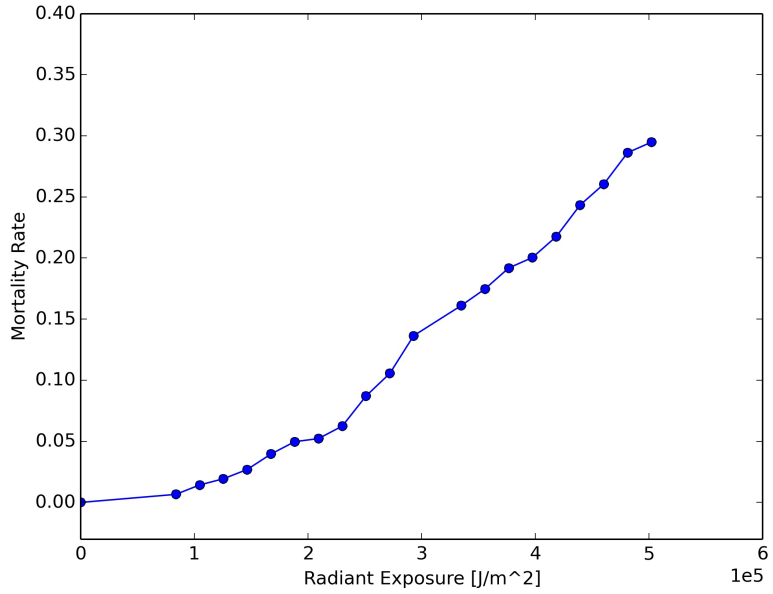

Figure 3.22: Mortality rate as a function of radiant exposure.

Clothing provides limited protection to thermal radiation because it can absorb thermal energy up to the point when it itself ignites and it was therefore assumed that only one third of TBSA can be burned before clothing ignites. (Glasstone and Dolan, 1977)

reports that cotton and denim clothing ignites at about 836800 $^{J}/_{m^2}$. Beyond this energy level clothing does not offer protection and it was assumed that 50 % of TBSA can be burned resulting in a mortality rate of 62 % (Phillips et al., 2012). Furthermore, at energy densities of 1255200 $^{J}/_{m^2}$, (Glasstone and Dolan, 1977) reports that sand explodes (popcorning), aluminium aircraft skin blisters and roll roofing material ignites. These conditions appear lethal to humans and a mortality rate of one is assumed for a population exposed to this energy level.

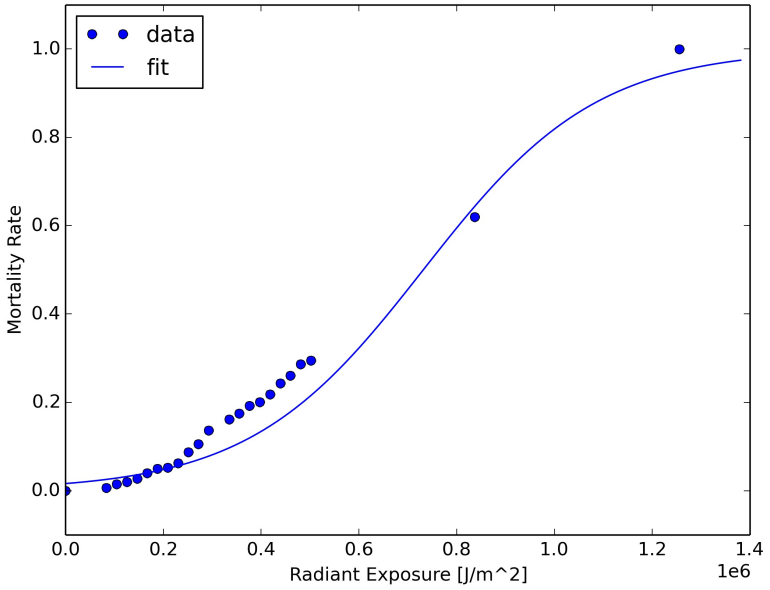

Figure 3.23: Mortality rate as a function of the full, applicable radiant exposure range.

Figure 3.23 presents the full range of thermal radiation mortality rate and shows the corresponding data points. Additionally, a sigmoid function has been least square fitted to the data and the corresponding mathematical description is:

$$\text{Mortality Rate}(\phi) = \frac{1}{1 + e^{-0.00000562327(\phi - 731641.664)}} \tag{3.82}$$

The mortality numbers derived above apply to the exposed population that is outside of sheltering buildings. It becomes necessary to estimate how many people are sheltered and unsheltered at any given time. In section 3.3.4.1, the estimation is derived and the outcome is that 78 % of the global populations are sheltered and 22 % are unsheltered. This assumption shall be used throughout this work where applicable.

For people inside of buildings the mortality rate will be moderated through the protective effect of walls. However, windows do not offer protection against thermal radiation and it is assumed that one third of the inside population (25 % of global population) is exposed through windows even though they are inside a building.

Furthermore, to achieve a sense of the variability in casualty prediction the proportions of sheltered/unsheltered populations were varied. For further analysis, it was assumed that in the worst case, the global population is unsheltered while in the best case, the entire population is sheltered. The expected case is that 22 % are outside and 25 % are exposed behind windows (totalling 47 %) while the remaining 53 % of the population are unaffected by thermal radiation. The mathematical expression of the expected case (a maximum of 47 % of the population are exposed) for the vulnerability function, is thus:

$$V_{\phi}^{\text{expected}} = 0.47 \times \left[\frac{1}{1 + e^{-0.00000562327(\phi - 731641.664)}} \right] \tag{3.83}$$

In the worst case, when all population is assumed to be exposed, the vulnerability function is:

$$V_{\phi}^{\text{worst}} = 1 \times \left[\frac{1}{1 + e^{-0.00000562327(\phi - 731641.664)}} \right] \tag{3.84}$$

And in the best case scenario - all population is sheltered but 25 % are exposed through windows - the vulnerability function is:

$$V_{\phi}^{\text{best}} = 0.25 \times \left[\frac{1}{1 + e^{-0.00000562327(\phi - 731641.664)}} \right] \tag{3.85}$$

The expected, best and worst case vulnerability models to thermal radiation are shown in Figure 3.24.

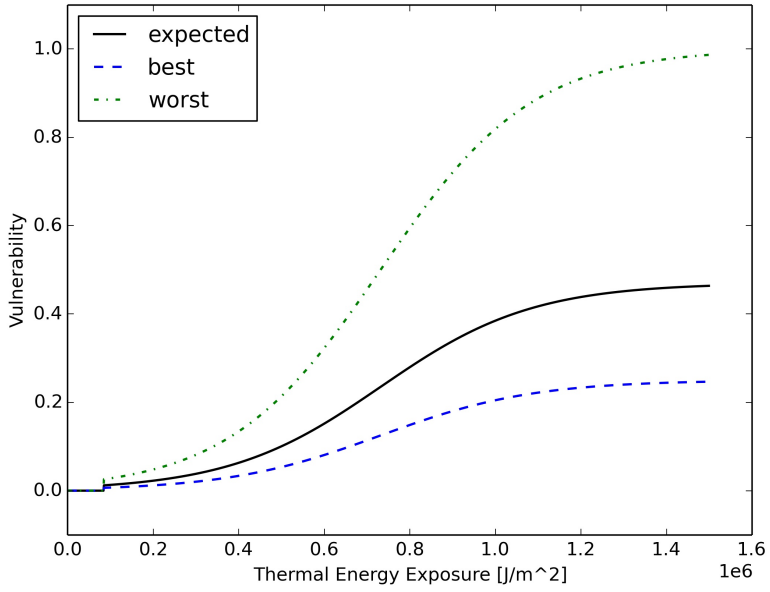

Figure 3.24: Best, expected and worst case thermal radiation vulnerability models.

3.3.4.1 Unsheltered Population

The vulnerability analysis required an assumption about the portion of global population that is unsheltered at any given time. Unsheltered means that an individual is outside a building.

The literature provides some data about the average time that people spend outdoors but the used data sets are limited to populations that share similar work patterns with the so called "western world". (Klepeis et al., 2001) finds that the average American spends 13 % ≈ 3.12 hours per day outside buildings. The meta study (Diffey, 2011) reports that people belonging to western nations spend an average of 1.99 hours per day outdoors which does not include time spent in vehicles. Vehicles offer negligible shelter against thermal radiation as well as shock waves and the time spent in vehicles will be counted towards unsheltered time. Commuting time will be used as a proxy for time in vehicles. The Labour Force Survey (Trades Union Congress, 2012) reports that the average commuting time in the UK in 2012 was 54.6 minutes. Similarly, the U.S. Census American Community Survey (U.S. Census Bureau, 2011) indicates that the average round-trip commuting time in the United States is 50.8 minutes. Adding commuting time as well as the outside 1.99 hours from the meta study provide the time spent outdoors as supported by the meta study and this time is about 2.87 hours or about 12 % of each day. Together, the findings indicate that the average westerner is unsheltered for about 13 % of each day.

The population that this work pattern was applied to is about 2.5 billion people (European Union, USA, Canada, Australia, New Zealand, Japan and parts of: Russia, China, India, Brazil, Argentina, Arab countries), while the global population is about 7.3 billion people. The data reported above does not account for non-western populations. Given the lower industrialisation standard in non-western countries, it is assumed that non-western populations spend twice as long outside as westerners (26 %). With this assumption the western and non-western populations could be connected and the weighted average time that the global population spends outdoors was computed as:

$$\frac{0.13 \times 2.5 + 0.26 \times (7.3 - 2.5)}{7.3} = 0.22 \tag{3.86}$$

For further analysis, it was assumed that 22 % of the population is unsheltered at any given time.

3.3.5 Strong Winds

The blast of an impacting or airbursting asteroid generates a pressure shock wave that delivers strong winds. No human vulnerability data relating to strong winds could be found in the literature and, instead, these data were derived here. Determining

vulnerability due to strong winds caused by asteroid impacts is a challenging task due to the lack of directly applicable research data. However, the wind profile of Tornados show similar characteristics to the profile that can be expected as a result of an asteroid impact. The Enhanced Fujita (EF) scale (Wind Science and Engineering Center, 2006) is used in the United States of America to appropriate the severity of Tornados to six categories (EF0 - EF5) and its criteria is the wind speed in the peak 3-second gust. The vulnerability to Tornados was estimated based on this scale and based on the expected damage for each EF category (listed in Table 3.6). Additionally, reference (Glasstone and Dolan, 1977) provides some data on strong wind interaction with humans.

Category	**3 s Wind Gust [m/s]**	**Typical Damage**
EF0	29 - 38	Large tree branches broken; Trees may be uprooted; Strip mall roofs begin to uplift.
EF1	38 - 49	Tree trunks snap; Windows in Institutional buildings break; Façade begins to tear off.
EF2	49 - 60	Trees debark; Wooden transmission line towers break; Family residence buildings severely damaged and shift off foundation.
EF3	60 - 74	Metal truss transmission towers collapse; Outside and most inside walls of family residence buildings collapse.
EF4	74 - 89	Severe damage to institutional building structures; All family residence walls collapse.
EF5	>89	Severe general destruction.

Table 3.6: Enhanced Fujita scale, corresponding wind speeds and expected structural damage. Data from (Wind Science and Engineering Center, 2006)

The damage data provided in Table 3.6 is dependent on a range of wind speeds (second column). The best, expected and worst case distinction is made by assigning the upper bounds of the wind speed ranges that determine EF category in Table 3.6 to the best case outcome, the mid-range speed to the expected outcome and the lower bounds to the worst case outcome. Table 3.7 lists the relevant data points for this concept.

EF0 According to the EF scale, EF0 corresponds to wind speeds between 29-38 m/s. Humans can be harmed in this condition by being thrown against objects or objects being hurled at them. (Glasstone and Dolan, 1977) provides estimates for lethality for objects turned into missiles that hit the body. According to this source, a 5 kg object entails a near 100 % rate of fracturing a skull when hitting the head with a velocity exceeding 7 m/s. On the other hand, lethality may occur when the body is thrown against solid objects with velocities in excess of 6 m/s. It is conceivable that these events may occur in a category EF0 tornado. Indeed, category EF0 tornados have been lethal

in the past (NOAA, 2015) but the casualty rate is low (3 people were killed by EF0 tornados between 1997 and 2005). Here, it was assumed that 1 % of the population that is outdoors is being hit by missiles or thrown against objects (affected population) and that 2 % of these individuals die as a direct result of the injury. These assumptions provide a vulnerability of 0.000044 for strong winds corresponding to a category EF0 tornado.

EF1 With increasing wind speed, a larger portion of the outside population will be affected, more people will be thrown against solid objects because the strong wind will be able to lift up more people. The wind will also generate more missiles that could hit people. Furthermore, the lethality for each person also increases because the impact speed of the body or the missile will be higher. (Glasstone and Dolan, 1977) estimates that 50 % lethality is reached when a body contacts a solid object with a speed of 16.5 m/s and 100 % lethality is reached at 42 m/s. It seems plausible that a body could be accelerated to speeds of 16.5 - 42 m/s in a EF1 tornado. However, it can be assumed that some of the outside population finds sufficient shelter. Hence, it was assumed that 10 % of the outside population is affected and that 5 % of those affected die. Housing still provides good protection against EF1 level winds but it was assumed that 1 % of the inside population can be affected and that 5 % of those affected die Vulnerability for winds corresponding to a EF1 tornado is thus set to 0.0015.

The assumed increase in vulnerability agrees well to the increase of lethality of recorded tornados between 2000 and 2004 (NOAA, 2015). During that time period 4284 EF0 tornados killed 2 people resulting in a casualty rate of 0.00047 per EF0 tornado. In the same time 1633 EF1 tornados killed 20 people yielding a casualty rate of 0.012 per EF1 tornado which is a 26 fold increase. Similarly, assumed vulnerability for strong winds increased by a factor of 33 from EF0 to EF1 level winds.

EF2 Increasing wind speed renders shelters less effective as houses start to exhibit significant damage. It is assumed that in addition to 40 % of the outside population, 5 % of the housed population is affected yielding a total of 12.7 % affected. Lethality for affected population increases to 10 % as wind speeds are capable of accelerating bodies beyond the 42 m/s body impact speed assumed for 100 % lethality (Glasstone and Dolan, 1977) and objects turned missiles have higher damage potential. Consequently, vulnerability is equal to 0.013.

The increase in vulnerability from EF1 to EF2-like wind speeds of a factor of 8.5 matches the casualty rate increase from EF1 to EF2 tornados. Between 2000 and 2004, 439 EF2 tornados killed 51 persons yielding a casualty rate of 0.12 per EF2 tornado corresponding to a 9.6 fold increase.

EF3 Tornados of this category destroy most housing shelter leaving basements and well constructed concrete buildings as viable shelter options. It was assumed that 80 % of the outside and 30 % of the inside population would be affected by winds of this strength. For those outside and inside, lethality increased to 30 % and 20 %, respectively due to missiles or by being thrown against fixed structures. The vulnerability thus increases 8 fold to 0.410. The record shows that 116 persons were killed by 127 EF3 tornados yielding a casualty rate of 0.913 that corresponds to an 8 fold increase from EF2 to EF3 tornados.

In fact, (Paul and Stimers, 2014) show that the vulnerability inside a zone affected by an average of EF3 tornado winds (Levitan et al., 2014), was 2.1 %. In contrast to a tornado, the wind blast in the case of an unforeseen asteroid impact would arrive without prior warning by the government or by meteorological cues that the population could be expected to correctly interpret. It is shown in (Paul and Stimers, 2014) and (French et al., 1983) that the presence of a warning decreases mortality by a factor of about three. In addition, housing standards in the USA ensure that protection of the population against wind blast is better than the global average by an assumed 50 % (factor 1.5). Taking into account the influence of warning and better protection, the observed vulnerability of 2.5 % can be expected to increase to a global average of over 9 % matching well with the wind blast vulnerability found here.

EF4 Persons who are sheltered in very well constructed concrete buildings will be protected against these winds. It was assumed that 40 % of the inside and 90 % of the outside population would be affected with corresponding lethality rates of 30 % and 40 %, respectively. Thus, vulnerability is 0.17.

EF5 The great majority of structures collapses in these winds offering diminishing protection. Consequently, it is assumed that 95 % of the outside and 50 % of the inside population is affected with a lethality rate of 50 % and 40 %, respectively. The resulting population vulnerability is 0.26 at 89 $^{m}/_{s}$ wind speed. Evidently, (Wurman et al., 2007) modelled EF5 tornados in an urban setting and assumed that 10 % of the inside population would be affected lethally. Taking into account the criticism that this is likely an overestimation for a setting in the USA (Ladue, 2016), 5 % lethality seems more likely. Considering the influence of warning (factor 3) and extrapolating to a global setting (factor 1.5), a value of 22.5 % was obtained which correlates closely to the value found previously.

Vulnerability Model The data from the previous section was used to compile three wind vulnerability models by fitting sigmoid functions to the values provided in Table 3.7. For the best and worst case scenario, it is assumed that the vulnerability from the

EF-category	Vulnerability	Worst [m/s]	Expected [m/s]	Best [m/s]
0	0.000044	23.5	33.5	43.5
1	0.0015	33.5	43.5	54.5
2	0.013	43.5	54.5	67
3	0.10	54.5	67	81.5
4	0.17	67	81.5	94.5
5	0.26	81.5	94.5	110

Table 3.7: Vulnerability values and wind speeds that realize these vulnerabilies in worst, expected and best case scenarios.

expected scenario is applicable to the higher and lower EF category, respectively. The three sigmoidal models are functions of wind speed in [m/s]. They describe the best, expected and worst case scenarios and their mathematical formulas are:

$$V_{\text{wind}}^{\text{best}} = \frac{1}{1+e^{-0.05036(v_{\text{wind}}-129.3)}} \tag{3.87}$$

$$V_{\text{wind}}^{\text{expected}} = \frac{1}{1+e^{-0.05483(v_{\text{wind}}-112.4)}} \tag{3.88}$$

$$V_{\text{wind}}^{\text{worst}} = \frac{1}{1+e^{-0.05549(v_{\text{wind}}-98.98)}} \tag{3.89}$$

Figure 3.25 visualizes the three models as they are implemented in ARMOR.

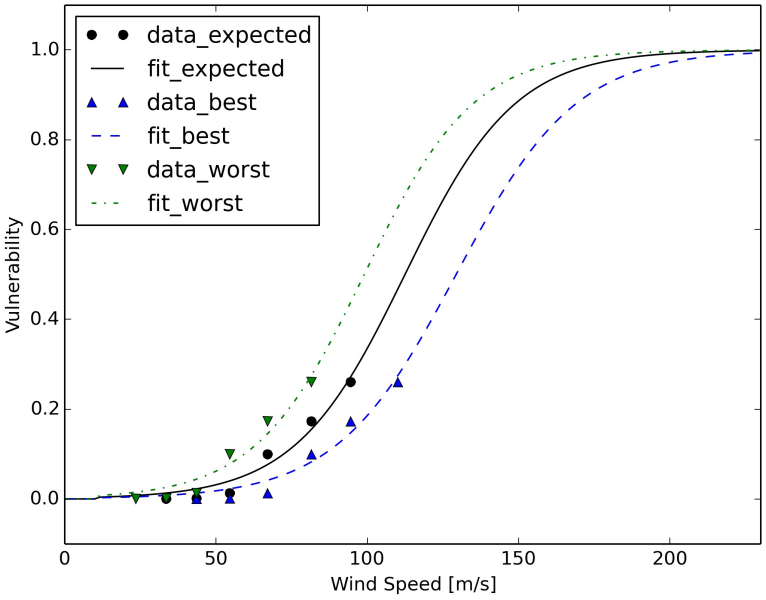

Figure 3.25: Wind vulnerability models for best, expected and worst cases.

3.3.6 Ejecta Blanket Deposition

The ground impact of an asteroid produces ejecta by throwing Earth crust material outwards. While persons may be hit directly by flying ejecta pieces, this work focuses on the longer term effect of ejecta deposition. Ejecta deposition is a hazard because it can lead to the collapse of buildings if the weight load of the settling ejecta blanket becomes big enough. Ejecta blanket thickness as a function of distance from the impact is described in section 3.2.3.

The vulnerability model used in this work follows closely the method described in (Norlund, 2013). A mean ejecta material density of $1600\,\mathrm{kg/m^3}$ is assumed. Equation 3.43 yields the ejecta blanket thickness in a map cell at a given distance. Given the ejecta density ρ_e, ejecta blanket thickness t_e and the standard gravitational acceleration g_0, the load of the ejecta blanket is:

$$p_e = t_e \rho_e g_0 \tag{3.90}$$

In (Pomonis et al., 1999), it is estimated that 20 % of the occupants in a house would be trapped in the event of a collapse and half of those would be fatalities. Keeping with previous assumptions that 22 % of the population would be outside at any given time, the remaining 78 % are located indoors. Taking these factors together, the maximum vulnerability of the population in the event of a roof collapse is $0.78 \times 0.2 \times 0.5 = 0.078$. However, to realize this vulnerability the roof of a building has to collapse in the first place. The likelihood of roof collapse can be modelled as a function of ejecta load as well as building strength and the corresponding models have been derived in (Pomonis et al., 1999). Best, expected and worst case outcomes are distinguished by building types. In the best case scenario, the affected population is situated in strong buildings while in the worst case scenario the affected population is inside weak buildings. Based on (Pomonis et al., 1999), (Norlund, 2013) provides:

$$V_e^{\text{best}} = 0.078 \times \left[1 + e^{-1.00(p_e - 5.84)}\right]^{-2.58} \tag{3.91}$$

$$V_e^{\text{expected}} = 0.078 \times \left[1 + e^{-1.37(p_e - 3.14)}\right]^{-4.6} \tag{3.92}$$

$$V_e^{\text{worst}} = 0.078 \times \left[1 + e^{-4.32(p_e - 1.61)}\right]^{-4.13} \tag{3.93}$$

Figure 3.26 visualizes the vulnerability as a function of ejecta blanket thickness and case severity.

3.3.7 Tsunami

A tsunami can inundate coastal regions and, thus, harm the population living there. How much of the coastline is inundated depends on the run-up height U and terrain slope s. A steeper terrain slope limits the extent to which water of a given run-up

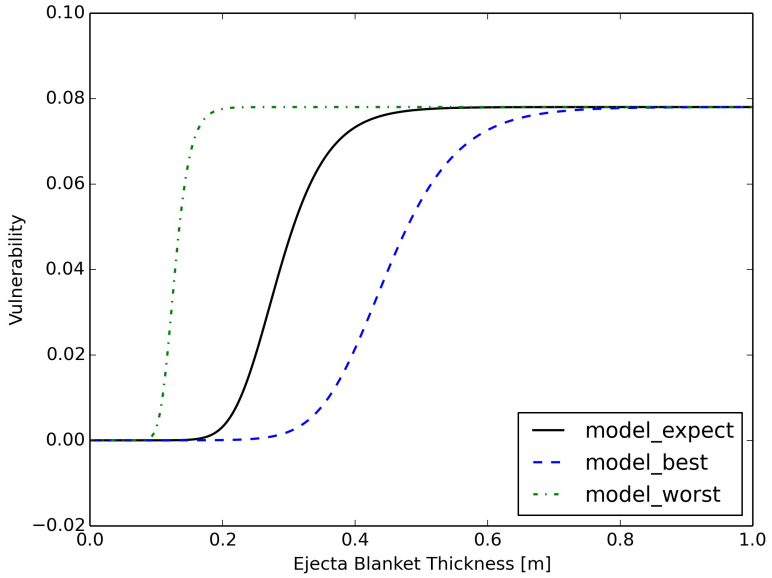

Figure 3.26: Vulnerability curve for building collapse due to ejecta blanket loading in the worst, expected and best case.

height can reach inland. Figure 3.27 visualizes this concept and in this figure, the red portion of one pixel (pixel length is p_{len}) is inundated by a wave with run-up U while the green portion is beyond the reach of the wave because of terrain elevation Δh over the length of one pixel.

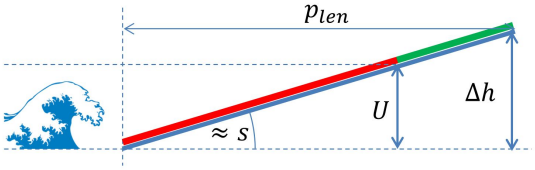

Figure 3.27: Tsunami run-in as it relates to runup and beach slope. Red terrain in one pixel is inundated and green terrain is safe. Note, that tsunami wave height and runup are not the same.

Assuming a sufficiently large wave, more than one map pixel can be inundated. In contrast to the linear model portrayed in Figure 3.27, multi-pixel inundation cannot be calculated linearly, because, depending on the local topography, the terrain slope changes from pixel to pixel. ARMOR's code accounts for this fact by recalculating slope between map pixels and comparing the topography height with the run-up height to determine wave run-in and local pixel inundation. Local inundation is equivalent with local run-up. Further, the code calculates the mean run-up height U_p for each map pixel, whether fully or partially inundated, for subsequent vulnerability estimation. In other words, if $U > \Delta h$, then the entire pixel is inundated and mean run-up in this pixel is $U_p = U - {}^{\Delta h_p}/_2$. In the next map pixel, run-up is reduced by Δh of the previous pixel

and the new local medium run-up is, thus, $U_p = U - \Delta h_{p-1} - {}^{\Delta h_p}/_2$. This formulation can further be expressed as:

$$U_p = U - \sum_{i=0}^{p-1} \Delta h_i - \frac{\Delta h_p}{2} \tag{3.94}$$

where i counts the pixels from the shore (pixel 1) to the local pixel p and $\Delta h_0 = 0$.

The above equation holds true for completely inundated pixels. The last pixel will generally only be partially inundated, as shown in Figure 3.27, and, thus, the local run-up is equal to the original run-up less the terrain height of the previous pixels. Finally, the mean local run-up of the last pixel is half of the run-up height at the last pixel:

$$U_p = \frac{U - \sum_{i=1}^{p-1} \Delta h_i}{2} \tag{3.95}$$

Furthermore, pixel vulnerability is scaled to pixel exposure - a pixel that is only 10% exposed cannot reach a larger vulnerability than 0.1.

Tsunami mortality as a function of runup is shown in Berryman (2005) and this model is based on literature research of tsunami records. The sole parameter in this mortality function is local runup and it should be noted that this represents a simplification as tsunami mortality is associated with more variables than only this one (Sinaga et al., 2011). For this work, a simple model is needed that can be applied globally, given the large scale simulations that are run by ARMOR, and the one dimensional model mentioned above shall be used for further analysis. A sigmoid function was fitted to the data provided in Berryman (2005). Subsequently, the covariance values for the fit have been used to establish the best and worst case functions using a variation of $\pm 1\sigma$. Figure 3.28 shows the vulnerability for expected, worst and best outcome. The equations that describe these curves are:

$$V_{\text{wave}}^{\text{best}} = \frac{1}{1 + e^{-0.45280749(U_c - 12.12768819)}} \tag{3.96}$$

$$V_{\text{wave}}^{\text{expected}} = \frac{1}{1 + e^{-0.37973734(U_c - 11.13677241)}} \tag{3.97}$$

$$V_{\text{wave}}^{\text{worst}} = \frac{1}{1 + e^{-0.30666719(U_c - 10.14585663)}} \tag{3.98}$$

3.3.7.1 Tsunami Algorithm Investigation

To gain an improved intuitive understanding of the tsunami algorithm, this section investigates example tsunami scenarios and statistical run-in results.

Runup and Run-in An array of impactors measuring 100, 150, 200, 300, 400 m are assumed to hit a deep water body with 17 ${}^{\text{km}}/_{\text{s}}$ (corresponding to the mean impact speed

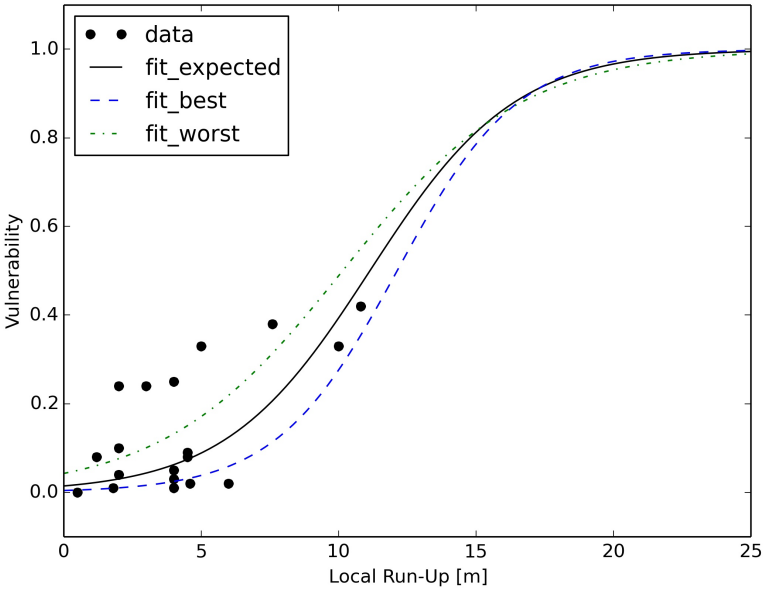

Figure 3.28: Population vulnerability as a function of local runup height based on data in Berryman (2005).

for NEOs) and an impact angle of 45 °. The scenarios generate transient craters in the sea and their diameters are listed in Table 3.8. Transient crater size correlates with

Asteroid Size [m]	100	150	200	300	400
Transient Crater [km]	2.83	3.88	4.86	6.67	8.35

Table 3.8: Transient crater diameters for impactors of various sizes (speed: 17 km/s; angle: 45 °)

tsunami wave amplitude (see Equation 3.66) and Figure 3.29 visualizes how the wave amplitude attenuates with distance from the impact site for these impact scenarios. The wave amplitude evolution is inversely proportional to distance (see Equation 3.66) and, as an example, the wave amplitude of a 150 m impactor is 16.3 m after 65 km.

When the wave approaches the shore, the slope of the coastal seabed compresses the wave water column and, thus, the wave height is modified and the final height is called runup height (see Equation 3.71). The linear models used in this work allow for wave height modification in the positive as well as negative direction: A steep slope can amplify wave height, while a shallow slope may also result in a smaller wave. Figure 3.30, visualizes how slope determines runup height. In this figure, the same impactor sizes and impact conditions as in Figure 3.29 have been used to calculate runup height for a coast that is 65 km from the impact site. Furthermore, for each asteroid size, the break-even point is marked on each curve, where the runup height is equal to the wave amplitude at coast arrival. For smaller slopes than the marker point, runup height is

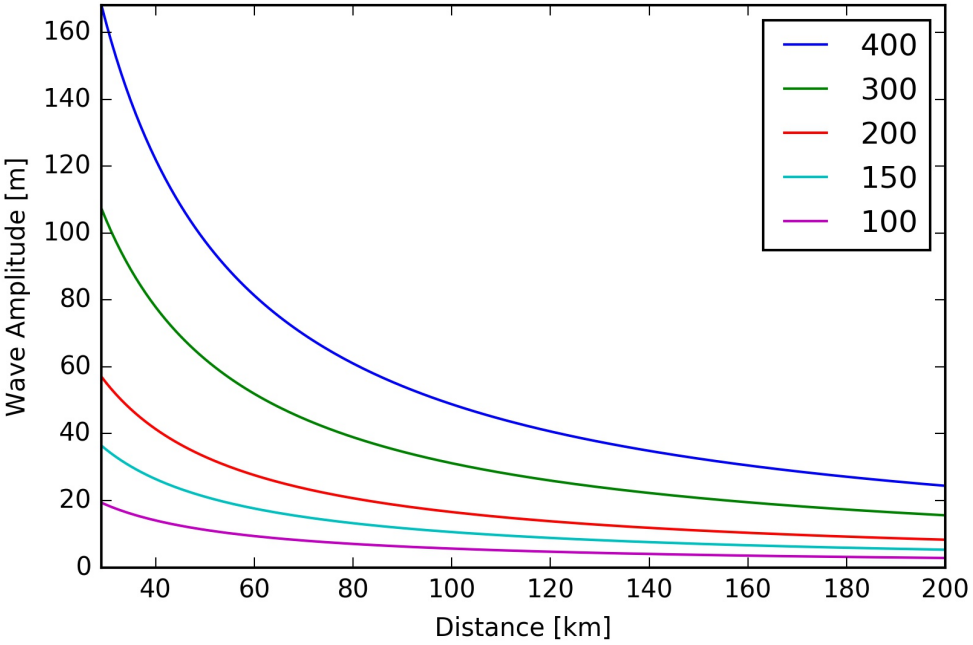

Figure 3.29: Wave amplitude over distance for deep water impacts of asteroid sizes between 100-400 m (speed: 17 km/s; angle: 45 °).

smaller than the arriving wave amplitude, while to the right of the marker, the wave height is amplified due to a steeper slope.

The conclusion here is that the employed models could predict a significantly reduced runup height compared to wave amplitude if the slope is small (such as in continental shelf regions with a slope ratio of about 0.002). However, results in Korycansky and Lynett (2007) shows in Figure 7 that Irribaren scaling breaks down for very small Irribaren numbers which depend on slope ratio. Specifically, the reference shows that runup is constant for Irribaren numbers smaller than $\xi = 0.11$. In accordance with Korycansky and Lynett (2007), it was therefore assumed in this work, that a constant Irribaren number of 0.11 was applied to Equation 3.69 when the calculated Irribaren number (Equation 3.68) was smaller than this value, for example in shallow shelf regions.

Using these insights about runup calculation and the mechanics that determine how far a wave can reach inland (run-in) allowed a statistical analysis showing what run-in distances may be reached. It was assumed that the beach slope that scales runup height (see equation 3.71) extends land-inwards and determines terrain slope[6] (in the real algorithm, slope is determined pixel by pixel).

These considerations help to obtain a physical understanding of how tsunami wave height relates to runup height as well as terrain slope to run-in distance. In Figure 3.31 run-in

[6]Note that, strictly speaking, slope s, is not an angle but, rather, a ratio between Δh and p_{len}. However, for small angles, the ratio is approximately equal to the angle in radians.

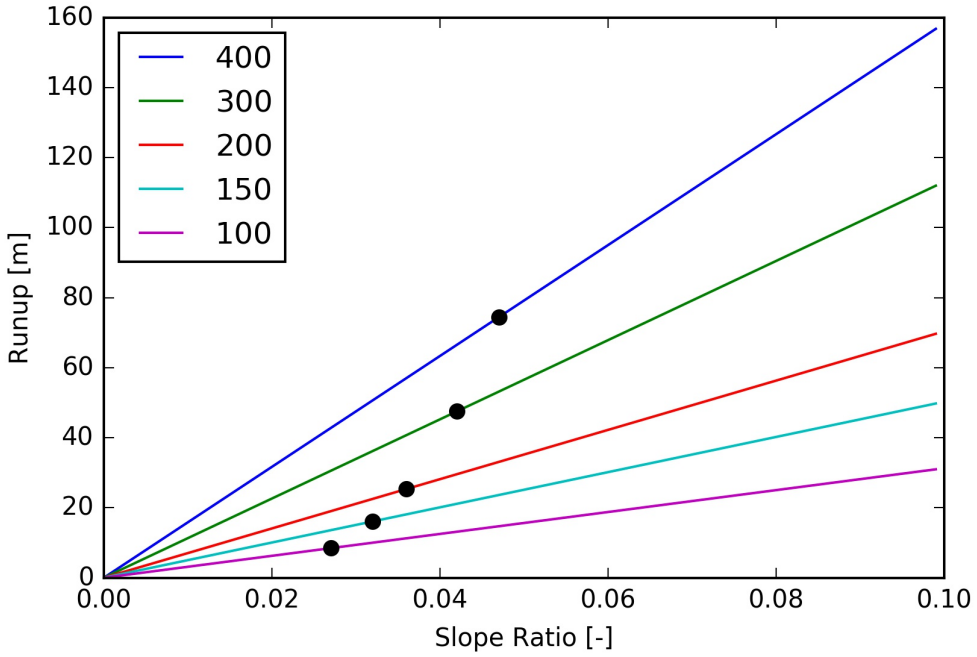

Figure 3.30: Runup height over a slope ratio range of $[0; 0.1]$ for 100-400 m sized impactors 65 km offshore (speed: 17 km/s; angle: 45 °).

distance in pixels is presented on a log10 scale and the thicker zero-line visualizes the one pixel inundation boundary. It is noticeable that even large waves (hundreds of metres runup) require very shallow slopes to reach further land inwards than one pixel (left side of thick red line).

In fact, 99% of impactors produced a run-in distance of less than 8 pixels in a simulation of 12261 impactors, each with a diameter of 400 m and impact locations within 500 km to the closest shore. The results of this simulation are shown in Figure 3.32. In the ARMOR algorithm, the maximum run-in distance was set to 50 pixels. This is a sufficiently large cut-off value as impactors with diameters of 400 m are at the upper limit of ARMOR's intended application regime and smaller impactors are expected to produce smaller run-in distances.

Protective Function of Continental Shelf The tsunami model in Equation 3.66 shows that initial wave amplitude is scaled by the sea depth at the impact site. If the impactor hits shallow waters, the initial wave height is proportionately scaled to that depth. The continental shelf is a region that extends for about 65 km offshore along much of the global shoreline. It features shallow waters, reaching only about 100-200 m depth at its farthest point from the coast and shallow slopes of about 0.1 ° (≈ 0.002 in terms of slope ratio) (Editors of Encyclopædia Britannica, 2016). While the deep water impact of a 150 m body results in a wave height of 16.3 m at a distance of 65 km, the same impact in a water body with 150 m depth yields a wave height of only 4.5 m at the

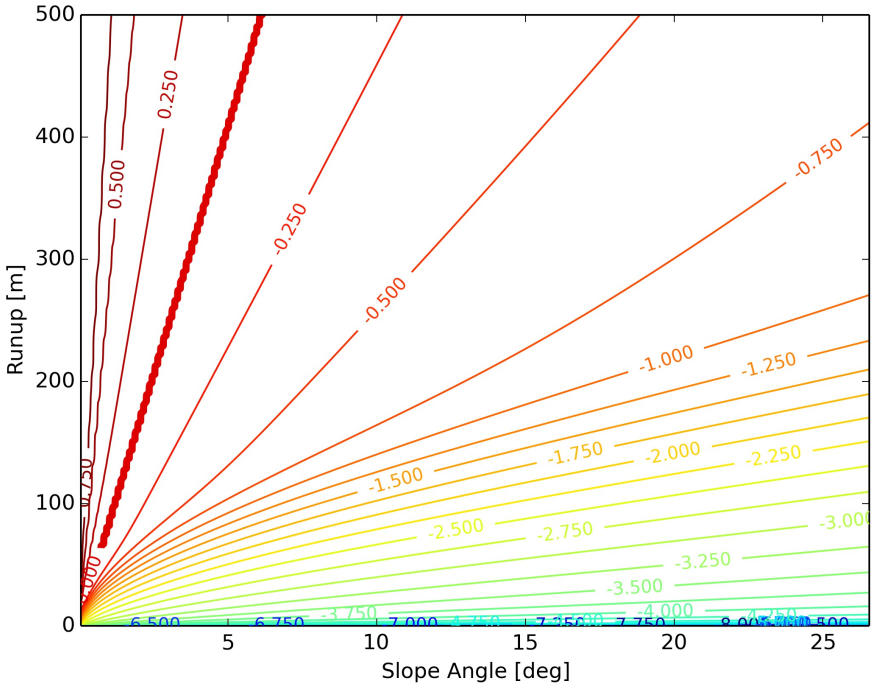

Figure 3.31: Tsunami run-in in map cells as a function of runup height and slope. Run-in distance is presented on a base ten logarithmic scale. The one pixel inundation line is thicker. Slope degrees correspond to a slope ratio range of $[0; 0.5]$.

same distance. Consequently, the continental shelf serves a protective function because it limits the initial tsunami wave height of near-coastal impacts. In fact, when assuming a constant shelf slope of s, it can be demonstrated mathematically, that the same small wave height will reach the shore no matter how far offshore the impactor hits the shelf.

It is assumed that continental shelf slope s is constant which provides sea depth h_{sea} as a function of impact distance from the shore D as

$$h_{\text{sea}} = sD \tag{3.99}$$

Substituting this relationship into Equation 3.66, yields that wave height at the shore is independent of impact distance D and that the wave heights are small because of small shelf slope values:

$$A = s\left(\frac{D_{tc}}{2}\right) \tag{3.100}$$

This observation leads to the conclusion that the continental shelf will serve a protective function against tsunamis for near-coastal asteroid impacts.

Tsunami Modelling Range An important simulation parameter is the maximum tsunami range that the algorithm uses. The maximum tsunami range is the distance

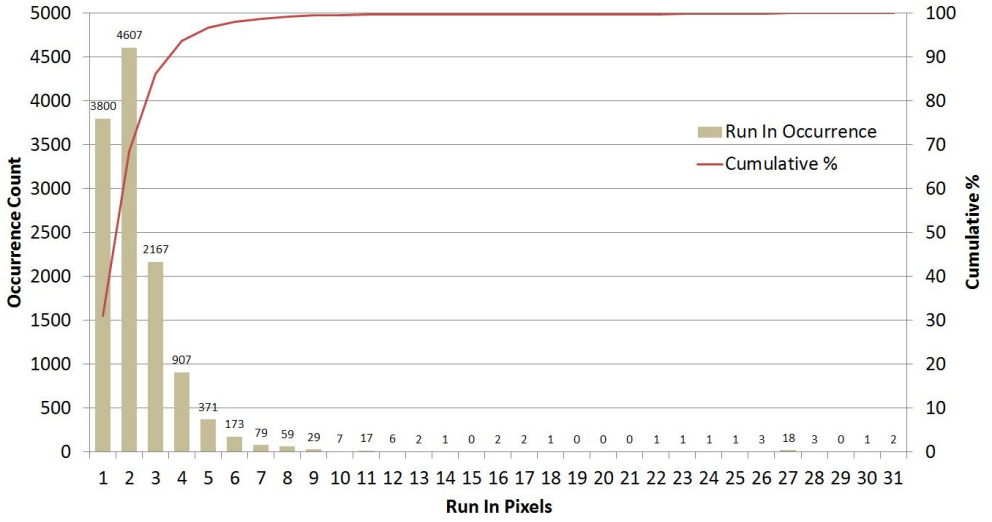

Figure 3.32: Histogram of run-in results from a simulation of 12261 impactors, each with a diameter of 400 m and impact locations within 500 km to the next shore. The results show how many pixels are at least partially inundated and the cumulative occurrence percentage is provided.

in pixels for which the wave is propagated over the global map. A larger tsunami range allows the algorithm to consider coastlines that are farther away from the impact point for tsunami loss calculation. However, it was expected that a maximum tsunami range exists where the wave height, attenuated by distance, diminishes in size such that its contribution to overall tsunami loss is insignificant. Amongst all effect models, tsunami modelling is the most computationally expensive and, thus, finding the maximum tsunami range that yields accurate results for the least computational effort was a practical consideration as well.

A simulation was set up in which 35984 artificial water impactors[7] were simulated and the maximum tsunami range was varied. Four simulation campaigns where performed where all impactors had either 100 m, 200 m, 300 m or 400 m diameters. Figure 3.33 shows the results of this analysis as the percentage of final tsunami loss over maximum tsunami modelling range.

The results of Figure 3.33 show that a maximum tsunami range distance of 2000 pixels (corresponding to $\approx$ 9200 km) achieved good completeness in terms of producing total casualty numbers (>97% of final tsunami loss value) while ensuring acceptable simulation speed.

[7] Corresponding to all water impactors in the impactor sample described in section 4.4.1 and visualized in Figure 4.17.

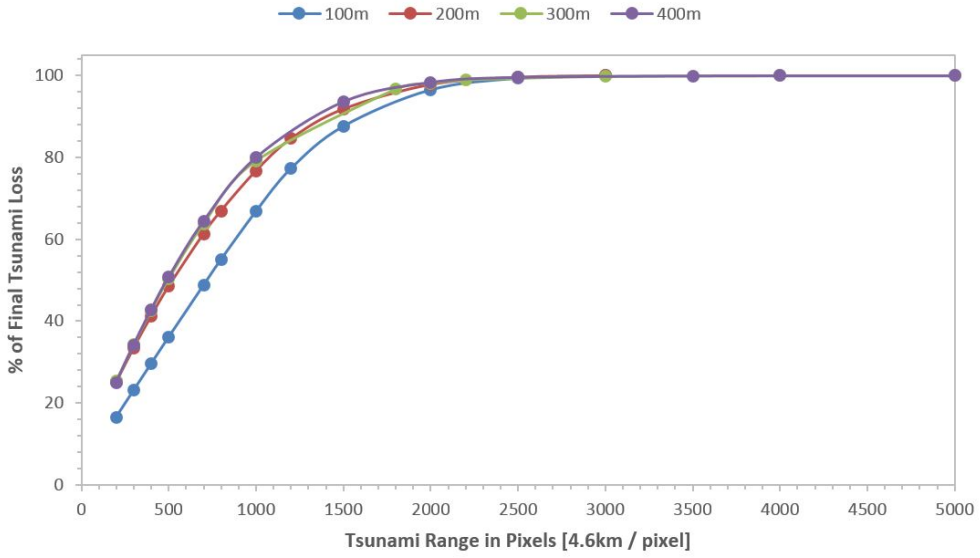

Figure 3.33: Percentage of final tsunami loss over maximum tsunami range modelling distance.

Chapter 4

Results

ARMOR was utilized to gain insights into the asteroid impact threat situation.

In section 4.1, the average impact distribution of NEOs on the global map is explored. To this end, ARMOR was utilized to calculate the impact corridors of 261 potential impactors based on observed asteroids. Additionally, a 10006 strong synthetic impactor population was utilized to confirm the findings made with ARMOR and it was found that the impact distribution of NEOs is near uniform. These findings have also been published in the journal *Icarus* (Rumpf et al., 2016b).

Next, it was of interest to understand the influence of higher fidelity modelling on risk estimation and section 4.2 addresses this topic. As the global impact distribution is near uniform, the global, long-term risk distribution closely resembles the population distribution, because, under the assumption of equal impact probability and population vulnerability, the exposure distribution dominates the results. However, when the impact risk of a specific asteroid is of interest, higher fidelity models need to be employed for accurate risk estimation. The results of this investigation have been published in the journal *Acta Astronautica* (Rumpf et al., 2016a).

Following the investigation of modelling fidelity, an example risk calculation was performed for the asteroid 2015 RN35 and the results are presented in section 4.3.

To better understand the contributions of individual impact effects to risk, simulations were performed that recorded the contribution of each effect to loss of population. To accomplish this analysis, the synthetic impactor sample of section 4.1 was enlarged to 50000 impactors. The sample enlargement was only possible by establishing statistical impactor distributions for impact location as well as impact speed and angle, and these distributions were, subsequently used to derive the global 50000 strong sample. The derivation of the impactor statistics and the results on impact effect significance are presented in section 4.4. Furthermore, these results have been published in the journal *Geophysical Research Letters* (Rumpf et al., 2017a).

4.1 Global NEO Impact Distribution

Previous research based on historical impact records has addressed the topic of the impactor distribution on the surface of the Earth, but none performed a quantitative assessment of the distribution. Three datasets that relate to the impact distribution problem and that are based on natural asteroids are known to the authors. They are based on historical impact records. The Russian "Institute of Computational Mathematics and Mathematical Geophysics" maintains the "Expert Database on Earth Impact Structures" (EDEIS) containing over 1000 impact crater features (EDEIS et al., 2006) and the results are available as a map that shows the locations of these impact features (confirmed and possible) in Figure 2.4. However, the geological traces of impacts on Earth suffer from erosion and many might have disappeared or are not easily detected. In addition, water impacts rarely leave long-lived traces. Consequently, the data is biased towards land impacts and also depends on the localized interest of the population or scientists to identify impact features, both of which introduce additional bias into the database. Therefore, EDEIS data are not suitable for a global impact distribution analysis nor has such a quantitative assessment been undertaken. A similar dataset with the same limitations is maintained by the Planetary and Space Science Centre of the University of New Brunswick in Canada (University of New Brunswick, 2014). The third dataset is comprised of airburst recordings obtained by a global infrasound microphone network. The network's original objective was to monitor atmospheric nuclear weapons tests, but as the signature of an airbursting asteroid shares enough similarities with that of a nuclear test, the network is able to detect these natural events and triangulate the airburst location. NASA has published these data in the form of a map that is based on recordings in the 1994-2013 timeframe (NASA, 2014b). These data are limited to the size regime of asteroids that experience an airburst when colliding with the Earth, but coverage is global and no bias was expected in the detection method. However, no quantitative assessment of the impact distribution based on these data has been performed by the publishing authors; the reason might be that the data are too sparse to support such assessment.

An alternative to using observed asteroids as the basis for impact distribution analysis is to use a representative, artificial population of virtual impactors and such a synthetic population was generated by (Chesley and Spahr, 2004; Grav et al., 2011). Their work focuses on the impactor distribution in a celestial, geocentric coordinate system that uses spherical coordinates with the ecliptic as reference and the Earth-Sun opposition point as origin. Notably, the work finds that most impactors approach roughly from the orbit or anti-orbit direction of the Earth with a minor concentration approaching from the opposition direction. Furthermore, it was shown that the majority of impactors are concentrated in the ecliptic plane. In contrast to the research presented here, the celestial frame does not rotate with the Earth and, thus, the locations on the Earth that the impactors would impact are not apparent, nor was this the aim of the study. In

(Grav et al., 2011) an impact location map of North America was shown that is based on the synthetic population, but without quantitative assessment of the impact location distribution.

In the research presented here, the future, potential impact distributions of observed asteroids were calculated and analyzed. The key motivating question was whether the impact distribution is uniform or if some regions are more likely to be hit than others. In (Chesley and Spahr, 2004), it was shown that impactors are expected to approach the Earth from directions that are roughly parallel to the Earth's orbit and that the majority of potential impactors reside in the ecliptic plane. In conjunction with the observation that the Earth performs a daily rotation under this constant influx, it can be asserted that all longitudinal sections of Earth are equally exposed to impacts and that the impact distribution in the longitudinal direction is uniform. However, an intuitive understanding of the latitudinal distribution of impact locations is not as easily obtained. Considering that most impactors are expected to originate from close to the ecliptic plane their impact velocity vectors should also be approximately parallel to the ecliptic plane. Further, assuming that the impactor influx density in the ecliptic normal direction is constant over the width of the Earth, the highest impact location density would be expected near the equator because the Earth surface bends away from the impactor influx towards the poles. This concept is depicted in Figure 4.1. Of course, impactors do not impact the Earth on a straight line: rather, the gravitational attraction of Earth bends the impactor's trajectory towards Earth. Consequently, impactors that would miss the Earth in the absence of Earth's gravitational field actually impact because their trajectory is changed under the influence of Earth's gravity. This means that the uneven distribution on the Earth expected without gravity is attenuated somewhat towards a more even distribution because gravitationally captured impactors from outside the physical diameter of the Earth impact closer to the poles (than the equator) resulting in a more balanced near-polar impact density Figure 4.1.

These geometric considerations have previously been investigated in the literature with varying conclusions. While Le Feuvre and Wieczorek (2006) and Halliday (1964), and Gallant et al. (2009) reported a strong bias in impact density towards the ecliptic equator of about 30 % more than at the ecliptic poles, this setup does not account for Earth's spin obliquity. The direction of Earth's spin axis remains stable in space as the Earth moves around the Sun over the duration of one year with the consequence that impacts which originate predominantly from the ecliptic equator will be biased towards to Earth's northern hemisphere during winter and spring and towards the southern hemisphere during summer and autumn (Halliday and Griffin, 1982; Rendtel and Knoefel, 1989). However, Gallant et al. (2009) subsequently includes the annual variation in latitudinal meteor influx and found a near uniform impact distribution in their simulation setup (1 % difference between Earth's poles and equator). The three studies have in common that they found a strong dependency of impact distribution to impactor speed where faster

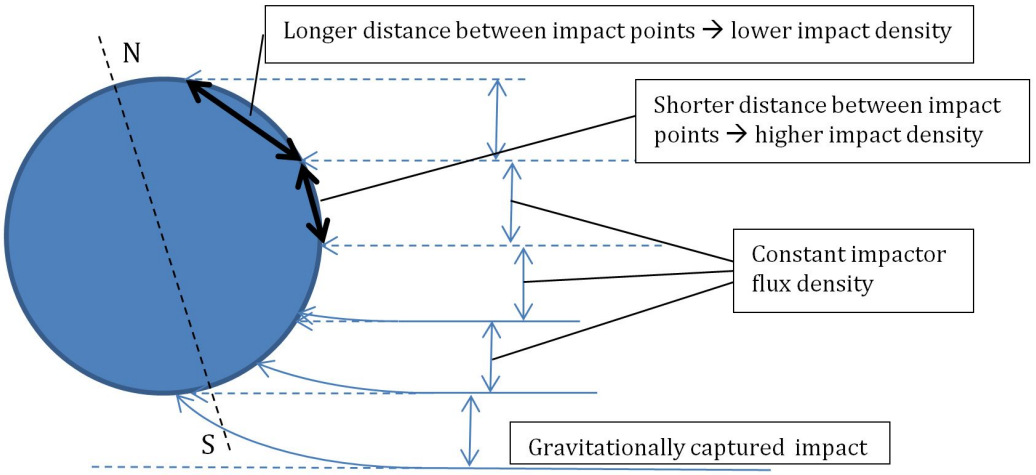

Figure 4.1: Depiction of intuitive impactor density distribution in latitudinal direction neglecting the attracting effect of the gravity of Earth (dashed impactor lines) and under gravitational attraction ("Gravitationally captured impact", solid lines).

impactors produced larger impact densities towards the equator because gravitational focusing of the Earth bends the trajectories less at high speeds. Less gravitational focusing results in fewer impactors near the poles.

To assess if the impact location distribution is uniform based on a real asteroid population set, the impact locations of 261 potential impactors (belonging to 69 observed asteroids), which can collide with the Earth before the year 2100, were calculated in a dynamic solar system simulation and visualized. The considered asteroids had a diameter range of an estimated 30 m to 341 m. For comparison, the Chelyabinsk event was associated with a 19 m sized asteroid (Popova et al., 2013; Borovicka et al., 2013) while the devastating 1908 Tunguska event was likely caused by a 30-50 m sized object (Boslough and Crawford, 2008; Chyba et al., 1993).

4.1.1 Impact Distribution Results

The method to calculate impact corridors (see section 3.1) was applied to all 261 potential VIs (see Appendix A) and the result is a set of impact corridors, each in the form of a Gaussian distribution, that reflects the impact probabilities of the assessed VIs. All impact solutions were combined within a global map and the result is shown in Figure 4.2.

It is noticeable that the impact probability distributions in Figure 4.2 cover the entire Earth and that an asteroid impact can potentially happen anywhere. The literature indicates that the impact distribution of asteroids is uniform (NASA, 2014b) based on historical impact records. However, results in Figure 4.2 clearly show that some areas experience higher impact probability than others. To consolidate both remarks, one

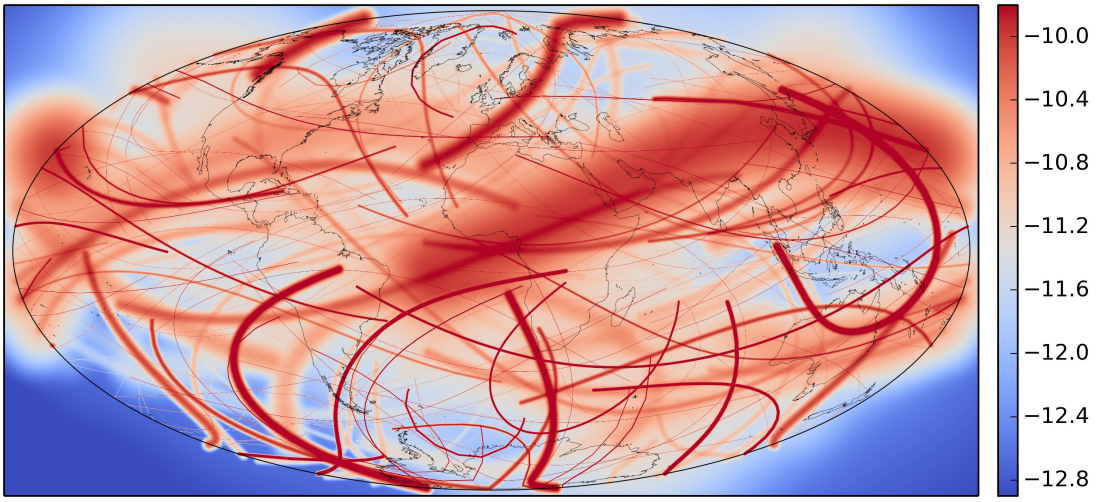

Figure 4.2: The Earth in the Hammer projection showing the impact probability distributions for 261 VIs. The colour coding represents the impact probability at each location using a logarithmic scale (shown right).

needs to recognize the difference between impact probability distribution and impact corridor distribution.

The impact corridor distribution shows where it is physically possible for the asteroids to impact, while the probability distribution also provides information about where an impact is more likely based on observational data. To visualize the impact corridor distribution, each virtual impactor was assigned an impact probability of one as well as a corridor width of 0.01 Earth radii and this representation of the impact corridor distribution is shown in Figure 4.3. Through this representation, it becomes apparent that impact corridors are more evenly distributed than suggested in the impact probability distribution shown in Figure 4.2. A quantitative assessment of the impact distribution is presented in the following.

Three probability density distributions are shown in Figure 4.4 as a function of longitude (top plot) and latitude (bottom plot). Uniform impact probability, as suggested by the literature, is represented by the blue line. Impact probability distribution, sampled in Figure 4.2 is represented by the red line. The green line shows the impact corridor distribution from Figure 4.3. Data sampling was accomplished using a fixed latitude (longitude) step width of 0.0357 ° to satisfy the Nyquist-Shannon limit. The maps used in this paper have a constant pixel area corresponding to 21.16 km^2 and the data may, thus, be compared between different regions and across maps as each pixel represents the probability density at the sampled coordinate. Finally, all three distributions have been normalized such that the integral of each distribution is one. This allowed them to be placed on the same scale for easier comparison.

Although the normalization of the plots in Figure 4.4 lessens some of the information carried by the numbers, it facilitates easy comparison between the distributions by

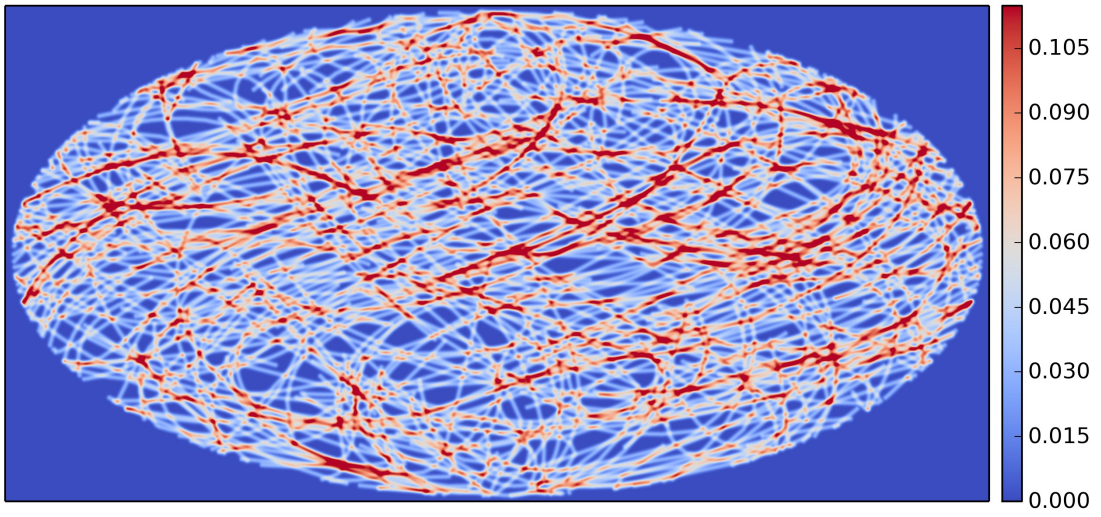

Figure 4.3: Representation of all impact corridors showing their uniform global distribution. The impact probability of each VI was set to one and the corridor width was set to 0.01 Earth radii to facilitate equal visualisation of all impact corridors.

evaluating differences between them. The predicted distribution of impact corridors (green line) agrees closely with the assumption of uniform impact probability (blue line) with a root mean square difference (RMS) of 7.627×10^{-6} for longitude and 3.452×10^{-5} for latitude. On the other hand, the impact probability distribution differs more considerably from uniformity and the RMS increases by an order of magnitude to 2.834×10^{-5} for longitude and 1.427×10^{-4} for latitude.

To enable a comparison between the two independent datasets, the synthetic population of 10,006 virtual impactors, mentioned in section 4.1 (Chesley and Spahr, 2004), was analysed for its impact distribution. To generate the discrete impact distribution based on the synthetic population, the VI impact points were plotted on the world map. In accordance with the method used on ARMOR's set, this map was subsequently sampled for the spatial impact density distribution and the result has been normalized and plotted on the same scale as ARMOR data in Figure 4.4. Figure 4.5 shows three distributions in two plots for longitudinal (top) and latitudinal (bottom) direction. In these plots, data shown in grey represents the discrete impact distribution and the dashed, blue line is the uniform distribution (same as in Figure 4.4). A moving average filter with a 2° window width was used to smooth the discrete impact distribution and the result is represented by the red line. The RMS difference between discrete impacts (grey) and the uniform distribution (blue) is 7.229×10^{-5} in the longitudinal direction and 2.096×10^{-4} in the latitudinal direction. This result may be compared to the corridor distribution of the ARMOR sample and one notices that the ARMOR sample has an order of magnitude smaller RMS difference. The key difference between the synthetic VI set and the ARMOR VI set is that the former consists of 10006 discrete impact locations while ARMOR treats each of its 261 VIs as a probability distribution, effectively

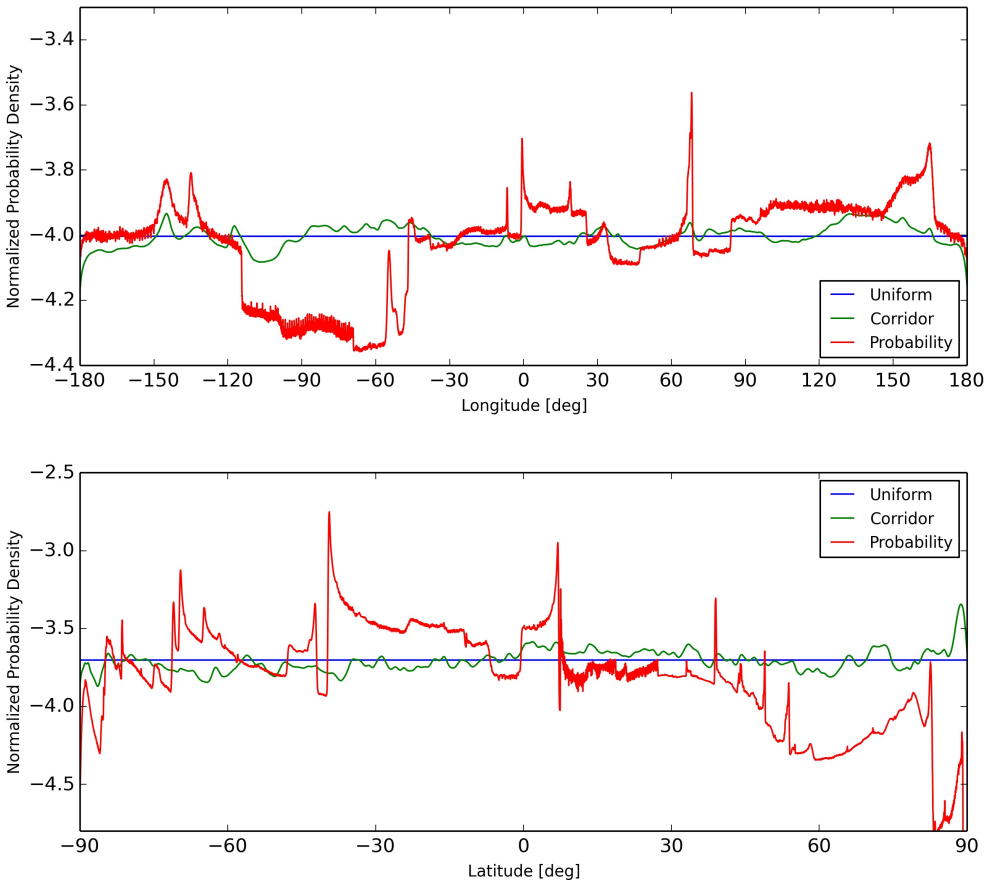

Figure 4.4: Normalized probability density distribution over (upper plot) longitude and (lower plot) latitude. The blue line shows the expected result for a uniform distribution. The green line shows the calculated distribution of impact corridors assuming equal impact probability for all corridors. The red line indicates the distribution of corridors accounting for their predicted impact probabilities. Data are shown on a base 10 logarithmic scale.

providing thousands of sample points per VI, and ARMOR's corridor distribution, thus, appears smoother (grey in Figure 4.5 vs green in Figure 4.4). In contrast to the discrete impact distribution in the longitudinal direction, which appears homogeneous over the entire longitudinal range, the distribution in latitude shows a recognizably different pattern near the poles (-90 °/+90 °) and it seems as if the impactor density increases towards the poles. However, analyses using the moving average filter reveals that the impact distribution remains, in fact, constant and that the peculiar appearance of the distinct impact distribution near the poles is due to increased variability in the data. The reasons for this increase in variability are that the area that corresponds to each latitude section ring decreases towards the poles and fewer VIs impact in these areas. Both aspects yield some empty section rings on the one hand, and some to accrue higher densities as a product of sparse impactors on small polar latitude band areas on the other hand. Effectively this situation allows for small sample artefacts to occur near the poles and this is reflected in the bottom plot of Figure 4.5 where data becomes sparse and

seemingly shows increasing density. However, the seemingly increasing impactor density is balanced by some empty latitude bands yielding zero impactor density. The zero impactor density latitude bands are not visible in Figure 4.5 due to the logarithmic plotting function. Application of a moving average filter remedies the situation and shows that impactor density remains approximately constant near the poles.

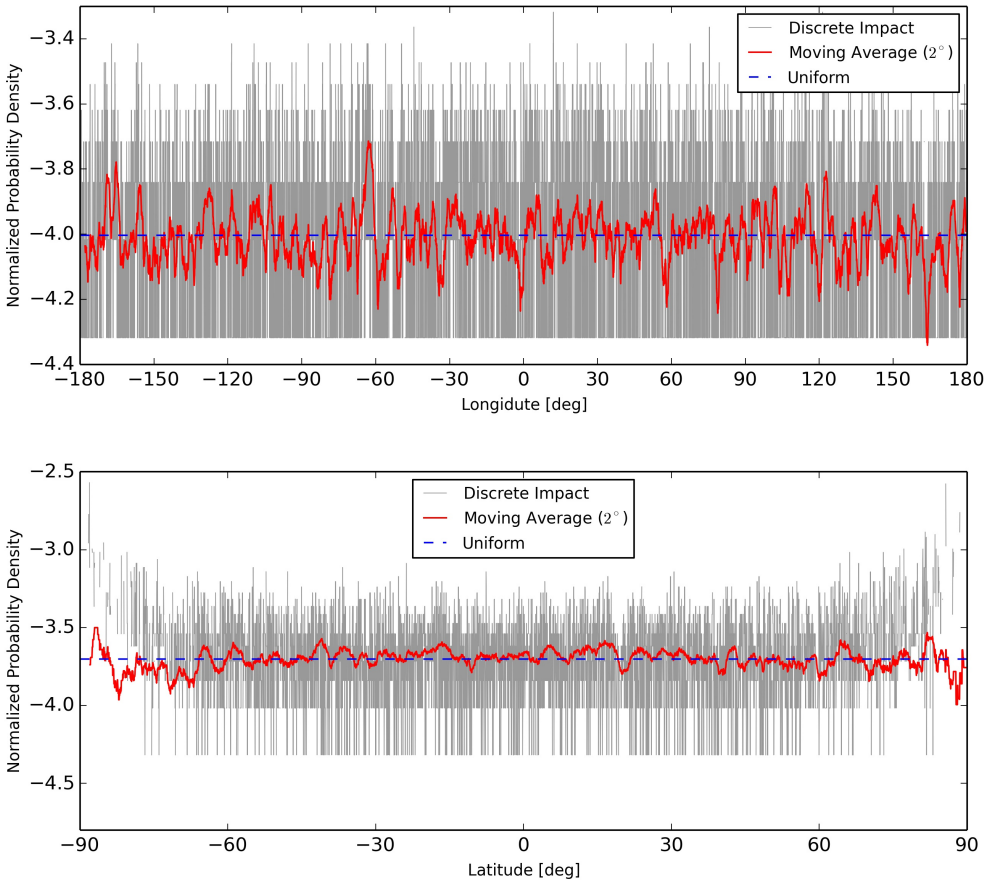

Figure 4.5: Impact distribution based on a synthetic virtual impactor set comprising 10006 impact points. Grey represents the discrete impact distribution, red is the result of a moving average filter with 2 ° window width that was used on the discrete impact data and blue is the uniform impact distribution. Data is shown on a base 10 logarithmic scale.

4.1.2 Impact Distribution Discussion

The two results that are based on the ARMOR sample and on the synthetic VI sample agree with each other and both results reinforce the assumption that the natural impact distribution is uniform. Furthermore, the results show that the sample size used for the analysis in ARMOR (Figure 4.4) is sufficiently large for the analyzed VIs to approach the natural, uniform impact distribution (blue and green line). This was expected intuitively for the distribution in the longitudinal direction. However, the results could not as easily be predicted for the impact density distribution in the latitudinal direction. The finding

appears to confirm that the mechanics that lower the impact distribution density towards the poles (due to impactors originating from close to the ecliptic plane; Figure 4.1) are cancelled by the gravitational attraction of impactors by Earth.

Natural impact distribution is determined by the occurrence of asteroids in the Solar System and their trajectories. However, the VIs that produce the impact corridors are not only analyzed for their potential impact locations but also for their currently predicted impact probability. The predicted impact probability depends on the measurement technique that entails number, timing and quality of observations that are available for the parent asteroid as well as the orbit determination procedure. Thus, in addition to the natural population of NEOs and their trajectories, the results in Figure 4.2 depend on technology and scientific techniques that are disconnected from the natural processes that produce the impact distribution. The measurement and orbit determination process introduces a large amount of variability in the results because the predicted impact probabilities vary by orders of magnitude and this is why the impact probability distribution in Figure 4.2 (and red line in Figure 4.4) does not reflect a uniform distribution (blue line in Figure 4.4). The fact that the probability distribution is not uniform indicates limitations in the data.

It is estimated that only about 1% of all NEOs in the relevant size regime have been discovered (Harris and D'Abramo, 2015). The impact probability distribution in Figure 4.2 reflects the current best knowledge of 69 analyzed asteroids which represent about 15 % of all known asteroids with a non-zero impact probability (519 at the time of this writing). Consequently, Figure 4.2 represents only a subset of the asteroids that may potentially impact the Earth in the future. It is possible that a larger sample size will approach uniform impact probability distribution. However, the variability in the probability distribution covers about five orders of magnitude (maximum impact probability: 7.4×10^{-4}; minimum impact probability: 9.69×10^{-9}). It is not clear if a large enough sample will ever be available to smooth out the variability in impact probabilities. This is because new observations may not only add potentially impacting asteroids to the sample when new objects are discovered but also remove them by confirming that a potential impact is, in fact, impossible. Thus, the sample size does not necessarily grow over time with the availability of new observations. Furthermore, the discovery of a new high impact probability asteroid would increase the variability in the distribution (e.g. Asteroid 99942 "Apophis" has had a 2.7% impact probability in the past (Giorgini et al., 2008)) and skew the impact probability distribution towards its impact corridor. The impact probability distribution is time dependent and may never reach a uniform distribution. The result in Figure 4.2 is, thus, a snapshot of the current situation based on our knowledge, and it will change over time. The result is representative of the type of information, with respect to impact probability distribution, that will be available in the future and has relevance as such: it represents humankind's present best guess at where an impact might occur.

4.1.3 Impact Distribution Conclusions

This section presented the impact corridor and probability distributions of 261 VIs belonging to 69 asteroids that currently have a chance of colliding with the Earth. Furthermore, it analysed the distributions for their conformity with the uniform impact distribution assumption. The distributions were calculated and visualized using the ARMOR software tool that can project impact probabilities of known asteroids onto the surface of the Earth. Results show that the natural impact corridor distribution supports the assumption of uniform impact distribution and, crucially, extends the evidence basis for this assumption from past impact records into the future. This finding is confirmed by parallel analysis of impact points belonging to a synthetic population of 10,006 VIs and by previous simulation work by Gallant et al. (2009). In contrast the deviation of the impact probability distribution from uniformity increased by an order of magnitude relative to the corridor distribution because of the large variation in VI-specific impact probabilities. The concept of impact probability is a product of the asteroid observation and orbit determination technique that is more dependent on technology rather than natural processes. Therefore, it introduces man-made variability of several orders of magnitude into the distribution. It is important to recognize this difference to set expectations about the characteristics of impact probability distributions that may be produced in the future. It can be concluded that every region on Earth has a similar, a priori likelihood of an asteroid impact but that humankind's knowledge about the current asteroid impact situation is limited. Nevertheless, it is worth considering probabilistic data for practical purposes because, in the event of a recognized asteroid threat, a response decision will, in part, be based on imperfect knowledge such as that shown.

4.2 Influence of Higher Modelling Fidelity on Risk Assessment

The NEO webpages (Universita Di Pisa and ESA, 2014; NASA, 2014a) provide information about the orbit, physical properties and impact probability of the listed objects. However, a risk assessment, involving the asteroid's possible impact locations, is not part of the available information. Only in rare cases, such as for asteroid Apophis (Schweickart, 2007), are impact locations (in the shape of an impact corridor) calculated. Impact locations can help to develop an intuitive understanding of the specific impact risk as it shows the areas that would be affected, but, to gain a reliable understanding for risk, impact effects and their implications for population have to be calculated at the impact locations. The calculation of impact effects has been treated in the literature, and two software tools exist that are capable of estimating impact consequences (Bailey et al., 2010; Collins et al., 2005). Although these tools calculate impact effects, they do not routinely close the loop between orbital characteristics that determine impact conditions, probability and location, and, thus, only offer limited utility in understanding impact risk. A comprehensive risk assessment, taking into account the physical impact effects that are governed by the asteroid's speed, impact angle and physical properties on one hand and the distribution of the human population along the impact corridor on the other hand, is, thus far, not available. Nevertheless, such a risk assessment is needed to help determine the political and technological response when an asteroid with a significant impact probability is discovered (Ailor and Tremayne-Smith, 2013). Could existing tools be used to perform such impact risk assessment?

Given that the practice of impact location calculation is already available to some entities within the planetary defense community (Chesley et al., 2015; Adamo, 2012) it is of interest to know how well this knowledge of impact locations enables impact risk estimation. The validity of an impact risk estimate that is based on impact location knowledge alone can be gauged through comparison with a similar risk estimate that takes impact effect modelling into account. Following this logic, two risk distributions are needed: A "simplified" one that considers impact location without impact effects and an "advanced" one that accounts for impact location as well as impact effects. To generate a global distribution of asteroid impacts, a sufficiently large set of orbital and physical data of, ideally, real asteroids should be used. Using real asteroid data not only allows calculation of impact locations but also facilitates determination of representative impact conditions such as impact energy and angle. Some variable that is exposed to the asteroid impact hazard needs to be identified to complete the risk estimation process, and the global, human population map represents a suitable dataset that is also publicly available (CIESIN et al., 2005). To meet the objectives mentioned above, the ARMOR tool was employed.

4.2.1 Modelling Fidelity Method and Results

In the simplified impact risk analysis, which did not account for physical impact effects, vulnerability V was set equal to one because the simulation did not calculate the severity and extent of impact effects. Instead, it was assumed that the impact cell's population is equal to the number of casualties (in other words, if an impact occurs in a cell then everyone in it dies). Risk, in this case was the product of impact cell population and the probability of impact in that cell. In contrast, the advanced results account for physical impact effects and, consequently, vulnerability (expected case as described in section 3.3) is modelled as a function of severity. Furthermore, the attenuation of impact effects with distance is modelled which allows account of the population in affected cells beyond the impact cell and varying vulnerability as impact effects weaken while they propagate into more distant cells.

Finally, the national risk of all countries is estimated by summing the risk distribution within each country's borders. The national risk values are divided by the global risk to produce the percentage of global risk that each country faces and this is called the relative risk of a nation. Equation 4.1 is the formula for relative risk in each map cell as a function of total risk in each map cell caused by a specific VI ($R_{i,c}$). Subscript c denotes one cell in the world map, and subscript i identifies the VI.

$$\text{relative risk}_c = \sum_{i}^{261} \frac{R_{i,c}}{\sum_c R_{i,c}} \tag{4.1}$$

In this way, both the simplified as well as the advanced risk distribution were normalized with respect to global risk producing relative risk estimates. The estimation of relative risk provides a basis for comparison between the simplified and advanced results. Furthermore, given that the simplified risk estimate can, by definition, account for land impacts only, only direct land impacts (and near coastal impacts in the case of the advanced result) are considered in the analysis to retain comparability between the two risk distributions. This means that asteroid impact-generated tsunamis are not part of the analysis. Relative risk, in contrast to absolute risk, does not retain information about the number of expected casualties through the process of normalization. Consequently, a statement about the magnitude of the expected risk is impossible with this approach. However, relative risk illustrates the risk level of one country in comparison with another and allows statements about which country is more at risk based on the given impact probability distribution.

The following results are based on the 261 impact probability distribution shown in Figure 4.2. Based on the combined probability corridors in this map, the impact probability in each map cell was determined for subsequent risk calculation. By means of combining Figure 4.2 with the world population, the global risk distribution without

consideration for physical impact effects was produced and this is the simplified risk distribution (Figure 4.6) (Rumpf et al., 2015).

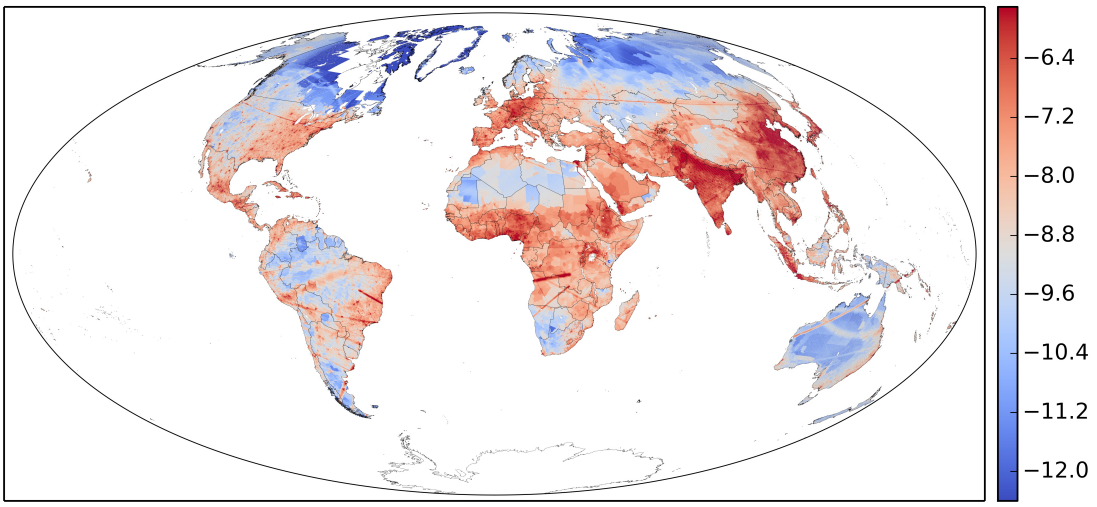

Figure 4.6: Simplified asteroid risk map. This is the product of impact probability and world population but does not account for physical impact effects. The colour in each region indicates the risk level. Risk is normalized with respect to global risk and is colour coded using a log10 scale.

To assess the significance of physical impact effects on the risk distribution, the global asteroid risk distribution was recalculated considering impact effects and the advanced risk distribution is shown in Figure 4.7. Noticeable differences between Figure 4.6 and Figure 4.7 are that some individual asteroid corridors disappear while others become more pronounced because they correspond to higher energy impacts (larger asteroids) that raise the risk in the areas that are crossed by these corridors. Furthermore, the risk landscape extends beyond continental territory and beyond the shores of islands because physical effects of near coastal impacts propagate onto closeby land (aerodynamic shockwaves and thermal radiation).

Finally, the national risk list based on risk results with and without physical impact effects was produced for quantitative analysis of changes in global risk distribution. Figure 4.8 shows the risk list and also includes the relative global population share that each nation accommodates. The data were sorted by population size of the 40 most populous nations in descending order.

4.2.2 Modelling Fidelity Discussion

The first, general observation, based on the risk list (Figure 4.8), is that population size is a close proxy for national direct asteroid impact risk. The risk data share large correlation coefficients with population data of 0.953 and 0.907 in the cases without and with impact effects, respectively. The inclusion of physical impact effects did not have

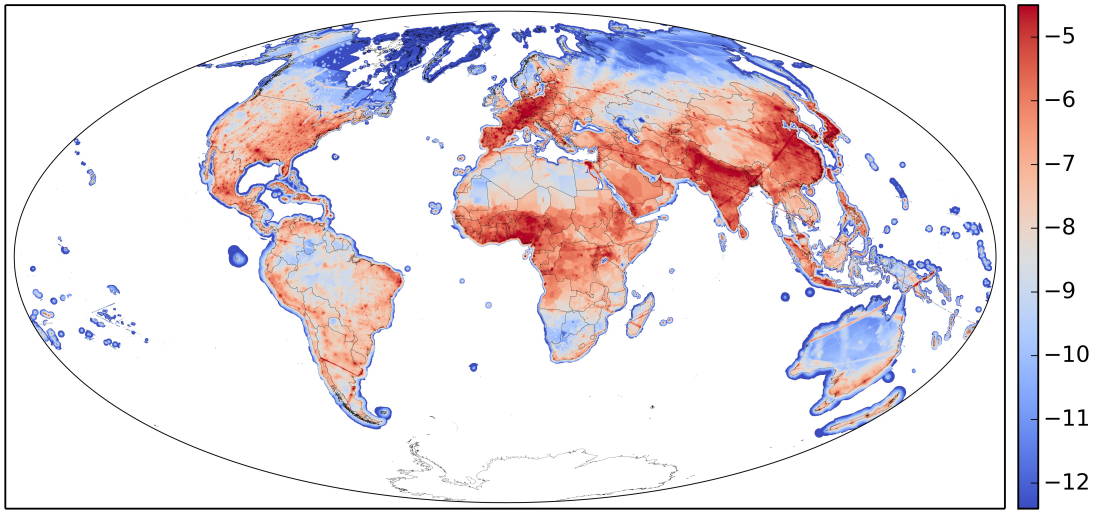

Figure 4.7: Advanced asteroid risk map. This combines impact probability, exposed population and the vulnerability of that population based on a physical impact effect calculation. The colour in each region indicates the risk level. Risk is normalized with respect to global risk and is colour coded using a logarithmic scale.

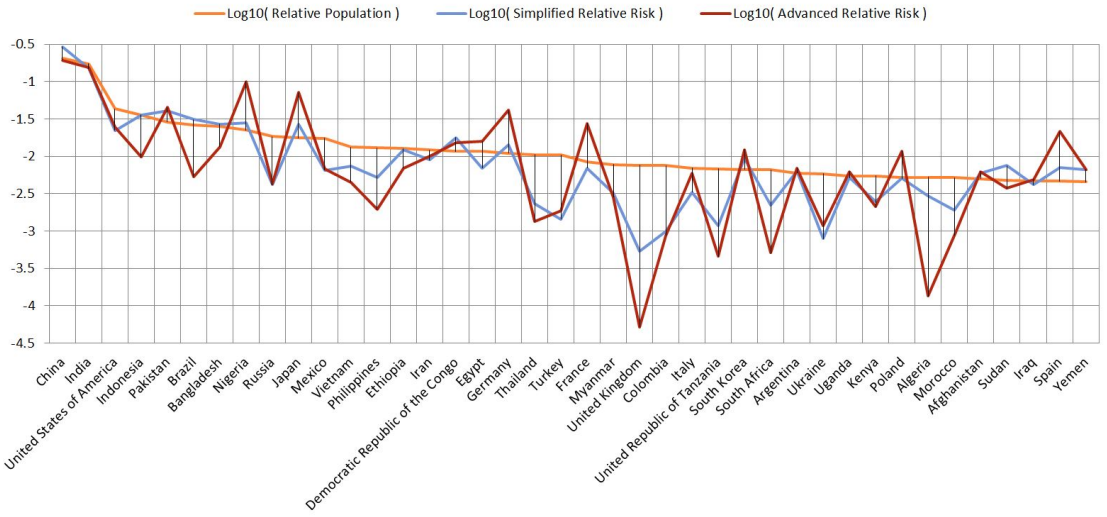

Figure 4.8: National risk list for the 40 most populous countries. Risk estimates are provided both with and without taking account of physical impact effects. Both sets of estimates focus on direct land impacts (and near coastal impacts in the case of the new results). The risk estimates (unit-less) are presented on a logarithmic scale and reflect relative values that express the global share of risk. On the same axis, the global population share per nation is plotted on a logarithmic scale.

a major impact on this rule of thumb. This assessment is further supported by visual inspection of the global risk distribution maps of Figure 4.6 and Figure 4.7. While the appearance of individual impact corridors varies, the occurrence of broader, high risk areas remains constant, such as central Africa, India, China's coastal region and central

Europe.

The close correlation of population size with direct impact risk distribution stems from the generally recognised assumption that over timescales measured in hundreds of years, the impact distribution of asteroids on Earth is approximately uniform (Rumpf et al., 2016b). However, two aspects result in a non-uniform risk distribution in the simplified case: First, the asteroid sample size is limited and results in a non-uniform impact distribution. Second, and more importantly, impact probabilities differ between the impact instances of the asteroids and, thus, their impact corridors carry varying weights in the risk calculation resulting in additional departure from uniformity (Rumpf et al., 2016b). If all asteroids had the same impact probability and if the sample size were infinite, the impacts in this analysis would also be uniformly distributed. Furthermore, if impact effects are disregarded, as has been done in the simplified results, the risk distribution would mirror the population distribution perfectly in the long-term (i.e., under the assumption of a uniform impact distribution). Consequently, the variation between population and risk estimates in the simplified analysis is a function of individual impact probabilities of the VIs and, to a lesser extent, limited sample size. These two factors account for the deviation in distribution that results in a correlation coefficient of 0.953 (instead of 1.0) between population and simplified risk. Importantly, the disregard for physical impact effects ignores the fact that the analysed asteroids differ in size and impact speed. Instead, the consequences of all impacts were treated equally by assuming that only the population in the impact map cell is counted as casualties.

With the inclusion of physical impact effects the above assumption of equal impact consequences (effectively disregarding physical properties of each asteroid such as size and speed) is corrected. On one hand, a national risk increase in the advanced analysis reflects that this nation happens to be affected by a high energy impact, while, on the other hand, a decrease means that this nation is affected only by low energy impacts with fewer consequences. Through the inclusion of physical impact effects, additional complexity is added to the analysis because the analysed asteroids differ in size as well as in impact speed and risk varies accordingly. Consequently, the advanced risk estimates reflect this additional complexity through a larger difference between population density and the advanced risk result. Noticeably, the correlation coefficient decreases from 0.953 to 0.907. This finding is confirmed in the risk list of Figure 4.8 where risk numbers that account for impact effects deviate more from population than those disregarding physical impact effects.

The increase in variation due to the inclusion of impact effects is moderate as expressed by the decreasing correlation coefficient (only 4.8% with respect to previous results) and might be weaker than expected. This outcome can be partially ascribed to the lack of tsunami modelling as it is expected that nations with a disproportionately long coastline relative to their country size would accumulate higher risk values if tsunamis were included (Bailey et al., 2010).

Figure 4.8 is ordered by population size. In reference (Rumpf et al., 2015), a similar list is sorted by decreasing risk presenting the 40 countries that experience highest risk based on results that do not account for impact effects. The inclusion of impact effects caused a substantial reshuffling in the risk ranking. Brazil, for instance, dropped by 32 positions from 5 to 37 (in a list of 206 countries). On the other hand, Russia climbed by 9 positions from 37 to 28. The median change in position in the 40 most populated countries was 9.5 ranks. These findings show that, to predict the specific risk faced by a country, models need to account for impact effects because predictions that are based solely on impact probability and population produce only moderately accurate risk estimates. While the assertion that population size serves as a proxy for asteroid risk remains true when considering the near-equally distributed background risk of asteroid impacts, analysis that includes physical impact effects as well as the spatial distribution of impact locations is needed to estimate risk levels for individual countries.

The asteroid lists maintained by ESA and NASA change over time with the discovery of new probability asteroids and the exclusion of asteroids that are certain to miss the Earth based on new observations. New observations will also adjust the impact probability of asteroids already present in the lists. Only about 1% of all Near Earth Asteroids have been observed (Harris and D'Abramo, 2015) and the majority, especially in the sub-km size regime, have yet to be discovered. Consequently, the results presented here represent only a snapshot in time of the known asteroid hazard and the risk landscape will change over time. However, the conclusions drawn based on the current analysis are independent of the characteristics of individual asteroids and the conclusions are, thus, expected to hold true in the future.

The results show that population size is an indicator for impact risk and, thus, existing tools that can calculate impact locations may be used to obtain an intuitive understanding of risk distribution. However, to assess the risk of individual countries or the risk posed by individual asteroids, asteroid impact effect modelling is a necessity.

4.2.3 Modelling Fidelity Conclusions

This section addresses the significance of impact effect modelling when estimating the global asteroid risk distribution. The impactor sample used was made up of the impact corridors and probability distributions of 261 VIs belonging to 69 asteroids that currently have a chance of colliding with the Earth before 2100. The distributions were calculated and visualized using the ARMOR software tool that can project impact probabilities of known asteroids onto the surface of the Earth and estimate impact effects as well as risk.

The predicted risk landscape changed moderately with the inclusion of physical impact effects. Furthermore, the observation from previous results that population size is a

suitable proxy for national risk remains valid after the introduction of impact effects. The relationship between population size and relative risk reduced by 4.8% when physical impact effects were introduced, and the population-risk correlation coefficient reduced from 0.953 to 0.907. The reason for the decrease in correlation is that physical impact effects add complexity to the analysis yielding greater variation in the risk estimates. As a rule of thumb, population size helps to estimate national risk, but high impact probability asteroids or large asteroids can significantly alter this expectation. Therefore, when considering the abstract background threat of asteroids, population size serves as a suitable proxy to identify those countries that would suffer most casualties. Additionally, it might be possible to obtain a qualitative understanding of risk distribution along the possible impact locations of an asteroid using existing tools that can calculate impact locations. However, when facing a concrete threat, population size is insufficient to identify which country is most at risk and more detailed analysis including physical impact effect modelling is needed.

4.3 Asteroid 2015 RN35 Risk Calculation

At the University of Southampton, the Asteroid Risk Mitigation Optimization and Research (ARMOR) tool has been developed (Rumpf et al., 2016a,b, 2017b). With ARMOR, the possible impact locations of a threatening asteroid can be computed in the shape of the spatial impact probability distribution projected onto the Earth. The spatial impact probability distribution is equivalent to the locus of the possible impact points forming the impact corridor of an asteroid with the addition of providing local impact probabilities within the corridor. ARMOR simulates an impact of the asteroid in each map grid cell using the local impact speed and impact angle (as these values change along the corridor) and calculates the consequences in terms of loss of human life for each impact point (Rumpf et al., 2017b). Following the formalism of of risk such that risk is the product of impact probability and consequences, the impact risk can be calculated in each grid cell within the impact corridor. This method was applied to asteroid 2015 RN35 which was discovered in September 2015 and had a potential impact instance on Wednesday, October 20th 2077 with an impact probability of 3.06×10^{-6} at the time of analysis (early 2016). The cross-corridor spatial impact probability 1-sigma value was 89.2 km determining the width of the impact corridor. Since the impact probability was small, the local impact probability was assumed to be constant along the direction of the corridor. While the maximum impact probability was observed along the corridor's center line, the local impact probability decreases in cross corridor direction according to a normal distribution with $1 - \sigma$ value given above. The integral of the probability distribution is equal to the global impact probability (Rumpf et al., 2016b) and the corridor is truncated to its sides where the local impact probability is smaller than 3.0×10^{-12} resulting in the risk corridor representation in Figure 4.9. The diameter size estimates for asteroid 2015 RN35 range from 79 m to 177 m and the mean value of 128 m was selected for impact risk analysis. Potential impact locations include Indonesia and Papua New Guinea in the East as well as Mexico, the United States of America, Portugal, Spain and Algeria towards the West.

The colour coding of the risk corridor allows to identify regions of higher and lower risk based on local impact probability (higher closer to the corridor's center line), local population densities and impact conditions that vary along the corridor.

Integrating over the risk corridor allows global impact risk estimation and, given the low impact probability and using the expected case for vulnerability models from section 3.3, global risk for this impact instance was 0.041 expected casualties. Using the best or worst case human vulnerability models, the casualty estimates varied by -24.2% in the best case and +47.5% in the worst case scenario.

The global impact probability may be adjusted to represent a certain collision of the asteroid and the Earth by assigning a value of 1.0 to it (equivalent to an integral value of one over the impact probability distribution). While this hypothetical scenario describes

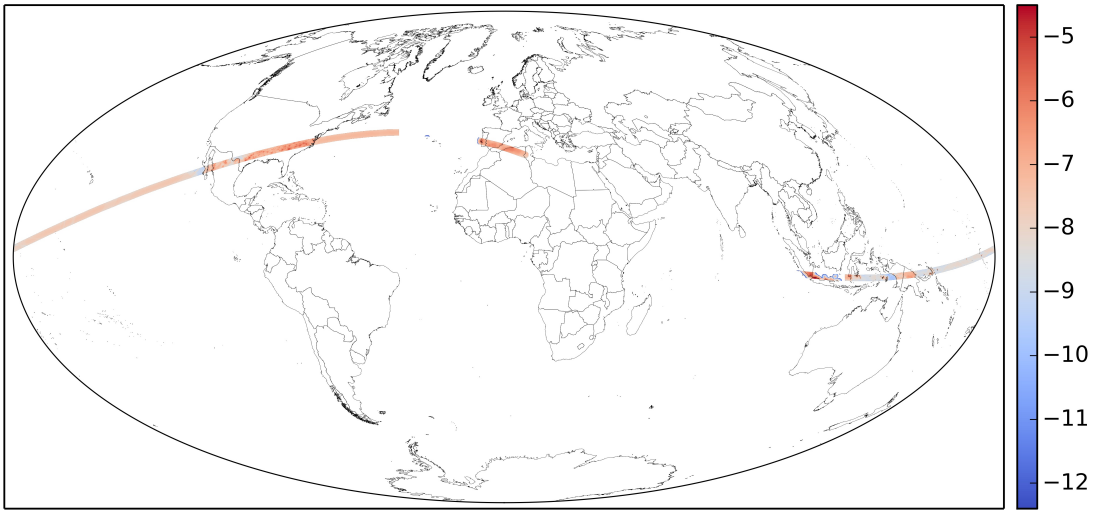

Figure 4.9: Risk corridor of the potential 2077/10/20 impact of asteroid 2015 RN35. The local risk is colour coded as powers of ten (logarithmic scale).

a certain collision between the Earth and the asteroid, the specific impact location within the risk corridor remains uncertain and continues to be expressed as a spatial impact probability distribution in the simplified shape of the impact corridor (Rumpf et al., 2016b). In this scenario, the expected casualty count increased to 13513 and this aggregate value may be understood as the average threat level across the corridor considering the best available information (taking into account local population, geography, impact speed, impact angle, asteroid size and mass, and impact probability). The average is formed by means of spreading the impact probability across the impact corridor, thus, the consequences of each impact point are weighted by the local impact probability and only contribute little to overall risk. Consequently, actual impact consequences may vary significantly upwards or downwards from the aggregate depending on the impact location.

A magnified view of the corridor portion that stretches over Indonesia is shown in Figure 4.10 to provide a detailed view of the corridor and to enable further discussion of the result.

4.3.1 2015 RN35 Risk Calculation Discussion

It is immediately noticeable in Figure 4.9 and Figure 4.10 that the risk corridor appears to be broken up into pieces over the Atlantic and close to Indonesia. The reason for this behaviour is the varying impact angle along the corridor that modifies the impact situation from an airburst to a surface impact. Towards the ends of the impact corridor, the impact angle decreases until it eventually reaches zero (the asteroid approaches the surface tangentially). In these shallow trajectories, the asteroid does not descend fast enough to impact the surface and, instead, experiences an airburst (Collins et al., 2016).

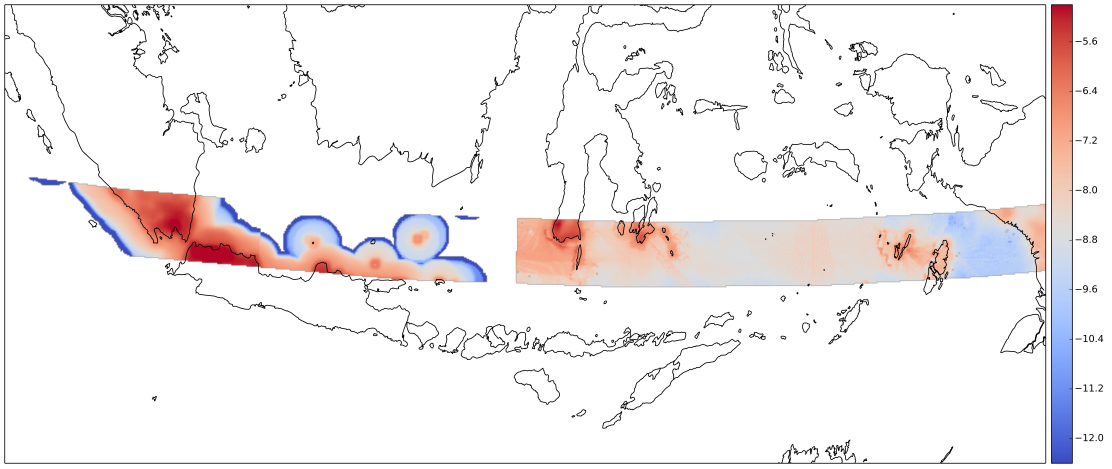

Figure 4.10: Magnified view of 2015 RN35 impact risk corridor over Indonesia. Colour coding represents local risk values as powers of ten.

The impact effects of airbursts (wind, pressure, thermal radiation) have a shorter reach than tsunamis generated by water impacts (Rumpf et al., 2017b). Consequently, no casualties might occur for airbursts over water and risk is zero in those impact location. Hence, some areas in the risk corridor do not show any risk because the airbursts that occur here are outside the reach of any inhabited zone. On the other hand, the resulting aerothermal effects may reach land and local populations as they propagate away from the airburst location for near coastal impact sites. This is clearly visible in Figure 4.10 where high risk areas are centered on small islands and follow the coastline of eastern Indonesia. From there, the impact angle increases in a easterly direction in Figure 4.10 and, once the impact trajectory is sufficiently steep, surface impacts start to occur that trigger tsunamis which hit the surrounding coastlines. The same effect is visible at the other end of the risk corridor over the Atlantic where surface impacts occur on the American side but stop abruptly as impact angles decrease in a westerly direction prompting airbursts. These airbursts are only able to cause damage as the impact locations shift onto Portugal, Spain and Algeria, while the eastern Atlantic appears to be risk free (except for a small risk patch near the Azores).

Further investigation of the water impacts on the eastern side of Figure 4.10 (Indonesia area) reveals that some ocean impacts lie in direct line of sight to populated areas which are visible to the ray-tracing algorithm for tsunami propagation. While any water impact produces tsunamis that travel outwards in every direction, these impact locations are positioned in a way that allows them to affect vulnerable, high exposure targets. These high risk impact locations typically lie in deep water which allows the generation of high amplitude waves that inundate shore areas such as the city of Pasarwajo (center of Figure 4.10) or in the Pulau Kai-Besar region (right side of Figure 4.10). In addition, the south coast of South Sulawesi and west coast of the Pulau Selayar island show high risk impact regions offshore in near-coastal areas due to their proximity to inhabited

regions and a narrow trench of deeper water that allows generation of high amplitude waves.

Tsunamis are efficient energy transporters which allows them to threaten coastlines that are thousands of kilometres away from the impact location and this capacity makes them a primary concern in the context of asteroid impacts. This behaviour is evident in Figure 4.9 where impacts that occurred far away from inhabited zones in the middle of the Pacific still resulted in significant risk levels as indicated by the orange colour coding of the risk distribution in that area.

The results demonstrate that the application of the risk concept to the asteroid threat provides valuable information about threatening asteroids. With the establishment of an impact corridor, the potential effects can be simulated and may be connected with the exposed population. In a first instance, the resulting risk corridor provides localised knowledge about the risk distribution which allows assessment of which impact zones would yield the greatest damage. Furthermore, integrating over the risk corridor allows global risk estimation and the unit of risk is loss (i.e. expected casualties). The global risk is an average value across the length of the risk corridor and facilitates early threat level assessment because the unit of expected casualties enables direct comparison to other natural disasters such as earthquakes or tornados. In this way, the method presented here can help establish asteroid disaster response procedures by assessing action triggering threat levels for other natural disasters and applying the same risk levels to asteroid scenarios. As an example, one simple response could be that an asteroid receives dedicated telescope time when its risk assumes one expected casualty. Higher risk levels might initiate the design of asteroid deflection missions or civil defence measures. As additional observations of the asteroid become available, impact probabilities may be revised and the extent of the risk corridor may be further constrained towards a more point-like impact location, reflecting the current knowledge about the asteroid. This development would improve risk estimates as the risk evaluation is no longer an average across the corridor but becomes specific to the constrained impact location. On the one hand, risk could be corrected upwards, if the impact location starts to focus on populated or oceanic areas, while, on the other hand, a desert impact would correct the expected casualty count downwards.

The best and worst case vulnerability models are mainly related to the percentage of the population that is inside or outside of sheltering buildings. If an impact event is known in advance but with little warning time, an effective, and immediate civil defence measure is to advise the population to remain inside shelters via a public broadcast, such as radio (Boslough et al., 2015). The best case casualty estimation indicates that the casualty count can be reduced by about 25% through a sheltering advice broadcast in the case of the example calculation used here. This observation opens up the possibility to implement specific vulnerability models to test the effectiveness of other civil defence measures, for example evacuation of the impact region.

The use of expected casualties to classify asteroid threat levels can facilitate communication of the asteroid impact threat with the general public. The unit of expected casualties is easier to understand and to interpret than numerical values without a unit as used in the Torino scale or Palermo scale. Furthermore, the asteroid impact threat is a low probability (low frequency) scenario which removes asteroids from the everyday concerns of the public. However, the past has shown that an asteroid impact can potentially have extreme consequences and it should, thus, be addressed. By consolidating impact probability and predicted consequences into a risk number, the concept of risk helps to make the asteroid threat fathomable to the general public despite the hard-to-grasp extremes of tiny probability and enormous hazard.

Finally, asteroid risk assessment has the potential to be integrated in ESA's and NASA's NEO webpages in parallel with the Torino and Palermo threat scales. The advantage of the risk assessment over the Torino and Palermo scales is that it calculates impact consequences directly instead of relying on kinetic energy as a proxy for impact consequences. The implementation of risk analysis as a threat scale could be further refined by weighting risk with time until impact where longer lead times are associated with a lower weighting factor. Furthermore, the current global risk situation on the NEO webpages could be represented visually by superimposing risk corridors from objects on the global maps in a similar way as shown in (Rumpf et al., 2016b).

These results have been published and were presented at the 2017 Planetary Defense Conference (Rumpf et al., 2017c).

4.4 Impact Effect Dominance

What are the consequences of an asteroid impact for the human population? This question is a significant driver for today's research activities that address the threat of asteroids that collide with the Earth (Ailor and Tremayne-Smith, 2013). Asteroid impacts produce an array of impact effects that can harm human populations. A list of seven such impact effects is recognized and described in Hills and Goda (1993); Collins et al. (2005). They are: wind blast, overpressure shock, thermal radiation, cratering, seismic shaking, ejecta deposition, and tsunami. The present work quantifies the contributions of each of these effects to overall losses due to an asteroid impact of a given size in a global setting.

Considerable work is available in the literature which addresses overall casualty numbers of asteroid impacts (Stokes et al., 2003; Harris, 2008; Shapiro et al., 2010; Boslough, 2013a; Reinhardt et al., 2016). Previous work has compared the loss of human life for impactors over land and water masses (Stokes et al., 2003; Shapiro et al., 2010) and these studies are currently being updated with an increased focus on individual impact effects (Mathias et al., 2017; Register et al., 2017). Additional work has focused on the loss quantification of single impact effects such as tsunamis (Chesley and Ward, 2006) facilitating limited insight into the quantification of relative impact effect dominance. The focus of the present work is comparing the contribution (dominance) of the seven impact effects to overall loss and thereby providing a nuanced view of impact effect dominance.

To estimate loss of human life due to an asteroid impact, the severity of each impact effect needs to be calculated based on input parameters such as impactor size, impactor density, impact speed and impact angle. A suite of analytical impact effect models is provided in Collins et al. (2005) and it enables estimation of impact effect severity as a function of distance from the impact site (except for tsunamis). The literature provides examples for numerical codes that typically model few effects each in great detail (Boslough and Crawford, 2008; Wünnemann et al., 2010; Gisler et al., 2011; Collins et al., 2012). However, the high impactor count simulations performed here prohibited the use of numerically intensive codes. A suitable tsunami propagation model is presented in Rumpf et al. (2017b) which utilizes ray tracing to determine affected coastlines on the global map depending on the impact location and calculates local coastal inundation based on bathymetry as well as topography data (Patterson and US National Park Service, 2015).

Here, the impact effects were propagated away from the impact location and across the local population utilizing global population data on a 2.5‘x2.5‘ grid from 2015 (CIESIN et al., 2005) to determine the number of affected people. The vulnerability of the affected population declines with increasing distance from the impact site as effect severity attenuates with distance. The vulnerability models used to determine local mortality,

and, thus, overall casualties, are described in Rumpf et al. (2017b). Instead of propagating impact effects directly, a radius of destruction for each impact effect was estimated in Stokes et al. (2003); Shapiro et al. (2010) based on work in Hills and Goda (1993). Because global averages were of interest, simplifications regarding the population distribution were used in Chesley and Ward (2006) and Stokes et al. (2003); Shapiro et al. (2010) by relying on statistical population numbers in coastal areas and by using the average land population density, respectively.

A large sample of artificial impactors was used in conjunction with the "Asteroid Risk Mitigation Optimization and Research" (ARMOR) tool (Rumpf et al., 2016b,a, 2017b) to estimate the dominance of each impact effect and to produce results about the total loss potential of impactors in a global impact scenario as well as in impact scenarios over land and water masses. The impact scenarios covered the possible variations of impact speed and impact angle.

4.4.1 Near-Earth Object Statistical Analysis for Sample Generation

To ensure that the analysis of impact effect dominance produces representative results, it was necessary to cover the Earth in a sufficiently high impactor density because the local impact environment, such as population count (CIESIN et al., 2005) and surface type (land or water) (Patterson and US National Park Service, 2015), vary across the globe. Furthermore, the impactor sample needed to be representative in relation to the possible variations in impact angle and speed. In (Grav et al., 2011; Chesley and Spahr, 2004), a random set of 10,006 artificial impactors was generated based on the solar system population of near-Earth objects (NEOs) and this set was used here to extract the distributions of impact location, angle and speed for Earth impactors. Subsequently, a fivefold larger artificial impactor sample of 50,000 impactors was generated randomly that reflects these distributions.

Longitude Distribution The longitudinal impact distribution was expected to be uniform (Rumpf et al., 2016b) and the analysis of the impactor sample agreed with this expectation, as shown in Figure 4.11. Figure 4.11a is a so-called probability plot which presents the agreement between the expected theoretical, fitted distribution – in this case uniform – and the sample. A probability plot is a tool to evaluate the quality of the proposed distribution function with an observed sample by producing a scatterplot that relates the theoretically expected values for a given quantile of the fitted distribution on the abscissa with the observed quantile values in the sample on the ordinate. If the fitted distribution and the observed values agree perfectly, the plot shows a straight line with the mathematical description $y = x$. This line is shown, for comparison with the scatter points, as the thin red line in Figure 4.11a. The uniform distribution agrees well with the observed distribution yielding a correlation coefficient of $R^2 = 0.9999$. Figure

4.11b shows the corresponding histogram of sample impact points over longitude (green bars) and the fitted uniform distribution (blue line).

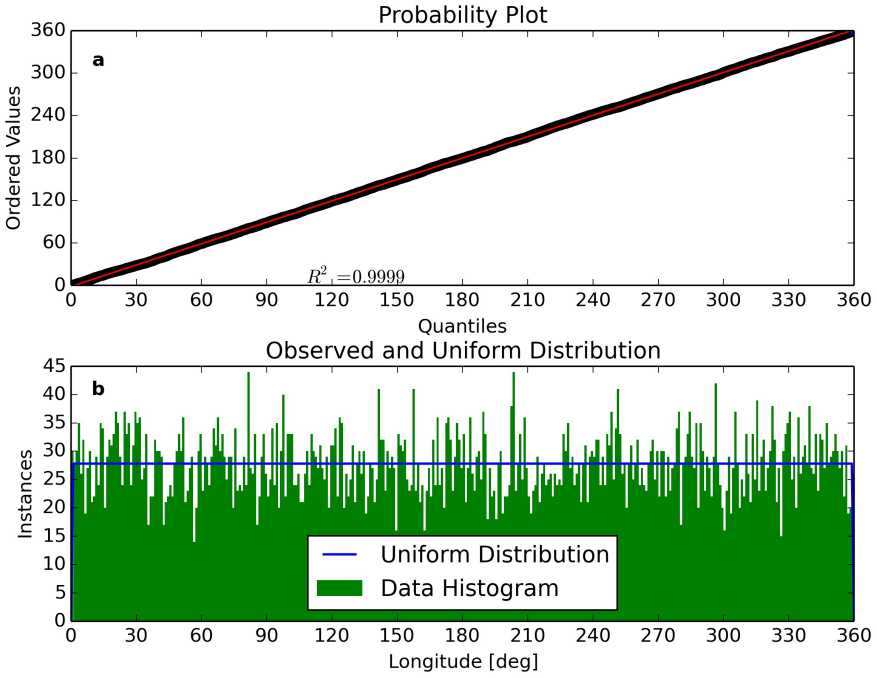

Figure 4.11: Probability plot (a) and sample histogram with fitted uniform distribution (b) for impact location longitude. The impact distribution in longitude is consistent with a uniform distribution.

Latitude Distribution In terms of spatial impact density, the latitudinal impact density is expected to be nearly uniformly distributed as well (Rumpf et al., 2016b). However, in this analysis, the impact count (as opposed to spatial density) as a function of latitude was needed, and, because the area that corresponds to each latitude band decreases from the equator to the poles, the impact distribution is non-uniform with larger impact counts near the equator and the smallest counts at the poles. Figure 4.12 shows the best-fit result of a beta distribution to the observed latitudinal impact distribution. Figure 4.12a is the probability plot which reveals a large correlation coefficient of $R^2 = 0.9999$ between the observed and expected quantile values for the beta distribution. Figure 4.12b shows the observed sample (green bars) and the superimposed beta distribution (blue line) with the probability density function:

$$pdf_{beta}(x) = \frac{\Gamma(a+b)x^{(a-1)}(1-x)^{b-1}}{\Gamma(a)\Gamma(b)} \tag{4.2}$$

Where $a = 2.3188480$ and $b = 2.3293272$ are the corresponding shape parameters and $\Gamma()$ is the Gamma function. An array of distribution functions was tested and the beta distribution produced the best fit amongst the tested distributions (for example, cosine: $R^2 = 0.9990$). The reasons for the good fit are the beta distribution's characteristics of

allowing a symmetric distribution, and to reach zero probability abruptly as opposed to trailing off in an asymptotic fashion.

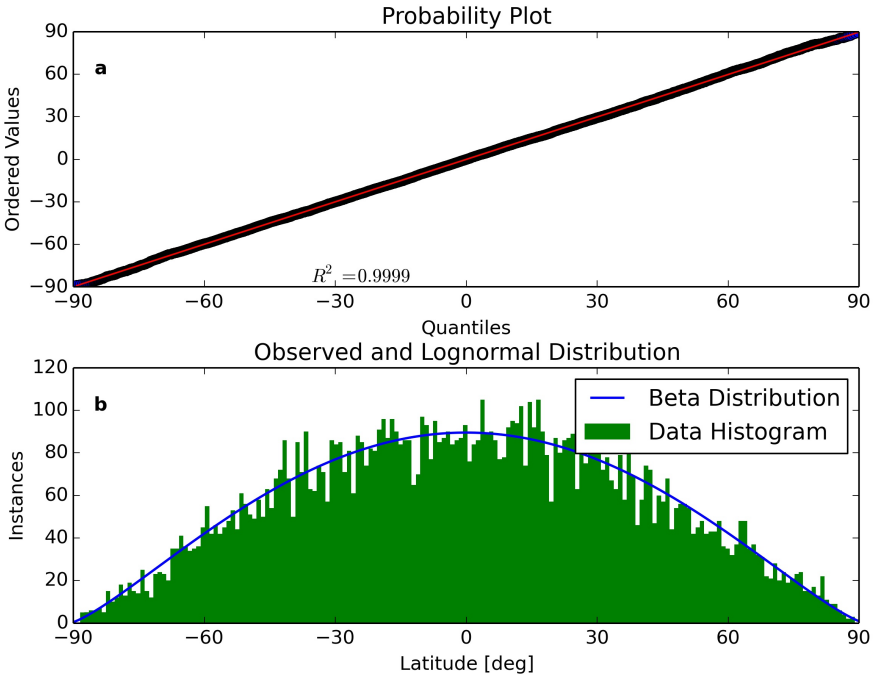

Figure 4.12: Probability plot (a) and sample histogram with fitted beta distribution (b) for impact location latitude. A beta distribution provided the best fit.

Impact Speed Distribution The minimum observed impact speed was 11.138 km/s, and this lower bound can be attributed mainly to the Earth's escape velocity. The maximum observed impact speed was 48.119 km/s even though it is possible for higher impact speeds to occur[1]. Furthermore, it should be noted that the calculation of impact speeds in the original sample did not account for the Earth's surface speed due to the planet's daily rotation. In theory, the impact speed of a very shallow impactor at the equator could be altered by ±460 m/s, depending on whether the impactor collides with the prograde or retrograde side of the Earth. The effect of rotational surface speed declines to zero as impacts occur closer to the poles and are also insignificant for steep impact angles (<5 % of minimum impact speed). Because rotational surface speed was not considered in the original sample and because of its limited effect, rotational surface speed was not considered in the derivation of the statistical impact speed distribution.

[1]For this, consider the orbital speed of Earth which is on average 29.8 km/s (slower at aphelion, faster at perihelion) and the escape velocity from the Sun at Earth distance which is about 42.1 km/s. It is possible that, in very rare instances, a long period object, such as one originating from the Oort cloud, could result in a head on collision with Earth and this would yield an impact speed of about $29.8 + 42.1 + 0.9 = 72.8$ km/s (orbital speed of Earth, Sun escape velocity and kinetic energy increase through Earth's gravitational potential). However, such an event would be extremely rare which is also not considered in our base sample from (Chesley and Spahr, 2004) and shall, thus be excluded from the extended sample.

It was found that a logarithmic normal distribution with probability density function:

$$pdf_{lognormal}(x) = \frac{1}{ax\sqrt{2\pi}} exp\left[-0.5\left(\frac{log(x)}{a}\right)^2\right] \tag{4.3}$$

where $a = 0.7533689$, best fitted the observed distribution of impact speeds. Figure 4.13a presents the probability plot for this fit along with the observed impact speed sample and the fitted logarithmic normal distribution in plot b. In this figure, the lognormal distribution agrees well with the observed sample up to impact speeds of about 35 km/s. However, the probability plot expected theoretical quantiles up to 90 km/s while the actual observed maximum impact speed was only 48.119 km/s. Consequently, the fitted distribution departs from the observed sample for higher impact speed quantiles and this is why the correlation coefficient for the impact speed range from 11.138 km/s to 90 km/s is relatively low with $R^2 = 0.9545$. In any case, the lower impact speed range is of higher practical relevance here because the cumulative probability for this distribution already covers 98.63 % of all instances of impact speeds up to 34.243 km/s. In fact, R^2 is 0.9903 in the lower range (11.138 – 34.243 km/s) and this finding clarifies that the smaller correlation coefficient for the entire range is due to a poorer fit for higher impact speeds which should only occur for 1.37 % of the artificial sample. To further contain any potentially detrimental effect of a poor fit for higher impact speeds, the larger sample was limited to a maximum impact speed of 50 km/s. The mean of the lognormal distribution is 16.6 km/s.

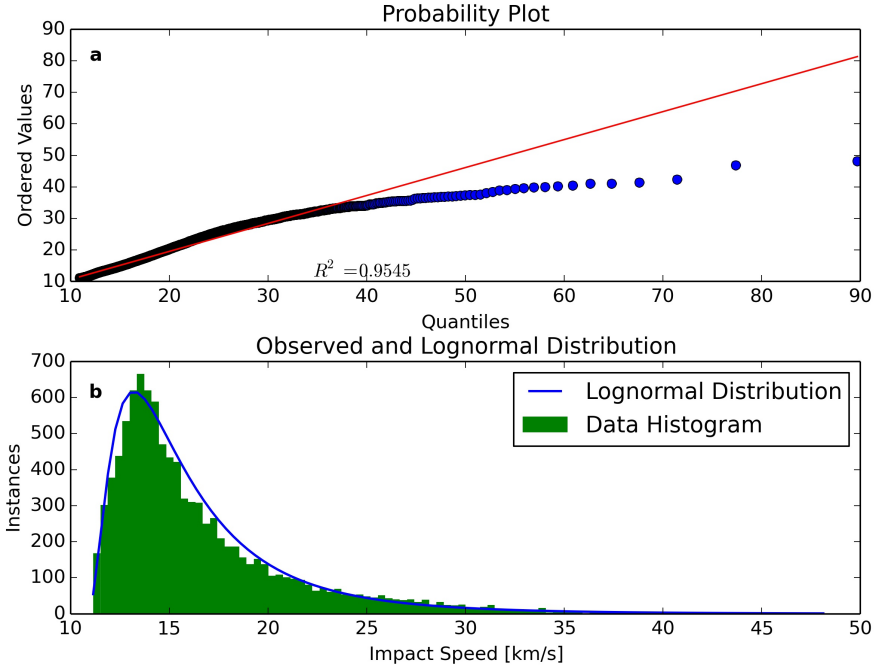

Figure 4.13: Probability plot (a) and sample histogram with fitted lognormal distribution (b) for impact speeds.

For the proper expansion of the original impactor sample, it was of interest to determine

if impact speed showed a significant sensitivity to impact latitude. The observed impact speeds of the sample over impact latitude are plotted in grey in Figure 4.14. A moving average filter with a window size of 40 impact instances (blue line) was applied to determine any trends in the data and the distribution appears to be uniform. However, visual inspection of the figure reveals the occurrence of higher peak impact speeds at near equatorial latitudes. To analyse this observation, the standard deviation of the moving average filter result was determined and it was found to remain near-constant over the entire latitude range. This confirms that higher impact speeds can be attributed to larger sample sizes towards the equator due to the larger available impact area per latitude band. Larger sample sizes allow for more extreme values to occur while maintaining a constant standard deviation. It appears that latitude does not have a significant effect on impact speed.

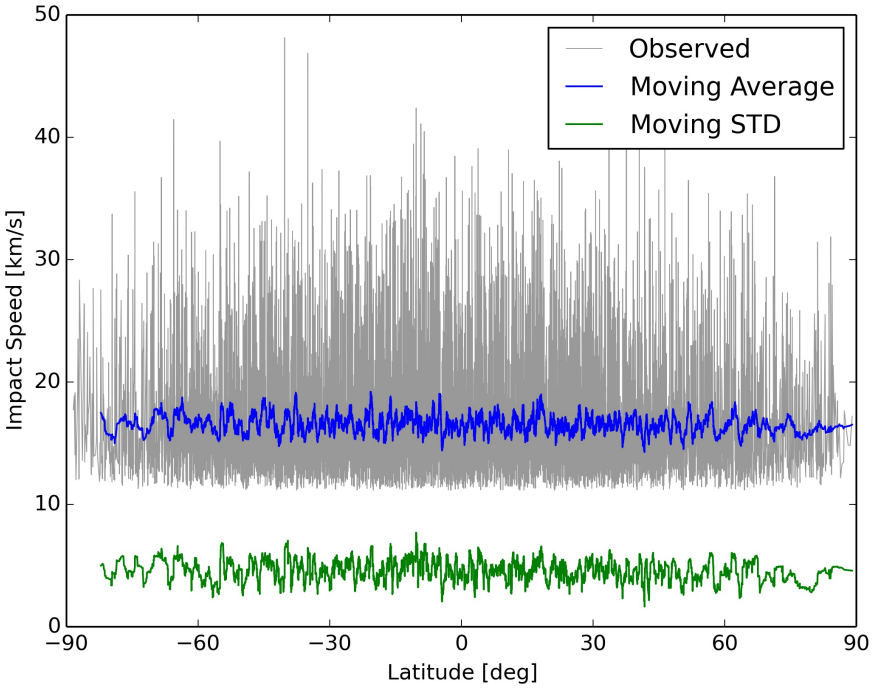

Figure 4.14: Impact speed plotted against latitude. No dependency of impact speed on impact latitude is discernible in the data.

Impact Angle Distribution The impact angle is an important characteristic that determines the immediate environmental consequences in an asteroid impact event and a beta distribution was found to provide the best fit with the observed impact angle sample data. Figure 4.15 presents the probability plot for the fit (a), as well as the observed impact angle histogram with superimposed least square fitted beta distribution (b). It should be noted that the Earth's surface speed due to the planet's daily rotation was not considered in the original sample and is not considered for the extended sample because of its limited potential to alter an impact angle by a maximum of $\pm 2.4\,^{\circ}$ (slowest

possible, perpendicular impact at the equator). The correlation coefficient of the fit is satisfactory with $R^2 = 0.9998$ for shape parameters $a = 1.9667805$, and $b = 2.2479362$ as applicable to Equation 4.2. It is noteworthy that the mean of this distribution is 42.87 ° (as opposed to the expected value of 45 ° as predicted by the analytical description of the problem (Shoemaker et al., 1962)) showing that the distribution has a small positive skew favouring shallow impact angles. A possible reason for this finding is that Chesley and Spahr biased their population to reflect the impact frequencies of asteroids given their orbital speed (Chesley and Spahr, 2004). .

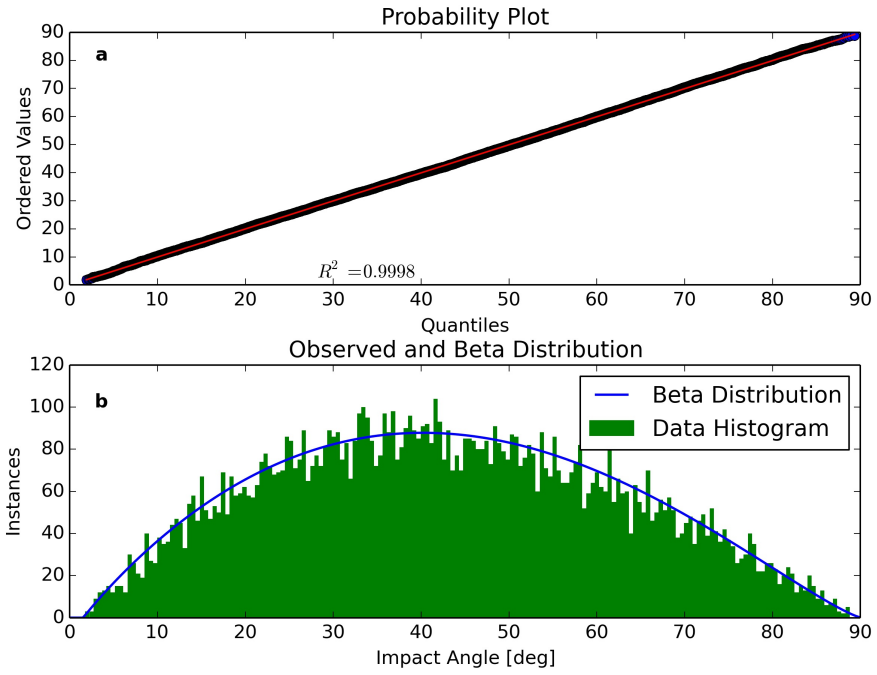

Figure 4.15: Probability plot (a) and sample histogram (b) with least-square fitted beta probability density function (b) for impact angles.

Similarly to impact speed, it was of interest to investigate any impact angle dependency on impact latitude. Such a dependency could occur if impactors have a preferred impact direction, from the ecliptic for example. Figure 4.16 presents the impact angle distribution plotted against latitude together with a moving average filter (window size is 40 impact instances) and the standard deviation of the filter. It appears that there is no impact angle dependency over latitude because the moving average remains near-constant over the entire latitude range. Similarly, the decreasing sample count near the poles does not seem to have a detrimental effect as the standard deviation of the filter remains near-constant as well.

The Impactor Sample Based on the distributions derived in the previous section, an artificial impactor sample covering the globe and counting 50,000 impactors was randomly generated. To illustrate the spatial impact density, Figure 4.17 shows the

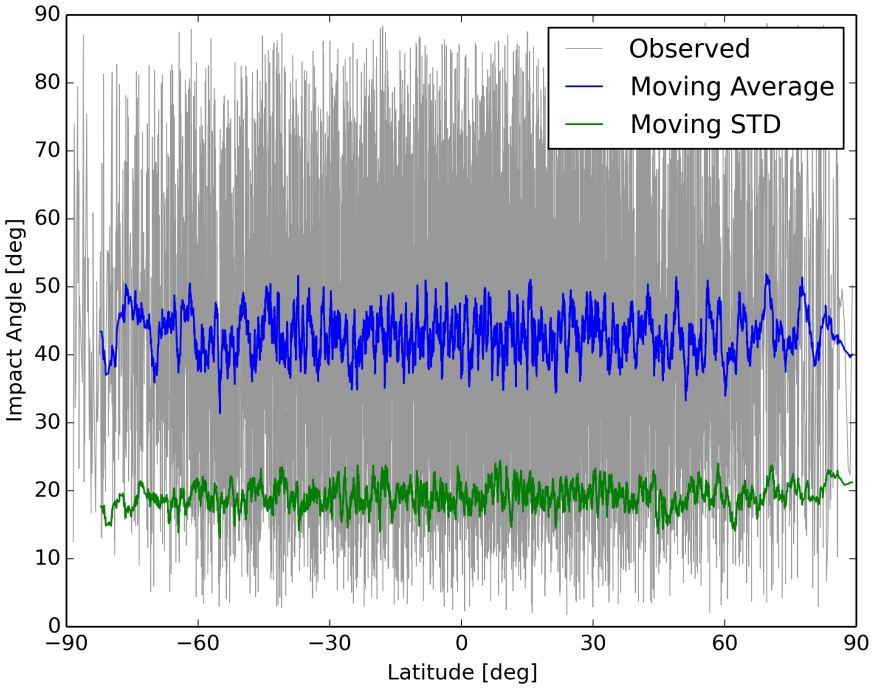

Figure 4.16: Impact angle distribution over latitude together with a moving average filter and its standard deviation are shown.

sample's impact locations over Europe and the colour coding indicates randomly assigned impact angles. The method yielded 35,984 impactors, or 71.97 % of the sample, that descended over water mirroring that 71 % of the Earth's surface is covered with water. The sample of impactors was used to assess the dominance of individual impact effects for the population of Earth.

Assessing Impact Effect Dominance The impact simulations were conducted using the ARMOR tool (Rumpf et al., 2017b, 2016b,a) (section 3) utilizing analytical impact effect models (Collins et al., 2005) to calculate the environmental consequences of a given impact under consideration of impactor size, impact speed and angle, as well as location.

The impactors were assumed to be of spherical shape with a density of 3100 $\mathrm{kg/m^3}$, reflecting the typical density of chondrites which make up about 90 % of the NEO population (Britt, 2014; Zellner, 1979). Of special interest was how the dominance of each impact effect changes with increasing impactor size (diameter), effectively increasing the impactor's kinetic energy. Thus, the impactor diameter was varied between each simulation run starting from 17 m and increasing to 400 m, while the same impactor diameter was assigned to the entire sample in each global simulation. That is, impactor size was used as the free parameter between simulations but was kept equal within each simulation for the whole asteroid sample. During simulations, the total casualty numbers that were attributed to each impact effect were recorded to gain insight into which impact

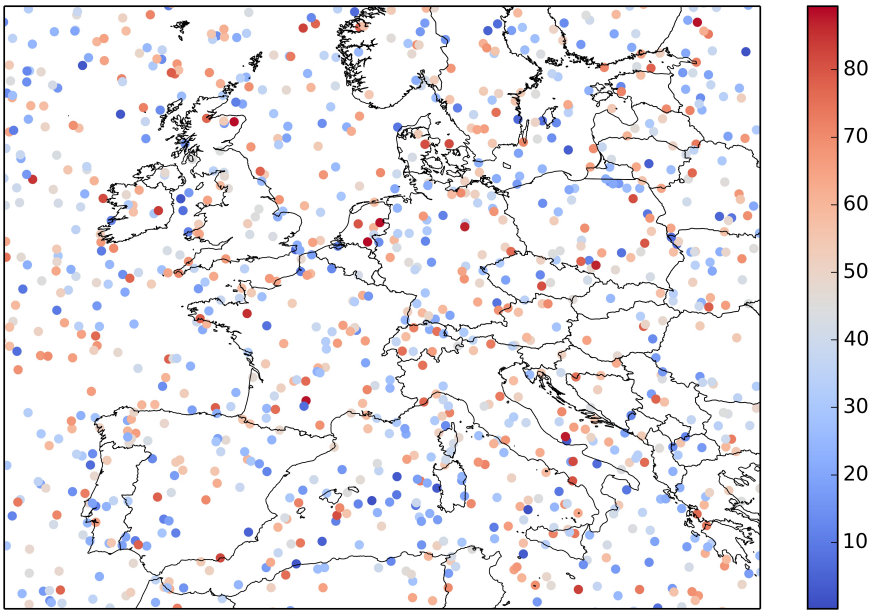

Figure 4.17: Spatial visualisation of the realised set of impact locations over Western Europe. The colour of the markers reflects the impact angle in degrees where 90 ° is a vertical impact.

effects are most dominant in a specific size regime. Seven impact effects were considered and these are: wind blast, overpressure shock, thermal radiation, seismic shaking, cratering, ejecta deposition, and tsunami (Collins et al., 2005; Rumpf et al., 2017b) (section 3.2). The impact effects were propagated away from each impact site and vulnerability models (section 3.3, "expected" case) were employed to estimate how many casualties are to be expected for each impact effect taking into account the population that lives in the affected area on a 4.6 km × 4.6 km global grid (CIESIN et al., 2005).

The allocation of casualties to individual impact effects was accomplished by treating all impact effects independently of each other. In other words, each impact effect was allowed to interact with the same population. This can lead to a situation where the same person can become a casualty multiple times as different impact effects affect that same person. To mitigate double counting of casualties that would follow from this method, the simulations also calculated a total casualty count that followed the standard process of ARMOR's casualty estimation. In the standard process, casualty double counting is avoided and the population vulnerability (equivalent to the likelihood that an affected person dies) is calculated taking into account all impact effects. Because population vulnerability to one impact effect (V_{effect}) is equivalent to the likelihood that any person in that population dies, the chance that any person survives an impact effect is simply $\lambda_{effect} = 1 - V_{effect}$, where λ_{effect} is the likelihood of survival for that person. Considering that the person is affected by all impact effects in sequence, the combined

chance of survival is the product of all effect survival probabilities:

$$\lambda_{combined} = \prod_{i=effects} \lambda_i \tag{4.4}$$

Finally, the combined effect vulnerability is equivalent to the likelihood of that person not surviving all impact effects or:

$$V_{combined} = 1 - \lambda_{combined} \tag{4.5}$$

The total casualty count determined with the standard vulnerability method was used to scale casualty counts of each impact effect such that the sum of the casualties of all effects was equal to the total casualty count.

4.4.2 Findings

Using the method described above, the dominance of asteroid impact effects was calculated, first, for a global impact scenario and, subsequently, for impacts over land and water masses separately. In the following figures, the total number of casualties recorded in each simulation run was divided by the sample size to obtain the average number of casualties per impactor.

The results presented in Figure 4.18 show that all asteroids below a threshold size experienced an airburst and this threshold was found to be 56 m for asteroids of density 3100 $^{kg}/_{m^{-3}}$. While the combination of impact angle and speed has to be very specific to produce a surface impact at the threshold size, larger asteroids increasingly reached the surface because their bigger size allowed them to pass the atmosphere before disintegrating for a wider range of angle/speed combinations (Collins et al., 2016; Toon and Covey, 1997). The asteroid population exhibits a range of densities between 1000-8000 $^{kg}/_{m^{-3}}$, however, about 80 % of asteroids have a density between 1500-3500 $^{kg}/_{m^{-3}}$ (Britt, 2014; Zellner, 1979; Hanus et al., 2016). Results presented here will vary for different asteroid densities and higher density will allow for smaller objects to reach the surface with regard to the surface impact threshold size.

For the chosen density, the minimum asteroid size to cause casualties was 18 m due to wind blast and thermal radiation. The harmful effect of an overpressure shock only became lethal for 40 m impactors (Figure 4.18). These findings correlate with observations made after the Chelyabinsk bolide event in 2013 where a 17-20 m object, travelling at 19 $^{km}/_{s}$ disintegrated mid-air (Brown et al., 2013; Borovicka et al., 2013). Most of the damage and injuries during that event, were caused by the aerodynamic shock that knocked people to the ground and damaged structures and windows causing indirect injuries by flying glass shards. The population also reported burns, heat sensation and temporary blindness due to the intense electromagnetic radiation emitted by the meteor

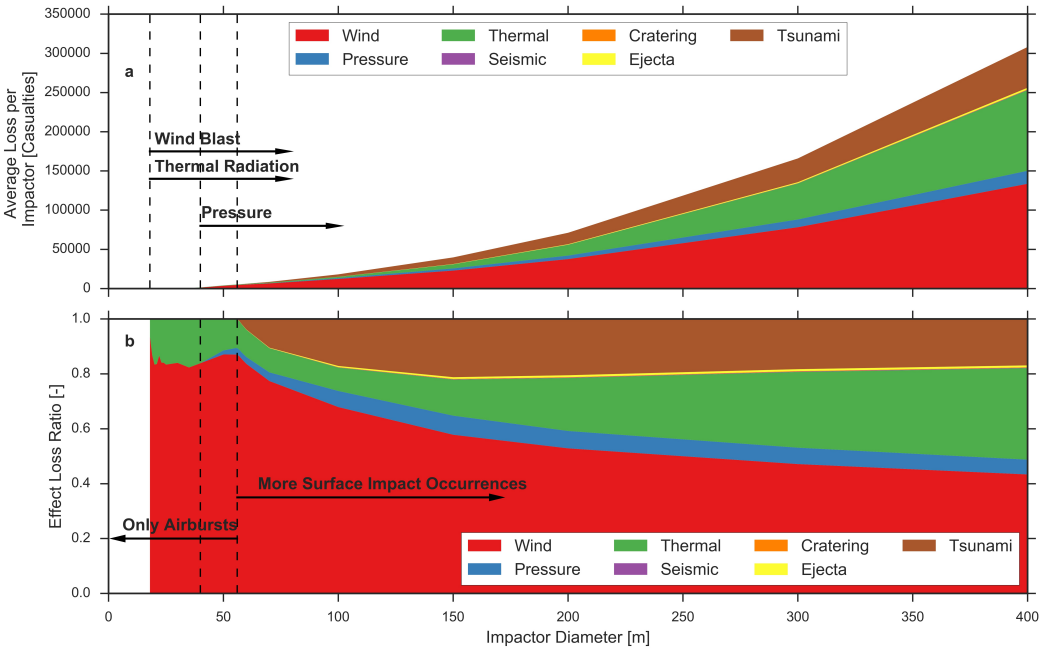

Figure 4.18: Plot a shows the increase in average casualties per impactor size and highlights the increasing contribution by each impact effect. First casualties due to wind blast and thermal radiation occurred at 18 m. Impactors of 40 m produced the first pressure losses and first surface impacts were recorded for impactors larger than 56 m. Plot b shows the impact effect dominance distribution over the asteroid size range up to 400 m.

(Popova et al., 2013). The Chelyabinsk meteoroid was a shallow impactor that entered the atmosphere with an angle of 18 ° resulting in an airburst at an altitude of between 30 and 40 km (Borovicka et al., 2013), which is consistent with the impact effect models used in this research that predicted an airburst altitude of 33 km (Collins et al., 2005). Given the possible impact conditions in terms of impact speed and angle distributions (Figures 4.13 and 4.15), these parameters reflect a medium energy event for an asteroid of this size, because of the shallow impact angle and no casualties were reported for the Chelyabinsk event. However, over 1,000 persons were injured (Popova et al., 2013) and it is possible that an impactor of the same size with higher impact speed or steeper impact angle would have resulted in some casualties due to aerothermal effects. The Tunguska airburst in 1908 is another event for which considerable aerothermal damage was reported for a roughly 30-40 m sized object (Boslough and Crawford, 2008; Artemieva and Shuvalov, 2016). During that event, over 2,000 km^2 of forest were flattened and trees in an area of 300 km^2 were burned by thermal radiation (Nemtchinov et al., 1994; Boslough and Crawford, 2008). While no human casualties have been reported for that event due to the remoteness of the impact location in Siberia, the released energy would certainly have sufficed to cause casualties in populated regions. These observations are in line with land impact simulation results presented in Figure 4.19a and Figure 4.20a where aerothermal impact effects are predicted to cause significant loss.

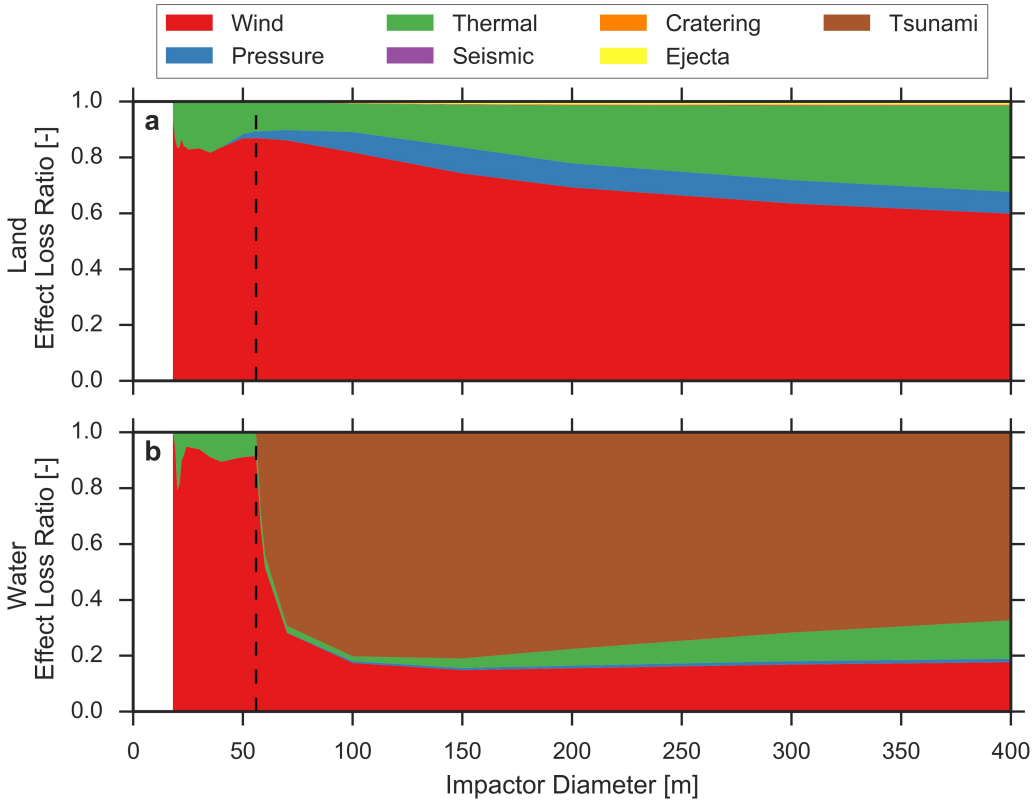

Figure 4.19: Plot a visualizes the effect loss ratios for land impactors of a given size up to 400 m. Conversely, plot b shows these ratios for average water impactors of a given size. The vertical dashed line indicates the occurrence of first surface impacts.

The evolution of total average loss per impactor is visualized in Figure 4.20a on a semi-logarithmic scale for the global (red, middle line), land (green, upper line) and water (blue, lower line) impact scenario. The average land impactor is about one order of magnitude more dangerous than the average water impactor. Loss growth changes behaviour around the point of first surface impact occurrence. The average expected fatality count for impactor up to 50 m in diameter as a function of impactor size in metres can be approximated by the fit (Pearson coefficient of 0.90):

$$y_{lower} = 0.083 \times 1.14^{1.75L_0} \tag{4.6}$$

Similarly, the average loss for impactors which may reach the surface (>50 m), can be approximated (Pearson coefficient of 0.97) as a function of asteroid size with:

$$y_{upper} = 4374.91 \times 1.01^{0.99L_0} \tag{4.7}$$

To gain insight into the variability of these results, best and worst case scenarios were designed intended to capture $\pm 1\,\sigma$ standard deviation (section 3.3) and the results are expressed in Figure 4.20b as the ratio of the average global impact loss. The sensitivity

analysis shows that results for small asteroid diameters may vary by a factor of two while larger asteroids show less sensitivity exhibiting variation of about +45/-30 % and these variations are in line with expected variations in previous work (Stokes et al., 2003). Figure 4.20c indicates the percentage of the impactor sample that contributed to loss generation. Values smaller than 50 % correspond to a median impactor loss of 0.

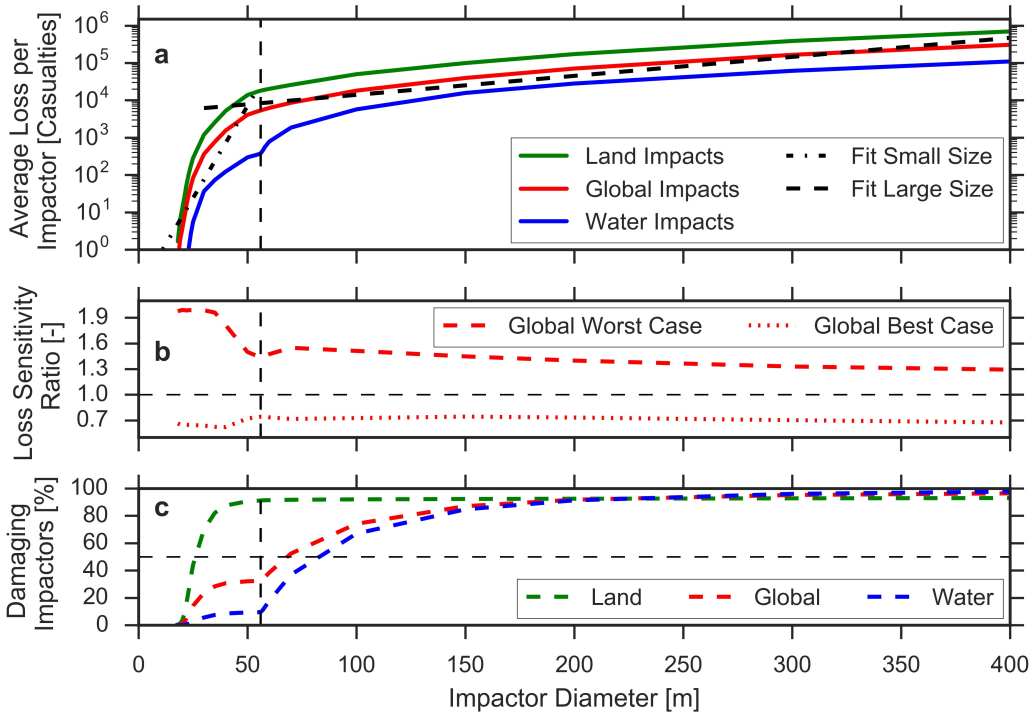

Figure 4.20: Plot a presents average loss in the global, land and water impact scenario along with exponential fits for global airburst losses and losses due to larger impactors. Plot b indicates the variability in global loss numbers through correction factors for best/worst case scenarios. The expected case (factor 1) is marked with a horizontal dashed line. Plot c presents the percentage of impactors that contributed to loss generation in land, water or global scenarios. The 50 % threshold is marked with a horizontal dashed line. To facilitate orientation, all plots show the size where first surface impacts occur with a vertical dashed line.

The average loss per impactor increased exponentially with increasing impactor size and this is reflected in Figure 4.18a. Interestingly, the slope of the average loss function is larger in the airburst regime as shown by the fitted exponential functions (Equations 4.6 and 4.7) and in Figure 4.20a. This is partially owed to the fact that an increasing number of impactors harm the population (Figure 4.20c) but, in addition, aerothermal effects appeared to be more efficient at transforming their energy into loss. The latter statement is supported by the observation that a land impactor was an order of magnitude more harmful than a water impactor (Figure 4.20a). Furthermore, airbursts transform all available energy in aerothermal effects and do not split their energy for less harmful ground effects (Figure 4.18a). They are, thus, more efficient at depositing

their destructive energy than larger impactors and this has relevance in connection with the fact that the asteroid catalogue is least complete (<1 % discovered) in the small asteroid diameter range (Harris and D'Abramo, 2015). Notably, the loss per impactor results agree well with previous work but extend the possibility for fatalities to smaller impactor sizes (Stokes et al., 2003; Chapman and Morrison, 1994). The residual risk from undiscovered asteroids might have to be corrected to smaller asteroid diameters (Stokes et al., 2003; Chapman and Morrison, 1994; Harris, 2013; Boslough, 2013a).

Knowledge about the average number of total casualties per impactor can aid early decision-making about whether to deflect an asteroid or to evacuate the impact area when a new impactor is discovered and the corresponding sensitivity analysis provides insight into the expected spread in the casualty estimate. These results may be used in the future to facilitate a new asteroid hazard scale (Binzel, 2000; Chesley et al., 2002; Boslough, 2013b; Boslough et al., 2015).

While airbursting impactors appeared very efficient at depositing their energy, it is also important to understand that the loss outcome for individual impactors showed higher variation for small impactors. This is due to the shorter range, but high severity, of airburst effects compared to tsunamis. Figure 4.20c presents the percentage of the impactor sample that produced losses. In the global scenario, the median impactor loss was actually zero (corresponding to <50 % damaging impactors) for asteroids smaller than 60 m. This is owed to the fact that twice as many asteroids impact over water compared to land and the short range airburst effects do not reach any population. Focusing on the water impact scenario illustrates this point as only a small impactor fraction corresponding to near-coastal airbursts contributed to loss (Figure 4.20c). The sharp increase in loss for small impactor sizes can, thus, mainly be attributed to land impactors which are naturally close to populations. However, even for land impactors, the median impactor (smaller than 25 m) produced zero casualties illustrating that the average loss is driven by those impact events that hit close to densely populated areas and cause severe losses. In fact, the most damaging impactor was about four orders of magnitude more severe than the average loss for small impactors and this discrepancy decreases to two orders of magnitude at 400 m.

Land impact effect dominance is visualized in Figure 4.19a and these results show that wind blast in conjunction with overpressure shock are the most critical impact effects (since they occur together) accounting for more than 60 % of the losses up to 400 m. Thermal radiation is significant but accounts for about 30 % losses. Notable is the increase in thermal radiation dominance for larger impact effects and this phenomenon is also present in the water impact scenario shown in Figure 4.19b. Not surprisingly, the most dominant effect for water impacts are tsunamis accounting for 70-80 % losses depending on size. Together, land and water impacts make up the global scenario (Figure 4.18) with a correspondingly heavier weighing for the more dangerous land impactors (Figure 4.20a). The global scenario illustrates that aerodynamic effects dominate for

all sizes (>50 %). Thermal radiation is a significant concern and appears to increase in severity for larger impactors. Tsunamis have been a major concern in the planetary defense community but the results here suggest that they only contribute 20 % to the overall threat of impacting asteroids.

Aerothermal effects dominate because they are caused by every impactor, while tsunamis can only be the result of an ocean impact. Furthermore, aerothermal losses are mainly caused by impactors over land which are naturally closer to population centres. In contrast, tsunamis can only reach populations close to the coast because their inland reach is limited to a few kilometres. While the reach of tsunamis is far, these long propagation distances attenuate wave height significantly reducing population vulnerability during landfall. Furthermore, the initial wave height is limited by sea depth at the impact point (Wünnemann et al., 2010). The continental shelf forms a protective region around most coastlines reaching only about 100-200 m depth and typically extending 65 km offshore. Even deep sea impacts of large asteroids are constricted by this upper boundary for wave height, while aerothermal effects can scale freely with impactor size and, thus, energy. In summary, it appears plausible that tsunamis contribute less than might be intuitively expected to global asteroid impact loss.

The findings provide valuable insight into which impact effects are most significant informing disaster managers about which effects the population should be prepared for in case of an impact. In the case of small impactors, aero-thermal effects are of greatest concern, and here, the population could seek shelter in a safe place such as a basement. For larger impactors, a complete evacuation might be necessary as high impact effect severity renders any affected region unsafe. For larger water impactors, tsunamis become a concern for near coastal populations which might need to be evacuated.

Conversely, knowledge about which impact effects are less significant is similarly valuable as it can help save resources otherwise spent on less critical impact effects. The influence of ejecta deposition is barely visible at the top of Figure 4.19a with a maximum contribution of 0.71 %. Even less significant are the contributions of cratering and seismic shaking with a maximum of 0.16 % and 0.16 %, respectively. The results indicate that ground impact effects, such as cratering, seismic shaking and ejecta deposition, play a minor role in loss generation compared to other effects.

4.4.3 Effect Dominance Conclusions

The analysis covered a wide range of possible impact conditions in terms of impact speed, angle and size using an impactor density of 3100 $\mathrm{kg/m^{-3}}$. Evaluation of this parameter space showed that the minimum asteroid size to cause fatalities was 18 m and that first surface impacts occur for asteroids with a minimum size of 56 m.

The total casualty estimation per impactor as a function of asteroid size was approximated by two exponential functions and these functions revealed that the loss generating mechanisms showed a significant change in behaviour around the surface impact size threshold. For smaller asteroids, only airbursts occurred and they appeared to be more efficient in transforming kinetic energy into loss than surface impacts. This finding may have implications for the assessment of residual asteroid impact risk of the yet undiscovered asteroid population which is biased towards smaller asteroid sizes (section F).

Using the exponential description for total casualty estimation allows quick assessment of the possible threat when a new, impacting asteroid is discovered. Total casualty estimation also revealed that the average land impactor is about an order of magnitude more dangerous than the average water impactor. Aerothermal effects, dominated loss generation in the global setting. Equally importantly, the results provide evidence that effects such as cratering, seismic shaking and ejecta deposition provide only a minor contribution to overall loss. Tsunamis were the most significant effect for water impacts, but were less important globally. In summary, the results help to better understand the asteroid impact hazard, including which impact effects are most and least relevant, and can be of help in formulating an adequate response to the threat. The small contribution of tsunamis to global loss was surprising but can be explained by initial wave height restriction due to the sea depth and wave height attenuation over distance whereas the other effects can scale freely with increasing impact energy and are naturally closer to populations. The data show, for the first time, how the dominance of impact effects changes for increasing impactor size.

Chapter 5

Discussion

During the past Planetary Defense Conferences, the planetary defense community has repeatedly called for better asteroid risk assessment tools (Ailor and Tremayne-Smith, 2013; Ailor, 2015). Specifically, the need for improved ways to communicate threat levels to disaster management agencies was identified as such institutions require easy-to-understand information about disaster consequences for the population (e.g. number of casualties/injuries) rather than information about the physical severity of the hazard.

The aspiration of this PhD research project was to build a tool that calculates the on-ground risk of asteroid impacts for applications in asteroid risk assessment and to enable future activities such as risk driven deflection mission design. To accomplish this goal, the ARMOR tool was developed and its method was published in Rumpf et al. (2016b, 2017b, 2016a). Risk estimation is based on the universal risk definition that risk for a given hazard is the product of probability, exposure and vulnerability, and this risk definition has been made amenable to the asteroid impact threat subject.

One of the first capabilities that was incorporated was the calculation of surface impact points based on the ephemeris data of known asteroids. At this point, it became feasible to investigate a long-standing assumption in planetary defense which has not been formerly tested previously. Namely, the assumption was that the long-term impact location distribution of asteroids is uniform across the globe. Using ARMOR, it was possible to assess the impact location distribution for a set of 261 natural potential impactors, and, in addition, a set of 10,006 artificial impactors. The results confirmed that the impact distribution is approximately uniform and the findings were published in the journal *Icarus* (Rumpf et al., 2016b). Thus, this reference may be used in the future to support the uniform impact distribution assumption whenever it is invoked. The findings show that, on average, every location on the Earth is equally prone to an asteroid impact.

It should be noted that the underlying mechanics that produce the near-uniform impact distribution still offer potential for investigation. Given that most objects reside in the

ecliptic plane, one could expect that equatorial impacts are favoured as the Earth's equator is exposed to the ecliptic. However, there are other influences such as the gravitational attraction of the Earth pulling in objects, or the fact that, since the Earth is orbiting the Sun together with other objects, it is not the inertial ecliptic velocity of an object that is important, but rather the relative velocity between the Earth and the incoming object that will determine impact location. In addition, Earth's obliquity could have an influence on impact location distribution. These aspects (and possibly others) appear to strike a balance that manifests itself in the observed near-uniform impact distribution, even as the nature of the balance remains to be investigated further.

As the development of ARMOR moved along, it became possible to compare simplified risk with advanced risk and this comparison allowed the evaluation of how risk modelling fidelity influences risk assessment. On one hand, the entire population of only the impacted map cell (equivalent to assuming vulnerability of 100% and effect reach limited to one cell) was considered for simplified risk. On the other hand, advanced risk used vulnerability models for accurate vulnerability modelling which also facilitated effect reach calculation, and therefore, exposure estimation. Both simplified and advanced risk calculations were constrained to impacts over land to maintain comparability. The analysis provides useful impact location information which is the next information available after the initial impact probability calculation and it is possible that ESA & NASA start to publish this information in the near future on a routine basis. Thus, this comparison clarifies the degree to which simple impact location knowledge may be extrapolated to obtain risk distribution knowledge. The results showed that simple impact location determination (and, therefore, simplified risk) is suitable as a coarse risk estimator, especially for abstract impact scenarios such as the uniformly distributed impact background threat. However, if the risk of a specific impact scenario, for example a newly discovered threatening asteroid, is of interest, then high fidelity exposure and vulnerability modelling become crucial to adequately assess the situation. This comparison allowed to appreciate the added value of ARMOR to the field of asteroid risk assessment. The findings, which were published in the journal *Acta Astronautica* (Rumpf et al., 2016a), supported further development of ARMOR and the development focus shifted towards impact effect and population vulnerability modelling.

Six analytical impact effect models for wind blast, overpressure shock, thermal radiation, cratering, seismic shaking and ejecta out-throw are provided in Collins et al. (2005) and these have been implemented in ARMOR. However, no tsunami propagation model that was suitable for the needs of ARMOR was included in this reference and a suitable model needed to be built based on other literature sources. The Irribaren number concept, together with analytical deep water propagation models, appeared most promising and was implemented. Furthermore, previous vulnerability models that determine the mortality of exposed populations as a function of the impact effect severity were not described in detail and did not offer a firm backing by literature (Bailey et al., 2009;

Norlund, 2013). Thus, such models were derived based on an extensive literature research for all impact effects. The implementation of the tsunami model together with all vulnerability models have been published in the journal *Meteoritics and Planetary Science* (Rumpf et al., 2017b). With this publication, the planetary defense community has access to a full suite of analytical impact effect models (including tsunami) and can extend these models with the presented vulnerability models to calculate casualty numbers for impact scenarios. The publication of the models is intended to fertilize further asteroid risk assessment activities in the planetary defense community by providing a necessary component for such analysis.

In a practical example application of ARMOR, the risk for asteroid 2015 RN35 was calculated. This asteroid had an impact probability of 3.06×10^{-6} for an impact in the year 2077. ARMOR calculated the possible impact locations in the shape of an impact corridor stretching from Indonesia across the Pacific, the USA, the Atlantic to Spain. At each of the possible impact locations within the corridor, an impact was simulated under consideration of the local impact angle and speed (>500,000 impact points in total). The resulting impact effects were propagated over the local population and their vulnerability was calculated. The results led not only to a total risk estimate over the entire corridor but also yielded the spatial risk distribution along the corridor.

Spatial risk distribution helps to identify local high risk regions that would require special attention if additional asteroid observations were to increase the impact probability to dangerous levels. This way of representing a specific asteroid impact threat has not existed before and such information can be helpful for planners to prepare efficiently for a future threat. The total risk estimate is the integral along the risk corridor and this scalar takes into account the impact hazard magnitude as well as current impact probability. In the case of 2015 RN35, the risk under consideration of the low impact probability was 0.047 expected casualties informing stakeholders of the urgency of the current threat situation. As such, the risk scale as provided by ARMOR is a reflection of the current threat level expressed in the unit of expected casualties.

To obtain a quick understanding of the potential loss magnitude, an impact probability of one may be assigned to the risk figure and and the resulting risk estimate communicates how many casualties would be expected if an impact was certain within the risk corridor. The assumption of certain impact yields the potential hazard loss as 13,513 expected casualties.

Expressing risk in the units of expected casualties provides an intuitive way of communicating the threat level of an observed asteroid. It is simple to understand that a risk of 0.047 expected casualties is not worrisome because, in fact, the expectation is that nobody dies after rounding the risk value to the closest integer. Values in this order of magnitude are common for most objects on the NEO web pages by NASA and ESA as they exhibit similar impact probabilities and sizes (79-177 m for 2015 RN35). On the

other hand, quantifying the potential hazard loss (13,513 for 2015 RN35) is a tangible measure of the hazard severity that provides direction to the amount of resources which should be expended to save the equivalent of a sizeable town, should the threat become more credible.

In fact, one of the key qualities of using the unit of expected casualties is its capacity of facilitating direct comparison between the asteroid impact hazard and other natural disasters. As long as another hazard poses a danger to human life, it is usually possible to estimate the corresponding number of expected casualties. For the sake of concreteness, the example of river flooding shall be used here to illustrate this point. It is possible to predict how many people will be threatened by an overflowing river through consideration of the topography around the river and the population living in that area. Given a predicted river flooding height, the number of threatened people may be estimated. The reason why flooding has been chosen as an example is that it is a common occurrence in nature - a characteristic that places flooding in stark contrast to rare asteroid impacts. Due to its frequent occurrence, it is well understood how many resources are commonly expended to counter a given threat level (as in threatened population) due to flooding. As asteroid impacts are rare compared to flooding, this previous experience does not exist for the impact hazard. However, using the risk unit of expected casualties, it is now possible to estimate the justifiable amount of resources (in terms of equivalent value) that should be expended to counter a given asteroid threat level which is comparable to the threat level of more common natural disasters. For the asteroid threat, risk mitigation measures might be in the form of dedicated telescope time to improve impact probability estimates, evacuation planning, conducting a deflection mission, or any other measure that seems suitable at the time.

The international community, represented by the Space Mission Planning Advisory Group (SMPAG) is currently working on establishing a protocol that formalises the response to a given asteroid threat. Such a response protocol would rely on threat threshold values that trigger appropriate actions to address the threat. The work in this thesis was presented at the 6th SMPAG meeting at the United Nations in Vienna as the concept of risk can facilitate such threshold definition and the appropriate response action.

The Torino and Palermo scale are currently in use for asteroid hazard quantification. However, both scales only allow for qualitative hazard assessment meaning that they are suitable to state that one possible asteroid impact is more threatening than another. However, they do not provide information about the consequences of an impact beyond very rough estimates such as *local*, *regional*, or *global*. The reason for this limitation is that these scales rely on impact kinetic energy as a proxy for consequences, when, in fact, consequences depend on more factors such as impact angle, impact surface type (water/land), propagation of impact effects, and affected population count as well as population vulnerability. The risk method employed in ARMOR takes these aspects

into account and can not only provide qualitative risk statements about one asteroid compared to another, but actually estimates direct consequences for the population. As such, the risk method presented here is suitable to form the basis for a new hazard scale to serve as a replacement or in conjunction with the Torino and Palermo scales. Time until impact is the one aspect that is currently not considered in risk estimation but should be included for a new hazard scale because time enables mitigation actions and, thus, reduces risk (see Appendix E).

The implementation of the new asteroid hazard scale could be facilitated through the following practical considerations. Calculation and propagation of impact effects is the computationally expensive part of the risk calculation, yet the results of that computation are the same for each asteroid when the impact speed, impact angle and size are the same. Therefore, it would be possible to pre-compute impact effects for all global grid cells while varying the impact angle, speed, and asteroid size in the appropriate range. Suitable ranges for impact angle, speed and location are available from related work that was performed as part of this research and that has been published in Rumpf et al. (2016b, 2017a) (section 4.4.1). In this way, a multi-dimensional interpolation scheme could be generated that would very rapidly produce the consequences of a given impact anywhere on the globe. The interpolation scheme would require the possible impact locations, corresponding impact angles and speeds, as well as size of the asteroid as input. These quantities can be determined by a fast orbital mechanics and Earth surface collision simulation. As an even quicker implementation option, the average damage per asteroid diameter function presented in section 4.4.2 (Equation 4.6, 4.7 and Figure 4.20) could be used to replace the interpolation scheme. This second option would be less accurate than the interpolation scheme but would still improve on existing hazard scales because the casualty figures are based on direct consequence modelling (see Appendix E).

Experience with large-scale explosions (such as nuclear bombs) and the observation of previous meteoritic events (Chelyabinsk, Tunguska) provide a good understanding of which impact effects to expect during an asteroid impact. They are: wind blast, overpressure shock, thermal radiation, cratering, seismic shaking, ejecta out-throw, and tsunami. However, it has not been previously investigated which of these effects are most relevant for the loss of human life. ARMOR calculates these impact effects as well as the corresponding population vulnerabilities for risk estimation. After appropriate adjustments to ARMOR's code, it was possible to record the dominance of individual effects to gain unique insights into the harmful processes of an asteroid impact.

Notable findings include that the wind blast impact effect can generally be regarded as the most harmful of all effects. Furthermore, a carbonacious chondrite with a density of 3100 $^{kg}/_{m^3}$ (accounting for >90% of all meteorites) needs to be at least 18 m in diameter to cause casualties and only reaches the ground for sizes upwards of about 56 m. Tsunamis are a major concern in the planetary defense community with opinions about their

severity ranging from "no threat" to "most harmful of all effects". The analysis here indicates that tsunamis are less dangerous than aerothermal effects (wind blast and thermal radiation) while still contributing significantly to asteroid impact loss. Given that great effort was spent on producing well founded impact effect and population vulnerability models, these results are expected to be robust. The general technique employed for the derivation of the models was the breaking down of essential assumptions into smaller components and backing those up as much as possible with literature values. The benefit of this process is that the overall assumption becomes more robust because inaccurate component estimates only have limited bearing on the final value of the assumption. This approach is especially apparent during the derivation of the outside population estimate (section 3.3.4.1) and for the derivation of the wind (section 3.3.5) and thermal radiation (section 3.3.4) vulnerability models.

The moderate danger of tsunamis also led to the finding that the average impactor over land is an order of magnitude more dangerous than its equivalent over water. However, it should be noted that an impact over water is generally twice as likely as over land given that the global impact location distribution is uniform, and that water covers twice the surface area as land. This finding can be useful in early stages of disaster planning when the possible impact locations of an asteroid are determined.

In addition to identifying the most dominant impact effects, the analysis also showed that land impact effects such as cratering, seismic shaking and ejecta deposition provide only a minor contribution to loss generation. This finding can help increase efficiency in disaster response planning as it provides insight into which effects disaster preparation should prioritize to increase resilience against an asteroid impact.

The extensive impact simulations for the effect dominance calculation provided population loss results for asteroids in the diameter range of 0-400 m (Equations 4.6 and 4.7). With these results, the average loss for an impactor up to 400 m in diameter could be deduced. These loss estimates agree well with but are based on more detailed analysis than previous work (Chapman and Morrison, 1994). They facilitate further applications such as fast threat estimation, a new hazard scale (as demonstrated in appendix E), and facilitate additional research, such as determination of the residual impact risk of the yet undiscovered asteroid population (see section F) (Stokes et al., 2003). The results in Stokes et al. (2003) also indicate that the findings in this thesis regarding best and worst case outcomes are robust as similar levels of uncertainty were found in their analysis. However, both Stokes et al. (2003) and Chapman and Morrison (1994) assign no loss potential to impactors smaller than 40 m but the results in this thesis provide evidence that this lower limit could extend to a smaller size of about 18 m.

Over 90% of all km-sized asteroids have been observed and it is clear that none of these large objects will collide with the Earth in the next century. Even though an impact of such an object would be devastating, the impact risk of these large, observed objects is

zero in the next 100 years, because no impact is predicted to occur in that timeframe. This means that most of the asteroid impact risk can mainly be attributed to smaller objects. A small portion of that risk is known with the objects that are currently listed on the NEO web pages. However, only a small fraction (<1%) of the asteroid population has been observed to date and the completeness of the asteroid catalogue is documented in Figure 4 of (Harris and D'Abramo, 2015). Thus, the overwhelming majority of the impact risk is due to the unobserved asteroid population and this is called the residual impact risk (see section F). In general, residual risk is a balance between asteroid size - there are more smaller objects and they impact more often, but cause less damage - and catalogue completeness - larger objects are easier to spot and their population is more completely observed. With the asteroid size-loss relationship, derived here, the known size-impact frequency (Harris, 2014), and asteroid completeness information, it is possible to accurately determine which size regime harbours most residual risk and similar analysis was done in previous work (Stokes et al., 2003). New telescope systems and surveys that are geared to find asteroids in the relevant size regime and, thus, reduce residual risk efficiently, can use residual risk information to justify their design choices improving their chances for funding. The current target size mandated by the United States Congress is 140 m (NASA, 2006), but it is likely that most residual risk originates from an even smaller size regime and this analysis would reveal this size based on a higher fidelity size-loss function.

To better characterize possible impact conditions, statistical distributions for impact angle and speed were derived in section 4.4.1. The results provide information about angle and speed mean values and their corresponding ranges. Interestingly, the mean impact angle did not match the analytical solution of the problem of 45 ° (Shoemaker et al., 1962) but produced a value of 42.87 ° and the reason for this lower-than-expected value begs further investigation. A possible reason for this finding is that Chesley and Spahr biased their population to reflect the impact frequencies of asteroids given their orbital speed (Chesley and Spahr, 2004). The distributions increase understanding of the nature of the impact threat and facilitate further research. Practical applications include informing disaster management stakeholders of expected impact situations, and providing relevant inputs into publicly available tools such as Collins et al. (2005).

ARMOR was designed with the intended use of on-ground risk driven asteroid deflection mission design. The underlying principle is that any deflection force that acts on an asteroid moves the projected impact point of that asteroid over Earth's surface until the asteroid misses competely. As such, ARMOR's orbital propagator can easily incorporate a variable deflection force representative of any given deflection action. To demonstrate this capability in a simulation, a weak, constant deflection force (corresponding to an acceleration of 7.7×10^{-9} m/s²), approximately normal to the ecliptic plane, was exerted on asteroid 2011 AG5 and the motion of select sample points of the impact corridor was plotted in Figure 5.1.

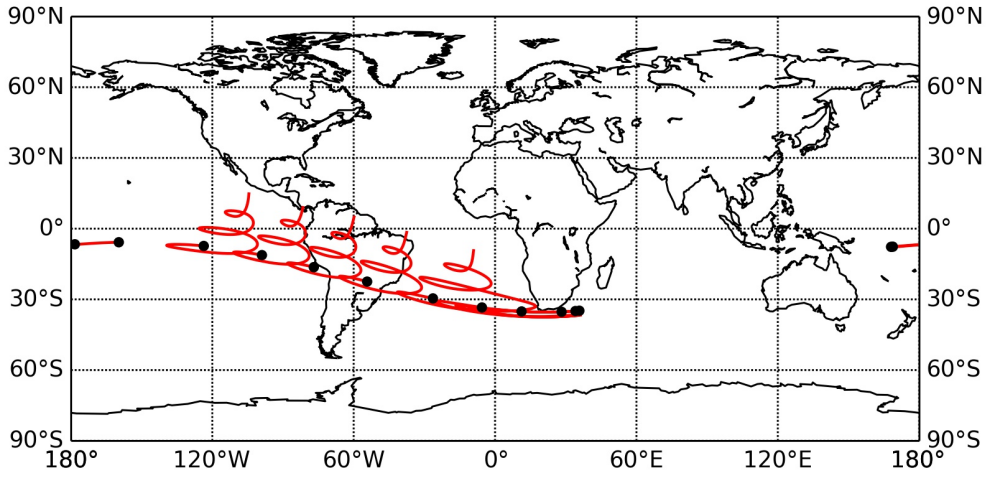

Figure 5.1: Impact point movement of asteroid 2011 AG5 under influence of a constant deflection force normal to its orbital plane.

The prevailing opinion in the planetary defense community is that deflection is most effective in, or against, the orbit direction of the asteroid and it is true that this represents the most energy efficient approach to deflection. Energy efficiency describes the achieved deflection amount per exerted deflection energy. A deflection force in, or against, the orbit direction of the asteroid would move the impact point along the impact corridor. The plot in Figure 5.1 demonstrates that the impact point of an asteroid may also be moved in other directions and this represents proof of concept that on-ground risk driven deflection mission design is feasible as the impact point could be manipulated to avoid high risk areas even if such an area is inside the original impact corridor. On-ground risk driven deflection mission design would come at an increased energy expense but would cater to the needs of the international community to safeguard their populations and might enable safer overall deflection mission design.

Any deflection mission has a chance of failing the original deflection goal of preventing a future impact by only exerting a partial deflection force (e.g. through spacecraft failure during deflection operations). In a deflection mission that is driven entirely by energy considerations, such a partial failure could mean that the projected impact point has moved from a low risk area (e.g. desert) towards a high risk area (e.g. city) and, thus, would have aggravated the threat. On the other hand, if on-ground risk is taken into consideration, a deflection mission could be devised with the intention of reducing on-ground risk as soon as deflection operations start such that the threat situation only improves over time. What is more, this approach enables deflection mission design that has partial deflection as a goal because the asteroid could intentionally be moved to a low risk impact point rather than expending additional energy to move it off the Earth.

The work presented here may be developed further in multiple ways: ARMOR's orbital propagator is a simple propagator based on gravitational attraction of the major bodies in the Solar System. The propagator's simplicity facilitates future development such as

on-ground risk driven deflection mission design. Moving forward, a higher fidelity orbital propagator could be implemented that would speed up propagation time and increase impact point prediction accuracy (see section 3.1.5). In its current state, the propagator is sufficiently accurate for the work in this thesis but higher fidelity is desirable in general terms and to increase robustness of potential risk driven deflection mission design. Furthermore, the impact probability distribution that is projected onto the surface of the Earth is based on assumptions about the nature of the line of variation (LoV). It is assumed that the LoV is approximately in line with the orbital direction of the asteroid and this assumption is true in the "vast majority of cases" (Milani et al., 2005). However, this assumption may break down in challenging cases, where the impactor has not been observed for an extended period and might have had close encounters with planetary bodies. To increase general applicability and accuracy of ARMOR, a method should be implemented that actually samples the asteroid's ephemeris uncertainty region and maps the uncertainty region onto the surface of the Earth. Furthermore, the generation of the on-ground impact probability distribution assumes constant probability distribution along the direction of the corridor and this assumption holds when the overall impact probability is low. However, as ARMOR would be used for deflection mission design, the scenario would likely feature high impact probabilities which correspond to a non-constant impact probability distribution along the corridor and this situation would have to be accounted for in future development.

The process from initial asteroid discovery to successful risk-driven deflection is outlined in Figure 5.2. ARMOR is currently in a state to perform the functional blocks inside the blue box. As such ARMOR already improves on the current state of the art (Torino, Palermo scale) in terms of asteroid risk assessment. With further work, on-ground risk deflection mission design is possible and this is represented by the feedback loop inside the red box in Figure 5.2.

On September 14th, 2016, the chief science advisor of President Barack Obama, John Holdren, addressed the moral obligation of preparing for the asteroid hazard by stating: "if we are going to be as capable a civilization as our technology allows, we need to be prepared for even those rare events, because they could do a lot of damage to the Earth." (Wall, 2016). Asteroid risk assessment using ARMOR's method is in line with this statement as it provides the best available risk estimation to date based on the accessible information and, thus, helps humanity be prepared for the asteroid hazard using current technology.

In summary, this thesis addresses the initial motivation outlined in the introduction. It provides comprehensive progress towards routine asteroid impact risk assessment and identifies benefits of findings as well as most promising development options for future development such as risk driven asteroid deflection mission design. Furthermore, the tools developed here were employed to gain insight into the nature of the asteroid impact

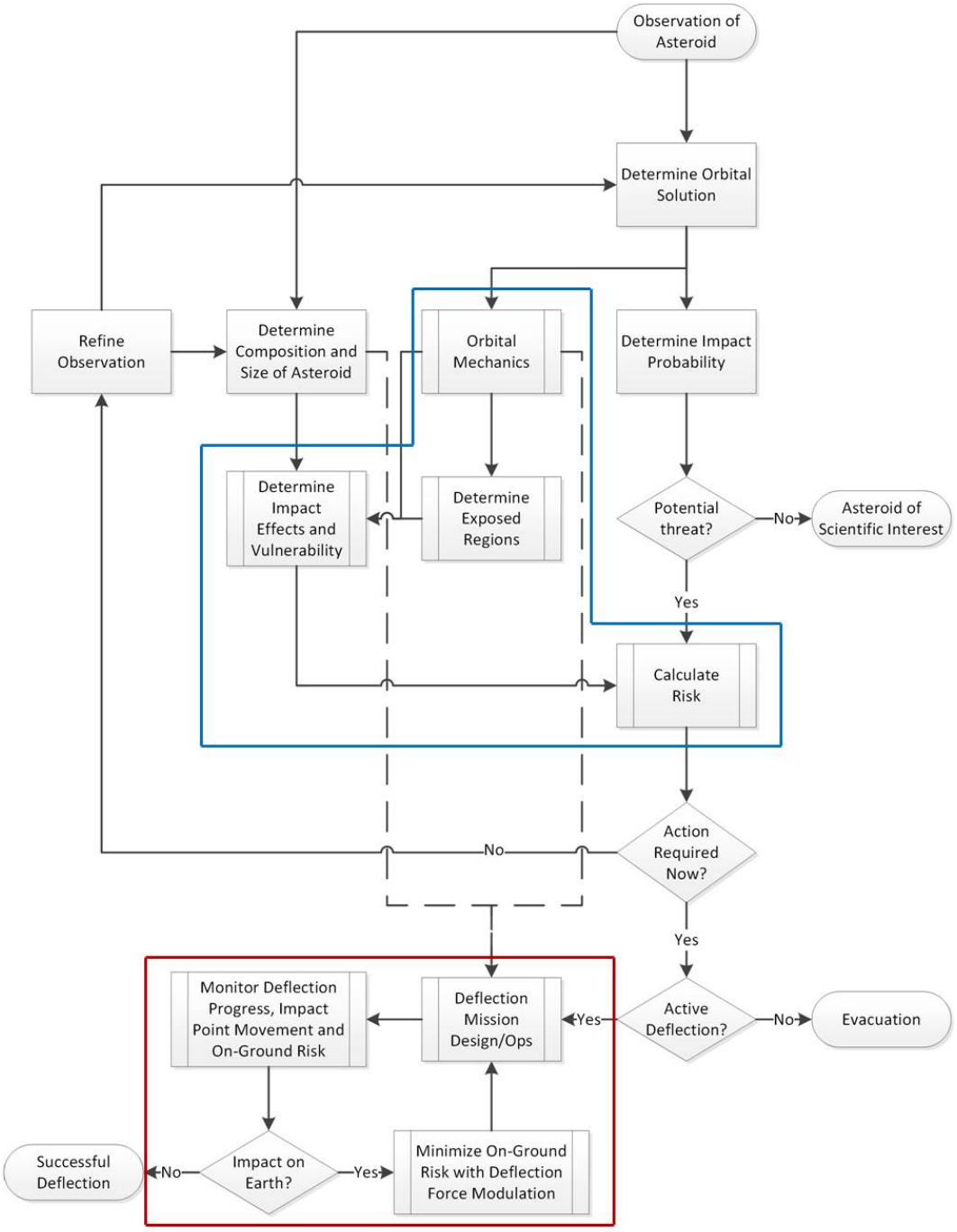

Figure 5.2: Functional description of the process from initial asteroid discovery, over risk assessment to successful risk-driven deflection mission design (red box). ARMOR currently performs tasks in the blue box.

hazard and questions in this regard raised in the introduction could be answered with these findings.

Chapter 6

Conclusions

The research presented here addresses asteroid impact risk assessment and has made several contributions to the field of planetary defense to achieve this goal.

The impact distribution of near-Earth objects has been investigated and provides, for the first time, formal, positive evidence for the assumption that impacts are distributed approximately uniformly over the globe (Rumpf et al., 2016b). Similarly, the statistical distribution of impact angles and impact speeds has been investigated and appropriate distribution functions were derived (Rumpf et al., 2017a). These distributions were used to facilitate asteroid effect dominance research and improve understanding of the impact threat.

Models to calculate the severity of impact generated effects such as wind blast, overpressure shock, thermal radiation, cratering, seismic shaking, ejecta out-throw, and tsunami are available in the literature. To relate the effect severity to the human population, vulnerability models were needed and these models were derived and are now available to the community (Rumpf et al., 2017b).

The need for high fidelity impact effect modelling became apparent in a comparative analysis between *simplified risk* (only dependent on impact location knowledge) and *advanced risk* (taking into account impact effect propagation and vulnerability calculation). The results show that advanced risk modelling is needed to address specific asteroid impact threats as risk distributions vary significantly from results obtained with the simplified approach (Rumpf et al., 2016a). The work represented here presents a suitable method and the necessary tools to achieve an adequate level of risk estimation fidelity.

ARMOR's risk estimation method was applied to calculate the full spatial risk distribution of the 2077 impact instance of asteroid 2015 RN35 (Rumpf et al., 2017b) and this method can be applied to any potentially impacting asteroid. The risk distribution conveys information about which areas are threatened by the impact in terms of how

likely they are to be hit and how severe the consequences would be. Therefore, such information enables early disaster planning and identifies regions of high risk that require special attention if the threat would become urgent.

Furthermore, the integral of the risk corridor provides the risk level as a scalar figure using the unit of expected casualties and this is useful in several ways. The total hazard magnitude of the threat can be estimated by assuming an impact probability of one and calculating the integral along the risk corridor. The resulting loss value expresses the severity that can be expected if the asteroid were to hit. If the impact probability remains unchanged, the risk value conveys the current threat level considering the available knowledge about impact probability, impact location and affected population. Using the unit of expected casualties has several advantages as it provides an intuitive way to communicate threat levels, it enables comparison of the asteroid impact threat with other natural disasters, and, thus, provides a common metric for risk mitigation resource allocation. The value of asteroid risk assessment using expected casualties as unit has been recognized by the international community and the work has been presented at the 6th SMPAG meeting at the United Nations in Vienna to facilitate asteroid threat response protocol definition.

Using ARMOR, it was possible to gain unique insights into the harmful processes delivered by an asteroid impact (Rumpf et al., 2017a). In extensive simulations, the loss generation of 50,000 artificial impactors was analysed to determine which impact effects are dominant in affecting the human population in the impactor size range of 0-400 m. The results show that aerothermal effects are most severe and that an impactor over land is approximately one order of magnitude more dangerous than its equivalent over water. The danger of tsunamis is understood least in the field and the results here indicate that they contribute only moderately to overall loss.

The impact effect analysis also provided average loss numbers per impactor of a given size up to 400 m and this loss estimation is the most thorough size-loss relationship provided to date (Rumpf et al., 2017a). One application for the relationship is fast threat characterisation for newly discovered asteroids because an asteroid size estimate is a characteristic that is known early after initial discovery. Additionally, the size-loss relationship enables determination of the size of asteroids that should be targeted by telescopes and surveys to efficiently reduce the residual asteroid impact risk of the, yet, undiscovered asteroid population (Appendix F).

In summary, the work in this thesis provides a comprehensive framework which applies the concept of risk to the asteroid impact hazard. It improves comprehension of the hazard by achieving comparability with other natural disasters with positive implications for threat communication and hazard response planning. The work has added knowledge to the nature of the impact hazard (impact distribution, expected impact situation

and loss, dominant impact effects) and to risk assessment aspects (modelling fidelity, vulnerability models).

Chapter 7

Future Work

In the future, ARMOR can be applied to on-ground risk driven asteroid deflection mission design. Until now, mission design has aimed to achieve energy-optimal deflection. However, the international community has identified the need for risk driven mission design as non-technical aspects are a concern when mitigating the risk of an incoming asteroid. An energy-optimal approach can aggravate the threat situation if the mission is only partially successful. On the other hand, a risk driven mission which can be achieved using ARMOR could aim to reduce risk continuously until complete deflection is achieved.

The Torino and Palermo scale are currently in use to quantify the threat level of threatening asteroids. These scales are suitable for relative risk analysis expressing if one asteroid is more threatening than another. However, they do not calculate impact consequences directly, using kinetic energy as a proxy instead, and thus only have limited value in predicting the severity of an impact. The risk methodology presented here rectifies these shortcomings and could form the basis for a new asteroid hazard scale (see appendix E).

While analysis presented in this work suggests that the impact location distribution of NEOs is approximately uniform, further work could address the underlying mechanics that result in this distribution. Aspects to consider in this respect are gravitational focusing, the obliquity of the Earth, as well as the the general orbital situations of the Earth and the asteroids.

In summary, the framework presented here can be the basis for a new asteroid risk scale as well as risk driven asteroid deflection mission design. It can also be utilized to further investigate the contributing factors to a near-uniform impact location distribution on the Earth.

Appendix A

Asteroid Table

This appendix provides data on the asteroid sample that was used to generate the results in section 4.1. It should be noted that asteroid diameters are derived based on absolute magnitude estimates and are subject to considerable uncertainties (roughly ±50 %) due to uncertainties in the albedo value used in Equation 2.1.

Asteroid Name	**Diameter [m]**	**Impact Date**	**Impact Probability**
2010GM23	341	14/04/2099	0.000002
		14/04/2099	4.92E-07
		13/04/2096	2.36E-06
2008YO2	40	24/12/2079	1.27E-06
		23/12/2092	2.47E-07
		24/12/2094	1.25E-07
1999RZ31	80	05/09/2056	3.91E-07
2006SC	40	13/09/2064	1.14E-07
2007XZ9	50	28/11/2068	7.38E-05
2007DX40	55	18/08/2062	0.000012
2008CC71	50	27/02/2034	3.17E-06
		26/02/2041	2.60E-06
		27/02/2055	1.45E-06
		27/02/2066	9.32E-05
		27/02/2067	1.06E-06
2008XC1	85	17/12/2085	1.34E-07
2008KO	55	02/06/2049	5.65E-07
		02/06/2061	3.43E-07
2006HF6	55	19/04/2070	2.56E-06
		19/04/2070	1.20E-06
		19/04/2070	2.12E-06
		19/04/2070	7.08E-07

		18/04/2053	4.95E-08
2008EX5	80	09/10/2072	0.000017
		08/10/2068	5.62E-07
		09/10/2071	7.71E-06
		08/10/2072	7.15E-07
		09/10/2074	6.18E-08
		09/10/2075	1.56E-08
		09/10/2079	6.38E-08
		09/10/2081	4.33E-08
		09/10/2082	4.49E-08
		09/10/2083	1.48E-05
		08/10/2084	1.42E-08
2006BC8	40	23/01/2081	1.52E-07
		25/07/2088	4.95E-07
		23/01/2096	1.58E-08
1994GK	65	03/04/2058	3.46E-07
		04/04/2039	1.89E-07
		03/04/2070	3.81E-07
2010WC9	95	16/05/2027	3.03E-06
		15/05/2082	1.60E-08
		15/05/2086	3.06E-07
2006QV89	35	09/09/2019	3.77E-05
		08/09/2023	5.35E-07
		08/09/2024	7.66E-08
		08/09/2028	1.04E-07
		08/09/2033	1.99E-08
2007KE4	40	26/05/2029	9.22E-06
		26/05/2091	1.11E-06
2000SB45	55	08/10/2080	2.86E-05
		08/10/2074	2.20E-07
		08/10/2078	1.35E-06
		08/10/2079	2.81E-06
		08/10/2078	1.35E-06
		08/10/2081	1.18E-07
		08/10/2081	5.20E-06
		08/10/2082	2.38E-07
		08/10/2082	2.43E-06
		08/10/2084	1.65E-06
		08/10/2084	1.73E-05
		08/10/2085	6.16E-06
		08/10/2085	2.38E-07

		08/10/2087	3.47E-07
		08/10/2087	6.98E-07
		08/10/2088	5.13E-07
		08/10/2088	6.92E-06
		08/10/2088	1.05E-06
		09/10/2091	3.81E-08
		09/10/2091	2.69E-07
		08/10/2093	1.25E-06
		08/10/2096	6.36E-06
		08/10/2074	1.85E-06
		08/10/2082	8.06E-07
		08/10/2097	4.14E-07
1996TC1	80	25/09/2064	5.03E-08
		26/09/2067	6.37E-07
2014GN1	55	16/09/2061	9.90E-06
2002XV90	35	11/12/2078	3.40E-09
2011UM169	40	23/10/2099	6.19E-08
2001SB170	145	17/03/2069	4.92E-10
		17/03/2074	1.10E-09
		17/03/2089	4.24E-08
2002MN	85	14/06/2068	1.26E-08
		15/06/2071	1.49E-06
		16/06/2074	1.16E-06
		14/06/2085	6.09E-10
1995CS	35	03/02/2061	1.53E-07
2008ST7	70	10/09/2074	3.59E-07
		09/09/2080	3.27E-08
		10/09/2079	3.53E-08
		09/09/2094	1.12E-06
		10/09/2094	9.03E-06
		10/09/2094	9.60E-06
2010CA	55	07/08/2022	2.91E-06
2009WQ25	80	27/10/2094	8.28E-08
		03/11/2051	1.07E-11
2003UQ25	70	17/03/2093	1.39E-07
2014OO6	115	11/01/2051	5.35E-07
		12/01/2054	9.56E-06
		12/01/2067	2.66E-06
		12/01/2067	6.37E-07
		12/01/2068	9.94E-08
		12/01/2084	3.31E-06

		12/01/2084	3.27E-08
		12/01/2093	9.69E-09
		12/01/2099	9.39E-09
2014QF33	85	17/08/2082	9.09E-08
		16/08/2076	4.89E-08
2005ED224	65	11/03/2018	4.06E-07
		10/03/2064	3.07E-07
2011VG9	180	01/11/2086	1.44E-07
		01/11/2086	1.09E-07
		01/11/2097	2.33E-09
2008KN11	105	20/06/2046	4.02E-08
2014FX32	45	12/03/2090	1.38E-07
		12/03/2076	1.18E-05
2014KC46	130	10/11/2091	1.20E-07
2010QG2	38	05/09/2051	2.59E-06
		05/09/2062	1.01E-07
		05/09/2070	1.67E-08
2013HT150	35	19/10/2052	2.23E-07
		20/10/2088	7.71E-08
		20/10/2088	3.56E-08
		19/10/2088	4.43E-07
		20/10/2090	1.83E-08
		20/10/2090	2.06E-07
		20/10/2091	9.02E-07
		19/10/2093	5.14E-06
		20/10/2095	4.10E-09
2002RB182	115	06/10/2076	3.84E-08
		07/10/2088	1.45E-07
		08/10/2092	1.19E-08
2014NZ64	155	17/09/2053	3.26E-09
		17/09/2072	2.92E-10
		17/09/2072	2.00E-09
		17/09/2072	1.75E-09
2005QK76	40	26/02/2030	3.06E-05
		26/02/2048	3.45E-06
		26/02/2038	1.46E-05
		26/02/2048	1.28E-05
2009CZ1	55	19/02/2058	4.26E-07
2001SD286	35	23/09/2080	2.32E-08
2008LG2	40	19/06/2070	7.82E-08
		17/06/2078	3.91E-09

2002VU17	50	16/11/2084	5.74E-06
		16/11/2084	2.23E-07
		17/11/2099	4.70E-06
		17/11/2099	6.20E-06
2009HC	50	11/04/2095	2.20E-08
2008UB7	80	31/10/2049	2.43E-07
		31/10/2060	7.97E-05
		31/10/2060	9.62E-05
		31/10/2060	8.94E-06
		01/11/2063	5.76E-07
		01/11/2063	4.29E-07
		31/10/2064	2.44E-07
		01/11/2070	1.68E-08
		01/11/2071	1.17E-06
		01/11/2063	4.29E-07
		01/11/2081	2.01E-08
		01/11/2082	6.10E-08
		31/10/2084	3.98E-08
		01/11/2086	1.72E-05
		01/11/2087	2.41E-08
		01/11/2089	7.65E-07
		31/10/2060	4.21E-05
2009UB7	80	31/10/2060	9.43E-05
2007WP3	95	11/11/2098	4.86E-07
2007VE8	35	06/11/2062	7.07E-05
2008FF5	115	27/03/2060	4.27E-07
2011CU46	35	12/08/2042	1.38E-07
		13/08/2043	4.20E-09
		12/08/2083	1.15E-06
		12/08/2084	8.84E-09
		08/02/2085	2.17E-09
		12/08/2087	1.01E-08
		12/08/2091	1.32E-08
		12/08/2091	8.27E-07
		12/08/2091	6.10E-07
		09/02/2092	1.02E-07
		09/02/2096	3.25E-07
2014UX34	165	15/04/2082	3.05E-06
		15/04/2073	5.48E-09
		15/04/2082	2.73E-06

2013RR43	35	08/09/2050	1.42E-07
2004VZ14	35	01/11/2076	4.44E-07
1994WR12	185	24/11/2067	8.94E-07
		24/11/2067	8.31E-07
		24/11/2067	5.82E-07
		24/11/2068	4.80E-09
		24/11/2069	1.22E-06
		24/11/2070	3.93E-09
		24/11/2071	5.76E-07
		24/11/2071	1.49E-06
		24/11/2072	4.63E-07
		24/11/2072	3.18E-08
		24/11/2073	2.48E-06
		24/11/2073	5.32E-06
		24/11/2073	7.56E-07
		24/11/2073	1.10E-06
		24/11/2075	2.12E-07
		24/11/2077	3.77E-07
		24/11/2078	1.20E-07
		24/11/2081	4.29E-07
		24/11/2083	8.27E-08
		24/11/2083	8.24E-10
		24/11/2085	1.04E-07
		24/11/2085	5.16E-09
		24/11/2055	7.19E-07
		24/11/2071	1.30E-06
2012ES10	80	05/03/2059	6.56E-07
2009FG	35	02/03/2036	2.81E-08
		02/03/2044	3.55E-09
		24/12/2066	1.88E-06
		24/12/2077	3.20E-06
		24/12/2091	5.23E-08
2014GY44	35	29/03/2080	8.83E-08
		02/10/2083	1.16E-07
2009OW6	35	20/08/2080	1.33E-05
2012QD8	115	08/03/2047	4.46E-06
		08/09/2092	1.40E-08
2002CB19	45	10/08/2049	5.11E-08
2000SG344	50	13/09/2072	0.000741
		17/09/2070	0.000244
		08/09/2072	0.000072

		10/09/2071	6.02E-05
		10/02/2074	1.76E-05
		07/08/2091	3.09E-06
		09/08/2092	1.75E-06
		04/08/2093	3.87E-06
		24/08/2096	7.28E-06
		27/08/2097	9.70E-06
		07/09/2097	1.11E-06
2005WG57	85	21/08/2029	2.73E-07
		23/08/2087	7.15E-09
		22/08/2087	9.81E-08
2009BR5	180	21/07/2059	1.32E-07
2005XA8	30	05/12/2069	7.55E-06
		06/12/2071	2.41E-06
		05/12/2073	2.72E-07
		06/12/2074	1.62E-06
		05/12/2076	0.000016
		06/12/2077	1.88E-07
		06/12/2079	6.56E-07
		05/12/2080	3.57E-07
		06/12/2081	3.42E-07
		05/12/2081	1.98E-07
		06/12/2082	2.10E-08
		06/12/2083	1.18E-06
		06/12/2086	1.05E-05
		05/12/2085	1.79E-07
2012EK5	35	24/03/2090	2.13E-07
		24/03/2095	2.08E-06
		24/03/2095	1.58E-05
		24/03/2095	7.45E-06
2009DE1	65	18/08/2099	1.30E-09
2009FJ	50	13/03/2088	1.24E-07
2012TV	40	03/04/2070	4.26E-07
		03/04/2070	4.14E-07
		02/04/2085	1.89E-08

Table A.1: This table contains details about the assessed virtual impactors. The table provides information about the asteroid name, the approximate diameter, possible impact dates and the corresponding impact probabilities.

Appendix B

Coordinate and Time Systems

This chapter will focus on the description of coordinate and time systems. It will also provide the transformations between the different systems. The symbols used to denote bodies in the solar system are listed in table 3.1.

B.1 Time Systems

Over the centuries, a multitude of time systems has been developed. The systems used in this work are Universal Time and Julian Day. These systems are based on the natural duration of an Earth day corresponding to the time Earth takes to complete one rotation with respect to the Sun. Earth's rotational period changes over time and, thus, the duration of one day changes. In contrast, the International Atomic Time is based on the fixed duration of one standard second. Even though Universal Time and Julian Day are of more direct applicability to this work, the International Atomic Time shall be mentioned here to provide more context for time systems.

B.1.1 International Atomic Time

Historically, time was measured by observing the change of seasons during a year and position of Sun during a day. Today, it is known that seasons exist due to the motion of Earth around the Sun in conjunction with the fact that the rotational axis of Earth is tilted with respect to the ecliptic plane. The ecliptic plane is the plane in which the orbit of the Earth lies. As time measurements became more accurate, it was discovered that the motion of Earth is in fact irregular (Wertz et al., 2011) and, thus, the length of one Earth day varies. However, especially in Physics applications, it is necessary to have a regular measurement of time which means that one second always has the same duration. Consequently, a new basis for the measurement was found. Today, one SI

standard second corresponds to 9,192,631,770 periods of radiation emitted by Cesium-133 at mean sea level as it transitions from one specific isotope to another. International Atomic Time (TAI) is defined by this standard second and is used for extremely precise time keeping.

B.1.2 Universal Time

Universal Time (UT) orients itself along the duration of the Earth day. Practically speaking, 12:00 UT (noon) is always the point in time when the Sun is in zenith and 00:00 UT (midnight) describes the time when the observer's side of Earth faces directly away from the Sun. Since the rotation of Earth is irregular, the period of one Earth day changes accordingly. This means that one day measured in UT does not necessarily last $24 \times 60 \times 60 = 86400$ standard seconds and, consequently, TAI and UT drift apart as time passes.

B.1.3 Universal Time Coordinated

Universal Time Coordinated (UTC) attempts to follow Universal Time, that is, it is determined by the length of an Earth day but it incorporates the standard second. However, one standard second has the constant length that is defined for TAI and UT allows for variable time durations. This apparent contradiction is solved by means of the leap second. Since Universal Time drifts away from TAI, a leap second is added[1] when the difference between UT and UTC becomes larger than 0.9 seconds to align UT and UTC. At the time of this writing, 25 leap seconds have been added. The future additions of leap seconds cannot be predicted because the future evolution of Earth rotation period is yet unpredictable.

B.1.4 Sidereal Time

Sidereal Time is defined by the inertial orientation of the Earth. One sidereal day passes when Earth completes exactly one rotation. This implies that one sidereal day is slightly shorter than an Earth day because of Earth's motion around the Sun. One sidereal day is roughly 23 hours and 56 seconds during which Earth rotates 360 ° in an inertial reference frame. Sidereal time is commonly expressed as an angle. It signifies the angle between vernal equinox and 0 ° longitude. This relationship is depicted in Figure B.4 where Θ is the sidereal angle.

[1] In theory, a leap second can also be subtracted but this has not happened to date.

B.1.5 Julian Day

The Julian time system counts the number of days starting at 12:00 UT on January 1st, 4713 BC. Compared to time systems that make use of individual components such as hours, minutes and seconds, the Julian system is easier to utilize in computations because it is only one number. One particularity is that a new Julian day starts at midday UT time. Thus, at midnight UT, half a Julian day has passed. For example, 00:00 UT of January 1st, 2014 is the Julian day 2456658.5. The system is designed by astronomers who were mostly located in the northern hemisphere, more specifically Europe, at the time of its inception in the year 1583 AD. For these astronomers, the system had the advantage that the day did not change during their observations at night (Wertz et al., 2011) making record keeping easier. The software developed during this research project utilizes the Julian Day.

B.2 Coordinates

It is sound practice to choose specific coordinate systems depending on the current application. This section describes the coordinate systems that were used in this research project.

B.2.1 Barycentre Inertial Coordinate System

In correspondence to the standards set by the International Astronomical Union, the fundamental coordinate system used in this work is closely related to the International Celestial Reference Frame (ICRF). The solar system propagator is operated in an inertial coordinate system centred at the barycentre of the solar system. The reference epoch for this system is J2000.0. The system's z-axis is parallel to Earth's rotational axis pointing North and the x/y-plane lies in the equatorial plane of Earth at epoch J2000.0. To fix the attitude of the reference frame, the x-axes is defined to point at vernal equinox. Vernal equinox is defined as the intersection line of the orbital plane and the equatorial plane of Earth at epoch. The intersection line is the line of vernal equinox and has historically pointed at the first point of Aries[2] Υ. The z-axis completes the right-handed coordinate system. Figure B.1 visualizes this concept. The Barycentre Inertial Coordinate System is abbreviated as BIQ and it is denoted by the superscript b because it originates from the barycentre.

[2]The equatorial plane changes orientation according to the tumbling motion of Earth's rotational axis. Consequently, the time and orientation of vernal equinox varies slightly from year to year. And today, vernal equinox has moved away from the first point of Aries considerably.

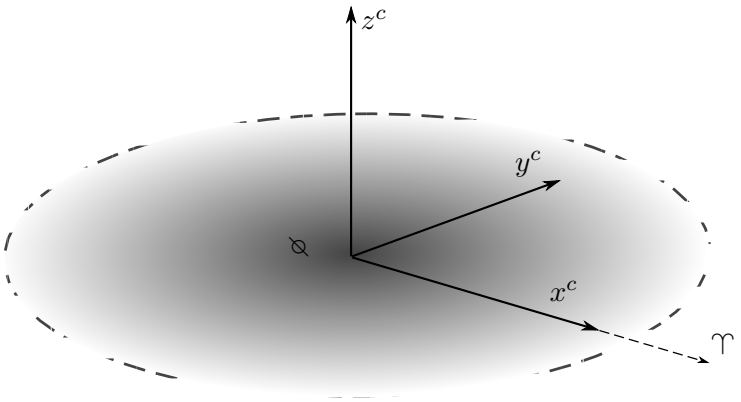

Figure B.1: The equatorial coordinate system located at the Solar System's barycentre. The shaded plane is the equatorial plane and the x-axis points towards Aries.

B.2.2 Ecliptic Barycentre Inertial Coordinate System

The ecliptic system is of relevance when initial ephemeris are provided in this frame. In this case, the ephemeris have to be transformed into the software's equatorial system. Ecliptic and equatorial coordinates differ in the orientation of their x/y-axes planes. In the equatorial system, this plane is parallel to Earth's equatorial plane while it is parallel to the ecliptic plane in the ecliptic system. A simple rotation suffices to transform one system into the other and it is described in section B.2.4. The ecliptic barycentric inertial coordinate system is abbreviated as BIC and denoted with a superscript c in formulas.

B.2.3 Earth Centred Equatorial System

The Earth Centred Equatorial System coordinate system is fixed within Earth and rotates with it. Its origin is located in the centre of the Earth which is defined as the intersection of Earth's rotational axis and the equatorial plane.

B.2.3.1 Euclidean System

Its x-, and y-axis lie in the equatorial plane with the x-axis pointing towards the prime meridian that runs through Greenwich. The z-axis completes the right-handed coordinate system and is parallel to Earth's rotational axis. The Earth Centred Equatorial System will be abbreviated as ECQ and denoted by the superscript q because it lies in the e**q**uatorial plane.

B.2.3.2 Spherical System

For terrestrial applications, the spherical realisation of the ECE system is employed. In this system, the coordinates of Longitude, Latitude and Altitude identify a point in space. Longitude is the angle between the prime meridian plane and the radial vector from Earth centre towards the point in question. This angle is positively counted towards East from the prime meridian plane. Latitude is the angle between the equatorial plane and the radial vector towards the point in question. Altitude is defined as the radial distance between the surface of the spherical Earth and the point in question.

B.2.4 Impact Latitude and Longitude

The following procedure describes how impact latitude and longitude are obtained from asteroid and Earth coordinates at the time of impact. Initial ephemeris were occasionally provided in the BIC frame and this is why the following procedure starts in the BIC frame. In this case, the coordinates have to be rotated into an equatorial frame to retrieve the impact latitude and longitude. The rotation is described in step two of the procedure. If the initial coordinates are already provided in an equatorial frame, step two is omitted. The formalism in step one is equally valid in an equatorial system.

The transformation was accomplished following these steps:

1. The BIC system is centred at the barycentre of the solar system. Therefore, the position vectors of Earth $\boldsymbol{r}^c_{\Qoppa\earth}$ and the asteroid at the time of impact are relative to the barycentre. The position of the asteroid at the time of impact is the impact location $\boldsymbol{r}^c_{\Qoppa\maltese}$. The position of impact relative to the centre of Earth $\boldsymbol{r}^c_{\earth\maltese}$ was obtained with the following subtraction:

$$\boldsymbol{r}^c_{\earth\maltese} = \boldsymbol{r}^c_{\Qoppa\maltese} - \boldsymbol{r}^c_{\Qoppa\earth} \tag{B.1}$$

2. The impact position vector needed to be transformed into the equatorial system ECQ. The attitude of BIC and ECQ are related by a simple rotation around the common x-axis. The rotation angle is the tilt angle of Earth's rotational axis with respect to the ecliptic's plane normal direction $\epsilon_{\earth}$. Figure B.2 depicts the relative position and attitude of BIC and ECQ.

   The direction cosine matrix (DCM) that transforms a BIC based vector into a ECQ based vector is defined as:

$$\boldsymbol{R}^{qc} = \begin{bmatrix} 1 & 0 & 0 \\ 0 & \cos\epsilon_{\earth} & \sin\epsilon_{\earth} \\ 0 & -\sin\epsilon_{\earth} & \cos\epsilon_{\earth} \end{bmatrix} \tag{B.2}$$

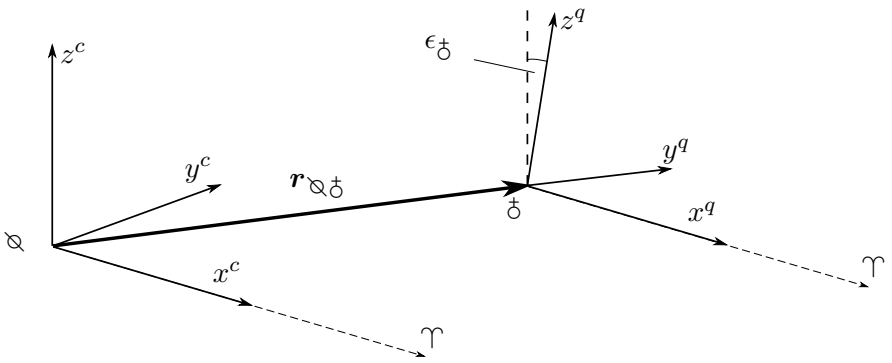

Figure B.2: The relative positions and attitude of BIC (superscript c) and ECQ (superscript q).

It should be noted that $\epsilon_{\text{♁}}$ in equation B.2 describes a rotation in the negative direction around the x-axis. Thus, for further calculation, the value $\epsilon_{\text{♁}}$ has to be negative. The impact position vector in ECQ coordinates is calculated as:

$$\boldsymbol{r}^q_{\text{♁}✠} = \boldsymbol{R}^{qc}\boldsymbol{r}^c_{\text{♁}✠} \tag{B.3}$$

3. The impact position vector was normalized according to:

$$\hat{\boldsymbol{r}}^q_{\text{♁}✠} = \frac{\boldsymbol{r}^q_{\text{♁}✠}}{|\boldsymbol{r}^q_{\text{♁}✠}|} \tag{B.4}$$

In accordance with Figure B.3, the latitude of the impact location Φ follows a sinus relationship to the z-component of $\hat{\boldsymbol{r}}^q_{\text{♁}✠}$.

$$\Phi = \sin^{-1}\hat{r}^q_{\text{♁}✠,z} \tag{B.5}$$

4. The derivation of longitude from the position vector is more complex because it is time dependent. One crucial part of the longitude derivation is knowledge of the Greenwich sidereal time at impact. (Curtis, 2012) provides excellent guidance on the transformation of UT to sidereal time. Universal time needs to be transformed into Julian date (JD) according to this equation:

$$JD = J_0 + \frac{UT}{24} \tag{B.6}$$

Here, J_0 is the Julian date at midnight UT of the given date and UT is the Universal time hour number. The latter can be obtained using Equation B.7 where hh, mm and ss are the hours, minutes and seconds respectively.

$$UT = hh + \frac{mm}{60} + \frac{ss}{3600} \tag{B.7}$$

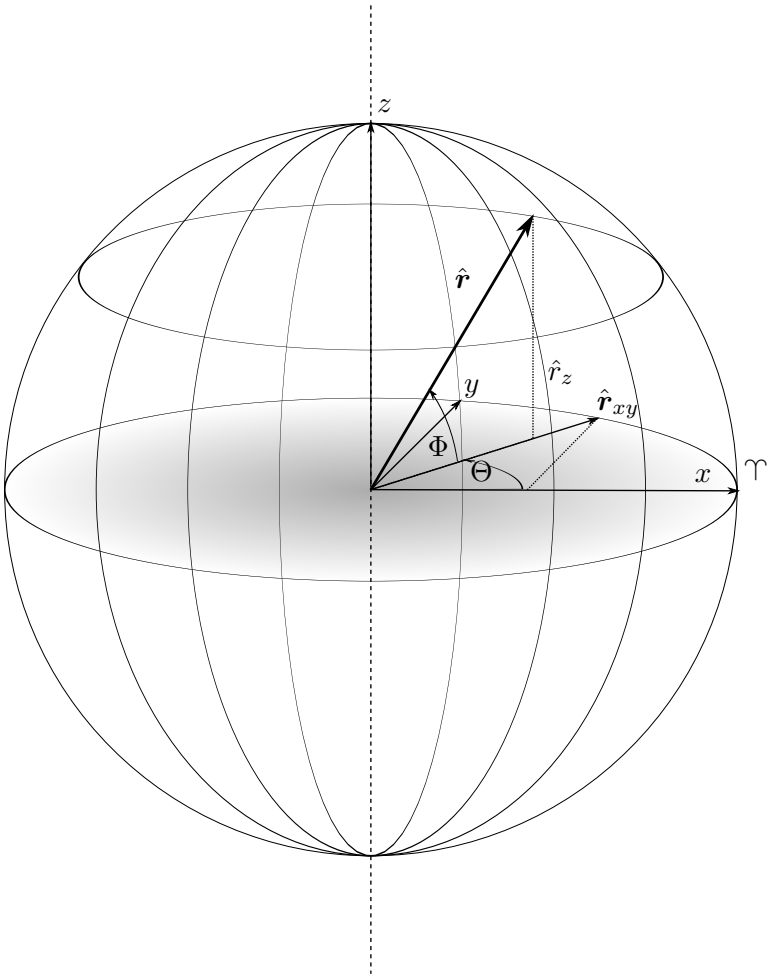

Figure B.3: Latitude Φ and sidereal time angle Θ deduction from the position vector $\boldsymbol{r}$. The shaded plane is the equatorial plane and the x-axis points towards the vernal equinox.

J_0 is obtained following an approximation provided in (Boulet, 1991). The relationship is:

$$J_0 = 367a - INT\left[\frac{7\left[a + INT\left(\frac{m+9}{12}\right)\right]}{4}\right] + INT\left(\frac{275m}{9}\right) + d + 1721013.5 \quad \text{(B.8)}$$

In this equation, a, m and d are years, months and days respectively. The function $INT()$ returns the integer part of a number without rounding. Relationship B.8 is valid in the period from 1901 until 2099. (Seidelmann, 1992) provides a formula that returns the sidereal time Θ_{G_0} in angular degrees for Greenwich 00:00 UT at a given Julian century T_0. Note that Equation B.9 may return Θ_{G_0} outside the interval $[0; 360]$. In this case, Θ_{G_0} has to be reduced to a value within $[0; 360]$ by subtracting integer multiples of 360.

$$\Theta_{G_0} = 100.4606184 + 36000.77004T_0 + 0.000387933T_0^2 - 2.583(10^{-8})T_0^3 \quad \text{(B.9)}$$

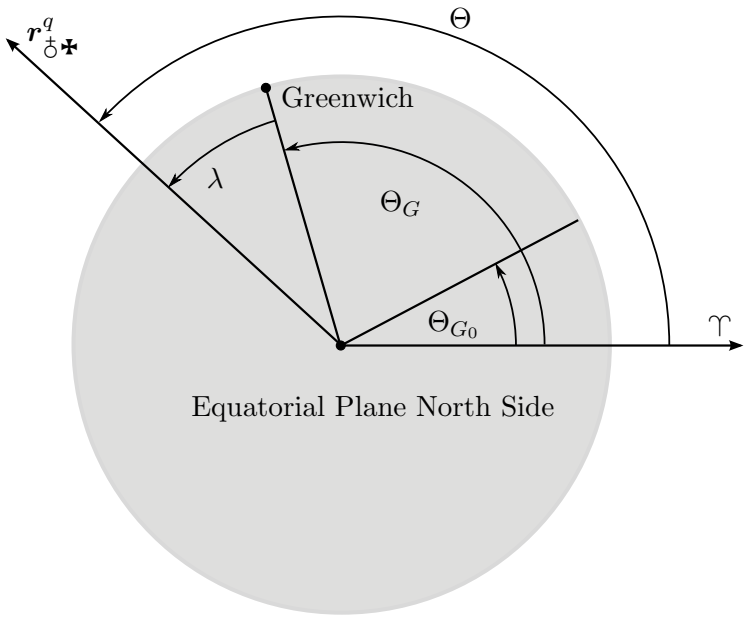

Figure B.4: Relation between sidereal time and longitude. The centre of the equatorial plane is the North Pole seen from above.

Equation B.9 is based on epoch J2000.0 and a Julian century T_0 after this epoch is defined as:

$$T_0 = \frac{J_0 - 2451545}{36525} \tag{B.10}$$

The Greenwich sidereal time in angular degrees at the time of impact was obtained using the following relationship:

$$\Theta_G = \Theta_{G_0} + 360.98564724\frac{UT}{24} \tag{B.11}$$

Similarly to B.9, Θ_G needs to be reduced to lie within $[0; 360]$. Figure B.4 depicts the geometric dependencies of the previous equations and also applies to the next equations.

The impact longitude can now be calculated using the impact position vector in ECQ coordinates. Longitude is measured in the equatorial plane which encompasses the x- and y-axis of the ECQ frame. The position vector is projected on the equatorial plane and normalized:

$$\hat{\boldsymbol{r}}^q_{\ddagger\mathfrak{O}\maltese,xy} = \frac{\boldsymbol{r}^q_{\ddagger\mathfrak{O}\maltese,xy}}{\sqrt{{r^q_{\ddagger\mathfrak{O}\maltese,x}}^2 + {r^q_{\ddagger\mathfrak{O}\maltese,y}}^2}} \tag{B.12}$$

The x component of $\hat{\boldsymbol{r}}^q_{\ddagger\mathfrak{O}\maltese,xy}$ is $\hat{r}^q_{\ddagger\mathfrak{O}\maltese,xy,x}$. This value is in a cosine relationship with the local sidereal time angle Θ:

$$\Theta = \cos^{-1} \hat{r}^q_{\ddagger\mathfrak{O}\maltese,xy,x} \tag{B.13}$$

As can easily be seen in Figure B.4, the longitude of the impact point is given by:

$$\lambda = \Theta - \Theta_G \tag{B.14}$$

Appendix C

Impact Effect Sensitivity to Impact Speed and Angle

The sensitivity of impact effects to impact angle and speed became a subject of curiosity during the development of ARMOR and this section is dedicated to this analysis. The analysis was facilitated by the need for a more efficient programming approach as described in the following.

During the analysis, it became evident that the computational burden to calculate impact effects is unacceptably high even when utilizing purely analytical models. The reason for the high computational demand is that each impact corridor is made up of tens of thousands of impact points for which impact conditions differ (angle and speed). Impact effect simulations have to be conducted for each impact point. What is more, the simulated impact effects propagate in an area of few thousand cells around each impact point. The result is that impact effect calculations have to be conducted to millions of impact cell for each VI. In the first iteration of model implementation, the calculation of one impact took 30 sec. After implementing faster and smarter computational techniques such as the interpolation scheme described below, the computational time could be reduced to 0.015 sec per impact point.

To speed up the computations of impact effects, a 2D interpolation scheme is employed that approximates the impact effects for a given pair of impact speed and angle. In order to find a suitable interpolation scheme, a sensitivity analysis of the impact effects with respect to impact angle and speed was conducted. Figure C.1 shows the surface that describes the wind speed generated by an impact of a 200 m asteroid at a distance of 50 km as a function of impact speed and angle.

To generate the surface, the impact corridor of 2000SG344 was analysed. The impact speeds and angles that are ticked in the figure represent the range of values that occurred along the impact corridor. Wind speed was insensitive to the variation of impact speed

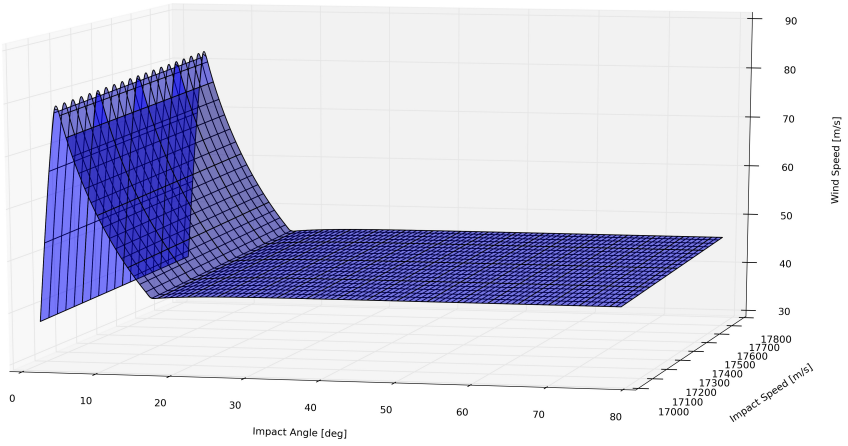

Figure C.1: Wind speed generated by an impact of a 200 m asteroid in a distance of 50 km as a function of impact speed and angle. The plot actually shows two surfaces: One represents data obtained with the impact wind speed model and the other one is the interpolated surface. Both surfaces agree sufficiently well with each other.

that was experienced along this impact corridor. Closer analysis revealed that wind speed continuously increases with higher impact speed. This is consistent because higher impact speeds deliver higher impact energy. However, the dependency was weak over the impact speed range of 850 m/s and it is expected that this impact speed variation is representative for other impact corridors.

In contrast, wind speed showed high sensitivity to the impact angle variation of 77 °. Wind speed experienced a peak between 0 ° and 18 ° and formed a smoothly increasing surface for higher angles. The reason for this behaviour is that the asteroid experiences an airburst for shallow impact angles and impacted the ground at steeper angles. A shallow impact angle, allows the asteroid to spend sufficient time in the atmosphere to experience an airburst before impacting the ground.

There is an "optimal" impact angle of about 5 ° where impact energy is most efficiently transformed into wind speed. At impact angles <5 °, the asteroid dissipates much of its energy in the thin upper atmosphere, and thus, the remaining kinetic energy is decreased and air burst wind speeds are low. for angles >5 °, the asteroid penetrates deeper into the atmosphere but loses energy through drag in the lower, denser parts of the atmosphere. A ground impact occurs for angles >18 °. Wind speeds increase with higher impact angles because the asteroid passes through the atmosphere quicker and has less time to dissipate energy through drag, thus, delivering more energy to the ground.

In addition to helping understand impact effect sensitivity to impact angle and speed, Figure C.1 also demonstrates good accuracy of the spline interpolation scheme. The

figure actually shows two surfaces - one representing the model data and the other representing the interpolated data. However, the surfaces are almost indistinguishable because they are in very good agreement corresponding to a RMS difference of 5.821×10^{-15} m/s which demonstrates validity of the interpolation scheme.

When impact speed is at the tipping point of producing an airburst or ground impact, it is generally possible that instead of the impact angle, impact speed is the more sensitive parameter. However, the chosen interpolation scheme is robust against changing the sensitive dimension of the interpolation parameters and it is expected that the interpolation scheme performs equally accurately in either scenario.

Appendix D

Deflection Technology

As the observational capacities improve, it is a matter of time until an asteroid is discovered that will collide with the Earth. In this case, it has to be decided if and how the asteroid should actively be deflected. The following sections present some of the possible methods by which an asteroid could be deflected.

D.1 Fast Deflection Methods

Deflection methods can generally be categorized into slow and fast deflection methods. This section describes fast deflection methods where strong deflection forces act in a short time.

D.1.1 Kinetic Impactor

The kinetic impactor deflection concept imparts a velocity change on the asteroid by colliding an impactor with it at high speed. The deflecting impulse is conveyed during the collision. Both, mass and speed are the primary parameters that determine the magnitude of the deflection impulse. The impactor is placed on a collision trajectory with the asteroid that yields a high relative velocity at the time of impact. This concept has been applied in the Deep Impact mission mentioned in section 2.2.2. In contrast to all other methods, this method thus has some proof of concept associated with it. The theory of kinetic impactors has been studied by many, including (McInnes, 2004; Dachwald et al., 2007; Izzo et al., 2006). One aspect in the theory that lacks sufficient research is the so called factor of restitution. The change in speed attributed to simple linear momentum transfer in a collision ($m_1 v_1 = m_2 v_2$) only accounts for an insignificant fraction of the kinetic energy carried by the impactor. The overwhelming majority of the available energy is transformed into explosive deformation of the impactor and asteroid

as well as heat and light. This process also produces ejecta that enhances the effect of collisional linear momentum transfer. The factor of restitution describes what multiple of the change in speed due to linear momentum transfer is achieved by the actual collision process. More research such as (Durda et al., 2011) is needed to better understand, characterize and facilitate predictability of this important contribution. The factor of restitution is crucial to accurately predict the outcome of a deflection mission using a kinetic impactor.

D.1.2 Nuclear Explosion

Detonating a nuclear device in the vicinity, on the surface or underground a threatening asteroid could yield the desired deflection impulse. This method has been reviewed in (Shapiro et al., 2010) and it was found that it is the most effective method for deflecting the largest objects in the kilometre size region. It may also be applicable for smaller objects if only a short lead time is available. One concern connected with the nuclear explosion method is the possible fragmentation of the asteroid instead of its deflection. This issue is addressed by (Bruck Syal et al., 2013) and (Korycansky and Plesko, 2012).

D.2 Slow Deflection Methods

In contrast to the fast methods, slow deflection methods are characterized by applying a small deflection force over a long time. The examples given are some of the more promising methods but do not represent an exhaustive list.

D.2.1 Gravity Tractor

Gravity tractors depend on the mutual gravitational attraction between objects. In this concept, a satellite with a specific mass is placed in the vicinity of an asteroid in the direction of the desired deflection. By hovering in this position for a long time, the satellite will slowly pull the asteroid in its direction through its gravitational attraction, thereby, imparting the deflection impulse. Gravitational attraction is proportional to satellite mass. Therefore, a heavier satellite is desirable to enhance the deflection action. However, space missions are constrained in their mass for other reasons such as launch vehicle capabilities. Feasibility of the concept has been analysed thoroughly in the literature including (Foster et al., 2013).

D.2.2 Laser Ablation

A high energy laser installed on a satellite can deflect an asteroid. Surface material of the asteroid is ablated by aiming an asteroid at one spot and heating that spot above the evaporation temperature of the material. The ablated material is ejected from the asteroid and thus imparts a linear momentum on the asteroid. A challenge to this method is the high control requirement that is possibly connected to it. The deflection effect could be enhanced over time when the ablated region takes the shape of a nozzle and thus directs the ablation ejecta to direct the impulse. The feasibility has been demonstrated experimentally by Gibbings et al. (2013) and theoretically by Thiry and Vasile (2017).

D.2.3 Ion Beam Shepherd

In this concept, a satellite is placed in the vicinity of the asteroid. It aims a collimated beam of ions at the asteroid and thus pushes the asteroid away. If a control engine is installed that keeps the distance to the asteroid constant, the asteroid can be deflected. The concept is studied by (Bombardelli et al., 2013).

D.3 A Likely Asteroid Threat Scenario

This section outlines how the response to an asteroid threat could reasonably look with the technologies and safeguarding mechanisms available today. Two scenarios are likely to occur and the first version does not allow for a deflection response:

D.3.1 No Deflection

The majority of asteroids is still unobserved because of the relatively young effort to systematically catalogue the asteroid population and because of the performance limitations of the existing observation capabilities. A scenario in which the Earth is struck by a significantly sized asteroid without prior warning remains the most likely scenario today[1].

[1] A subcategory of this scenario is the discovery of the impactor few days before the impact as the object's apparent size and brightness increases while closing in on the Earth. In this case, evacuation of the projected impact region can be a viable response. However, a deflection mission presumably requires a longer lead time than a couple of days.

D.3.2 Deflection

The second scenario allows for a deflection response as enough warning time will be available. The following paragraphs play this scenario out:

Discovery Phase Routine sky observation campaigns discover an object and calculate that there is a collision probability in the future. This scenario will allow for a multi-year asteroid response lead time because it is more likely that a generic asteroid[2] is discovered on its "nominal" orbit rather than under the special condition where its orbit and the Earth's orbit intersect catastrophically in the near future. Thus, the response to an asteroid threat will in all likelihood be a process spanning tens of years. Usually, the calculated impact probability will initially increase as new measurements shrink the uncertainty region of the asteroid's location. Eventually, enough observations become available to shrink the uncertainty region sufficiently to exclude the possibility of a future impact with the Earth. However, in the case that the impact probability continues to increase over time, it has to be evaluated how to respond to this issue.

Tracking Phase Earth based observations of asteroids are very capable but naturally limited in terms of the accuracy they can deliver. The position of a deep space probe that is tracked from Earth is known with significantly higher accuracy because the target is active in this case. Consequently, the position knowledge of an asteroid can be improved greatly by placing an observer spacecraft in the vicinity of the target asteroid. The observer can perform relative position measurements of the asteroid with respect to the spacecraft and the spacecraft can be tracked from the Earth. By combining these measurements, an accurate position estimate of the asteroid can be obtained. This measurement will crucially improve certainty to the question if the asteroid is a threat or if it will miss the Earth in the future. Observation missions have been performed successfully in the past as presented in section 2.2.2 and can be designed for low cost (see AIDA mission, section 2.2.2). An observation mission could be launched to measure the position as well as characterize the asteroid some ten years before the anticipated impact. The characterisation mission has general scientific value and also serves to predict the outcome of a possible deflection mission by determining the asteroids mass, composition and other physical aspects.

Deflection Phase In the event that the accurate position survey of the asteroid yields a likely impact with the Earth, it can be assessed if the mutual gravitational attraction between the observation spacecraft and the asteroid suffices to deflect the asteroid. In this case, the observer would have to be designed as gravity tractor vehicle from the start. Another possible outcome of the physical characterisation and trajectory mapping of the

[2] Especially if the asteroid is of significant size (50 m).

asteroid is that a fast deflection method is required to impart the necessary deflection impulse. It can further be evaluated if a nuclear or kinetic deflection method is more suitable based on the asteroid's composition.

Verification and Correction Phase After utilization of a fast deflection action, the observer can furthermore determine the outcome of the deflection action and verify that the asteroid is now on a miss trajectory. If desirable, the observer could once again act as a gravity tractor to fine tune the asteroid's miss trajectory. This deflection concept yields general scientific return as a minimum mission outcome and enables successful asteroid deflection when utilized to its full potential.

Deflection Scenario Conclusions The modular deflection response ensures that the mission is not designed as a full capability deflection from the start. This helps to keep the initially required investment into the mission low[3]. Furthermore, the modular design allows to tailor the asteroid threat response to changing conditions as new observations become available while the mission is ongoing. In other words, the threat response design is robust to initially unknown physical characteristics of the asteroid. This approach ensures a flexible response that only allocates additional resources when new findings show that they are required.

D.4 Uncertainty in Deflection Outcome

Section D.1.1 hints that every deflection method has some degree of uncertainty associated with it in terms of the direction and magnitude of the delivered deflection impulse. As pointed out in (Schweickart, 2004), the deflection of an asteroid does not necessarily need to occur in a linear way. The magnitude and direction of a deflection force can be varied over time. This would enable to navigate the projected impact point in between high risk areas and would add security to the overall mission as it makes it robust against the event of catastrophic deflection force loss. It is the long-term aim of this work to provide the capabilities to accommodate the possibility of varied deflection force for deflection mission design.

[3]It would be undesirable to design a combined impactor/observer mission from the start when there is still a significant chance that the asteroid might miss the Earth naturally. Considerable resources would have been spent inadequately in this case.

Appendix E

Southampton Asteroid Risk Scale

The results of this thesis can form the basis of a new asteroid risk scale, that in line with previous convention, could be named Southampton Asteroid Risk Scale. The work in the section has been presented at the 2017 Planetary Defense Conference (Rumpf et al., 2017c). In addition to incorporating the concept of risk in terms of vulnerability, exposure and probability, the scale should also consider lead time until impact because far off impacts deserve a lower priority. *Vulnerability* and *exposure* was combined into *consequences* and equations 4.6 and 4.7 provide corresponding values for the diameter range 0-400 m. *Probability* of and *lead time* until an impact is information that is available from government sources such as the NEO risk webpages maintained by ESA (Universita Di Pisa and ESA, 2014) and NASA (NASA, 2014a).

The lead time should also consider that humankind requires a reaction time when a threatening asteroid is discovered in order to capitalize on their ability to deflect the asteroid. It is proposed that the lead time until impact should be shortened by 10 years to account for implementation time of a potential deflection mission. Effectively, the shortened lead time corresponds to the lead time until a decision about the deflection mission should be made and, consequently, could be called *decision lead time*. Furthermore, an impact that is far into the future requires a drastically lower priority than imminent impacts and this should be reflected in the decision lead time term. Equation E.1 reflects these considerations and presents the unit-less decision lead time τ_{decision} as a function of lead time until impact t_{impact} in years. The term reaches a value of one when the decision time is reached, and weighs short lead times heavier (up to factor 5) while decreasing significance for long lead times:

$$\tau_{\text{decision}} = \min\left(\frac{10^2}{t_{\text{impact}}^2}, 5\right) \tag{E.1}$$

In combination, the risk scale equation for the impactor diameter range of 0-50 m is:

$$\text{Southampton Rating} = 0.083 \times 1.14^{1.75L_0} \times P \times \tau_{\text{decision}} \tag{E.2}$$

and for the impactor diameter range of 50-400 m, it is:

$$\text{Southampton Rating} = 4491.33 \times 1.01^{0.98L_0} \times P \times \tau_{\text{decision}} \tag{E.3}$$

where L_0 is the asteroid diameter in meters. The output of this scale has the unit of expected casualties given the current information on the specific asteroid threat.

The proposed risk scale was applied to the three historical objects that received a positive Palermo rating and the results are shown in Table E.1

Asteroid	L_0 [m]	P	t_{impact} [yr]	Torino	Palermo	Southampton
large urgent	140	0.1	10	4	1.25	2200
Apophis	325	0.027	25	4	1.17	776
medium urgent	40	0.1	5	3	0.25	299
1950 DA	1100	3.3×10^{-3}	878	2	-0.017	32
2002 NT7	2000	1×10^{-6}	17	1	-1.2	26
small urgent	19	0.1	5	0	-0.52	3
normal	140	1×10^{-6}	40	0	-4.35	0

Table E.1: Risk scale comparison for artificial and historical impact scenarios based on their maximum threat level. Torino and Palermo scale are unit-less while the Southampton scale is expressed in expected casualties with its basis in risk assessment.

The results in table E.1 provide insight into how the different rating systems compare to each other and the examples are sorted by Southampton scale rating revealing that all scales show the same trend. A *large urgent* impactor is consistently rated highest amongst all scales reflecting its potentially large consequences, high impact probability and imminent threat. However, the Torino and Palermo scales provide abstract numbers that are not directly intuitive, while the Southampton scale is expressed in terms of expected casualties which a human being can grasp naturally. The *Apophis* and *medium urgent* case receive a similar rating on the Southampton scale because of their high impact probability and large size or short lead time, respectively. Interestingly, the *medium urgent* case receives a significantly lower rating in both the Palermo and Torino scale compared to *Apophis*. The *medium urgent* is inspired by the Tunguska event, and we have a good understanding of the potential consequences such an impact could cause. This outcome highlights the fact that small to medium impactors were only attributed with significant damage potential in recent research such as this thesis and (Boslough and Crawford, 2008). The cases of *1950 DA* and *2002 NT7*, both receive

significant risk ratings with 32 and 25 expected casualties, respectively, because of their extreme damage potential. In the case of *1950 DA*, the impact probability is large but the impact is far into the future, while for *2002 NT7*, the impact is very unlikely but the lead time is short. These situations make them comparable. At the lower end of the scale, the *small urgent* case (inspired by Chelyabinsk) receives a low yet significant rating of 3 expected casualties as opposed to insignificant ratings on the Palermo and Torino scale, emphasizing once again the increased attention paid to small impactors in recent research. All hazard scales provide a consistently insignificant rating for the *normal* case of a very unlikely and far off impact event.

It should be noted that the scale would currently only be valid for asteroids up to 400 m in size as this is the range supported by results in this thesis. With caution, the scale may be applied to larger asteroids (as has been done in Table E.1) when the contribution of the consequence term (equations 4.6 and 4.7) is limited to a maximum value of the world population (7.4×10^7 as of 2016). Furthermore, the scale implicitly assumes a mean impact velocity of 16.6 $^{km}/_{s}$ and and an asteroid density of 3100 $^{kg}/_{m^3}$. The scale could be modified to account for impact kinetic energy instead of asteroid diameter. This could be accomplished through additional analysis where the loss parameter space is analysed for variations of impact speed and asteroid density. Such a modification would provide a practical improvement of the risk scale as it would become more sensitive to the specific asteroid situation, while only depending on readily available parameters such as size, impact speed, impact probability and lead time (and an assumed value for density).

Finally a more advanced scale could be built taking full advantage of the method of ARMOR. Here, the impact corridor, including local impact angle and speed variations would be accounted for and the asteroid density could be adjusted to the best estimate value available for the specific asteroid. ARMOR's method could, thus, provide the *consequence* term with higher fidelity and consider impact probability and decision lead time as outlined above.

Appendix F

Residual Risk Analysis

The asteroid impact risk can be resolved as a function of the impactor diameter taking into account the expected impact frequency associated with each size. Fundamentally, the two mechanisms of a larger number of smaller impactors with their correspondingly higher impact frequency and the fact that larger impactors cause significantly more damage are weighted against each other. The analysis performed here allows to identify in which size regime this balance yields the largest hazard for populations on the ground. Similar analysis has been conducted in (Stokes et al., 2003; Harris, 2008; Shapiro et al., 2010; Boslough et al., 2015) but, in contrast, the analysis conducted here, focuses on smaller asteroids up to 400 m in diameter and the average loss per impactor function is based on a more detailed simulation environment. The average loss per impactor size data, including best and worst case scenarios, (Figure 4.20) was combined with the average impact frequency[1] per impactor size (Harris and D'Abramo, 2015) and these information is shown in Figure F.1.

Following the formalism of risk which may be articulated as the product of event frequency and consequences of an event, the average loss per impactor and the impact frequency were multiplied with each other to obtain the risk distribution expressed in expected casualties per year over the size regime of 0-400 m in 0.5 absolute magnitude (H) wide bins (each bin has a width of 0.5 absolute magnitudes and this relates directly to asteroid diameter according to Equation 2.1 using an albedo of $\alpha = 0.14$). The resulting risk distribution is shown in Figure F.2a and the total risk (summation of all bins) over the size range 0-400 m is 32 casualties per year.

However, Figure F.2a does not take into account the fact that humankind has already discovered some asteroids and it is known that an impact from these discovered asteroids in the next 100 years is extremely unlikely. Figure F.2b visualizes the ratio of the asteroid

[1]Note that (Brown et al., 2002) provides an analytical description for impact frequency over asteroid diameter as estimated in 2002.

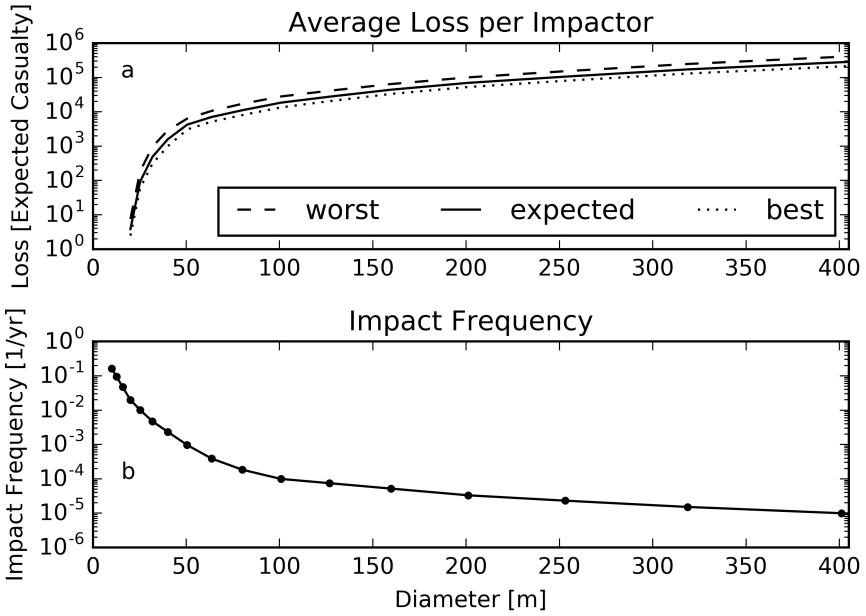

Figure F.1: Average loss per impactor size is shown in plot a. Plot b visualizes the average impact frequency per asteroid size and the markers indicate the mid point of each bin which are 0.5 absolute magnitudes wide.

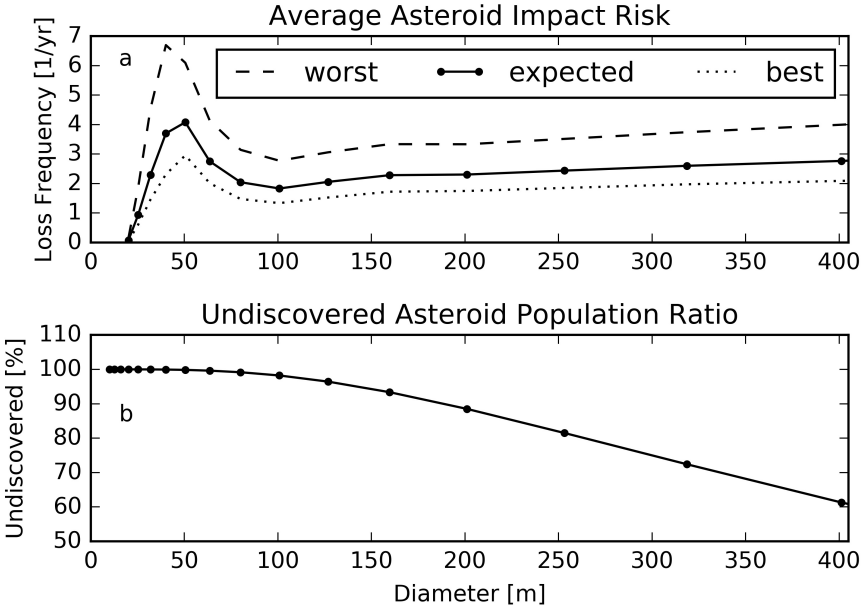

Figure F.2: Risk distribution over asteroid size is shown in plot a. In plot b the ratio of the asteroid population (0-400 m) is shown that is not yet discovered. The markers indicate the mid point of each size bin.

population in each size bin that was still undiscovered at the time of this writing (Harris and D'Abramo, 2015).

The ratio of undiscovered asteroids in each asteroid size bin was obtained with data by Harris and D'Abramo (2015) (Table 2) and this formalism:

$$\text{undiscovered ratio} = \frac{\#_{\text{Asteroid Population(size)}} - \#_{\text{Asteroids Discovered(size)}}}{\#_{\text{Asteroid Population(size)}}} \tag{F.1}$$

Taking into account that some size regimes are better observed than others, the residual risk of the yet undiscovered asteroid population could be calculated: Residual risk was obtained by multiplying the risk-size distribution (Figure F.2a) with the ratio of undiscovered asteroids (Figure F.2b). The residual risk-size distribution is visualized in Figure F.3 and total residual risk over the size regime of 0-400 m is 29 casualties per year.

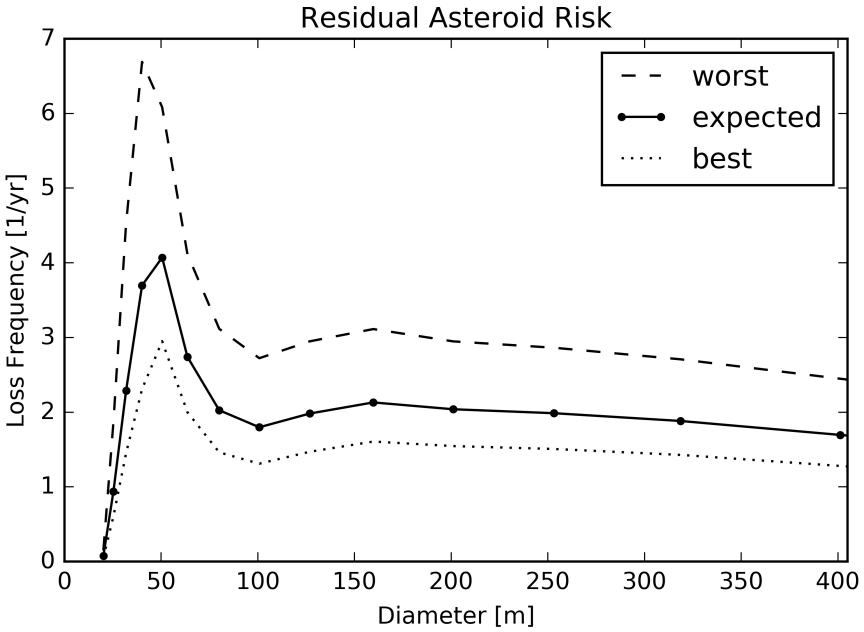

Figure F.3: Residual asteroid impact risk distribution over size. The data considers the risk-size distribution and the ratio of undiscovered asteroids for a given size.

The results in Figures F.2a and F.3 show that impact frequency and damage potential balances around 50 m for a maximum risk value of about six expected casualties per year from this bin alone. It should be noted that the relative variations of best and worst case risk with respect to expected risk align closely with the amount of variation shown in (Stokes et al., 2003). The results also appear robust considering that Boslough et al. (2015) found a risk peak in the same size regime, while other analysis (Stokes et al., 2003; Harris, 2008; Shapiro et al., 2010) focuses on larger asteroids and does not offer the required resolution in the small asteroid sizes to identify this phenomenon. The results represents long term averages and impacts of this size are only expected to occur roughly every 1000 years (Harris and D'Abramo, 2015). However, the damage potential of such an impact is significant with about 4100 casualties on average as shown in this

thesis (Figures 4.20 & F.1a). The vast majority of asteroids remain undiscovered to date (Figure F.2b) and, consequently, there is little difference between the risk and residual risk distributions in Figure F.2a and F.3, respectively. However, as larger asteroids are considered, the knowledge about the location and future trajectory of a larger ratio of the population pays off and residual risk for 400 m objects is about half compared to that of the complete population. This result shows the value of the continued effort to discover larger portions of the overall asteroid population in reducing the overall asteroid impact risk. In the small size range (0-400 m) considered here, the observational knowledge helped to reduce risk from 32 to 29 casualties per year and this situation can be improved through further survey efforts in the future. Residual risk analysis also helps to identify which size regime still yields highest risk today and here it was found that asteroids of about 50 m account for highest risk for the human population. Currently, survey efforts aim to discover large portions of the asteroid population with a minimum size of 140 m (Harris, 2008) but the results here suggest that new surveys should focus on a smaller size regime including 50 m sized objects for effective residual risk reduction.

References

Adamo, D. R. (2012). Earth Risk Corridor Computations for 2011 AG 5 on 5 February 2040.

A'Hearn, M. F., Belton, M. J. S., and Delamere, W. a. (2005). Deep Impact: excavating comet Tempel 1. *Science (New York, N.Y.)*, 310(5746):258–64.

Ailor, W. (2015). 2015 IAA Planetary Defense Conference Summary and Recommendations. In *2015 IAA Planetary Defense Conference*, Rome, Italy. International Academy of Astronautics.

Ailor, W. and Tremayne-Smith, R. (2013). 2013 IAA Planetary Defense Conference White Paper. Technical report, International Academy of Astronautics, Flagstaff, Arizona, USA.

Alvarez, L. W., Alvarez, W., Asaro, F., and Michel, H. V. (1980). Extraterrestrial cause for the cretaceous-tertiary extinction. *Science*, 208(4448):1095–1108.

Artemieva, N. A. and Shuvalov, V. V. (2001). Motion of a fragmented meteoroid through the planetary atmosphere. *Journal of Geophysical Research*, 106(2):3297.

Artemieva, N. A. and Shuvalov, V. V. (2016). From Tunguska to Chelyabinsk via Jupiter. *Annual Review of Earth and Planetary Sciences*, 44(1):37–56.

B612 Foundation, The Economist, and Comprehensive Nuclear-Test-Ban Treaty Organization (2014). Map of Asteroid Impacts larger than 1 kiloton. http://www.economist.com/news/science-and-technology/21601232-skyfalls?fsrc=scn/tw_ec/skyfalls. Accessed 2014-6-6.

Bailey, N. J., Swinerd, G. G., Lewis, H. G., and Crowther, R. (2009). NEOImpactor - a tool for assessing Earth's vulnerability to the NEO impact hazard. In *1st IAA Planetary Defense Conference: Protecting Earth from Asteroids*, page 8, Granada, Spain.

Bailey, N. J., Swinerd, G. G., Lewis, H. G., and Crowther, R. (2010). Global vulnerability to near-Earth object impact. *Risk Management*, 12(1):31–53.

Battjes, J. A. (1974). Surf similarity. In *14th international conference on coastal engineering*, pages 466–480.

Bell, J. F., Davis, D. R., Harmann, W. K., and Gaffey, M. J. (1989). Asteroids - The big picture. In *Asteroids II*, number February 1989, pages 921 – 945. University of Arizona Press, Tuscon.

Berryman, K. (2005). Review of Tsunami Hazard and Risk in New Zealand Review of Tsunami Hazard and Risk in New Zealand. Technical Report September, Institute of Geological & Nuclear Sciences, Lower Hutt, New Zealand.

Binzel, R. P. (2000). The Torino Impact Hazard Scale. *Planetary and Space Science*, 48(4):297–303.

Bombardelli, C., Urrutxua, H., Merino, M., Peláez, J., and Ahedo, E. (2013). The ion beam shepherd: A new concept for asteroid deflection. *Acta Astronautica*, 90(1):98–102.

Borovicka, J., Spurny, P., Brown, P. G., Wiegert, P., Kalenda, P., Clark, D., and Shrbeny, L. (2013). The trajectory, structure and origin of the Chelyabinsk asteroidal impactor. *Nature*, pages 1–13.

Borovička, J. and Kalenda, P. (2003). The Morávka meteorite fall: 4. Meteoroid dynamics and fragmentation in the atmosphere. *Meteoritics & Planetary Science*, 38(7):1023–1043.

Boslough, M. (2013a). Airburst warning and response. *Acta Astronautica*, pages 1–6.

Boslough, M. (2013b). Impact decision support diagrams. *Acta Astronautica*, pages 1–4.

Boslough, M., Brown, P., and Harris, A. (2015). Updated population and risk assessment for airbursts from near-earth objects (NEOs). In *IEEE Aerospace Conference Proceedings*, volume 2015-June, pages 1–12, Big Sky, MT. IEEE.

Boslough, M. and Crawford, D. (2008). Low-altitude airbursts and the impact threat. *International Journal of Impact Engineering*, 35(12):1441–1448.

Boulet, D. L. (1991). *Methods of Orbit Determination for the Microcomputer*. Willmann-Bell, 1 edition.

Britt, D. (2014). The Physical Properties of Near Earth Asteroids. In *steroid Grand Challenge: Virtual Seminar Series*, pages 1–30.

Brown, P. G., Brachet, N., Brown, D., Assink, J. D., Astiz, L., Blaauw, R., Boslough, M., Borovic, J., Ceranna, L., Cooke, W., Drob, D. P., Edwards, W. N., Evers, L. G., Garces, M., Gill, J., Hedlin, M., Kingery, A., Laske, G., Pichon, A. L., Mialle, P., Moser, D. E., Saffer, A., Silber, E. A., Smets, P., Spalding, R. E., Spurny, P., Tagliaferri, E., Uren, D., Weryk, R. J., Whitaker, R., and Krzeminski, Z. (2013). A

500-kiloton airburst over Chelyabinsk and an enhanced hazard from small impactors. *Nature*, pages 1–4.

Brown, P. G., Spalding, R. E., ReVelle, D. O., Tagliaferri, E., and Worden, S. P. (2002). The flux of small near-Earth objects colliding with the Earth. *Nature*, 420(6913):294–6.

Bruck Syal, M., Dearborn, D. S., and Schultz, P. H. (2013). Limits on the use of nuclear explosives for asteroid deflection. *Acta Astronautica*, 90(1):103–111.

Carry, B. (2012). Density of asteroids. *Planetary and Space Science*, 73(1):98–118.

Ceplecha, Z. (1992). Influx of interplanetary bodies onto earth. *Astronomy and Astrophysics (ISSN 0004-6361)*, 263:361–366.

Chapman, C. R. and Morrison, D. (1994). Impacts on the Earth by asteroids and comets: assessing the hazard. *Nature*, 367(January).

Chapman, C. R., Williams, J. G., and Hartmann, W. K. (1978). The Asteroids. *Annual Review of Astronomy and Astrophysics*, 16:33–75.

Cheng, A. F., Rivkin, A. S., Reed, C., Barnouin, O., Fletcher, Z., Ernst, C., Galvez, A., Carnelli, I., and Michel, P. (2013). AIDA: ASTEROID IMPACT & DEFLECTION ASSESSMENT. In *64th International Astronautical Congress*, pages 1–8, Beijing, China.

Chesley, S., Chodas, P. W., Milani, A., Valsecchi, G., and Yeomans, D. K. (2002). Quantifying the Risk Posed by Potential Earth Impacts. *Icarus*, 159(2):423–432.

Chesley, S. R., Chodas, P. W., and Yeomans, D. K. (2014). Asteroid 2008 TC3 Strikes Earth: Predictions and Observations Agree.

Chesley, S. R., Farnocchia, D., Brown, P. G., and Chodas, P. W. (2015). Orbit Estimation for Late Warning Asteroid Impacts: The Case of 2014 AA. In *IEEE Aerospace Conference*, pages 1–8, Big Sky, MT. IEEE.

Chesley, S. R. and Spahr, T. B. (2004). Earth Impactors : Orbital Characteristics and Warning Times. In Belton, M., Morgan, T., Samarsinha, N., and Yeomans, D. K., editors, *Mitigation of Hazardous Comets and Asteroids*, chapter 2, pages 22–37. University Press Cambridge, Cambridge, UK.

Chesley, S. R. and Ward, S. N. (2006). A Quantitative Assessment of the Human and Economic Hazard from Impact-generated Tsunami. *Natural Hazards*, 38(3):355–374.

Chyba, C. F., Thomas, P. J., and Zahnle, K. J. (1993). The 1908 Tunguska explosion: atmospheric disruption of a stony asteroid. *Nature*, 361(January).

CIESIN, Columbia University, United Nations FAO, and CIAT (2005). Gridded Population of the World, Version 3 (GPWv3): Population Count Grid, Future Estimates.

Collins, G. S., Lynch, E., McAdam, R., and Davison, T. (2016). A numerical assessment of simple airblast models of impact airbursts. *Meteoritics and Planetary Science*, submitted.

Collins, G. S., Melosh, H. J., and Marcus, R. a. (2005). Earth Impact Effects Program: A Web-based computer program for calculating the regional environmental consequences of a meteoroid impact on Earth. *Meteoritics & Planetary Science*, 40(6):817–840.

Collins, G. S., Wünnemann, K., Artemieva, N. a., and Pierazzo, E. (2012). *Numerical Modelling of Impact Processes, in Impact Cratering: Processes and Products*. Wiley & Sons, Chichester, UK.

Commons (2014). Asteroids and Inner Solar System. http://en.wikipedia.org/wiki/Asteroid#mediaviewer/File:InnerSolarSystem-en.png. Accessed 2014-07-04.

Curtis, H. D. (2012). *Orbital Mechanics for Engineering Students*. Elsevier Butterworth-Heinemann, Oxford, UK, 2 edition.

Dachwald, B., Kahle, R., and Wie, B. (2007). Head-On Impact Deflection of NEAs : A Case Study for 99942 Apophis. In *2007 AIAA Planetary Defense Conference*, number March, pages 5–8, Washington D.C.

DeMeo, F. E., Alexander, C. M. O., Walsh, K. J., Chapman, C. R., and Binzel, R. P. (2015). The Compositional Structure of the Asteroid Belt. In Michel, P., DeMeo, F. E., and Bottke, W., editors, *Asteroids IV*, chapter 2.1.1, pages 13–42. Arizona, USA.

Diffey, B. L. (2011). An overview analysis of the time people spend outdoors. *British Journal of Dermatology*, 164(4):848–854.

Drolshagen, G. (2014). Terms of Reference for the Near-Earth Object Threat Mitigation Space Missions Planning Advisory Group (SMPAG). Technical report, SMPAG, Darmstadt, Germany.

Durda, D. D., Movshovitz, N., Richardson, D. C., Asphaug, E., Morgan, A., Rawlings, A. R., and Vest, C. (2011). Experimental determination of the coefficient of restitution for meter-scale granite spheres. *Icarus*, 211(1):849–855.

Dworkin, J. (2014). OSIRIS-REx Update. In *Small Bodies Assessment Group*, Greenbelt, USA. Goddard Space Flight Center.

EDEIS, Tsunami Laboratory, and ICMMG SD RAS (2006). Earth Global Impact Features.

Editors of Encyclopædia Britannica (2016). Continental shelf.

Folkner, W. M., Williams, J. G., Boggs, D. H., Park, R. S., and Kuchynka, P. (2014). The Planetary and Lunar Ephemerides DE430 and DE431. Technical report, NASA.

Foster, C., Bellerose, J., Mauro, D., and Jaroux, B. (2013). Mission concepts and operations for asteroid mitigation involving multiple gravity tractors. *Acta Astronautica*, 90(1):112–118.

French, J., Ing, R., Von Allmen, S., and Wood, R. (1983). Mortality from flash floods: a review of national weather service reports, 1969-81. *Public health reports*, 98(6):584–588.

Fritz, H. M., Kongko, W., Moore, A., McAdoo, B., Goff, J., Harbitz, C., Uslu, B., Kalligeris, N., Suteja, D., Kalsum, K., Titov, V., Gusman, A., Latief, H., Santoso, E., Sujoko, S., Djulkarnaen, D., Sunendar, H., and Synolakis, C. (2007). Extreme runup from the 17 July 2006 Java tsunami. *Geophysical Research Letters*, 34(July 2006):1–5.

Gallant, J., Gladman, B., and Ćuk, M. (2009). Current bombardment of the Earth-Moon system: Emphasis on cratering asymmetries. *Icarus*, 202(2):371–382.

Gibbings, A., Vasile, M., Watson, I., Hopkins, J.-M., and Burns, D. (2013). Experimental analysis of laser ablated plumes for asteroid deflection and exploitation. *Acta Astronautica*, 90(1):85–97.

Giorgini, J., Benner, L. A., Ostro, S., Nolan, M., and Busch, M. (2008). Predicting the Earth encounters of (99942) Apophis. *Icarus*, 193(1):1–19.

Giorgini, J. and Yeomans, D. K. (2013). Horizons (Version 3.75).

Gisler, G., Weaver, R., and Gittings, M. (2011). Calculations of asteroid impacts into deep and shallow water. *Pure and Applied Geophysics*, 168:1187–1198.

Glasstone, S. and Dolan, P. J. (1977). *The Effects of Nuclear Weapons*. United States Department of Defense & Energy Research and Development Administration, USA, third edit edition.

Gradie, J. and Tedesco, E. (1982). Compositional Structure of the Asteroid Belt. *Science*, 216:1405–1407.

Grav, T., Jedicke, R., Denneau, L., Chesley, S., Holman, M. J., and Spahr, T. B. (2011). The Pan-STARRS Synthetic Solar System Model: A Tool for Testing and Efficiency Determination of the Moving Object Processing System. *Publications of the Astronomical Society of the Pacific*, 123(902):423–447.

Halliday, I. (1964). The Variation in the Frequency of Meteorite Impact with Geographic Latitude. *Meteoritics*, 2(3):271–278.

Halliday, I. and Griffin, A. A. (1982). A study of the relative rates of meteorite falls on the earth's surface. *Meteoritics*, 17(I):31.

Hanus, J., Viikinkosko, M., Marchis, F., Durech, J., Kaasalainen, M., Delbo, M., Herald, D., Frappa, E., Hayamizu, T., Kerr, S., Preston, S., Timerson, B., and Talbot, J. (2016). Volumes and bulk densities of forty asteroids from ADAM shape modeling. *Astronomy and Astrophysics*, under revi:1–49.

Harris, A. (2008). What Spaceguard did. *Nature*, 453(June):1178–1179.

Harris, A. (2013). The Value of Enhanced NEO Surveys. In *Planetary Defense Conference*, Flagstaff, Arizona, USA.

Harris, A. (2014). NEA populations and impact frequency. In *Asteroid Grand Challenge: Virtual Seminar Series*, pages 1–30. Solar System Exploration Research Virtual Institute.

Harris, A. W. and D'Abramo, G. (2015). The population of near-earth asteroids. *Icarus*, (May).

Hills, J. G. and Goda, M. P. (1993). The Fragmentation of Small Asteroids in the Atmosphere. *The Astronomical Journal*, 105(3):1114–1144.

Hunt, I. A. J. (1959). Design of Seawalls and Breakwaters. *Journal of the Waterways and Harbors Division*, 85(3):123–152.

Ivanov, B. A., Deniem, D., and Neukum, G. (1997). Implementation of Dynamic Strength Models into 2D Hydrocodes: Applications for Atmospheric Breakup and Impact Cratering. *International Journal of Impact Engineering*, 20:411–430.

Ivezic, Z., Tyson, J. A., Acosta, E., Allsman, R., Anderson, S. F., Andrew, J., Angel, R., Axelrod, T., Barr, J. D., Becker, a. C., Becla, J., Beldica, C., Blandford, R. D., Bloom, J. S., Borne, K., Brandt, W. N., Brown, M. E., Bullock, J. S., Burke, D. L., Chandrasekharan, S., Chesley, S. R., Claver, C. F., Connolly, A., Cook, K. H., Cooray, A., Covey, K. R., Cribbs, C., Cutri, R., Daues, G., Delgado, F., Ferguson, H., Gawiser, E., Geary, J. C., Gee, P., Geha, M., Gibson, R. R., Gilmore, D. K., Gressler, W. J., Hogan, C., Huffer, M. E., Jacoby, S. H., Jain, B., Jernigan, J. G., Jones, R. L., Juric, M., Kahn, S. M., Kalirai, J. S., Kantor, J. P., Kessler, R., Kirkby, D., Knox, L., Krabbendam, V. L., Krughoff, S., Kulkarni, S., Lambert, R., Levine, D., Liang, M., Lim, K.-T., Lupton, R. H., Marshall, P., Marshall, S., May, M., Miller, M., Mills, D. J., Monet, D. G., Neill, D. R., Nordby, M., O'Connor, P., Oliver, J., Olivier, S. S., Olsen, K., Owen, R. E., Peterson, J. R., Petry, C. E., Pierfederici, F., Pietrowicz, S., Pike, R., Pinto, P. A., Plante, R., Radeka, V., Rasmussen, A., Ridgway, S. T., Rosing, W., Saha, A., Schalk, T. L., Schindler, R. H., Schneider, D. P., Schumacher, G., Sebag, J., Seppala, L. G., Shipsey, I., Silvestri, N., Smith, J. A., Smith, R. C., Strauss, M. A., Stubbs, C. W., Sweeney, D., Szalay, A., Thaler, J. J., Vanden Berk, D., Walkowicz, L., Warner, M., Willman, B., Wittman, D., Wolff, S. C., Wood-Vasey, W. M., Yoachim, P., Zhan, H., Berk, D. V., Walkowicz, L., Warner, M., Willman, B.,

Wittman, D., Wolff, S. C., Wood-Vasey, W. M., Yoachim, P., and Zhan, H. (2014). LSST: from Science Drivers to Reference Design and Anticipated Data Products. Technical report.

Izzo, D., Bourdoux, A., Walker, R., and Ongaro, F. (2006). Optimal trajectories for the impulsive deflection of near earth objects. *Acta Astronautica*, 59(1-5):294–300.

Keller, H. U., Arpigny, C., Barbieri, C., Bonnet, R.-m., Cazes, S., and Coradini, M. (1986). First Halley Multicolour Camera imaging results from Giotto. *Nature*, 321:320 – 326.

Klepeis, N. E., Nelson, W. C., Ott, W. R., Robinson, J. P., Tsang, A. M., Switzer, P., Behar, J. V., Hern, S. C., and Engelmann, W. H. (2001). The National Human Activity Pattern Survey (NHAPS): a resource for assessing exposure to environmental pollutants. *Journal of exposure analysis and environmental epidemiology*, 11(3):231–252.

Korycansky, D. and Plesko, C. (2012). Effects of stand-off bursts on rubble-pile targets: Evaluation of a hazardous asteroid mitigation strategy. *Acta Astronautica*, 73:10–22.

Korycansky, D. G. and Lynett, P. J. (2007). Run-up from impact tsunami. *Geophysical Journal International*, 170(3):1076–1088.

Ladue, J. (2016). Private Correspondence.

Le Feuvre, M. and Wieczorek, M. A. (2006). The Asymmetric Cratering History of the Terrestrial Planets: Latitudinal Effect. In *37th Annual Lunar and Planetary Science Conference*, League City, Texas. Lunar and Planetary Institute.

Levitan, M. L., Jorgensen, D. P., Kuligowski, E. D., Lombardo, F. T., and Phan, L. T. (2014). Investigation of the May 22, 2011 tornado in Joplin, Missouri. Technical report, National Institute of Standards and Technology, USA.

Mainzer, A., Bauer, J., Cutri, R. M., and Grav, T. (2014). Initial Performance of the NEOWISE Reactivation Mission. *The Astrophysical Journal*, pages 1–39.

Mathias, D. L., Wheeler, L. F., and Dotson, J. L. (2017). A Probabilistic Asteroid Impact Risk Model: Assessment of Sub-300 m Impacts. *Icarus*, 289:106–119.

McInnes, C. R. (2004). Deflection of near-Earth asteroids by kinetic energy impacts from retrograde orbits. *Planetary and Space Science*, 52(7):587–590.

Melosh, H. J. (2003). IMPACT-GENERATED TSUNAMIS: AN OVER-RATED HAZARD. In *Lunar and Planetary Science*, number XXXIV.

Milani, A. (2004). Virtual asteroids and virtual impactors. In *Proceedings of the International Astronomical Union*, pages 219–228.

Milani, A., Chesley, S., Chodas, P. W., and Valsecchi, G. B. (2002). Asteroid Close Approaches: Analysis and Potential Impact Detection. In Bottke, W., Cellino, A., Paolicchi, P., and Binzel, R., editors, *Asteroids III*, chapter 2.1, pages 55–69. University of Arizona Press and Lunar and Planetary Institute.

Milani, A., Chesley, S. R., Boattini, A., and Valsecchi, G. B. (2000). Virtual Impactors: Search and Destroy. *Icarus*, 145(1):12–24.

Milani, A., Chesley, S. R., Sansaturio, M. E., Tommei, G., and Valsecchi, G. B. (2005). Nonlinear impact monitoring: line of variation searches for impactors. *Icarus*, 173(2):362–384.

Milani, A., Gronchi, G. F., Tommei, G., Bernardi, F., Cicalo, S., Farnocchia, D., Knezevic, Z., Novakovic, B., Sansaturio, M. E., Arratia, O., Valsecchi, G. B., Chesley, S. R., Carpino, M., Muinonen, K., Cattaneo, L., Baccili, S., and La Spina, A. (1997). The OrbFit Software Package. http://adams.dm.unipi.it/orbfit/. Accessed 2015-01-08.

Morrison, D. (1992). Spaeguard Survey Report. Technical report, Jet Propulsion Laboratory, Pasadena, California.

NASA (2006). 2006 Near-Earth Object Survey and Deflection Study. Technical Report December, NASA.

NASA (2014a). NASA NEO Impact Risk. http://neo.jpl.nasa.gov/risk/. Accessed 2014-06-09.

NASA (2014b). World Bolide Events 1994-2013.

Nemtchinov, I. V., Popova, O. P., Shuvalov, V. V., and Svetsov, V. V. (1994). Radiation emitted during the flight of asteroids and comets through the atmosphere. *Planetary and Space Science*, 42(6):491–506.

Nemtchinov, I. V., Shuvalov, V. V., Artemieva, N. A., Ivanov, B. A., Kosarev, I. B., and Trubetskaya, I. A. (1998). Light flashes caused by meteroid impacts on the lunar surface. *Solar System Research*, (32):99–114.

NOAA (2015). NOAA's National Weather Service, Storm Prediction Center, Killer Tornados by Year. http://www.spc.noaa.gov/climo/historical.html. Accessed 2015-04-28.

Norlund, C. (2013). *Evacuation Simulation Modelling in the event of a Near Earth Object impact*. PhD thesis, University of Southampton.

Ortiz, J., Sada, P., Bellot Rubio, L. R., Aceituno, F., Aceituno, J., Gutierrez, P., and Thiele, U. (2000). Optical detection of meteoroidal impacts on the Moon. *Nature*, 405(6789):921–3.

Patterson, T. and US National Park Service (2015). CleanTOPO2.

Paul, B. K. and Stimers, M. (2014). Spatial analyses of the 2011 Joplin tornado mortality: Deaths by interpolated damage zones and location of victims. *Weather Climate and Society*, 6(2):161–174.

Pettit, D. (2012). Earth Photography: It's Harder Than It Looks. http://www.airspacemag.com/daily-planet/earth-photography-its-harder-than-it-looks-108176156/?no-ist. Accessed 2014-07-03.

Phillips, B., Bessey, P. Q., Casavant, C., Edelman, L., Kemalyan, N., Lentz, C., Reigart, C., and Schurr, M. (2012). National Burn Repository Report of Data From 2002-2011. Technical report, American Burn Association, Chicago, IL.

Plane, J. M. C. (2012). Cosmic dust in the earth's atmosphere. *Chemical Society Reviews*, 41(19):6507.

Pomonis, A., Spence, R., and Baxter, P. (1999). Risk assessment of residential buildings for an eruption of Furnas Volcano, Sao Miguel, the Azores. *Journal of Volcanology and Geothermal Research*, 92(1-2):107–131.

Popova, O. P., Jenniskens, P., and Emel'yanenko, V. (2013). Chelyabinsk airburst, damage assessment, meteorite recovery, and characterization. *Science (New York, N.Y.)*, 342(6162):1069–73.

Radhakrishnan, K. and Hindmarsh, A. C. (1993). Description and Use of LSODE, the Livermore Solver for Ordinary Differential Equations. Technical report, NASA - Lawrence Livermore National Laboratory, Livermore, CA.

Register, P. J., Mathias, D. L., and Wheeler, L. F. (2017). Asteroid fragmentation approaches for modeling atmospheric energy deposition. *Icarus*, 284:157–166.

Reinhardt, J. C., Chen, X., Liu, W., Manchev, P., and Pate-Cornell, M. E. (2016). Asteroid Risk Assessment: A Probabilistic Approach. *Risk Analysis*, 36(2):244–261.

Rendtel, J. and Knoefel, A. (1989). Analysis Of Annual And Diurnal Variation of Fireball Rates And The Population Index Of Fireballs From Different Compilations Of Visual Observations. *Bulletin of the Astronomical Institutes of Czechoslovakia*, 40(1):53–62.

Rumpf, C. M., Lewis, H. G., and Atkinson, P. M. (2015). GLOBAL IMPACT DISTRIBUTION OF ASTEROIDS AND AFFECTED POPULATION. In *IAA Planetary Defense Conference*, number 4th.

Rumpf, C. M., Lewis, H. G., and Atkinson, P. M. (2016a). On the influence of impact effect modelling for global asteroid impact risk distribution. *Acta Astronautica*, 123:165–170.

Rumpf, C. M., Lewis, H. G., and Atkinson, P. M. (2016b). The global impact distribution of Near-Earth objects. *Icarus*, 265:209–217.

Rumpf, C. M., Lewis, H. G., and Atkinson, P. M. (2017a). Asteroid impact effects and their immediate hazards for human populations. *Geophysical Research Letters*, 44.

Rumpf, C. M., Lewis, H. G., and Atkinson, P. M. (2017b). Population Vulnerability Models for Asteroid Impact Risk Assessment. *Meteoritics and Planetary Science*, accepted.

Rumpf, C. M., Lewis, H. G., and Atkinson, P. M. (2017c). Southampton Asteroid Impact Hazard Scale. In *5th IAA Planetary Defense Conference*, number May, Tokyo, Japan. IAA.

Schultz, P. H. and Gault, D. E. (1975). Seismic Effects From Major Basin Formations on the Moon and Mercury. *The Moon*, 12:159–177.

Schweickart, R. L. (2004). THE REAL DEFLECTION DILEMMA. In *2004 Planetary Defense Conference: Protecting Earth from Asteroids*, pages 1–6, Orange County, California.

Schweickart, R. L. (2007). THE NEO THREAT : INTERNATIONAL POLICY ISSUES. In *2007 AIAA Planetary Defense Conference*, pages 1–6, Washington D.C.

Schweickart, R. L. (2009). Decision program on asteroid threat mitigation. *Acta Astronautica*, 65(9-10):1402–1408.

Seidelmann, P. K. (1992). *Explanatory supplement to the astronomical almanac*. University Science Books, USA.

Shapiro, I. I., Vilas, F., A'Hearn, M., Cheng, A. F., Abell, P., Benner, L. A., Belton, M. J. S., Boslough, M., Chapman, C. R., Close, S., Day, D. D., and Jackson, P. (2010). Defending Planet Earth : Near-Earth Object Surveys and Hazard Mitigation Strategies. Technical report, National Research Council, Washington D.C.

Shoemaker, E. M., Brouwer, D., Dollfus, A., Evans, J. V., Fessenkov, V. G., Grainger, J. F., Groves, G. W., Hori, G.-I., Kopal, Z., Koziel, K., Kozyrev, N. A., Link, F., Ring, J., Sinton, W. M., and Urey, H. C. (1962). *PHYSICS and ASTRONOMY of the MOON*. Academic Press Inc, London, UK.

Shuvalov, V. V., Svettsov, V. V., and Trubetskaya, I. a. (2013). An estimate for the size of the area of damage on the Earth's surface after impacts of 10–300-m asteroids. *Solar System Research*, 47(4):260–267.

Silber, E. a., ReVelle, D. O., Brown, P. G., and Edwards, W. N. (2009). An estimate of the terrestrial influx of large meteoroids from infrasonic measurements. *Journal of Geophysical Research*, 114(E8):E08006.

Sinaga, T. P. T., Nugroho, A., Lee, Y. W., and Suh, Y. (2011). GIS mapping of tsunami vulnerability: Case study of the Jembrana regency in Bali, Indonesia. *KSCE Journal of Civil Engineering*, 15(3):537–543.

Stokes, G. H., Yeomans, D. K., Bottke, W., Jewitt, D., Chesley, S. R., Kelso, T. S., Evans, J. B., McMillan, R. S., Gold, R. E., Spahr, T. B., Harris, A. W., and Worden, S. P. (2003). Study to determine the feasibility of extending the search for near-Earth objects to smaller limiting diameters. Technical report, NASA, Washington D.C.

Thiry, N. and Vasile, M. (2017). Theoretical peak performance and optical constraints for the deflection of an S-type asteroid with a continuous wave laser. *Advances in Space Research*, 59(5):1353–1367.

Toon, O. B. and Covey, C. (1997). Environmental Impacts Perturbations and Caused By the of Asteroids Comets. *Geophysics*, (96):41–78.

Trades Union Congress (2012). Average Commuting Times in UK.

Tsou, P. (2003). Wild 2 and interstellar sample collection and Earth return. *Journal of Geophysical Research*, 108(E10):8113.

UNCOPOUS and ESA (2014). Space Missions Planning Advisory Group - Homepage. http://cosmos.esa.int/web/smpag/home. Accessed 27-6-2014.

Universita Di Pisa and ESA (2014). NEODyS-2 Risk Page. http://newton.dm.unipi.it/neodys/index.php?pc=4.1. Accessed 2014-06-09.

University of New Brunswick (2014). Planetary and Space Science Centre.

U.S. Census Bureau (2011). Average Commute Times in the United States.

US Geological Survey (2015). The Severity of an Earthquake.

Van Dorn, W. G., Le Mehaute, B., and Hwang, L.-S. (1968). *Handbook of Explosion-Generated Water Waves.* Number TC-130. Office of Naval Research, Washington D.C.

Veverka, J., Klaasen, K. P., A'Hearn, M., Belton, M. J. S., Brownlee, D., Chesley, S., Clark, B., and Economou, T. (2012). A Second Encounter with 9P/Tempel 1: Overview of Stardust-NExT Results. *Icarus*, page 6171.

Wall, M. (2016). Earth Vulnerable to Major Asteroid Strike, White House Science Chief Says. http://www.space.com/34070-earth-vulnerable-to-major-asteroid-strike.html. Accessed 2016-09-26.

Ward, S. N. and Asphaug, E. (2000). Asteroid Impact Tsunami: A Probabilistic Hazard Assessment. *Icarus*, 145:64–78.

Weiss, R., Wünnemann, K., and Bahlburg, H. (2006). Numerical modelling of generation, propagation and run-up of tsunamis caused by oceanic impacts: Model strategy and technical solutions. *Geophysical Journal International*, 167:77–88.

Wertz, J. R., Everett, D. F., and Puschell, J. J. (2011). *Space Mission Engineering: The New SMAD*. Microcosm Press.

Wind Science and Engineering Center (2006). A Recommendation for an Enhanced Fujita Scale (EF-Scale). Technical report, Texas Tech University, Lubbock, Texas.

Wu, S., Jin, J., and Pan, T. (2015). Empirical seismic vulnerability curve for mortality: case study of China. *Natural Hazards*, 77(2):645–662.

Wünnemann, K., Collins, G. S., and Weiss, R. (2010). Impact of a cosmic body into Earth'S Ocean and the generation of large tsunami waves: Insight from numerical modeling. *Reviews of Geophysics*, 48(2009):1–26.

Wurman, J., Alexander, C., Robinson, P., and Richardson, Y. (2007). Low-level winds in tornadoes and potential catastrophic tornado impacts in urban areas. *Bulletin of the American Meteorological Society*, 88(1):31–46.

Zel'dovich, Y. B. and Raizer, Y. P. (1966). *Physics of Shock Waves and High-Temperature Hydrodynamic Phenomena*. Academic Press, New York.

Zellner, B. (1979). Asteroid taxonomy and the distribution of the compositional types. In Gehrels, T., editor, *Asteroids*, pages 783–806.